An Experimental Study of Fusion of Vortex Rings

Thesis by

Paul Russell Schatzle

In Partial Fulfillment
of the Requirements for the Degree of
Doctor of Philosophy

California Institute of Technology
Pasadena, California

1987
(Submitted 15 May 1987)

In memory of

Buckaroo Banzai

ACKNOWLEDGMENTS

I would like to take this opportunity to thank all of my friends at GALCIT for their encouragement, patience, and sense of humor over the past few years. Their contributions in the laboratory and in the hallways were substantial and always appreciated.

I would also like to thank the National Science Foundation for their financial support under grant MEA-8315042, and the Douglas Aircraft Corporation for providing me with a fellowship during my first year at Caltech.

I am grateful to my advisor, Donald Coles, for sharing his broad knowledge and keen sense of experimental technique with me. His deliberate approach to problem-solving will serve as a guide for many years to come.

I wish to thank my mother for taking me seriously and my father for not taking me seriously.

Most of all, I want to thank my wife, Gail Vanderlee...she knows why.

ABSTRACT

A two-component laser-Doppler velocimeter with frequency bias is used to measure the velocity field produced by the oblique collision of two laminar vortex rings. The Reynolds number, defined here as the ratio of ring circulation to kinematic viscosity, is about 1800. The rings are generated underwater and approach each other along intersecting paths. The plane defined by the two paths is a plane of symmetry, and is the plane in which the measurements were done. The out-of-plane components of vorticity and strain rate are computed from finite differences of the velocity data. The state of the rings prior to the collision is determined in order to provide a set of starting conditions for future numerical simulations. In addition, the circulation of each vortex core is computed as a function of time during the collision.

The principal result of this work is that the circulation of each vortex core is observed to decrease during the interaction; furthermore, the fluid viscosity is shown to be responsible for this decrease. The exact mechanism by which the reduction in circulation is effected is unclear, but it appears to be related to the out-of-plane stretching. A time scale is proposed for this cancellation process which combines the effects of viscosity and stretching.

The measurements also show that the structure of the vorticity field changes during the collision. In particular, each vortex core is observed to split into two vortices under the action of the local in-plane strain field.

TABLE OF CONTENTS

LIST OF FIGURES

LIST OF TABLES

LIST OF SYMBOLS

Symbol	Description
AR	Amplitude ratio of digital filter
d	Vortex core diameter
L_p	Piston stroke
r	Radial distance out from center of vortex core
R_m	Radius of circle tangent to mouth of vortex guns
t_c	Time scale of cancellation process
u	Fluid velocity along x-axis
U_p	Piston speed
v	Fluid velocity along y-axis
w	Fluid velocity along z-axis
Δx	Grid point spacing in x-direction
Δz	Grid point spacing in z-direction
Γ	Circulation
ε	A measure of the strain rate
θ	Azimuthal coordinate around center of vortex core
θ_g	Gun-to-Gun angle
ν	Kinematic viscosity of the fluid
ω	Vorticity
∇^2	Laplacian operator
$\vec{\cdot}$	Vector quantity
$\bar{\cdot}$	Averaged quantity

CHAPTER 1

INTRODUCTION

A large part of contemporary research into turbulent fluid motion has as its basis the concept of coherent structure. According to this concept, turbulent shear flows are not entirely random, but instead exhibit some degree of spatial organization or coherence. In particular, it is believed that the observed structural features correspond to organized regions of vorticity. The presence of such structures in the flow would suggest that it might be possible to describe turbulence in terms of "...the creation, evolution, interaction, and decay" of these structures (Saffman 1981). This thesis is a contribution toward understanding a part of this process, namely, the interaction of vortex structures.

1.1 Description of Process

A few definitions are in order before proceeding further. In subsequent discussions, a *vortex line* will refer to a line that is everywhere tangent to the local vorticity vector, a *vortex tube* will refer to the collection of all vortex lines passing through a closed curve in the fluid, and a *vortex filament* will refer to a vortex tube embedded in an otherwise irrotational flow. A *vortex ring* is then just a vortex filament that closes on itself.

The fluid phenomenon of interest in the present study is a particular type of vortex interaction in which two laminar vortex rings come into contact. It is assumed that the features exhibited by this flow will be shared, at least qualitatively, by more general types of vortex interaction. This particular vortical structure was chosen for study because of the relative ease with which it can be produced, and because the generation process can be made repeatable. In addition, the collision of two such structures can be made to occur in a quiescent environment at any desired time and place.

The situation is depicted in Figs. 1.1 and 1.2. These photographs show the various stages in the collision from two orthogonal viewpoints. The vortex rings approach one another along intersecting paths and are observed to touch in photo number 4. In photo 6, the two vortices appear to have joined into a single structure, a process referred to as *vortex fusion.* The distorted ring then evolves under the influence of its self-induced velocity into a geometrical configuration in which two parts of the vortex again come into contact (photo 17 or 18). At this point, the vortex appears to split back into two vortex rings, a process referred to as *vortex fission.* It is believed that the fusion and fission processes are fundamentally the same, with any observed differences being attributable to differences in the collision geometries.

The impression made by the photographs is that vortex lines within a filament are somehow cut and then joined to corresponding lines in the other filament. There is an implied cancellation of vorticity as the vortex lines touch, and subsequent regeneration of vorticity as the reconnected lines move apart. In the literature, this process is referred to as *reconnection.* The mechanism by which reconnection occurs is unknown, but it is generally supposed that the fluid viscosity is somehow responsible.

1.2 Previous Investigations

1.2.1 Experimental Work. The earliest published account of vortex fusion seems to be that of Wood (1901). He described the fusion of two vortex rings moving side-by-side in air and published a sequence of photographs depicting the process. A similar study was conducted a few years later by Northrup (1912), except that the fluid medium in that case was water. Northrup presented a series of stereoscopic images which showed the union of two vortex rings as they moved side-by-side. Neither of these investigators mentioned the subsequent occurrence of fission, and their photographs do not suggest such an occurrence. The first observers to report both fusion and fission appear to be Kambe and Takao (1971), who published stroboscopic photographs of the phenomena and gave an interpretation of what they saw. They recognized, for example, that vortex fission did not always occur and stated that they observed the process only within a narrow range of the initial impulse of the rings. However, they gave no

indication of the size of the critical range. The suggestion of a critical range was later explored by Oshima and Asaka (1975, 1977a). In their work, both the initial impulse imparted to the rings and the distance between the rings were varied. They were able to organize their data to indicate the range of parameters for which fusion would be followed by fission.

While all of the work thus far has dealt with the interaction of rings moving side-by-side, Fohl and Turner (1975) studied the collision of two rings travelling along intersecting paths in water. They reported the existence of a critical approach angle above which fusion and fission were always observed. Below this critical angle, fusion occurred, but was not always followed by fission. This uncertainty in the outcome of the collision below the critical angle suggests one of two possibilities; either the vortex rings were turbulent prior to the collision, or the generation conditions were not identical from one set of rings to the next. Each of these conditions complicates the study of the fusion and fission processes. Whereas the work of Fohl and Turner was carried out for a single value of the Reynold's number, Oshima and Asaka (1977b) studied the collision of two vortex rings in air for a variety of approach speeds and collision angles. From flow visualization, they identified six possible final states of the rings for various initial conditions. Two of the final states are fusion alone and fusion followed by fission; the significance of the four remaining states is unclear.

To date, all of the published experimental work on vortex ring collisions has relied exclusively on flow visualization. Although Oshima (private communication, 1986a) has recently undertaken a set of velocity measurements using an X-wire probe to study the collision of two rings in air, the results of this study are not yet available in usable form.

1.2.2 Numerical Work. Most numerical simulations of vortex fusion have employed vortex methods with various degrees of sophistication. These methods are essentially inviscid. Since the fluid can be considered inviscid throughout most of the flowfield, the global dynamic behavior of the vortex filaments is fairly well predicted by these methods. However, when the filaments come close together, the simulations predict fluid velocities that are much higher than one would reasonably expect. The viscous effect is evidently important at these smaller scales,

and users of vortex methods have addressed this issue in various ways.

For example, the first simulation of the fusion of two vortex rings was that of Leonard (1974). In his model, each ring was divided into a number of segments and each segment was moved according to the Biot-Savart law. In addition, the diameter of each core segment was allowed to vary locally in a manner that included the effects of stretching and diffusion. The use of such a core model allows the vortex filaments to approach one another more closely than would otherwise be possible. When the cores of the two filaments overlapped by an appreciable amount, the geometry of the filament was redefined (to mimic the reconnection process) and the simulation was allowed to continue. The resulting motion of the filaments was consistent, at least qualitatively, with the experimentally observed behavior of the rings.

In more recent work (Anderson and Greengard 1984, Shirayama and Kuwahara 1984, Oshima and Kuwahara 1984, Oshima 1986b), attention has been focussed on a computational scheme that is loosely referred to as the "stick" method. In this scheme, the three-dimensional vorticity field is discretized into a number of unconnected segments (or "sticks"), and the motion of each segment is followed independently of the motion of neighboring segments. This method has the potential advantage of modelling reconnection directly; however, intervention of some sort is still necessary whenever two segments come into close proximity.

A few investigators have attempted direct numerical solutions to the Navier-Stokes equations for the flow under consideration. Chamberlain and Liu (1985) have set up a finite-difference scheme in terms of the vorticity and vector potential, and have obtained a solution for the collision of a particular set of rings. Unfortunately, the results of their simulation are presented as contour plots of the vector potential and are therefore somewhat difficult to interpret. Probably the most realistic simulation of vortex fusion is that by Ashurst and Meiron (1987). They used a vortex method to start their simulation and followed the motion of the vortex filaments until they approached to within a core diameter or so of each other. At this point, the simulation was interrupted and the induced velocity field was computed on a 32 x 32 x 32 rectangular grid centered on the collision area. A finite-difference scheme was then started

using these velocities as initial conditions. The results of the simulation show the reconnection process clearly. Ashurst and Meiron claim that the time scale of the reconnection process is of the order d^2/Γ, where d is the core diameter and Γ is the circulation of the vortex. While this time scale is probably close to the correct order of magnitude, it cannot be strictly correct since it ignores the effect of viscosity.

1.2.3 Analytical Work. The only analytical model of the fusion process seems to be that of Takaki and Hussain (1985). In their work, the velocity and vorticity fields are expanded in polynomials expressed in terms of coordinates centered in the interaction region. These expansions are then substituted into the vorticity equation (including the viscous term). It is assumed that the various terms all exhibit the same time dependence; the result of this assumption is an ordinary differential equation for the unknown common function of time. The equation is solved analytically, and an expression is given for the time scale of the fusion process. This time scale evidently includes the effect of viscosity, but Takaki and Hussain state only that the time scale is of order d^2/Γ.

1.3 Relevance of the Present Study

The present study is an attempt to deal with the fusion process experimentally on a quantitative level. The velocity field produced by the collision of two laminar vortex rings will be measured with laser-Doppler velocimetry, and the variation in the circulation of each of the vortex cores will be determined as a function of time during the interaction. Chapters 2 and 3 describe the experimental apparatus and instrumentation used in the measurements, while Chapter 4 describes the procedure by which the measurements were carried out. The manner in which the velocity data were processed is explained in Chapter 5, and Chapter 6 presents the main results of the experiment. A summary of the results is given in Chapter 7 along with some recommendations for future work.

CHAPTER 2

EXPERIMENTAL APPARATUS

2.1 The Facility

The experiment was conducted in water in a glass-walled tank one meter on a side, shown in Fig. 2.1. The rings were generated near the top of the tank and travelled downward during their interaction. To achieve thermal stability in the tank, the outside walls were covered with one inch of foam insulation, and the top was covered by a thick polyethylene sheet. Small sections of the foam were removable to allow for visual inspection of the generators and to provide passage for the laser beams. With the tank insulated in this manner, the water temperature remained very nearly constant. Day-to-day variations were usually less than 0.1° C, and the total temperature variation was kept to ± 0.2° C for the duration of the experiment. This thermal stability was important because it inhibited the formation of large-scale convective currents in the tank. The presence of such currents would alter the vortex trajectories in an unpredictable fashion and thereby destroy any chance of obtaining reproducible collisions.

In addition to these passive flow-control measures, an active means was provided to break up any large-scale eddies that might inadvertently form. This breaking up was accomplished by periodically towing a wire mesh grid up and down inside the tank. The grid itself was a piece of stainless steel wire-mesh cloth that covered the bottom of the tank. It was raised and lowered like a marionette by pulling on a set of nylon strings extending out through the top of the tank. The mesh wire diameter (.041") and spacing (5 mesh cells/inch) were chosen according to two criteria: (1) the cloth should be stiff enough to remain flat when being towed, and (2) the porosity of the grid should be high enough (>60%) so that only small-scale motion is induced by passage of the grid through the water. The second criterion was necessary to insure the effectiveness of the grid in disrupting the large-scale currents.

2.2 The Vortex Generator

The entire apparatus for generating the vortex rings was mounted on a thick aluminum baseplate which was in turn mounted on a structure affixed to the top of the tank, as shown in Fig. 2.2. The system was designed so that the baseplate and all attached hardware could be rotated 90° about the mechanical axis of symmetry. Thus flow in orthogonal planes could be measured without moving the laser-Doppler instrumentation. The vortex generator consisted of two parts--the vortex guns and the actuating mechanism. These two components are described below.

2.2.1 The vortex guns. The vortex guns were attached to the bottom of the baseplate in Fig. 2.2 by two other plates which also held the guns in their proper relative orientation. Each gun was of the piston-cylinder type that has also been employed by previous investigators (Liess 1978, Didden 1977, Glezer 1981). With this type of gun, the vortex rings are produced by the impulsive motion of a close-fitting piston along the axis of a cylindrical cavity.

As shown in Fig. 2.3, each gun consisted of a piston guide threaded into a housing and surrounded by a dye shroud. All of these components were to be submerged for an extended period of time and therefore had to be constructed from non-corroding materials. While the housing was machined from 316 stainless steel, the piston, piston guide, and dye shroud were initially fabricated from lucite so that the inner workings of the guns could be observed without dismantling the hardware. After immersion for several months, however, the lucite had absorbed enough water so that several critical dimensions had changed by a few thousandths of an inch--enough change so that the piston could not travel the length of the gun without binding. Moreover, the quality of piston fit had not degraded equally for the two guns, making it unlikely that a symmetrical, reproducible flow could be obtained. New pistons and piston guides were therefore fabricated from 316 stainless steel; subsequently there were no further problems with erratic piston motion.

Each piston was connected to the actuating mechanism by the pushrod linkage shown in Fig. 2.4. One end of a small universal joint was pinned into the top of the piston, and a 1/8"

diameter precision ground shaft was set into the other end. The opposite end of the shaft was inserted into a close-fitting hole bored into the head of a socket-head screw; the shaft was held in place by pins at each end. These components were all made of stainless steel for corrosion resistance. The socket-head screw was threaded into a teflon-lined, spherical-bearing rod end (NMB part no. ANF-4) that attached directly to the actuator rod. The length of the pushrod assembly could be altered a slight amount by turning the screw in the rod end. A locknut was used to secure the screw once the desired pushrod length was obtained.

2.2.2 The actuating mechanism. The pistons were set in motion by a mechanical linkage driven by a stepping motor (Fig. 2.5). The double-ended motor was mounted on top of the baseplate with the shaft horizontal. Parallel to the motor shaft and offset laterally from it was the actuator rod, a length of 1/4" diameter precision ground shaft on which the pushrods were mounted. The two shafts were rigidly connected by a pair of aluminum bars clamped onto the shaft ends. Rotation of the motor thus caused the actuator rod to sweep out a cylindrical surface in space. The upper pushrod ends were constrained to move along circular arcs, but the spherical bearings allowed them to pivot and rotate about their attachment points. The motion of the pushrods was conveyed to the pistons, which were constrained to move along straight-line paths in the vortex guns.

To simplify the operation of the vortex generator, the motor was run at a constant speed. In principle, it is the pistons that should move at a constant speed, but this would only be possible if the geometry of the linkage was such that a linear relationship existed between motor shaft motion and piston motion. In practice, it turned out to be possible to choose the lengths and angles of the various members such that the departure from linearity was minimal (less than 1 part in 300) over the desired range of motion.

It was imperative that the actuating mechanism perform in a reliable and reproducible manner. In part, this reproducibility was achieved by eliminating all mechanical clearances in the linkages and by designing the system for low frictional and inertial loads. However, no matter how well-designed and well-built the system might be, the overall performance would

still be decided by the stepping motor and the means for controlling it.

To meet this need, a commercially available motion-control system was purchased from Parker COMPUMOTOR. The system consists of three parts--an indexer, a microstepping driver, and a stepping motor, as shown in Fig. 2.6. The indexer (model 2100-P-488) accepts motion commands from a computer or from thumbwheel switches on the front panel and produces a train of pulses that is sent to the driver. The driver interprets the pulses and produces the current necessary to drive the motor as commanded. The position resolution of the motor/driver combination (model M106-178) is 25,000 steps/revolution, compared to the inherent motor resolution of 200 steps. For frictional and inertial loads within the torque capacity of the motor, the open-loop performance quoted by the manufacturer is as follows:

Absolute accuracy .....0.08°
Step-to-step accuracy.....0.006°
Repeatability.....0.001°

The motor produces about 700 oz-in of torque in the speed range of interest. The calculated torque from frictional and inertial loading is about 60 oz-in.

One drawback of this system was high-frequency electromagnetic noise radiated by the motor/driver. This signal was picked up by the LDV photodiode circuitry and was visible on an oscilloscope as a train of spikes with a magnitude of a few tenths of a volt. The spikes were attenuated to an acceptable level by shielding both the photodiode circuit and the driver-to-motor cable with aluminum foil.

2.3 Flow Visualization

As the piston moves along the vortex gun it pushes fluid out in front of it. A discontinuity in the velocity at the exit creates a free shear layer that rolls up to form the vortex ring. In the present experiment, the rings were made visible by injecting dye into this shear layer from a small annular slit at the lip of the piston guide (see Fig. 2.7). This slit was approximately 3/4 mm wide and was bounded by the piston guide and the dye shroud. The space between the guide and shroud was filled with dye supplied by a large reservoir above the tank. The dye flowed from the reservoir to each vortex gun through a feed line equipped with a solenoid

valve. The valve could be opened and closed on command to control the quantity and timing of dye injection. The dye used was B1-G1 (7K Color Company). It has the useful property of bleaching in the presence of chlorine, so that many rings could be produced without degrading the clarity of the water in the tank. The dye was mixed to a specific gravity slightly less than that of the water in the tank so that it would be more likely to be entrained into the low-pressure region at the center of the vortices. In this manner the dye was mostly confined to the vortex cores. The cores could be made to look fatter or thinner by injecting more or less dye. The most photogenic vortices were produced by allowing the dye to flow for a time approximately equal to one-half the piston-stroke time. In addition, it was found better to start the dye injection slightly before starting the piston motion.

The photographs in Figs. 1.1 and 1.2 were taken using an Olympus OM-1D 35mm camera equipped with a motor drive operating at a nominal speed of 5 frames per second. For this particular set of photographs, the framing rate was somewhat lower; the resulting time between frames is 0.23 seconds. A 50mm f/1.4 lens was used with a 3X focal extender to provide magnification. The camera was mounted on a tripod as close to the tank as possible and inclined downward about 10° from the horizontal to provide a slightly oblique view of the rings. The field was back-lit by a 1000 W tungsten light source (Berkeley Colortran) diffused by a piece of vellum paper on the far tank wall. Ektachrome Professional Tungsten film (ASA 160) was used, and the aperture and exposure time were f/5.6 and 1/125 second, respectively. With this arrangement, the rings almost filled the camera's field of view, and it was necessary to traverse the camera downward to follow the rings as they moved. This was done manually and required a little practice, but was not particularly difficult since the required speed was only a few centimeters per second.

CHAPTER 3

INSTRUMENTATION

3.1 The LDV System

The laser-Doppler velocimeter used in this experiment was designed and built by Glezer and Coles (1982) and is described in detail in Glezer's thesis (1981). Only those operational aspects that are relevant to the present work will be mentioned here.

3.1.1 Optical and mechanical components. The low fluid velocities in this experiment were measured using a two-component LDV with frequency bias. Beam splitting and frequency shifting were accomplished simultaneously by passing the input beam from a helium-neon laser through a pair of rotating, overlapping radial phase gratings and then isolating the four first-order beams (see Fig. 3.1). Each grating was driven by a hysteresis synchronous motor, and the two bias frequencies were determined from the sum and difference of the two motor speeds. In the present study the motor speeds were chosen to yield bias frequencies of about 195 kHz and 1755 kHz. The LDV was operated in the four-beam forward-scatter mode with all four beams crossing at a single point. The angle (measured in air) between the two beams in each channel was determined to be about 4.84°, giving a Doppler gain constant of 1.335 kHz/(cm/s). The $1/e^2$ diameter and length of the focal volume were calculated to be about 0.2 mm and 6 mm, respectively.

3.1.2 Electronic components. The light scattered from the particles in the focal volume was collected by a lens and focused onto a single silicon avalanche photodiode. The signal from the photodetector thus contained the velocity information for both channels. Since the grating motor speeds had been chosen to give bias frequencies more than three octaves apart, the two Doppler signals could be electronically separated by bandpass filtering. This separation was achieved by first amplifying the detector output and then feeding it to a bank of analog filters (Krohn-Hite model 3202) with a combined roll-off of at least 48 db/octave.

The filtered Doppler signals were then fed into a two-channel tracking processor that determined the period of each signal by counting pulses from a high-frequency clock for a predetermined number of Doppler cycles. The precision with which this period could be determined was limited by the frequency of the clock (60 MHz) and the number of Doppler cycles counted (30 cycles for the low-frequency channel and 450 for the high-frequency one). The calculated frequency resolution was 21 Hz and 114 Hz on the two channels, corresponding to velocity resolution of 0.2 mm/s and 0.9 mm/s, respectively.

Inside the processor, each signal was fed into a digital phase-locked loop that was adjusted to track changes in the input Doppler frequency over a range of about ± 25 kHz. The number of pulse counts representing the Doppler period for each channel was updated every millisecond, and a pair of 16-bit words containing the data was sent to the data acquisition system. In addition, signal validation circuitry checked that the amplitudes of the Doppler signals were above certain thresholds; the status bit in the appropriate data word was flagged whenever a signal failed the test.

3.1.3 Grating noise. When measuring the velocity in a quiescent fluid one expects to obtain a constant zero reading. With the LDV system used in this experiment, however, a velocity trace such as the one in Fig. 3.2a is obtained. Glezer and Coles (1982) determined that this signal was periodic and phase-locked to the rotation of the diffraction gratings. It consists primarily of four sinusoidal signals whose frequencies match the rotational and pole-passage frequencies of the two motors driving the gratings. In the present study, the periods of these signals were : 42 msec, 33.6 msec, 7 msec, and 8.4 msec. Since the corresponding frequencies are known precisely, it is possible to determine the phase and amplitude of the four sine waves by a least-squares analysis. Fig. 3.2b shows the original noise record with the four noise components subtracted out. In the algorithm used by Glezer (1981), the components were subtracted one at a time; in the present study they were all removed at once. The two techniques are not equivalent, and the latter method seems to give improved results.

In general, the resulting record still contains noise spikes from dropouts and other sources

that degrade the quality of the least-squares fit. The fitting process was therefore repeated with the noise spikes removed. The criterion used for detecting and removing a spike was that the jump in velocity from one sample to the next was more than three times the r.m.s. value of all point-to-point velocity jumps in the record. This screening process was repeated until all jumps passed the criterion. The final zero-velocity noise record is shown in Fig 3.2c. The r.m.s. value of the remaining noise is less than 1 mm/sec.

This grating noise is always present in the velocity data and can be removed from the data only if vortex generation and data acquisition are synchronized with the grating rotation. This synchronism is achieved by driving the grating motors and LDV processor with TTL pulse trains derived from the same quartz-crystal oscillator. In the case of the motors, the TTL pulses are first converted to sine waves and then fed to a stereo power amplifier before being sent to the motors.

3.1.4 Seeding the flow. The tank was filled with distilled water and seeded with 6.4-μm diameter latex particles (styrene divinylbenzene) to a density of approximately 1.6×10^4 particles/cm^3. Using the aforementioned focal volume dimensions, this density represents, on average, about 2 or 3 particles in the focal volume at any instant. The particles, manufactured by Seragen Diagnostics, have a specific gravity of 1.05.

The particles were supplied in an aqueous suspension that also contained a small amount of surfactant to keep the particles from clumping together. When the suspension was added to the water in the tank it was diluted by a factor of about 10^4. Under these conditions the surfactant loses its effectiveness, and the manufacturer recommends that additional surfactant be added to stabilize the suspension. The surfactant used in this experiment was Triton X-100, manufactured by Rohm and Haas. Supplied in liquid form, this chemical resembles honey and requires vigorous agitation to dissolve it. To this end, 100 ml of the surfactant were first added to a beaker containing 1 liter of distilled water and placed on a magnetic stirring plate for several hours. This soap-like solution was then easily dispersed in the tank.

3.2 The Position Transducers

The transmitting optics of the LDV system were mounted on an optical bench carried by a massive 2-D traverse mechanism. With this arrangement the LDV could be moved about in a vertical plane perpendicular to the optical axis (see Fig. 3.3). The horizontal and vertical positions of the LDV within the plane were determined by a pair of electronic linear position transducers (Dynamics Research Corporation model LMT-600) equipped with digital readouts (C-Tek model DDC-150-31-4B-S-L). The resolution of each linear encoder was 0.01mm, and the readouts displayed the distance travelled with the same precision.

One of the transducer/readout combinations was about ten years older than the other. After the stepping motor had been installed in the vortex generator, it became apparent that the new, improved transducer and readout were much more susceptible to electromagnetic noise radiated by the motor and driver than were the older ones. This increased susceptibility was indicated by the fact that the display on the newer readout would change in an unpredictable fashion whenever the stepping motor was operating, making it impossible to record the vertical position of the LDV with certainty. After a reasonable repair effort, and in the interest of speed and economy, the vertical transducer and readout were replaced with a precision long-range dial indicator (Starrett model 656-5041) with a least count of one thousandth of an inch (0.025 mm). It was quite easy to interpolate the indicator reading and to obtain precision comparable to that given by the electronic system.

3.3 The Data-Acquisition System

Vortex generation and data acquisition were under the control of a laboratory computer system (Data Translation LAB-DATAX model DT4236). The system was assembled around a DEC LSI-11/23 CPU with 256 kbytes of RAM, and included a Winchester/floppy disk storage system (Scientific Micro Systems model FWT01177) with 35.6 Mbytes available on the hard disk and 1 Mbyte on floppy. The backplane also housed a fast floating point processor (DEC FPF11), four serial interface ports (DEC DLV11-J), a line time clock (DEC KPV11-A), and a full complement of data acquisition boards, including:

1. 8-channel 12-bit A/D converter.....(DT3382)
2. 2-channel 12-bit D/A converter.....(DT3371)
3. 32-line parallel digital I/O *(non-DMA)*.....(DT2768)
4. 32-line parallel digital I/O *(DMA)*.....(DRV11-B)
5. IEEE-488 GPIB Interface.....(DT2791)
6. Programmable real-time clock.....(DT2769)

A DEC VT240 programmable graphics terminal was used to communicate with the system, and text output was available from a Diablo 630/ECS printer.

3.4 System Integration

The grating motors and the LDV processor are driven by TTL pulse trains derived from a parent 1-kHz signal called "PACER", derived in turn from a 10-MHz crystal-controlled frequency source. Synchronization of vortex generation and data acquisition with PACER is accomplished by a device referred to as the delay box (see Glezer 1981). The commands to start and stop operation of the experimental apparatus are sent to the delay box over two digital control lines from the D/A board. The delay box then performs the following functions:

1. sends a pair of start/stop pulses to operate the LDV processor for 1 sec (to obtain a grating-noise tare record),
2. sends a start signal to the vortex generator and simultaneously starts a timer (to allow time for the vortices to travel to the measuring region),
3. sends another pair of start/stop pulses to the processor when the timer counts down to zero (to collect real data).

The velocity data are sent from the LDV processor to the computer via the 16 input lines of the parallel digital I/O board (DMA version). Whereas the command to start the vortex generator is issued by the delay box, the actual motion commands are pre-programmed into the indexer by the computer over one of the serial interface lines; the indexer then waits for the delay box to send its remote start command. A block diagram of the device interconnections is given in Fig. 3.4, while Fig. 3.5 shows the relative timing of different events in the data-acquisition process.

CHAPTER 4

EXPERIMENTAL PROCEDURE

4.1 Experimental Conditions

The vortex-generation conditions that were used in the present experiment were determined from flow-visualization studies conducted with an early version of the vortex generator. In this early version, the piston speed and stroke length and the angle between the vortex guns were variable.

4.1.1 The defining parameters. For a vortex ring produced by a single vortex gun, the initial circulation is proportional to the product of piston speed and stroke length. These two parameters were adjusted to obtain a vortex ring that not only remained laminar as it travelled across the tank, but also did not develop instability waves before travelling a distance of at least ten ring diameters. The angle between the axes of the two vortex guns was then set to ensure that the rings collided prior to the onset of instability by a comfortable margin. In addition to these requirements, it was desired to set the generation conditions so that the vortices would undergo fission as well as fusion. For a piston diameter, D_p, of 3 cm, the conditions that were finally selected are as follows:

1. Piston speed	U_p	8 cm/sec
2. Piston stroke	L_p	3 cm
3. Gun-to-gun angle	$2\theta_g$	15°
4. Radius of circle tangent to mouths of vortex guns	R_m	24.2 cm

These parameters are indicated in Fig. 4.1.

In practice, the piston speed is not constant because the piston must accelerate and decelerate at the beginning and end of the stroke. The stepping motor was therefore programmed so that the piston speed ramped linearly in time from 0 to 8 cm/sec for the first 5 percent of the stroke, remained constant at 8 cm/sec for the next 90 percent of the stroke, and ramped linearly back to zero for the final 5 percent.

4.1.2 Adjusting the pistons. When the vortex generator was finally assembled, all components were adjusted to provide identical piston motion in the two vortex guns. However, flow visualization indicated that the resulting vortex collisions, while reproducible, were not symmetrical--one vortex ring always reached the collision region slightly before the other. Attempts were made to remedy this condition by switching the pistons and dye feed lines between the two vortex guns, but the asymmetry persisted. The flow was finally made symmetrical (to the eye) by adjusting the relative lengths of the piston pushrods; the pushrod in the vortex gun that produced the faster ring was shortened by about 3 mm. This arrangement was believed to be satisfactory until preliminary velocity measurements on the axis of symmetry indicated otherwise. It was found to be necessary to shorten the other pushrod by about 1 mm to improve the symmetry of the flow. The reason that this second step was necessary is probably that the flow-visualization system was turned off for the LDV measurements. The act of injecting dye into the free shear layer emanating from the lip of the piston guide must have an influence on the vortex formation process. Thus, it may be that small differences in the two dye shrouds were responsible for the observed differences in the vortex rings.

4.2 The Measurement Region

Fig. 4.2 shows the coordinate system used in this experiment, as well as an outline of the area in which the fluid velocities were measured. The unit of length is the centimeter, and the figure is drawn to scale (1.4 times actual size). Two sets of measurements were made, and they will be referred to as the in-plane and offset-plane data, respectively.

4.2.1 In-plane measurements. The in-plane measurements were conducted in the $x - z$ plane, which is the plane of symmetry defined by the axes of the two vortex guns. Note that the positive z-axis is directed downward in Fig. 4.2. This plane slices vertically through the two vortices. The intersection of the plane with the vortex cores occurs where the out-of-plane velocity is zero. As a result, the only non-zero component of vorticity is the one perpendicular to this plane. *The primary goal of this research is to determine the manner in which this*

vorticity component changes as the vortex interaction proceeds.

The in-plane velocities were measured on a rectangular grid with 1-mm spacing between grid points. The overall dimensions of this grid were 3 cm by 10 cm, but considerations of experimental run time and data storage dictated that measurements not be done at every grid point. Instead, three sub-regions were chosen that would encompass the trajectories of the vortex cores. Velocity measurements were performed at 1283 grid points out of 3131 possible. The largest region was located near the center of the rectangular grid and was the area in which the cores of the two vortices would come into contact. The two other regions, referred to as the "wings", were located near the edges of the rectangular grid. It was in the wings that measurements of the undistorted rings were made to establish their initial characteristics. These characteristics are given in Appendix A.

4.2.2 Offset-plane measurements. When the in-plane measurements were completed, it was obvious that the flow was not as symmetrical as had been originally hoped. The initial plan to do measurements in the other plane of symmetry of this flow (that is, parallel to the $y-z$ plane) was therefore discarded. Instead, measurements were undertaken in a series of planes that were parallel to the $x-z$ plane but offset in the $\pm y$-direction. In principle, sufficient information can be obtained in this manner to compute the out-of-plane velocity component from the measured in-plane velocities and the equation of continuity. Consequently, all three components of velocity would be known on a three-dimensional grid, and it should be possible to examine the dynamics of the fusion process in detail.

Five auxiliary planes were located on either side of y=0 and were spaced 1 mm apart. As with the in-plane measurements, the velocity data in this case were taken on a rectangular grid with 1-mm point spacing. The planes were 1 cm by 1 cm square and were stacked surrounding the area where the cores were believed to collide. In all, measurements were done at 1331 grid points.

4.3 Experimental Protocol

The experiment was conducted over a six-month period. No measurements were made during the second and third months because the stepping-motor indexer failed and was returned to the factory for repair. In the four working months, measurements were done on a daily basis. The water temperature in the tank was 24.7°C ± 0.2°C for the duration of the experiment. This temperature corresponds to a kinematic viscosity of 0.009 cm^2/sec (Riddick and Bunger 1970).

The diameter and specific gravity of the latex particles used for the LDV measurements were such that the settling rate of the particles was about 10 cm/day. Since the measurements were done about 15 cm below the water surface, the first step taken each day was to stir the water in the tank to redistribute the particles. The water was vigorously agitated for about ten minutes with a large paddle. The wire-mesh grid was then towed up and down in the tank for about five minutes to break the large-scale eddies into smaller ones. After about two hours, the water in the tank was visually checked for signs of motion. This motion was easily detected by looking at the light scattered from particles in the paths of the LDV beams. If the water in the tank was moving, even slowly, the beams appeared to sparkle; if the water was stationary, the beams appeared static. A waiting time of two to three hours was usually sufficient to guarantee that all motion had died out.

The first data record taken each day was a repeat of the last data record taken on the previous day. The two sets of velocity traces were compared to check that nothing of significance had changed the apparatus overnight. Measurement of the two velocity components at a given point as functions of time constituted a record.

The start command was issued by striking the *RETURN* key on the computer keyboard. The LDV processor was then operated (without vortex generation) for 1 second to obtain the grating-noise tare record. At the end of 1 second the vortex generator was triggered. A delay of 1500 msec was introduced to allow time for the vortices to travel to the measurement region. The LDV processor was then reactivated to collect velocity data for 3400 msec after the end of the delay period. A command string was then sent from the computer to the indexer to retract

the pistons. The upper limit of piston travel was set by a microswitch which signalled the indexer upon being triggered by the pistons.

Once a data record was complete, several versions were displayed on the terminal for inspection. The first signals to be displayed were the raw grating-noise traces for both LDV channels (*e.g.*, Fig. 3.2a). If these signals were acceptable, they were then filtered and the results of the filtering were displayed. If the filtered noise traces were also acceptable, then the grating noise components were removed from the real velocity data. The filtered velocity data were then displayed for final approval. If the data were judged to be acceptable, they were stored in a file on a floppy disk and a record summary was listed on the line printer. The transmitting and receiving optics were then moved to the next location and the measuring process was repeated. At least five minutes were allowed between runs for the motion induced by the vortices to subside.

At any stage in this process the current data could be discarded and the run repeated. Primitive criteria used to discard data records included too many dropouts and too much scatter. Occasionally, a record was discarded because the velocity traces did not fit the pattern of progression established by the data at nearby points. The most common reason for discarding a data record, however, was that the raw grating-noise record itself had too many dropouts. The presence of a large number of dropouts in the noise record is explained by the fact that the water in the tank is nominally stationary for this measurement. As a consequence, the very slow drift of particles into and out of the focal volume causes the Doppler signal to be intermittent. A momentary scarcity of particles in the focal volume occurring after the beginning of the noise record thus produces a large number of dropouts. When this is the case, the quality of the least-squares fit to the grating noise is poor. This poor quality was subsequently reflected in the filtered velocity data. Approximately 10% of the data records were rejected the first time, so that the corresponding velocities had to be remeasured.

The information stored in each record included the current coordinates of the LDV focal volume, the water temperature, the time of day, the raw grating noise, and the raw velocity data.

The filtered velocity data were not stored because the grating-noise-removal algorithm used during each run was actually a crude version of the algorithm discussed in Sec.3.1.3. This cruder version had the advantage of executing quickly to allow for rapid inspection of the data, but was not as accurate as the more sophisticated version. The velocity data therefore had to be reprocessed later; thus there was no point in storing the crudely filtered data.

CHAPTER 5

PROCESSING THE VELOCITY DATA

This chapter describes the procedure that was used to smooth the raw velocity data. Two stages of processing were required: temporal smoothing of the individual pointwise velocity measurements, and spatial averaging of the global velocity field at each instant.

5.1 Temporal Smoothing

Fig. 5.1 shows the temporal variation of the two velocity components contained in a typical data record. For clarity, only every fifth point has been plotted. The grating noise has already been removed from the data by the process described in section 3.1.3. These signals have three features that made the smoothing operation difficult. They are:

- high dropout rate (~30 %)
- regions of high scatter
- low- and high-frequency data present simultaneously.

The simplest way to fill in dropouts in the data is to average the good data from a specified number of neighboring points. This procedure produces acceptable results for isolated dropouts, but if a large number of dropouts occur together in a region where the data are changing rapidly, the situation shown in Fig.5.2a can result. A better scheme for filling in the dropouts in this case is to fit a low-order polynomial to a number of points on either side of the dropout region. This procedure seems to work well for signals that do not exhibit an appreciable amount of scatter. On the other hand, if the signal does contain a significant number of noise spikes, this scheme can produce the kind of results shown in Fig. 5.2b. This problem can be circumvented in a brute-force manner simply by using more points in the fitting algorithm. The drawback to this approach, however, is that increasing the number of points used lowers the maximum frequency that can be resolved by the smoothing process. However, if few enough points are included so as to allow resolution of the high-frequency components of the signal,

then the noisy low-frequency portions of the signal will not be adequately smoothed. The key to resolving these issues is to first identify and then discard the noise spikes and the obviously bad data points in regions of high scatter. This screening process was carried out in several stages.

The data record was first divided into 50 segments (if a record contained no dropouts, there would thus be 68 points per segment). Each segment was then subdivided into a number of velocity bins, with the width of each bin being 2.5 mm/sec. This procedure is illustrated in Fig. 5.3a. The number of points in each bin was determined, and the average number of points per bin was computed for each segment. Points were discarded if they were located in bins containing fewer than the average number of points. The advantage of this technique is that it preserves points where the point density is high and eliminates points where the density is low. After each segment had been screened in this manner, overlapping cubic curves were fit to the remaining data. Twenty-one points were used in each fit, but only the middle 11 points were replaced by the values generated by the fit.

In some regions, the screening process would occasionally produce a staircase pattern of points as shown in Fig. 5.3b. This pattern indicates that the screening process may have been too severe. To compensate for this error, the data in each segment were "un-screened" in the following way. The smoothed data in each segment were averaged together, and the average values in neighboring segments were connected by straight lines. The r.m.s. deviation of the data from the straight lines was computed, and previously discarded points were put back into the data set if they deviated from the straight lines by less than the r.m.s. value. The reconstituted data set was then subjected to the cubic fitting operation already mentioned.

At this stage of processing, dropouts in the data record have been filled in and wild data points have been replaced with more reasonable ones. With the exception of occasional, minor ripples, the resulting velocity trace is a good representation of the original data. The ripples are most noticeable in the low-frequency regions, and are the result of using too few points in the curve fits. Recall that the number of points used in the fitting process was chosen to enable the

high-frequency portion of the signal to be captured.

In an effort to remove these ripples, the data were subjected to a final smoothing step. This fitting process once again involved overlapping cubic segments; however, the number of points involved in each fit was variable. The algorithm was made self-adjusting by marching along the curve for a specified arc length and choosing the number of points based on the horizontal component (time) of the distance travelled. For a low-frequency curve, the horizontal component and, therefore, the number of points in the fit, would be large, while substantially less horizontal movement (and fewer points) would be generated by marching an equal distance along a high-frequency curve. This situation is shown in Fig. 5.4. This means of adjusting the number of points employed in the fitting process was quite satisfsactory. Figure 5.5 shows the data from Fig. 5.1 after passing through the smoothing process just described.

This procedure worked quite well for smoothing the in-plane velocity data over 95 % of the measurement region. The area in which difficulty arose is the area between the colliding vortex cores, and is characterized by a high dropout rate and a large amount of signal scatter. This region will be shown later to have the greatest out-of-plane strain rate in the flow. The velocity components in a typical data record from this region are shown in Fig. 5.6. Even though it is obvious to the eye which data points are good and which are not, the smoothing algorithm was unable to discriminate adequately between the two, and would usually discard too many points. This problem was resolved by manually digitizing the velocity traces in this region. Sixty-six measurement points were involved. For each point, the velocity traces were displayed on the VT 240 terminal, and the crossed-hair graphics cursor was moved over the data and used to select about fifty representative points from each trace. These points were then connected by straight lines, and all points that deviated from the lines by more than a specified amount (2.5 mm/sec) were discarded. The remaining data were then fit with overlapping cubic segments as described earlier. The result of this process applied to the data of Fig. 5.6 is shown in Fig. 5.7.

The offset-plane measurements were made in the same general area of the flow, and were also characterized by high dropout rate and a large amount of signal scatter. The original

smoothing algorithm also proved inadequate here, so that consideration was given to digitizing these data as well. This task was judged to be impractical, however, since over 1300 points were involved. Therefore, these data were not processed and will not be discussed further in this report.

5.2 Spatial Averaging

As mentioned earlier, each data record contains the two components of velocity measured at a specific grid point as functions of time. What is needed for further processing, however (such as computing the vorticity field), is knowledge of the velocity at *all* grid points at many different times. Such a representation of the data at a specific time will be referred to as a "frame", and may be thought of as a snapshot of the data at that time. A frame was generated for every tenth point in the data set, to yield 340 frames representing 3.4 seconds of experimental data. A motion picture made from these frames and projected at 100 frames/sec would thus reproduce the flow in real time.

It should be remembered that these measurements were made on 1283 individual realizations of the flow, and that there may, therefore, be small differences from one realization to the next. In order to even out these differences, the velocity data at each grid point were averaged together with the data from eight neighboring points as illustrated in Fig. 5.8. Of course, fewer than eight points were used for grid points on the measurement boundaries. Since this averaging scheme is equivalent to a digital low-pass filter, it is necessary to determine the degree of attenuation experienced by signals of various frequencies. For the one-dimensional case (three-point averaging), determining the amplitude response of such a filter is straightforward (see Hamming 1977). An input signal of unit amplitude will emerge from the filter with an amplitude, AR_1, given by

$$AR_1 = \frac{1}{3} \left[1 + 2 \cos (2\pi/n) \right] , \tag{5.1}$$

where n is the number of points per cycle of the signal. This response curve is plotted in Fig. 5.9. Determining the amplitude response for the two-dimensional case is not so straightforward,

but it is possible to obtain some serviceable estimates based on the 1-D result. If the 2-D signal varies much more slowly in one direction than the other, then the amplitude response of the 2-D filter, AR_2, will be comparable to that of the 1-D filter:

$$AR_2 \approx AR_1 \ . \tag{5.2}$$

If the signal variation is comparable in the two directions, then

$$AR_2 \approx AR_1^2 \ . \tag{5.3}$$

These estimates will be needed in the next chapter when discussing the accuracy of the computed velocity field. It is expected that the actual attenuation will lie within these bounds.

CHAPTER 6

DISCUSSION OF RESULTS

A large amount of data was collected in this experiment. The fact that the measured flow was unsteady complicates the task of choosing a suitable format for presentation of the results. It was decided to display the various field quantities (*e.g.*, velocity, vorticity) as if they were sequences of frames from a motion picture. This is, in fact, the reason for referring to the collection of velocity data at a given instant as a "frame" in Sec. 5.2. Although 340 frames of velocity data were generated during the smoothing process, this is clearly too much data to present in a printed medium. For such a large number of frames, the time between successive frames is only 10 msec. It was later determined that an adequate visual impression of the flow could be obtained with a frame time of 100 msec. In this chapter, therefore, only every tenth frame of the set of 340 frames will be displayed for the field quantity of interest. In addition, the last few frames of this reduced set will be omitted, since nothing of significance occurs at these late times.

Every figure is therefore composed of 28 frames, and is arranged so that there are 4 frames to the page (thus, 7 pages per figure). The frames on any given page are arranged in chronological order with the earliest time at the top of the page. Included in each frame is a set of dotted lines which serve to mark the boundaries of the measurement region (refer back to Fig. 4.2). It may be helpful to think of these regions as "windows" through which parts of the flow may be viewed. The data are presented in the form of contour plots; any contours that stray outside the measurement region are simply the result of an over-zealous plotting routine and should be ignored. Contours of positive quantities are drawn with solid lines, while negative quantities are represented by dashed lines. It is recommended that all 28 frames of each figure be scanned briefly to get a feeling for the progression of the data prior to concentrating on individual frames.

Figure 6.1 shows a typical frame (without data) and the approximate location of the vortex rings at the beginning of the measurements. The sign convention for the coordinates and the velocities is also indicated. The unit of length on each axis is the centimeter; the measurement region is drawn to scale and is shown approximately 1.4 times true size. Recall that the plane being viewed is the plane formed by the axes of the vortex guns.

6.1 The Velocity Field

6.1.1 The data before spatial averaging. The first data to be examined are the velocity measurements, since they are the basis upon which the remaining data were developed. Figures 6.2 and 6.3 show the x-component of the velocity, u, and the z-component, w, respectively, prior to the spatial averaging scheme of Sec. 5.2. The contour value code is [-7.5 : (1.0) : +7.5] cm/sec ([least value : (increment) : greatest value]).

The first thing to notice is the general appearance of the data. The overall impression that is made is one of coherence in the measurements. For the most part, the individual contours are reasonably smooth and regular; the transition between adjacent contours is likewise fairly smooth. The most ragged contours seem to be the lowest-level ones, *i.e.*, ± 0.5 cm/sec. This observation can be explained by the fact that the signal-to-noise ratio is lowest for data on these contours. Occasional spikes are also evident in the data as can be seen, for example, in frame 1 of Fig. 6.2. The important point here is that the presence of these spikes and other contour irregularities suggests that the character of the data was preserved throughout the temporal smoothing operation. The fact that the observed variations are small also indicates that a high degree of reproducibility was attained in the vortex generation process.

The second characteristic to notice is the symmetry of the flow. Prior to frame 11 (T=1.00 sec), the flow appears quite symmetrical; however, this symmetry is eroded at later times. It will be shown in a later figure that this is approximately the time at which the vortex cores of the two rings come into contact. The primary source of the asymmetry is believed to be differences in the distribution of vorticity within the cores. The slight difference in arrival times of the vortices is believed to contribute only slightly to the asymmetry.

The final feature of the flow to notice is the magnitude of the velocity components. The largest velocity that was measured in the flow was about 6 or 7 cm/sec. This maximum value occurred in the region between the colliding vortex cores at about frame 15 of Fig. 6.3. Local extrema in the vertical component of velocity (w) were approximately twice the magnitude of those in the horizontal component (u).

6.1.2 The data after spatial averaging. The spatial-averaging scheme of Sec. 5.2 was applied to the frames of velocity data in Figs. 6.2 and 6.3 in an effort to even out the small irregularities that were present. The results of this process are shown in Figs. 6.4 and 6.5 for the u and w velocities, respectively. It can be seen that the smoothness of the equi-velocity contours has indeed been improved, most noticeably for the lowest-level contours. The shapes of the higher-level contours are essentially unaltered, but it is evident that the peak values have been reduced somewhat. This attenuation is to be expected, however, since the averaging process acts as a digital filter in the spatial variables. The amount that the filter attenuates peaks in the data can be estimated in the following manner. Equation 5.1 indicates that the amplitude of a periodic input signal is reduced by a factor that depends on the number of sample points per cycle. Even though the velocity data shown here do not exhibit spatial periodicity, the distance between like-signed velocity peaks can be used as a measure of the spatial variation in the flow. The shortest such distance appears to be about 12 mm; since the grid spacing is 1 mm, the corresponding number of points per "cycle" is 13. By using Eqs. 5.1 through 5.3, the amplitude of the filtered velocity data is determined to be roughly 85% to 92% that of the unfiltered data. Of course, in regions where the velocity gradients are smaller, the amplitude ratio is closer to unity.

6.2 Velocity Gradients

The most interesting quantities in the flow do not depend on the velocity *per se*, but rather on the spatial gradients of the velocity. If the velocity field is sufficiently smooth, then good estimates of the spatial derivatives can be obtained simply by using various finite-difference schemes. Based on the observed smoothness of the velocity contours in the previous section, it

was hoped that the computed velocity gradients would have a comparable degree of smoothness. In the present study, the derivative of any quantity, f, at the point (x_i, z_k) was approximated using second-order central differences:

$$\left[\frac{\partial f}{\partial x}\right]_{i,k} \approx \frac{f_{i+1,k} - f_{i-1,k}}{2\Delta x} \qquad \left[\frac{\partial f}{\partial z}\right]_{i,k} \approx \frac{f_{i,k+1} - f_{i,k-1}}{2\Delta z} \tag{6.1}$$

Of course, if the point under consideration happened to fall on the boundary of the measurement region, then the appropriate one-sided difference formula was used. One point to remember is that the velocity gradients were computed from the spatially-averaged data; as a consequence, the peak gradients are expected to be reduced by roughly the same amount as the peak velocities.

Four velocity gradients were calculated directly from the measurements using Eqs. 6.1. They are $\partial u/\partial x$, $\partial u/\partial z$, $\partial w/\partial x$, and $\partial w/\partial z$, shown in Figs. 6.6 through 6.9, respectively. The contour value code is [-38 : (4) : +38] $\sec^{-1}$ in all plots. The important point to notice when looking through these figures is that the contours are still quite smooth. The observation from the previous section that the flow is approximately symmetrical until frame 11 is borne out by these data as well. These figures are included partly for the sake of completeness; however, some of them will be useful in future discussions of the behavior of the vorticity field.

Figure 6.10 shows the gradient of the out-of-plane velocity, $\partial v/\partial y$. This quantity is of interest because in regions where it is large and positive there is significant motion of the fluid away from the $x - z$ plane. Extension of the fluid elements in this manner can produce local intensification of the vorticity field and may therefore be significant. The derivative $\partial v/\partial y$ was inferred from the measured velocities using the equation of conservation of mass of an incompressible fluid:

$$\frac{\partial v}{\partial y} = -\left[\frac{\partial u}{\partial x} + \frac{\partial w}{\partial z}\right] \tag{6.2}$$

The data from Figs. 6.6 and 6.9 were simply added together and negated to give Fig. 6.10. The contours are obviously much more ragged in this case than for the other velocity gradients. The

magnitude of $\partial v/\partial y$ is quite small throughout most of the flow ($\approx$ 1 contour), and the raggedness of the contours is probably the result of trying to compute a small number from two larger numbers of opposite sign. Another feature worth mentioning is the presence of a region of extension in front of each ring and one of compression at the rear. These regions are evidently associated with the self-induced flow through the ring.

The most prominent feature in Fig. 6.10, though, is depicted in frames 12 to 19 in the region just to the right of center. Here, the value of $\partial v/\partial y$ increases dramatically for a short time and then, just as rapidly, subsides. The discussion of the mechanism that is supposed to be responsible for this high-strain area will be deferred until after the vorticity data have been presented.

6.3 The Vorticity Field

As mentioned earlier, the variable of greatest interest in this problem is the vorticity. The task at hand is to examine the behavior of the vorticity field during the collision of the vortex cores. The component of the vorticity under scrutiny here is the one perpendicular to the $x - z$ plane, ω_y. From the definition $\vec{\omega} = \nabla \times \vec{u}$, this component is

$$\omega_y = \frac{\partial u}{\partial z} - \frac{\partial w}{\partial x} \quad . \tag{6.3}$$

The value of ω_y was computed at each grid point by using Eqs. 6.1 and 6.3. The result of this operation is shown in Fig. 6.11, where the contour value code is [-38 : (4) : +38] $\sec^{-1}$, the same as that used for the velocity gradients. Two facts are immediately apparent from the figure: first, the vorticity is confined to well-defined regions in the flow, and second, the vorticity contours are remarkably smooth and regular. These observations should help to build confidence in the repeatability of the whole process of generating the vortices and measuring their properties. The noise level in the computed vorticity field is evidently below the first contour level. Since the value of ω_y on this contour is $\pm$ 2 $\sec^{-1}$ and the peak value of ω_y is about $\pm$ 30 $\sec^{-1}$, the relative uncertainty in the vorticity is in the range from 6 to 7 percent.

The value for the absolute uncertainty in ω_y ($\pm$ 2 sec^{-1}) can also be obtained from consideration of the resolution of the LDV system. Each channel in the system was configured to measure velocity in the range of $\pm$ 20 cm/sec with a precision on the order of 1 mm/sec. According to Eq. 6.1, uncertainty of $\pm$ 1 mm/sec in the velocity corresponds to an uncertainty of $\pm$ 1 sec^{-1} in the velocity gradient (for 1-mm grid spacing). Compounding the effect from two velocity gradients to get the vorticity gives an absolute uncertainty of $\pm$ 2 sec^{-1}. A similar line of reasoning using the maximum and minimum values of velocity in Eq. 6.1 gives the maximum value of vorticity that can be measured as about 400 sec^{-1}.

Recall that the vortex rings are inclined toward one another at a small angle. The vortices first become "visible" as the outer parts of the vortex cores enter the wings of the measurement region. To the eye, each core appears to travel at uniform speed in a straight line through the wings. It is shown in Appendix A that this observation is not quite correct. The peaks of the cores travel through the wings from frame 4 to frame 8. The cores are approximately halfway through the wings at frame 6 (T = 0.50 sec), and it is apparent that there is never a time at which the whole of a vortex core is present within the boundaries of the measurement region. This fact complicates, but does not prevent, determination of the intial state of the vortices.

As the outer parts of the vortex rings approach the bottoms of the wings, the inner parts of the vortices can be seen entering the top of the central measurement region. These are the portions of the rings that will eventually collide. The cores are observed to approach one another, and appear to come into contact at about frame 11 or 12. In the discussions to follow, each reference to a frame number will be followed by a number in parentheses. This number indicates the photograph in Figs. 1.1 and 1.2 that shows the visual appearance of the flow at the nearest corresponding time. For reference, frame 11 (photo 2) will be considered to represent the state of the flow at the instant of contact. The impression made by this photograph is that the rings are not yet in contact. However, it should be remembered that the visual appearance of the vortices depends on the amount of dye injected. In this case, evidently, the vortex cores were not "filled" with dye. As the interaction proceeds, the vortex cores are observed to flatten

and to become elongated in the mean direction of travel. Beginning with frame 14 or 15, (photo 4) an indentation appears in the vorticity contours, as indicated by the arrows in the figure. The presence of the indentation suggests that fluid is being drawn laterally into the heart of the interaction region. Supporting evidence for this idea comes from the contour plots of $\partial v/\partial y$. In the corresponding frame from Fig. 6.10, the z-location at which the out-of-plane strain is large coincides with that of the indentations in the vorticity contours. Furthermore, the horizontal in-plane velocity gradient, $\partial u/\partial x$, is observed in Fig. 6.6 to be negative in this region, corresponding to compression of the fluid as it approaches the plane of symmetry. As the interaction progresses, the vortex cores become more elongated and the indentations more pronounced until, in frame 20 (photo 6) of Fig. 6.11, each core is observed to split in two. This splitting process results in *two* pair of oppositely-signed vortices which are then convected out of the measurement region by the globally-induced flowfield. For future reference, these vortices will be labelled as shown in frame 20. During this time, the only further change in the cores seems to be that the vorticity contours tend to become circular.

6.4 Circulation

A useful measure of the amount of vorticity contained in a region is the circulation, denoted by Γ. The circulation of fluid around a closed contour l bounding a surface S is defined by

$$\Gamma = \int \vec{u} \cdot \vec{dl} = \iint \vec{\omega} \cdot \vec{dS} \tag{6.4}$$

For a contour lying in the $x - z$ plane, Eq. 6.4 reduces to

$$\Gamma = \iint \omega_y \, dxdz \tag{6.5}$$

The significance of the circulation is that for an inviscid fluid of uniform density, the circulation is constant around a contour that moves with the fluid. If the bounding contour is stationary, the same result is obtained, provided there is no transport of vorticity across the boundary. If the fluid is viscous, however, the circulation is no longer constant. The rate of change of circulation is then given by

$$\frac{d\Gamma}{dt} = \nu \iint \nabla^2 \vec{\omega} \cdot d\vec{S} \tag{6.6}$$

(see Batchelor 1967).

One feature of the interaction that was anticipated is the strong reduction that occurs in the ω_y component of the vorticity field after the cores come in contact. This decrease is apparent at a qualitative level since fewer contour levels are required to describe the vorticity distribution in the cores. The observation can also be made that the area occupied by vortical fluid decreases with time. According to Eq. 6.5, these two facts imply that *the circulation of each vortex core decreases as the interaction proceeds.*

To verify this statement, the circulation of each vortex core was computed as a function of time during the collision. The calculation scheme was somewhat indirect and thus requires an explanation. In principle, all that is required to determine the circulation of a vortex is to surround the vortical fluid completely with a contour, and then compute either the line integral or surface integral in Eq. 6.4. If the value of the circulation is desired only at a particular instant, then this procedure is straightforward. If the circulation is to be evaluated at successive times, however, the situation becomes more complicated. For example, if a material contour is employed in the calculation, it is necessary to track the motion of points on the contour from one time to the next. This tedious process can be avoided by using a fixed contour, but the contour should be chosen large enough so that all the vorticity is contained within its boundaries. In the present case, the situation is made more difficult by the fact that the colliding vortex cores are composed of vorticity of opposite sign. If there are equal but opposite amounts of vorticity present within the contour, then straightforward application of Eq. 6.5 gives only the net circulation, which is zero. The obvious remedy is to choose two separate, fixed contours with which to enclose the two vortices, but this turns out to be impractical due to the asymmetry of the collision. Some other means is therefore required to keep track of the positive and negative components of the circulation. The scheme that was eventually developed is described as follows.

The surface integration was carried out over a fixed surface, the central measurement region. The surface was divided into many 9-point cells (3 x 3), and a biquadratic function in x and z was fitted to the vorticity values at the 9 points using a least-squares technique. The contribution of the vorticity in the cell to the total circulation was then determined by analytically integrating the biquadratic function over the cell according to Eq. 6.5. This incremental circulation was then put into one of two bins depending on whether it was positive or negative. This process was repeated for all cells in the central measurement region. At the end, therefore, the bins contained the total positive and negative components of the circulation. The positive component was allocated to the vortex core on the left of the central region, since it is composed of positive vorticity; the negative contribution went to the core on the right. The results of these calculations are shown in Fig. 6.12. The solid line shows the variation in the circulation of the left-hand core, while the dashed line shows the equivalent process for the right-hand core. For plotting convenience, the sign of Γ has been reversed for the right-hand core. Two general comments about these curves are in order.

First of all, it should be remembered that the integration of Eq. 6.5 is carried out over a fixed surface. Initially, the contour contains no net vorticity, so that the net circulation at the beginning of the process is zero. Likewise, at the end of the process the vorticity has been convected out of the measuring region and the net circulation is again zero. It can be seen in the figure, however, that the positive and negative components of the circulation are not individually zero at these times. This result is readily understood once it is realized that there is always a small amount of noise present in the computed vorticity field. Since the incremental circulation from individual cells is equally likely to be positive or negative, the act of separately collecting the positive and negative components will produce the small, non-zero values observed in the figure.

The second general comment concerns the size of the measurement region. As the vortices move into this region, the positive and negative components of the circulation increase. In principle, the measuring region should be large enough so that all of the vorticity in each vortex

core has moved into the region prior to the actual collision. In this way, the positive and negative components of circulation would reach a plateau corresponding to the actual value of the circulation around each core. The curves in Fig. 6.12 never quite reach a plateau. This fact suggests that some of the vorticity was still outside the region as the collision commenced. The vorticity contours in Fig. 6.11 indicate that this is indeed the case. The maximum values of the circulation (relative to the noise level) are:

$$\Gamma_+ = 14.5\ cm^2/sec \qquad \Gamma_- = -15.4\ cm^2/sec$$

The line marked "Γ_0" in the figure shows the estimated value for the circulation of each core prior to the collision. The technique used to obtain Γ_0 is described in Appendix A. The estimated values for Γ_0 are

$$\Gamma_{0_L} = 16.2\ cm^2/sec \qquad \Gamma_{0_R} = -15.9\ cm^2/sec$$

The *R* and *L* subscripts refer to the vortex cores on the right side and left side of the central measurement region, respectively.

The most interesting part of these curves is contained in the time interval from 1.0 to 2.8 seconds. It may be useful at this point to refer back to the associated frames in Fig. 6.11. In particular, note the labeling scheme for the vortices in frame 20. As stated in the previous section, the collision is assumed to begin at T = 1.00 seconds. From Fig. 6.12, it can be seen that the rate of change of the circulation, $d\Gamma/dt$, begins to decrease at approximately the same time. The circulation reaches a maximum at 1.2 seconds and decreases rapidly thereafter. Since no vorticity is being transported out of the measurement region, *this decrease in the value of $d\Gamma/dt$ can only be attributed to cancellation of vorticity by the action of viscosity*, as indicated in Eq. 6.6. As mentioned in Chapter 1, the mechanism by which this cancellation is effected is unclear; nevertheless, the evidence that cancellation occurs is quite strong.

For the moment, it will be helpful to consider only the positive component of circulation. This component continues to decrease until approximately 2.1 seconds (frame 22), when it is observed to reach a plateau. Since no positive vorticity has been transported across the lower

edge of the measurement region, it must be concluded that the cancellation process has stopped. The height of this plateau above the noise level corresponds to a circulation value of about 3 cm^2/sec; the circulation around the core has therefore decreased by over 80 % during the collision. The positive circulation decreases further from 2.2 seconds to 2.4 seconds as a result of vortex A^+ being convected out of the region. This second plateau above the noise level represents a circulation of about 0.5 cm^2/sec. The final decrease in positive circulation at 2.7 seconds is due to vortex B^+ leaving the region. The strengths of the two positive-signed vortices can now be estimated from the plateau values:

$$\Gamma_{A^+} = 2.5\ cm^2/sec \qquad \Gamma_{B^+} = 0.5\ cm^2/sec$$

The situation is similar for the negative component of circulation. This component decreases at about the same rate as the positive component, and should be expected to reach a plateau at the same time as the positive component. This leveling-off is not observed, however, because vortex A^- is being convected out of the measurement region at this time. A plateau is reached at 2.2 seconds, when vortex A^- has left the region entirely; the decrease of circulation from 2.5 to 2.7 seconds corresponds to vortex B^- leaving the region. The height of the plateau above the noise level corresponds to a circulation value of about -1.3 cm^2/sec. If it is assumed that the total change in the negative component of circulation is equal and opposite to the corresponding change in the positive component, then the strengths of the negative-signed vortices can also be estimated:

$$\Gamma_{A^-} = -1.4\ cm^2/sec \qquad \Gamma_{B^-} = -1.3\ cm^2/sec$$

A few words are in order regarding the factors that determine how the vorticity from the two initial vortex cores is divided among the final four vortices. One obvious factor is the degree of symmetry of the collision. If the vortex rings are identical and the collision geometry is symmetrical, then the A^+ and A^- vortices should have equal strengths, as should the B^+ and B^- vortices. For such an arrangement, the relative amount of vorticity distributed between the A and B vortices of the same sign is then determined by the collision angle, the vortex ring

diameter, and the initial circulation of the ring. The initial distribution of vorticity in the core may also play a role.

It should be kept in mind that the total decrease in circulation corresponds to a reduction in the amount of the y-component of vorticity in the $x - z$ plane. This reduction of ω_y does not necessarily mean that all of the vorticity is "lost", for during the reconnection process, ω_y is converted into ω_x. It is unclear whether or not the total amount of ω_x after reconnection is the same as the amount of ω_y before reconnection. The possibility thus exists that the circulation of the vortex filaments is less where they cross the $y - z$ plane than at any other point along the vortex rings. At first glance, such variation in the circulation is in violation of Kelvin's theorem on the constancy of circulation of a vortex filament. Recall, however, that this theorem applies only to inviscid fluid motion; since the x-component of vorticity has emerged from a region in which the viscous effect is essential, there is no reason to expect that the total circulation in the $y - z$ plane will be the same as that in the $x - z$ plane.

One final point is in order regarding the decrease in circulation of the vortex cores during the collision. At least in principle, the possibility exists that the observed decrease in circulation is artificial and is due to the limited spatial resolution of the velocity measurements. Since the measurements were done on a grid with 1-mm spacing, any structural feature of the flow on a scale smaller than this will not be resolved. In particular, thin sheets or ribbons of vorticity could be imbedded in the flow, and they would be undetectable *provided that they did not cross over any grid point.* An estimate for the minimum size of such a structure is easily obtained. If it is assumed that all of the "lost" circulation in Fig. 6.12 ($\approx$ 12 cm^2/sec) is contained in unresolved vortex structures, then the minimum size of these structures would be determined from the maximum value of the vorticity resolvable by the measurement process. This figure was given in Sec. 6.3 as approximately 400 sec^{-1}; the corresponding area occupied by unresolved vortical fluid is therefore about 3 mm^2. As previously stated, in order for this vorticity to remain undetected, the structures must move in such a way that they are *always* between grid points. In view of the degree of asymmetry of the collision studied here, it is

extremely unlikely that a filamentary structure of this size would always remain hidden from view.

6.5 Time Scale of the Cancellation Process

An important issue in this research is how to explain the speed with which the process of vorticity cancellation occurs. From Fig. 6.12, the time during which the circulation decreases is seen to be of the order of 1 second. It was established in the preceding section that the fluid viscosity must be involved in the cancellation process. However, a simple estimate of the viscous time scale turns out to be much longer than 1 second. In the present case, for example, the center-to-center distance, d, between the vortex cores at the instant of contact is approximately 1 cm. The viscous time scale, $t \approx d^2 / \nu$, is thus of the order of 10^2 seconds ($\nu \approx$ 0.01 cm^2/sec in water). The same result is obtained by using the core diameter as the length scale. The problem, then, is to find a mechanism which allows the viscous effects to occur more rapidly.

A clue regarding the nature of this mechanism can be found by examining the contours of the out-of-plane strain rate, $\partial v/\partial y$, in Fig. 6.10. As previously stated, cancellation is assumed to begin with frame 11 and continue until approximately frame 22. It can be seen in Fig. 6.10 that $\partial v/\partial y$ takes on large values only during this time. By examining Figs. 6.6 and 6.9, it can also be seen that where the value of $\partial v/\partial y$ is large and positive, both in-plane velocity gradients ($\partial u/\partial x, \partial w/\partial z$) are negative. The out-of-plane stretching therefore has the effect of drawing fluid into the collision region from the $x-z$ plane. As shown in Fig. 6.11, this inward motion of the fluid distorts the vorticity contours in such a way that the spatial gradients of the vorticity are increased. The steeper gradients in vorticity reduce the time required for diffusion to occur, thereby accelerating the cancellation process.

By recognizing that strain plays a role in the cancellation process, it is possible to obtain a revised estimate of the associated time scale strictly from dimensional considerations. If ε denotes some average measure of the out-of-plane strain rate, then the time required for cancellation to progress across a vortex core of diameter d is

$$t_c \approx d / (\varepsilon \nu)^{1/2} \tag{6.7}$$

From frames 11 through 22 of Fig. 6.10, a representative value for ε is 9 or 10 sec^{-1}. For a core diameter of 1 cm, the resulting time scale is about 3 seconds--much closer to the observed value of 1 second. The manner in which the proposed time scale depends on the strain rate and viscosity is plausible. For example, a higher value for the out-of-plane strain would mean that vortical fluid was being drawn into the cancellation region more rapidly. Eq. 6.7 shows that the time scale would then be reduced. Similarly, increasing the viscosity of the fluid would enhance the cancellation process, thereby reducing the associated time scale.

It is proposed that the role played by other physical parameters is indirect, in the sense that their effect on the cancellation time scale enters through their effect on the strain rate. These parameters include the circulation and size of the vortex rings, as well as the collision geometry. It is noted in passing that the proposed time scale can also be constructed from a certain combination of two length scales in the flow: $d \approx (\nu t)^{1/2}$ and $d \approx (\nu/\varepsilon)^{1/2}$. Eq. 6.7 can be obtained by raising the first expression to the fourth power and then substituting for d^2 / ν from the second expression. At present, it is unclear whether any significance should be attached to this observation. For the sake of completeness, it should be noted that another time scale can be constructed for the cancellation process using the vortex core size, the circulation Γ, and the viscosity, namely

$$t_c \approx d^2 / (\Gamma \nu)^{1/2} \tag{6.8}$$

In the present experiment, $\Gamma \approx 16\ cm^2/sec$, so that this time scale is also about 2 or 3 seconds. However, Eq. 6.8 implies that the time scale for cancellation would be the same regardless of the angle at which the vortex rings collided. This implication may be valid; it cannot be disproved by the present data. However, it is proposed here that the collision geometry *does* affect the time scale. For example, vortex fusion would be expected to occur more rapidly for a nearly head-on collision than for collision of rings travelling side-by-side.

In recent discussions with Profs. Saffman and Leonard, it was pointed out that a simple

one-dimensional model of the cancellation process could be constructed; the associated time scale for cancellation is different from that given in Eq. 6.7 or 6.8. In this model, two regions of oppositely-signed vorticity are in contact in the presence of a uniform strain field, denoted by ε. The initial width of each region is d, and the strain field is such that the regions are pressed together along their plane of contact and elongated in the direction parallel to the vorticity vector. In the notation employed in the remainder of this thesis, the vorticity is parallel to the y-axis and the plane of contact is the $y-z$ plane. Fluid particles are carried by the strain field into the $y-z$ plane along the x-axis according to

$$u = \frac{dx}{dt} = -\varepsilon x \tag{6.9}$$

which can be integrated to give the position of the particles as a function of time:

$$x = x_0 e^{-\varepsilon t} \tag{6.10}$$

x_0 is the initial location of a particle. Where the vortex regions are in contact, there will be a zone of width

$$x \approx (\nu/\varepsilon)^{1/2} \tag{6.11}$$

in which the cancellation of vorticity occurs. The time scale of the cancellation process can then be identified with the time required for a fluid particle to travel from the outer edge of the vortex region ($x_0 = d$) to the interaction zone. Equating Eqs. 6.10 and 6.11 yields the following expression for the time scale:

$$t_c \approx \frac{1}{2\varepsilon} \log_e \frac{d^2 \varepsilon}{\nu} \quad . \tag{6.12}$$

Using the previously mentioned parameter values, the cancellation time scale predicted by the model is about 0.4 seconds. The interpretation given to Eq. 6.12 is that the time scale is established primarily by the strain field and modified by the fluid viscosity. Eq. 6.12 is somewhat more appealing than either Eq. 6.7 or 6.8, because it was derived from a physical model of the flow instead of from dimensional arguments. Nevertheless, all three results are

valid time scales, and further work will be required in order to choose the most appropriate scale.

6.6 Production of Out-of-plane Strain

In the preceding section, attention was drawn to the way in which the out-of-plane component of strain rate influences the time scale of the cancellation process. What was neglected at that point was a discussion of how the out-of-plane strain arises in the first place. The sequence of events leading up to the appearance of the strain is as follows. At this point, it may be useful to refer back to Fig. 6.1 and to fix the coordinate system in mind.

As the two vortex rings approach one another, their combined flowfield is such that a stagnation point appears on the centerline of the measurement region. This is best seen in Fig. 6.5, the contours of the vertical velocity component, w. In frame 9, a point appears on the centerline (marked by "+") where the value of w changes sign; above this point the fluid is moving upward ($-z$), and below it is moving downward ($+z$). In addition, the horizontal velocity component, u, is directed toward the centerline in the region between the stagnation point and the vortex cores. Consequently, the value of the corresponding in-plane velocity gradient ($\partial u/\partial x$) is negative, as shown in Fig. 6.6. This negative gradient means that the fluid is being squeezed laterally as it moves upward through the region between the cores. This situation persists until something begins to impede the upward motion of the fluid in this vicinity. When this happens, both in-plane velocity gradients become negative and the fluid is squeezed not only from side-to-side but also top-to-bottom. Because the fluid is incompressible, it has no choice but to emerge from the collision area at right angles to the $x-z$ plane.

It is conjectured here that the reconnected vorticity field is responsible for impeding the upward motion of the fluid between the cores. As illustrated in Fig. 6.13, such an arrangement of vorticity will induce a downward flow, in opposition to the primary upward flow. As the cancellation process continues, and as more vorticity undergoes reconnection, the downward flow is strengthened. This produces more out-of-plane stretching, which in turn enhances the

cancellation of vorticity as described in Sec. 6.5. The cancellation process can then operate in this self-sustaining cycle for as long as vorticity is present to feed the process. This conjecture cannot be proven from the present data, but it is, at least, consistent with those data.

CHAPTER 7

CONCLUSIONS AND RECOMMENDATIONS

The present study has been concerned with the changes that occur in two laminar vortex rings as they collide at a shallow angle. In particular, the velocity field produced by the collision was measured using laser-Doppler velocimetry. Special precautions were taken to promote reproducibility in the flow, and the regularity of the measured velocity field indicates that a high degree of repeatability was achieved. Spatial finite differences of the velocity data were calculated and used to compute the vorticity field and the strain field resulting from the collision.

The vorticity was observed to be concentrated in well-defined cores; the distribution of vorticity within the cores was seen to be approximately Gaussian prior to the interaction. The initial state of the rings was determined in order to provide information to guide future numerical simulations. This information included the vorticity distribution, the circulation, the ring diameter, the core diameter, and the initial relative position and orientation of the two rings.

A dramatic change was observed in the structure of the vorticity field during the interaction. The vortex cores were observed to become elongated in the mean direction of travel due to the straining field produced by the collision. At the same time, indentations appeared in the boundaries, and these indentations became more pronounced as the interaction progressed. The vortex cores were ultimately split in two by this process, producing two pair of smaller vortices. The relative sizes and strengths of the smaller vortices were presumed to depend on the geometry of the collision.

The circulation of each vortex core was computed as a function of time during the collision. The main result of this study is that the circulation of the colliding cores decreases during this

time. It was shown that this result implies cancellation of vorticity due to the action of viscosity. The time scale associated with this cancellation process was seen to be much shorter than a purely viscous time scale, and two alternative time scales were proposed. It was recognized that the strain field also plays a role in the cancellation process, so the proposed time scales included the effects of viscosity and strain together. In one of these time scales, the strain is included directly:

$$t_c \approx d / (\varepsilon \nu)^{1/2} \quad ,$$

while in the other time scale, the effect of strain enters through the circulation:

$$t_c \approx d^2 / (\Gamma \nu)^{1/2} \quad .$$

The primary difference between the two time scales is that the second one shows no effect from the collision geometry. Since the present experiment cannot distinguish between the two time scales, it was proposed that other experiments be conducted to allow such a distinction to be made. In the simplest case, all that would be required would be to shoot the vortex rings together at different angles, keeping all other parameters fixed. A third time scale for the cancellation process was suggested by Saffman and by Leonard, based on a one-dimensional model of the process:

$$t_c \approx \frac{1}{2\varepsilon} \log_e \frac{d^2 \varepsilon}{\nu} \quad .$$

In this scaling, the strain field appears to play the dominant role, and the Reynold's number effect is seen to be weak.

Finally, it was hypothesized that a feedback mechanism was present that related the process of vorticity cancellation to the production of out-of-plane strain. The conjecture was made that the out-of-plane strain results from a competition between the reconnected vorticity field and the remainder of the vortex rings. This conjecture was shown to be consistent with the available experimental data. The minimum effort required to establish the validity of this conjecture would be to determine the reconnected component of the vorticity field as a function

of time during the collision. For the present arrangement, this corresponds to the x-component of the vorticity in the $y-z$ plane, and would involve a set of measurements similar to those undertaken in the $x-z$ plane. In the ideal case, it would be best to have a set of measurements performed on a three-dimensional grid and giving the full flowfield. These measurements would be tedious to carry out, but there is nothing, in principle, that would prevent such a scheme from being successful. At the same time, it would be useful to have the equivalent set of data generated by a computational scheme of some sort. As the computational methods for this type of flow mature, it should be possible to generate and process significantly more information on the flow than can be obtained practically in an experimental effort. Such detailed information will probably be required before a full understanding of the vortex fusion process is at hand.

APPENDIX A

CHARACTERIZATION OF THE VORTEX RINGS

One purpose of the present study was to provide a set of starting conditions from which numerical simulations of this flow could proceed. In practice, all that is required is to specify the vorticity field at some particular instant. This procedure is somewhat complicated in the present case because the measurement region is too small to capture all of the vorticity in the flow at any instant. Fortunately, the wings of the measurement region are large enough to contain most of the vorticity in the cores as they pass through. The properties deduced from studying this part of each vortex ring will therefore be assumed to be representative of the entire ring. This is a reasonable assumption, provided that the rings are undistorted at the time chosen for characterization.

A.1 Paths of the Vortex Cores

The first items that need to be determined are the paths of the vortex cores as they move through the measurement region. The feature that was tracked from one time to the next was the location of the maximum (or minimum) value of vorticity in the core. This location was determined by dividing the measuring region into 9-point cells and fitting a biquadratic surface in x and z to the values of the vorticity at the nine points. At each instant, the location of the maximum (minimum) value within each cell was determined, and the maxima (minima) from all cells were compared to find the global maximum (minimum). This process was carried out for each time step in which an extremum was obviously present in the measurement region. Figures A.1 and A.2 show the x and z locations of the cores in the wings as functions of time for the left-side and right-side vortices, respectively. It was expected that the cores would be moving at constant speed; both x and z would then be linear functions of time and the speed of

the cores would be given by the ratio of the slopes of the curves $x(t)$ and $z(t)$. The variation in the x-component of each core's position is represented fairly well by a straight line, as the figures indicate. In contrast, the z-components of position do not exhibit this linear behavior. This situation suggests either that the cores are not moving at constant speed, or that the point used to represent the core is moving with respect to the core as a whole. The actual paths of the vortex cores are shown in Fig. A.3. The time t = 0.7 seconds (frame 8) was selected as the instant of time at which the initial relative position and orientation of the vortex rings should be specified; the circles in the figure indicate the relative locations of the core centers at that time.

The diameter, D, and inclination angle, θ, of each vortex ring were obtained from the core trajectory data in a straightforward manner. At any given time, the diameter of each ring was put equal to the straight-line distance between corresponding points on the appropriate core paths. The angle of inclination was determined from the slope of this straight line. The values for D and θ for each ring were computed at six successive times (0.7 to 0.75 seconds), and the results were averaged together to get a more reliable estimate for these quantities. In addition, the location of the center of each ring was determined at 0.7 seconds. The starting conditions recommended for this flow are given in Fig. A.4.

A.2 Vorticity Distribution in the Cores

Given that the locations of the cores are known at different times, it is possible to determine the distribution of vorticity within the cores, subject to the requirement that most of the core in question lies within the measurement area. This determination was made as follows.

At a given instant in time, the location of the center of the vortex core as it moved through the wings was determined from the core-tracking procedure already described. A two-dimensional polar grid was constructed about this center point, and the value of the vorticity at each grid point was interpolated from the actual vorticity data. The interpolation scheme made use of the same nine-point biquadratic fit to the vorticity field that was mentioned previously. The polar grid was composed of 21 radial increments (0.5 mm each) and 36 azimuthal increments (10° each). The interpolated vorticity values at each radial location were then

averaged around the azimuth. This fitting and averaging process was done for each of the cores in the wings of the measurement region at four successive times (0.50 to 0.53 seconds). The data from the four times were then averaged together, and the final, averaged vorticity distributions are given in Figs. A.5 and A.6 for the left-side and right-side cores, respectively. The data are also presented in Table A.1. The distributions are seen to be quite similar; the primary difference in the two distributions is that the peak vorticity is lower for the right-side core. It would be convenient to have an analytical expression for these vorticity distributions, but the question arises as to what form of expression is appropriate. For example, in the well-known Oseen-Hamel solution for the decay of a concentrated line vortex in a viscous fluid, the spatial distribution of vorticity at any time is Gaussian. In the present case, however, there is no reason to expect that the vortex cores will have a Gaussian structure because they have not evolved from concentrated line vortices. The evolution of a vortex from a more general initial state was examined by Kirde (1962). He studied the viscous decay of vortices from initial states in which the velocity field was described by a power law, and obtained solutions for the velocity and vorticity distributions at later times in terms of confluent hypergeometric functions. In the present case, such a distribution may be more suitable than the Gaussian. The solid lines in Figs. A.5 and A.6 represent Gaussian distributions that were fit to the vorticity data. The fit is quite good near the center of the core, but the data values in the outer region are consistently larger than those given by the Gaussian. Considering the amount of work required to improve on this degree of fit, determination of the confluent hypergeometric function that best approximates the measured distributions will be deferred until the velocity field can be examined in more detail.

The initial circulation of the vortex cores was computed from the measured vorticity distributions using Eq. 6.4:

$$\Gamma_0 = 2\pi \int r\, \bar{\omega}_y(r)\, dr \quad , \tag{A.1}$$

where r denotes the radial distance from the center of the core, and the overbar on ω_y indicates that the vorticity has been averaged around the azimuth. The integration scheme employed was

Simpson's 1/3 rule. The values obtained for the circulation are:

$$\Gamma_{0_R} = 15.9\ cm^2/sec \qquad \Gamma_{0_L} = -16.2\ cm^2/sec \quad .$$

A measure of the size of each vortex core was obtained by replacing the actual vorticity distribution with a constant vorticity equal to the original value at the center of the core, and then requiring that the core diameter be such that the circulation was the same for the two cases. The results of this calculation are:

$$d_R = 8.2\ mm \qquad d_L = 7.9\ mm \quad .$$

Whereas Figs. A.5 and A.6 show the vorticity as a function of radius, averaged over the azimuth, Figs. A.7 and A.8 show another version of the data. What is plotted here is the vorticity as a function of azimuth at different fixed radial locations. The distributions from the innermost radial locations are plotted near the top of the page, and they progress monotonically downward. The blank regions near the bottom of the figures correspond to those parts of the vortex cores that were outside the measurement region at the time under consideration. These figures show that the vorticity distribution is not axisymmetric with respect to the center of the vortex core. This is not surprising, however, considering that the vortex filaments are curved. As a result of this curvature, individual vortex lines are alternately stretched and compressed as they orbit the center of the core. Associated with this change in the length of the vortex lines is a change in the local value of the vorticity; if the vortex lines move in circular paths as they orbit the core, then the variation in the vorticity along the path will be sinusoidal in nature. Consequently, the spatial distribution of vorticity at any time can be approximated as follows:

$$\omega(r,\theta) \approx \omega_0(r) + \omega_1(r)\sin\theta \quad . \qquad (A.2)$$

The ω_0 term is the axisymmetric part of the distribution, and represents the vorticity that would exist if the filament were straight. The value of ω_0 at a given radial location is determined from the mean value of the corresponding curve in Fig. A.7 or A.8; the value of ω_1 is then given by the maximum departure of the curve from that mean value. The distributions of ω_0 are equal to

those already presented in Figs. A.5 and A.6. It does not appear to be useful to try to compute ω_1, however, because the distributions do not appear to be sinusoidal. This point is arguable in the case of the left-side core (Fig. A.7), but the right-side data are definitely not sinusoidal in appearance. It might be possible to alter the distributions in a favorable way simply by shifting the origin of the polar grid by a slight amount. Such an adjustment will be attempted at a later time so that the vorticity distributions can be better characterized.

Finally, Fig. A.9 shows the variation with time of the circulation in the wings of the measurement region as the vortex cores move through. The computations were done in the same way as for the vortices in the central part of the measurement region (see Sec. 6.4). At most, only 80% to 90% of each vortex core was present in the measurement region at one time. Fig. A.10 is an expanded version of Fig. A.9.

TABLE A.1 AVERAGED VORTICITY DISTRIBUTIONS IN VORTEX CORES

r (mm)	$\bar{\omega}_{yL}$ (sec^{-1})	$\bar{\omega}_{yR}$ (sec^{-1})
0.00	32.8	30.4
0.05	32.1	29.9
0.10	30.2	28.3
0.15	27.4	25.7
0.20	23.9	22.6
0.25	20.1	19.2
0.30	16.3	15.9
0.35	13.0	12.8
0.40	10.1	10.3
0.45	7.9	8.2
0.50	6.2	6.6
0.55	4.9	5.2
0.60	3.8	4.0
0.65	2.9	2.8
0.70	2.1	1.9
0.75	1.6	1.4
0.80	1.2	1.1
0.85	0.9	0.9
0.90	0.7	0.8
0.95	0.6	0.7
1.00	0.5	0.7

APPENDIX B

CALCULATION OF TERMS IN THE VORTICITY EQUATION

Once the vorticity field has been obtained, it is a relatively simple matter to compute the various terms in the vorticity equation. This information can be used to assess the relative importance of these terms at different points in the flow and at different times during the collision. The variation of each term throughout the measurement region is shown in contour plots; the same format is used here that was used in Chapter 6 to present the velocity and vorticity field data. As a reminder, solid lines correspond to positive quantities and dashed lines correspond to negative ones. The contour value code is [-500 : (100) : +500] sec^{-2}. The various terms in the vorticity equation are written below, along with the figure numbers that indicate where the data are plotted:

Term:	$\frac{\partial \omega_y}{\partial t}$	+	$(\vec{u}\cdot\nabla)\omega_y$	$\equiv$	$\frac{D\,\omega_y}{Dt}$	=	$\omega_y \frac{\partial v}{\partial y}$	+	$\nu\nabla^2\omega_y$
Figure:	B.1		B.2		B.3		B.4		B.5

The way in which each term was computed is described below.

$\frac{\partial \omega_y}{\partial t}$

The value of the local derivative of ω_y at time t_0 was computed by fitting a cubic curve to the values of ω_y at t_0 and at the two previous and two subsequent times. The slope of this curve at t_0 is the desired quantity.

$(\vec{u}\cdot\nabla)\omega_y$

The value of the convective derivative of ω_y at t_0 was computed by expanding the derivative

operator and using the finite-difference approximations in Eq. 6.1 to compute the spatial derivatives of ω_y.

$$\frac{D\omega_y}{Dt}$$

The value of the material derivative of ω_y at t_0 was computed simply by adding the data from Figs. B.1 and B.2 together point-by-point.

$$\omega_y \frac{\partial v}{\partial y}$$

The value of the stretching term at time t_0 was computed by multiplying the data in Figs. 6.10 and 6.11 together point-by-point.

$$\nu\nabla^2\omega_y$$

The value of the diffusion term at time t_0 was computed by subtracting the data in Fig. B.4 from Fig. B.3 point-by-point.

REFERENCES

Anderson, C. and Greengard, C. (1984). On Vortex Methods. *Lawrence Berkeley Laboratory Report LBL-16376.*

Ashurst, W. T. and Meiron, D.I. (1987). Numerical Study of Vortex Reconnection. *Phys. Rev. Lett.*, **58**, 1632-1635.

Batchelor, G. K. (1967). *An Introduction to Fluid Dynamics.* Cambridge University Press.

Chamberlain, J. P. and Liu, C. H. (1985). Navier-Stokes Calculations for Unsteady Three-Dimensional Vortical Flows in Unbounded Domains. *AIAA J.*, **23**, 868-874.

Didden, N. (1977). Untersuchung laminarer, instabiler Ringwirbel mittels Laser-Doppler-Anemometrie. *MPIS Bericht 64*, Göttingen.

Fohl, T. and Turner, J. S. (1975). Colliding Vortex Rings. *Phys. Fluids*, **18**, 433-436.

Glezer, A. (1981). An Experimental Study of a Turbulent Vortex Ring. *Ph.D. Thesis*, Caltech.

Glezer, A. and Coles, D. (1982). A Two-grating Method for Combined Beam Splitting and Frequency Shifting in a Two-component laser-Doppler Velocimeter. *Phys. Fluids*, **25**, 2142-2146.

Hamming, R. W. (1977). *Digital Filters.* Prentice-Hall, Inc.

Kambe, T. and Takao, T. (1971). Motion of Distorted Vortex Rings. *J. Phys. Soc. Japan*, **31**, 591-599.

Kirde, K. (1962). Untersuchungen über die zeitliche Weiterentwicklung eines Wirbels mit vorgegebener Anfangsverteilung. *Ingenieur-Archiv*, **31**, 385-404.

Leonard, A. (1974). Numerical Simulation of Interacting, Three-Dimensional Vortex Filaments. *Proceedings of the Fourth International Conference on Numerical Methods in Fluid Dynamics*, Springer-Verlag, 245-250.

Liess, C. (1978). Experimentelle Untersuchung des Lebenslaufes von Ringwirbeln. *MPIS Bericht 1*, Göttingen.

Northrup, E. F. (1912). A Photographic Study of Vortex Rings in Liquid. *Nature*, **88**, 463-468.

Oshima, Y. and Asaka, S. (1975). Interaction of Two Vortex Rings Moving Side-by-Side. *Natural Science Report of Ochanomizu University*, **26**, 31-38.

Oshima, Y. and Asaka, S. (1977a). Interaction of Two Vortex Rings along Parallel Axes in Air. *J. Phys. Soc. Japan*, **42**, 708-713.

Oshima, Y. and Asaka, S. (1977b). Interaction of Two Vortex Rings. *Proceedings of the International Symposium on Flow Visualization, Tokyo*, Hemisphere Publishing Corp., 81-86.

Oshima, Y. and Kuwahara, K. (1984). Experimental and Numerical Study of Vortex Interaction. presented at *AIAA 17th Fluid Dynamics, Plasma Dynamics, and Lasers Conference*, Snowmass, Colorado.

Oshima, Y. (1986a). *Private communication.*

Oshima, Y. (1986b). *Private communication.*

Riddick and Bunger (1970). *Techniques of Chemistry, vol. II*, 29.

Saffman, P. G. (1981). Vortex Interactions and Coherent Structures in Turbulence. *Transition and Turbulence*, Academic Press, 149-166.

Shirayama, S. and Kuwahara, K. (1984). Vortex Method in Three-Dimensional Flow. *Proceedings of the Ninth International Conference on Numerical Methods in Fluid Dynamics*, Springer-Verlag.

Takaki, R. and Hussain, A. K. M. F. (1985). *Private communication.*

Wood, R. W. (1901). Vortex Rings. *Nature*, **63**, 418-420.

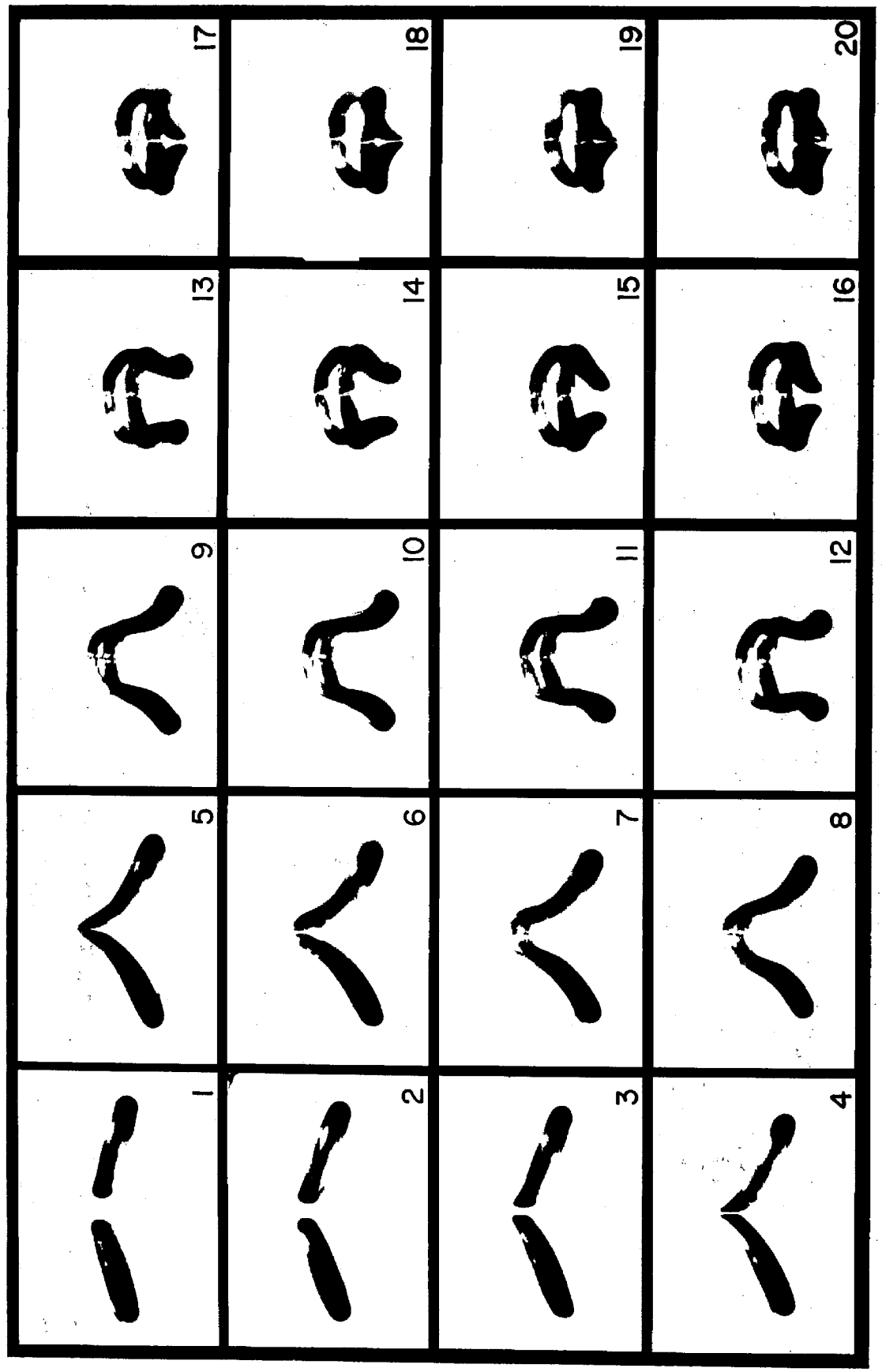

Fig. 1.1 Front View of the Collision

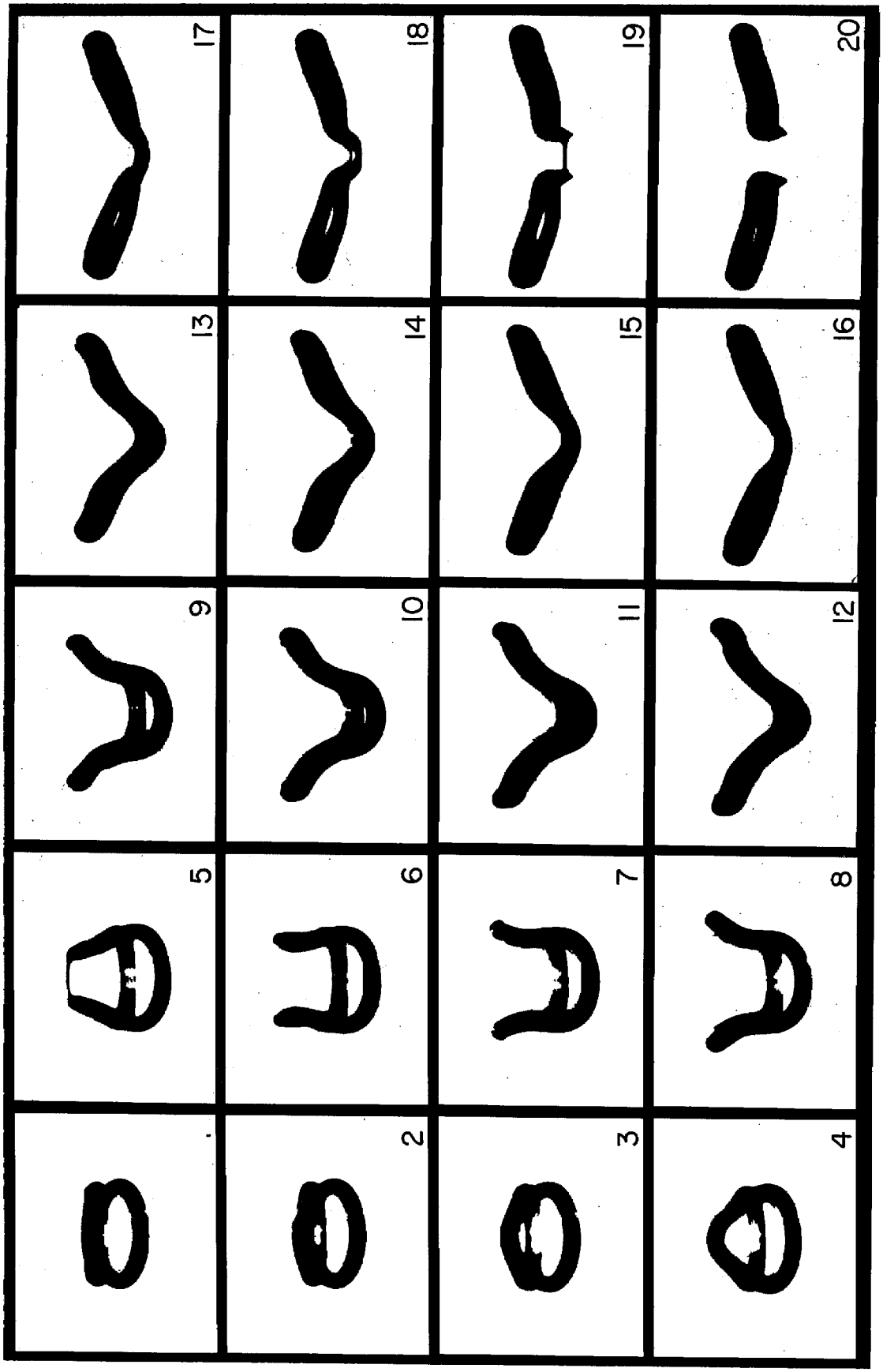

Fig. 1.2 Side View of the Collision

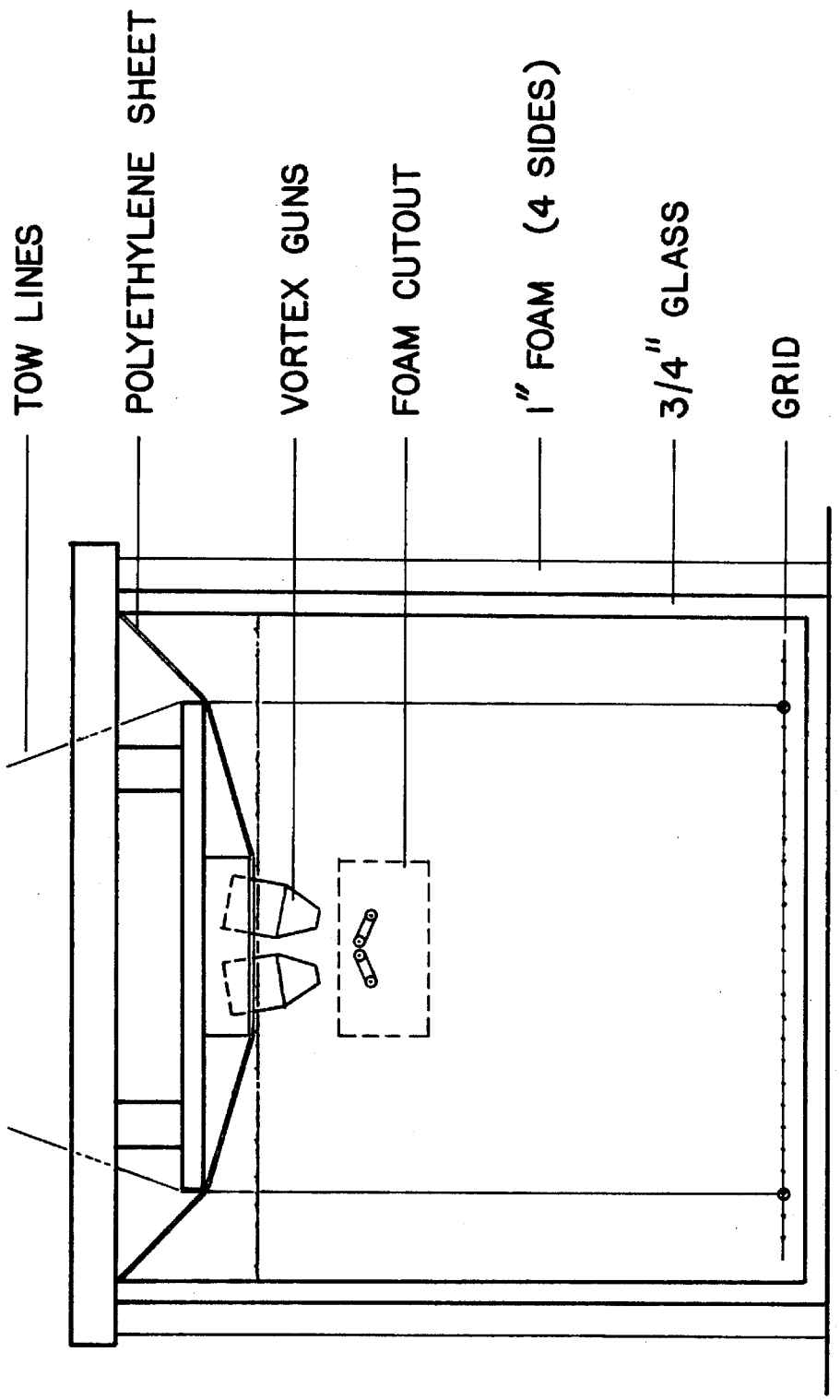

Fig. 2.1 Experimental Apparatus

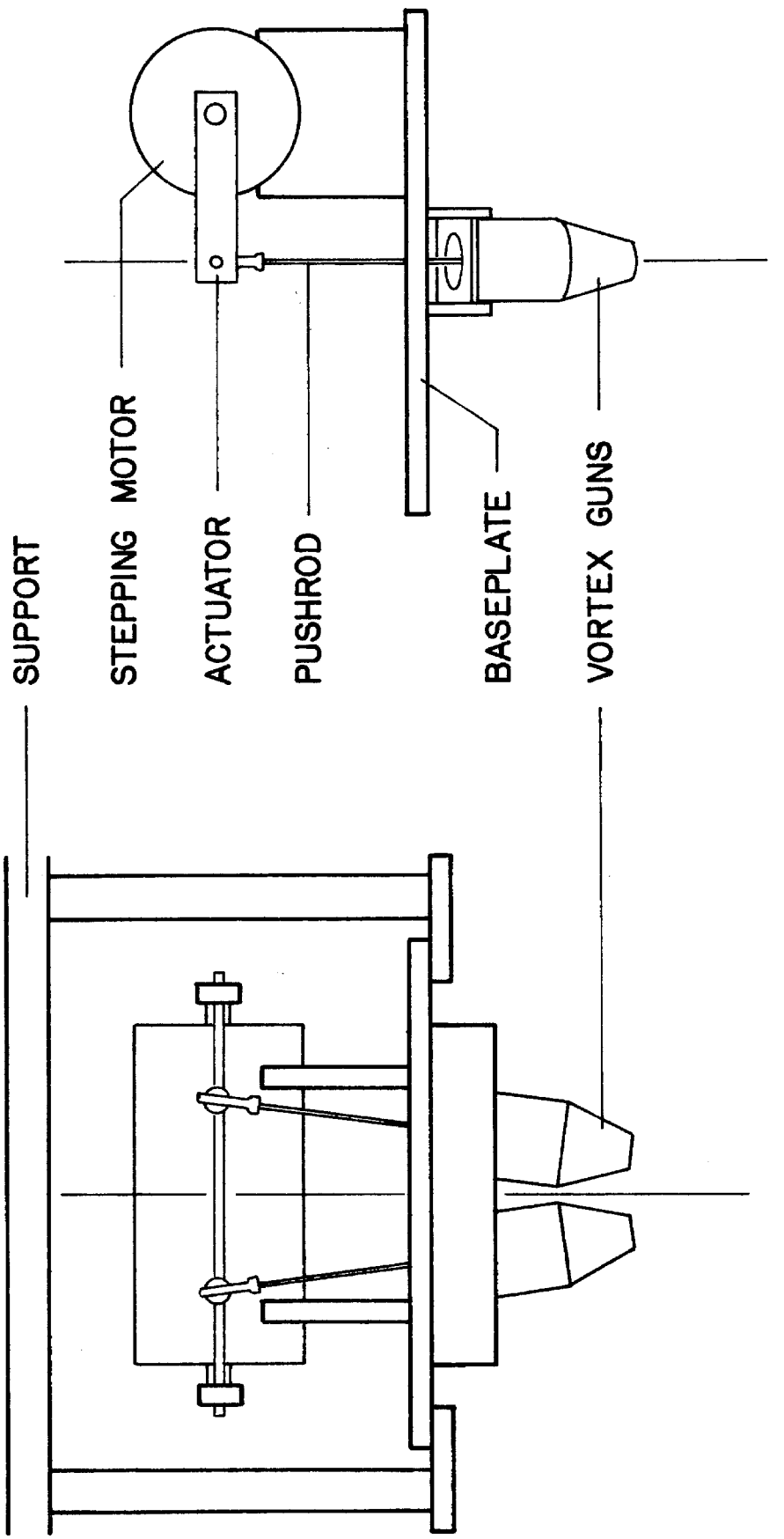

Fig. 2.2 Detail of Vortex Generator

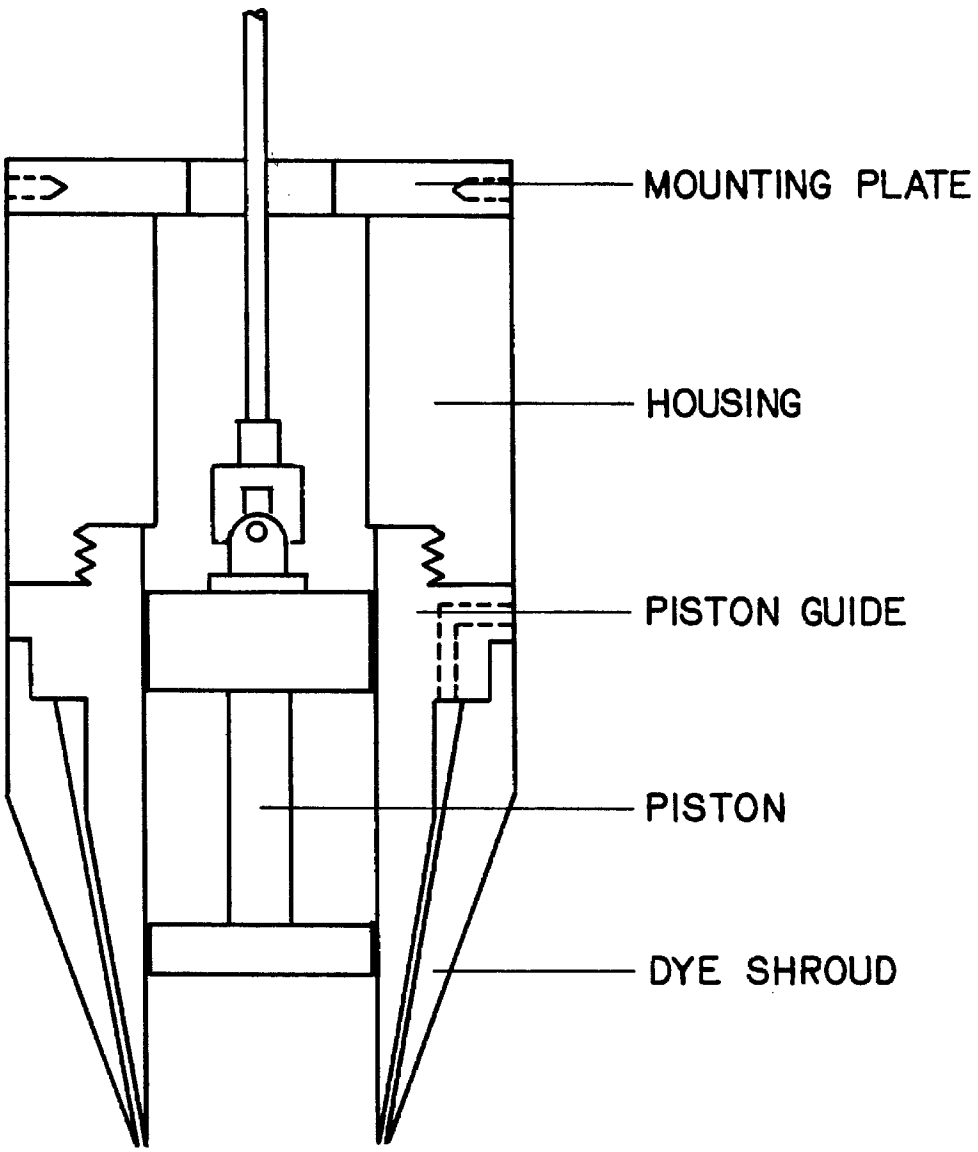

Fig. 2.3 Detail of Vortex Gun Assembly

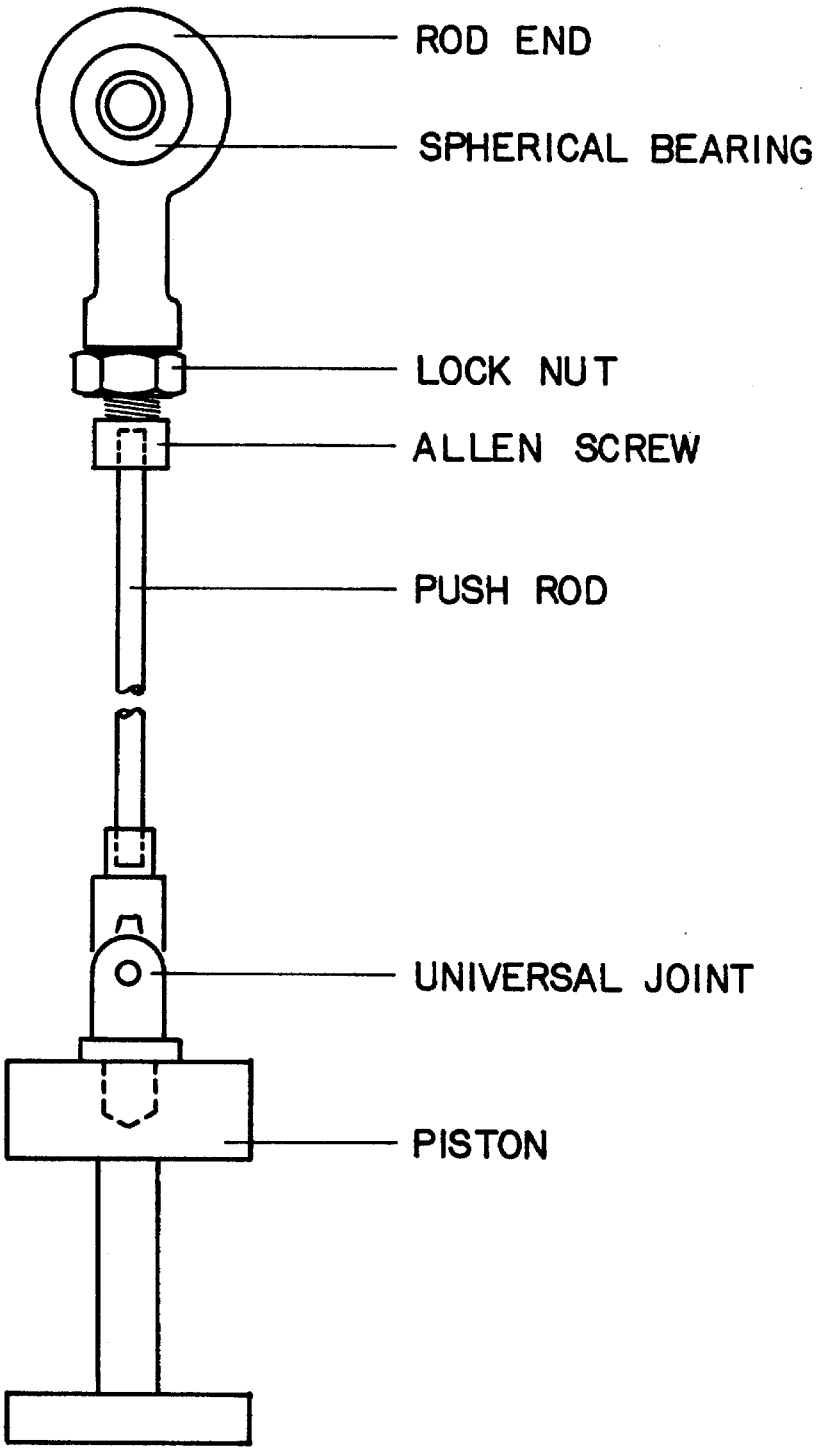

Fig. 2.4 Detail of Pushrod Assembly

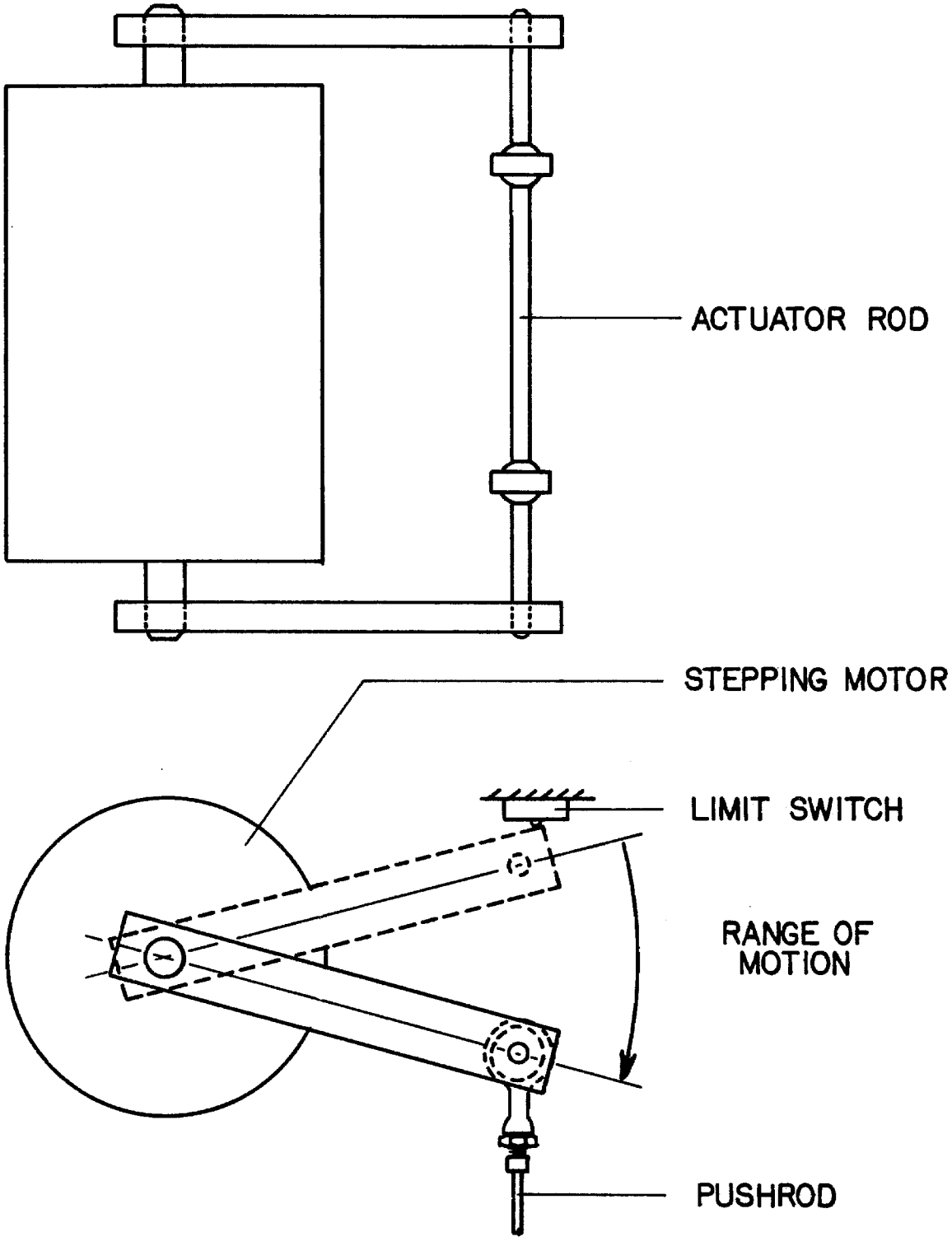

Fig. 2.5 Detail of Actuating Mechanism

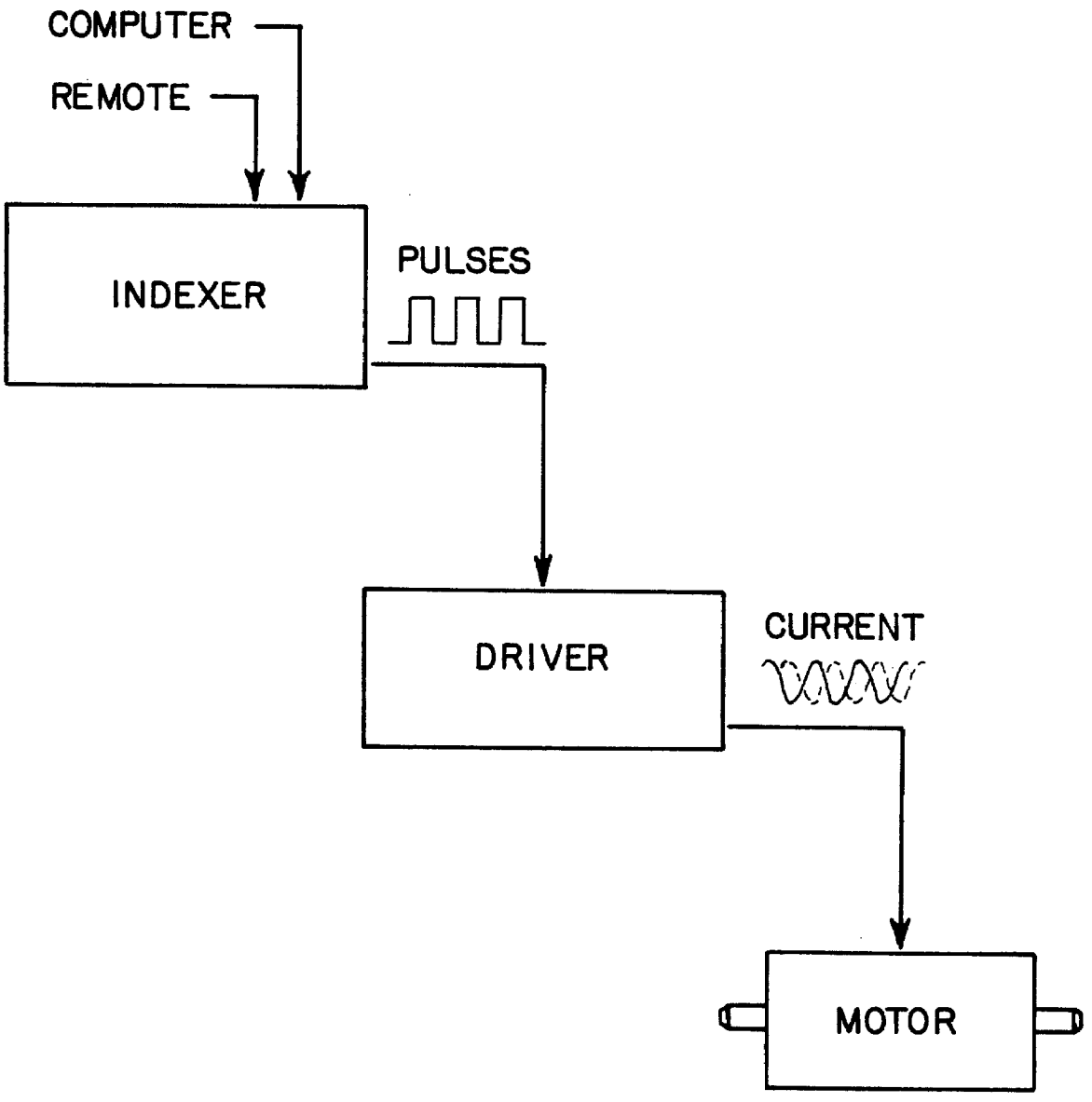

Fig. 2.6 Motion Control System

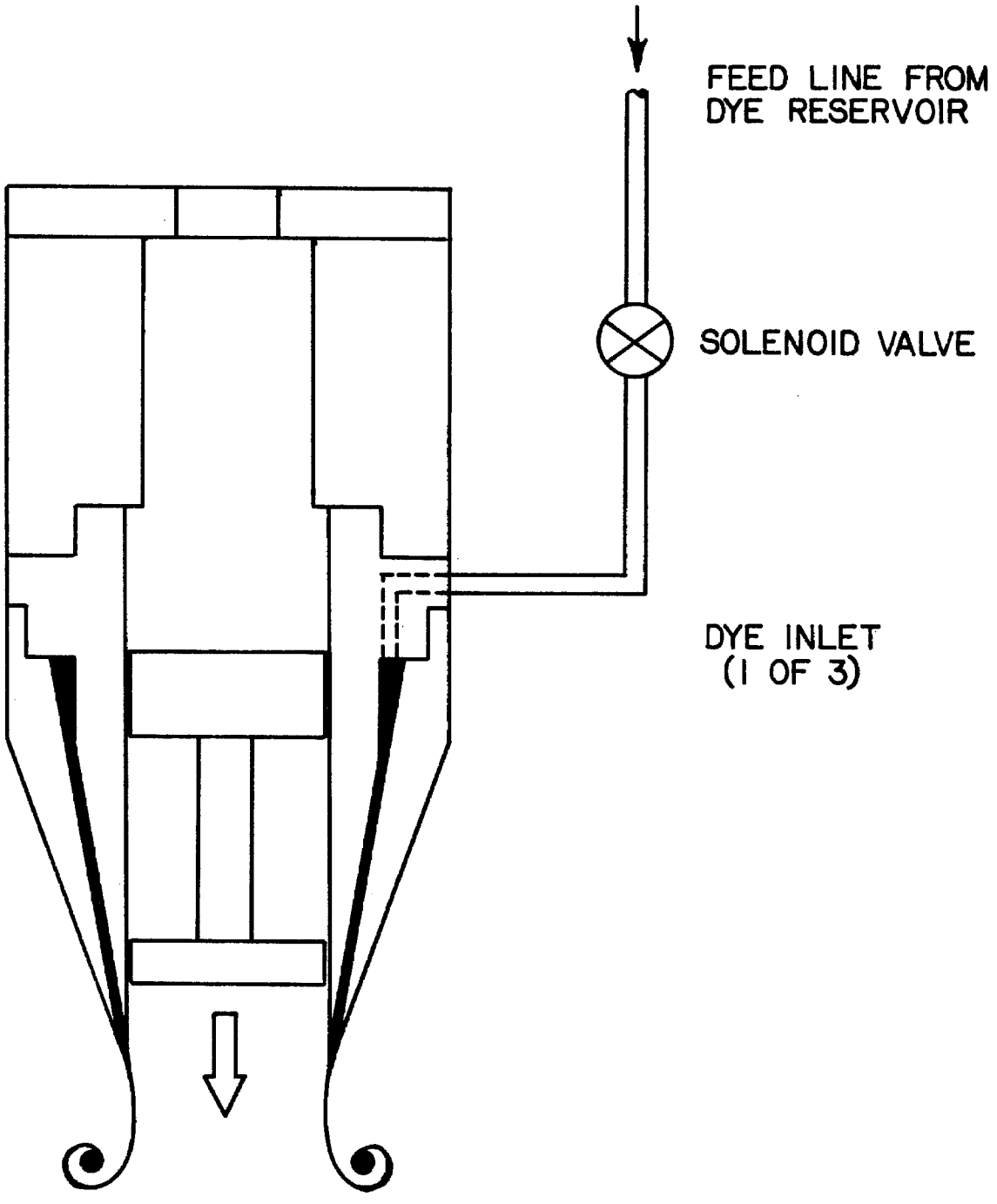

Fig. 2.7 The Dye Injection System

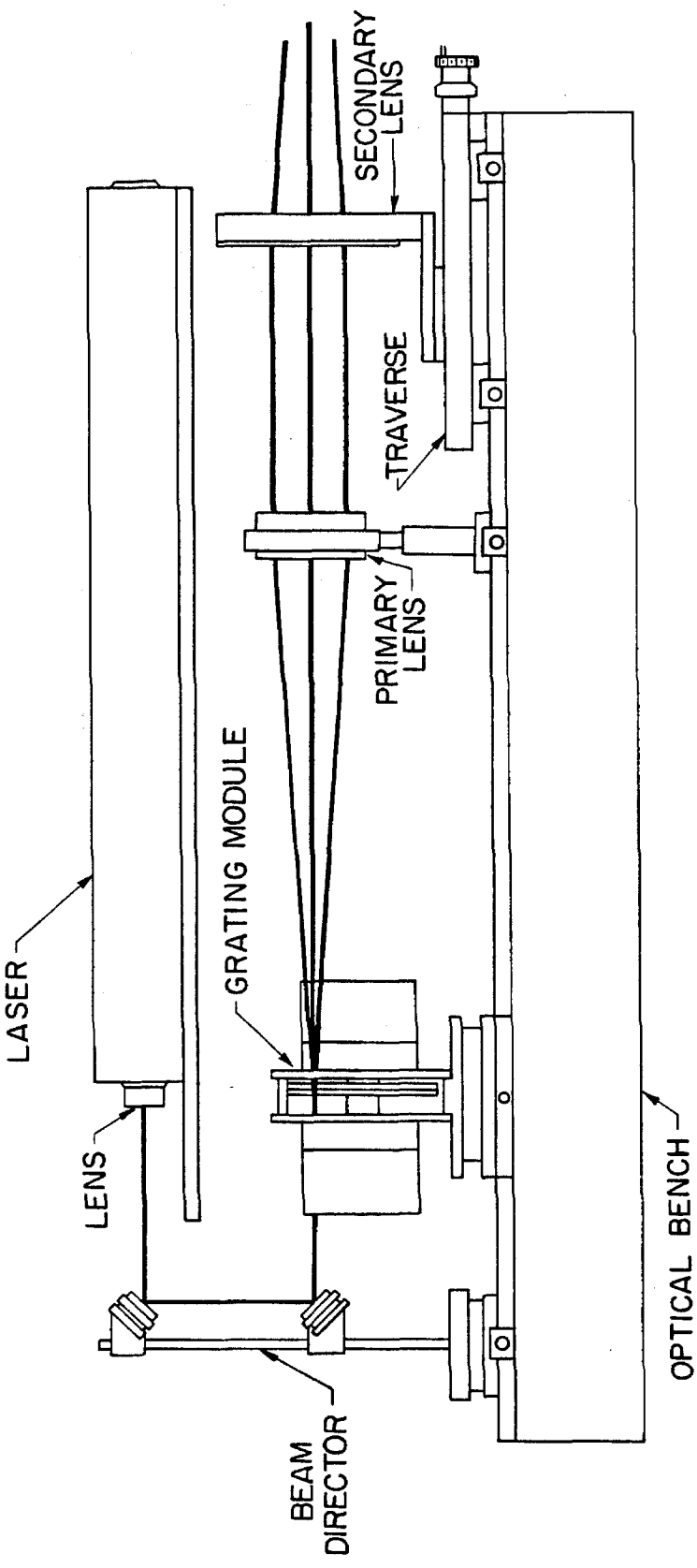

Fig. 3.1 Side View of the Two-channel LDV System (Glezer (1981))

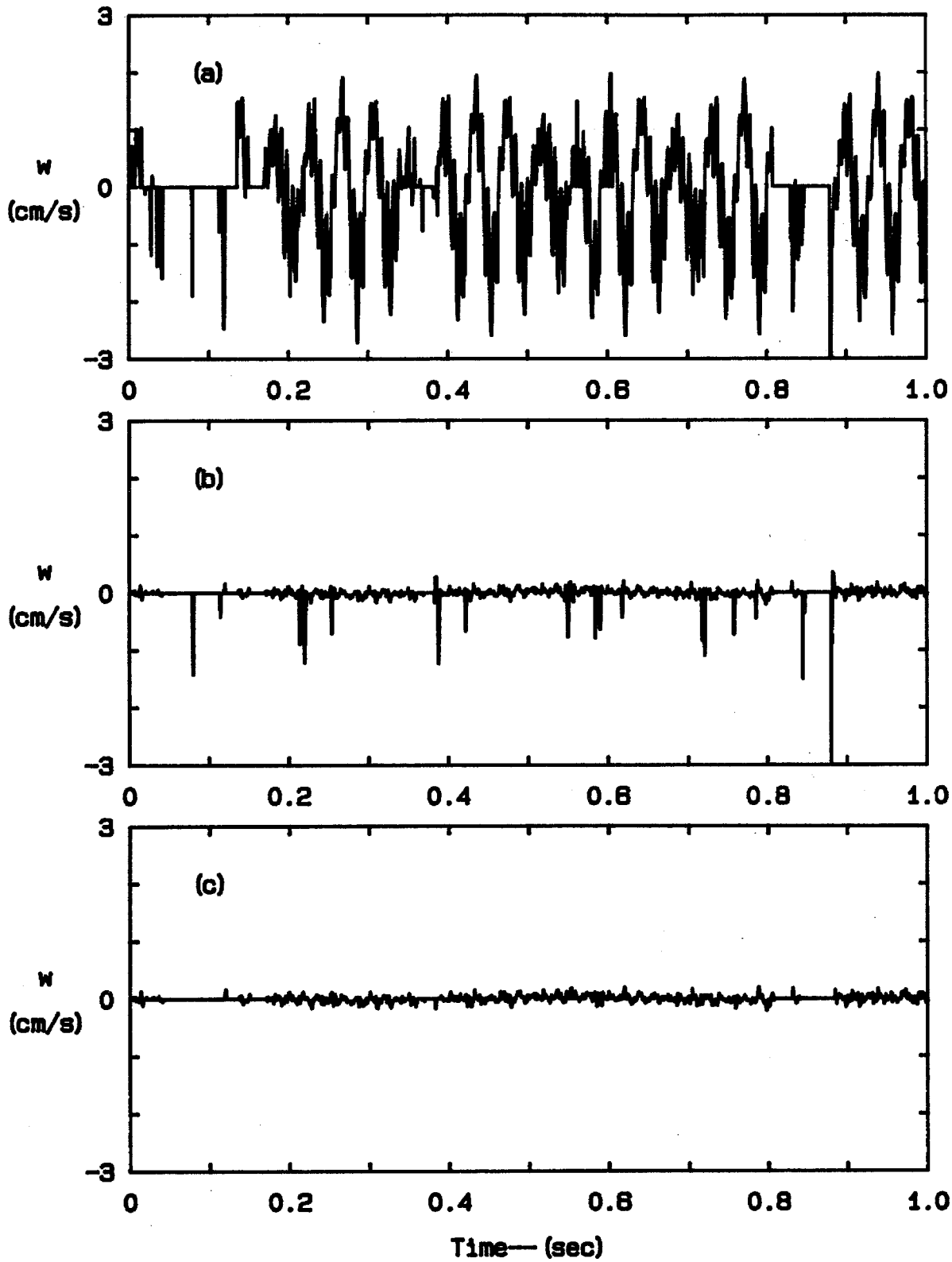

Fig. 3.2 Filtering the Grating Noise

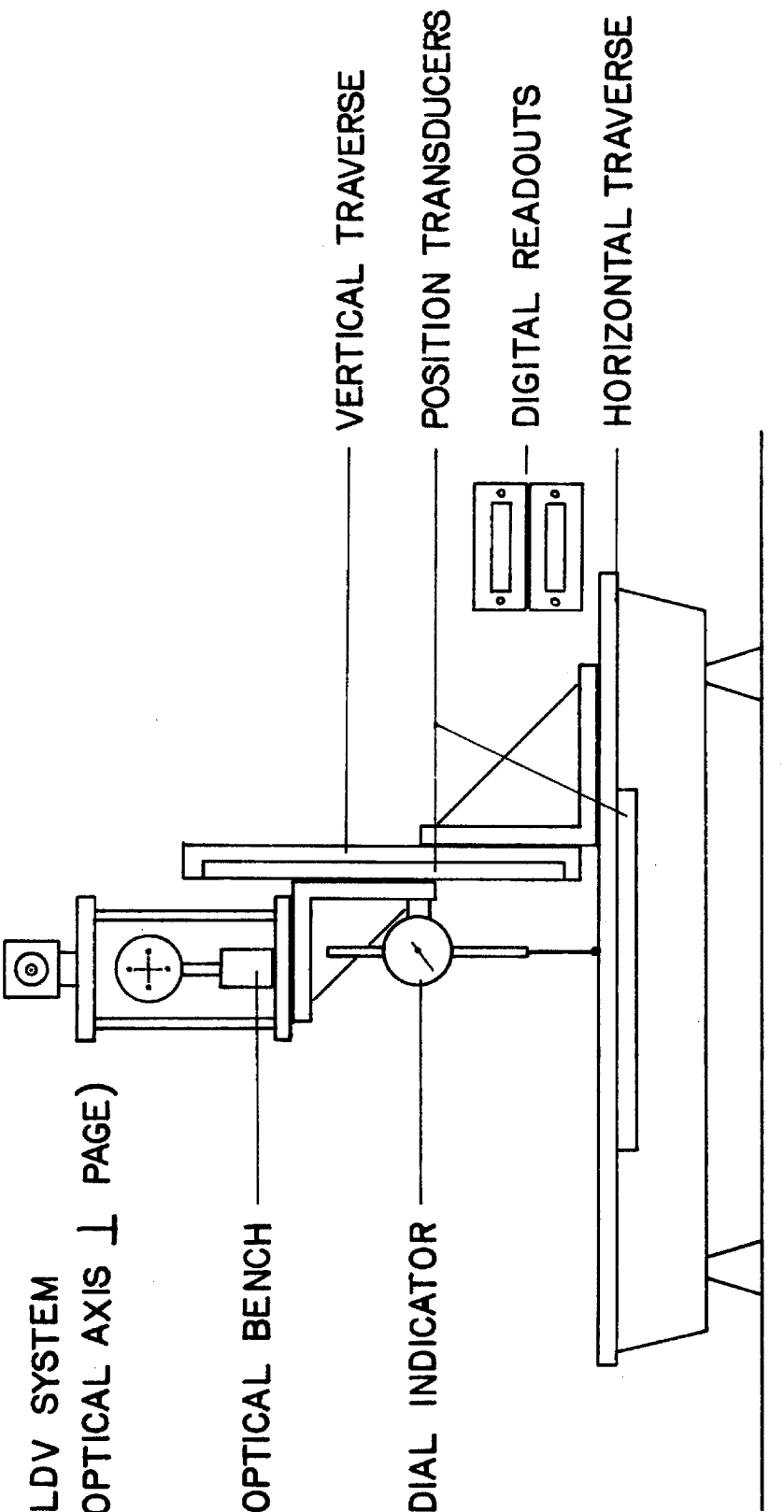

Fig. 3.3 Installation of Position Transducers

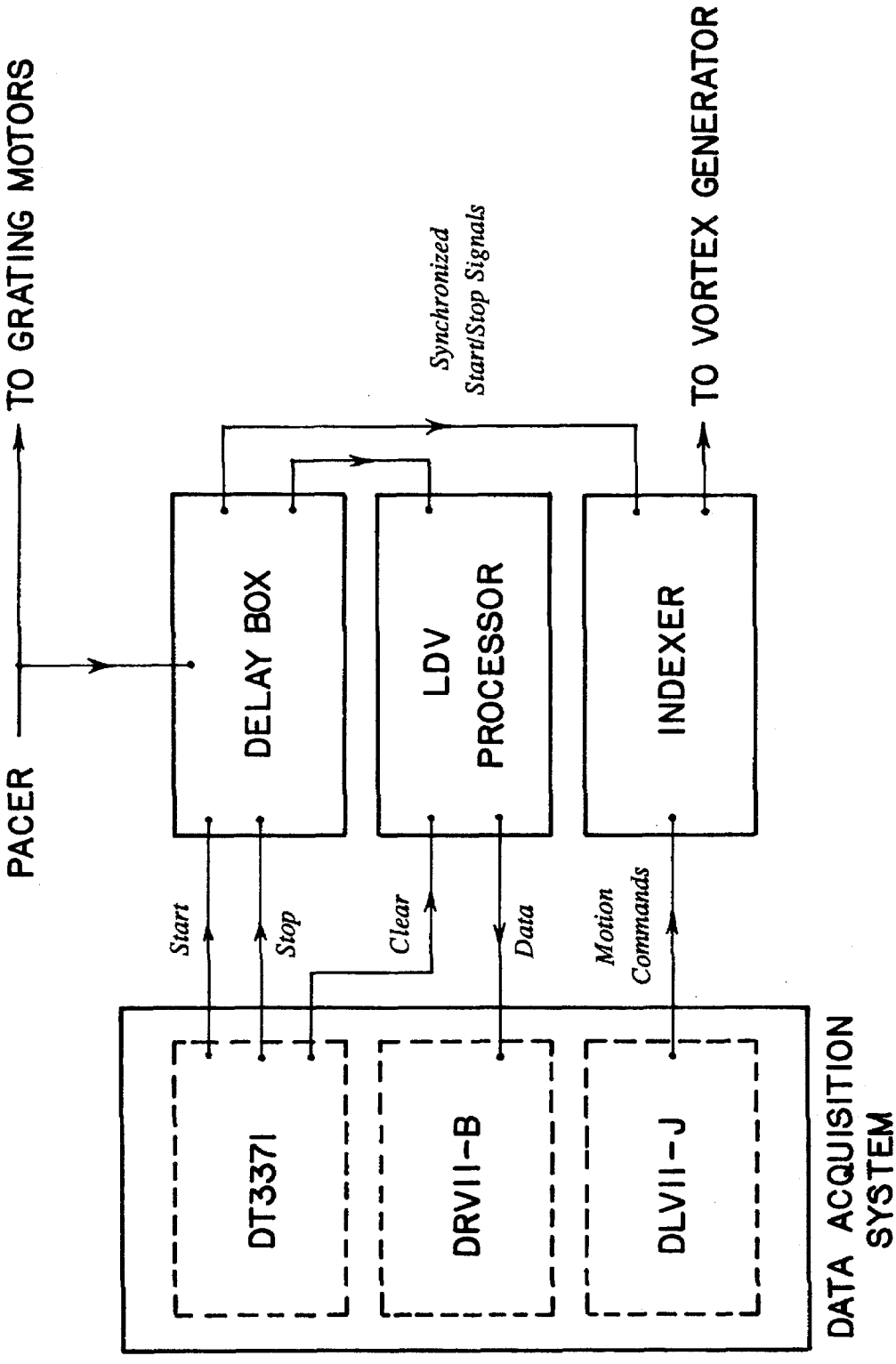

Fig. 3.4 Device Interconnections

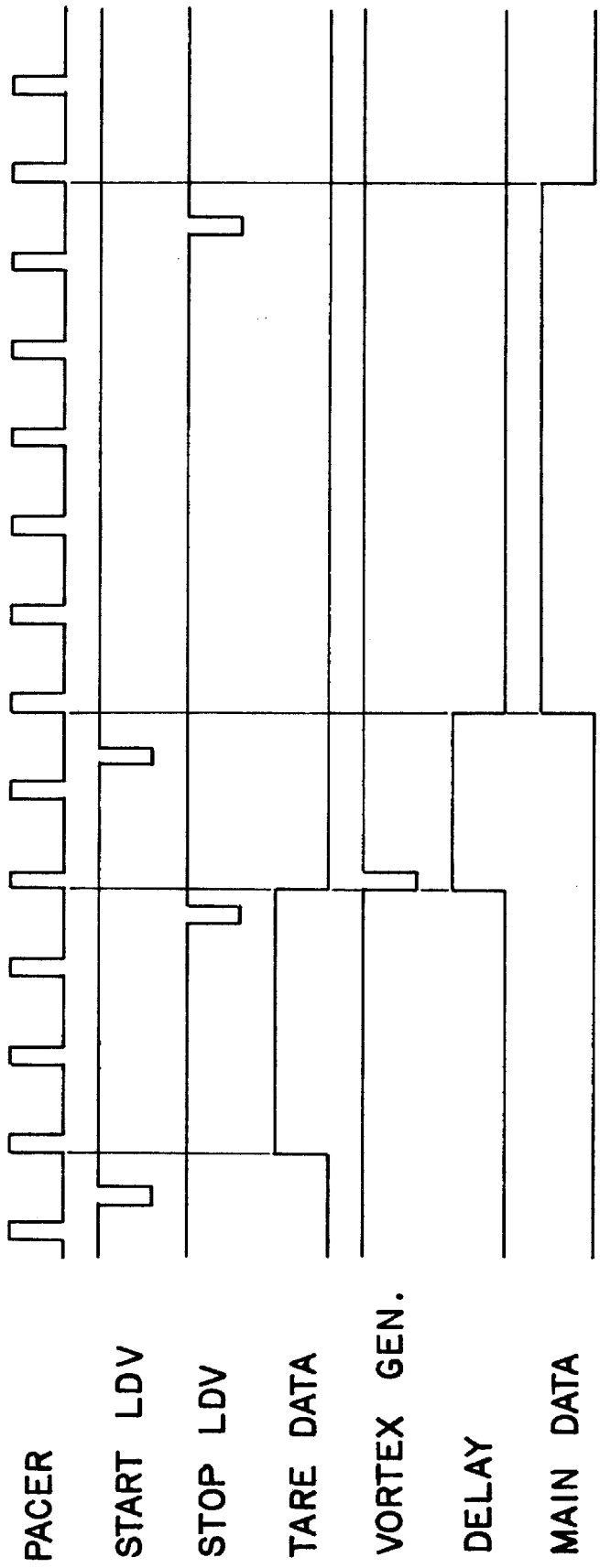

Fig. 3.5 Timing Diagram

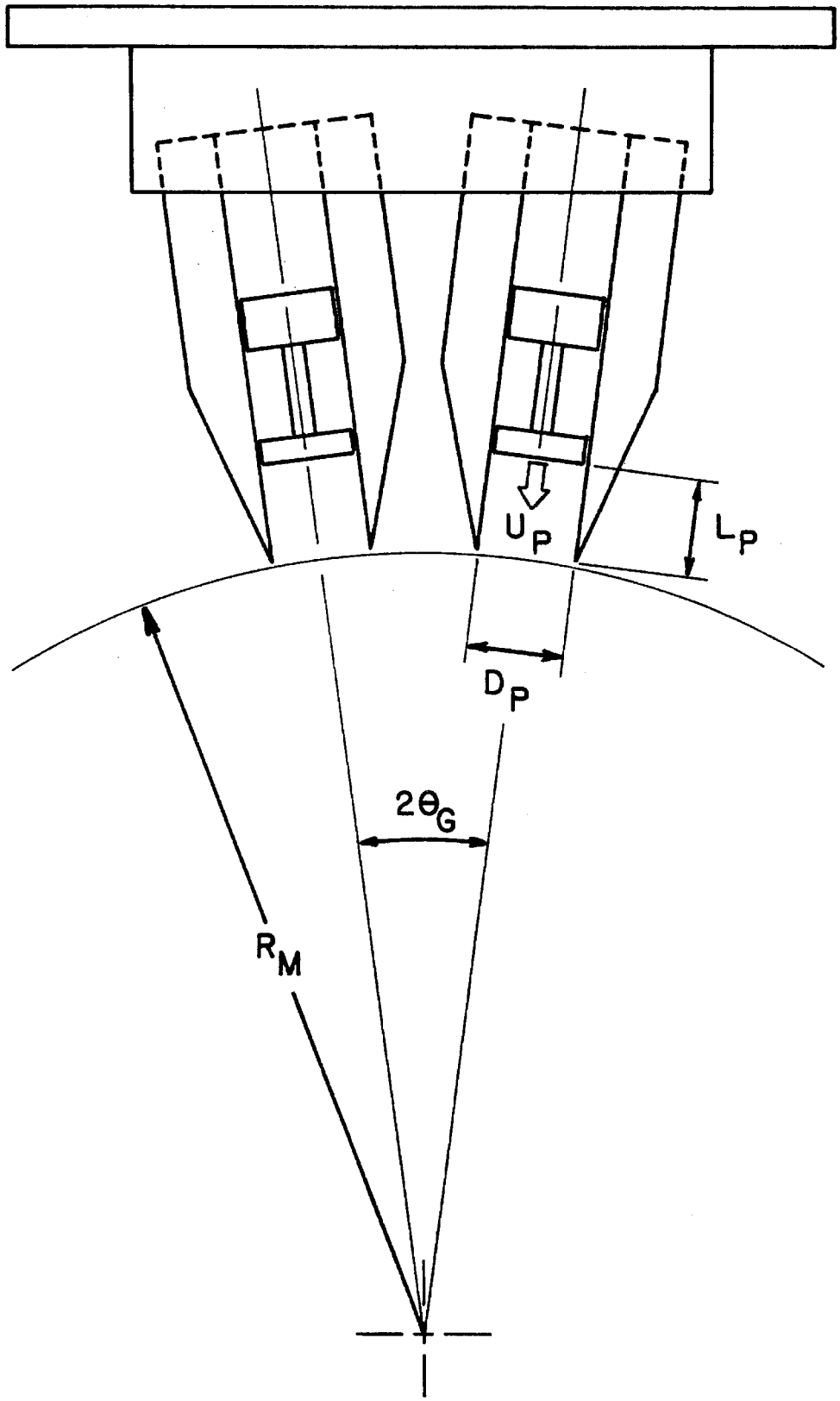

Fig. 4.1 Generation Conditions

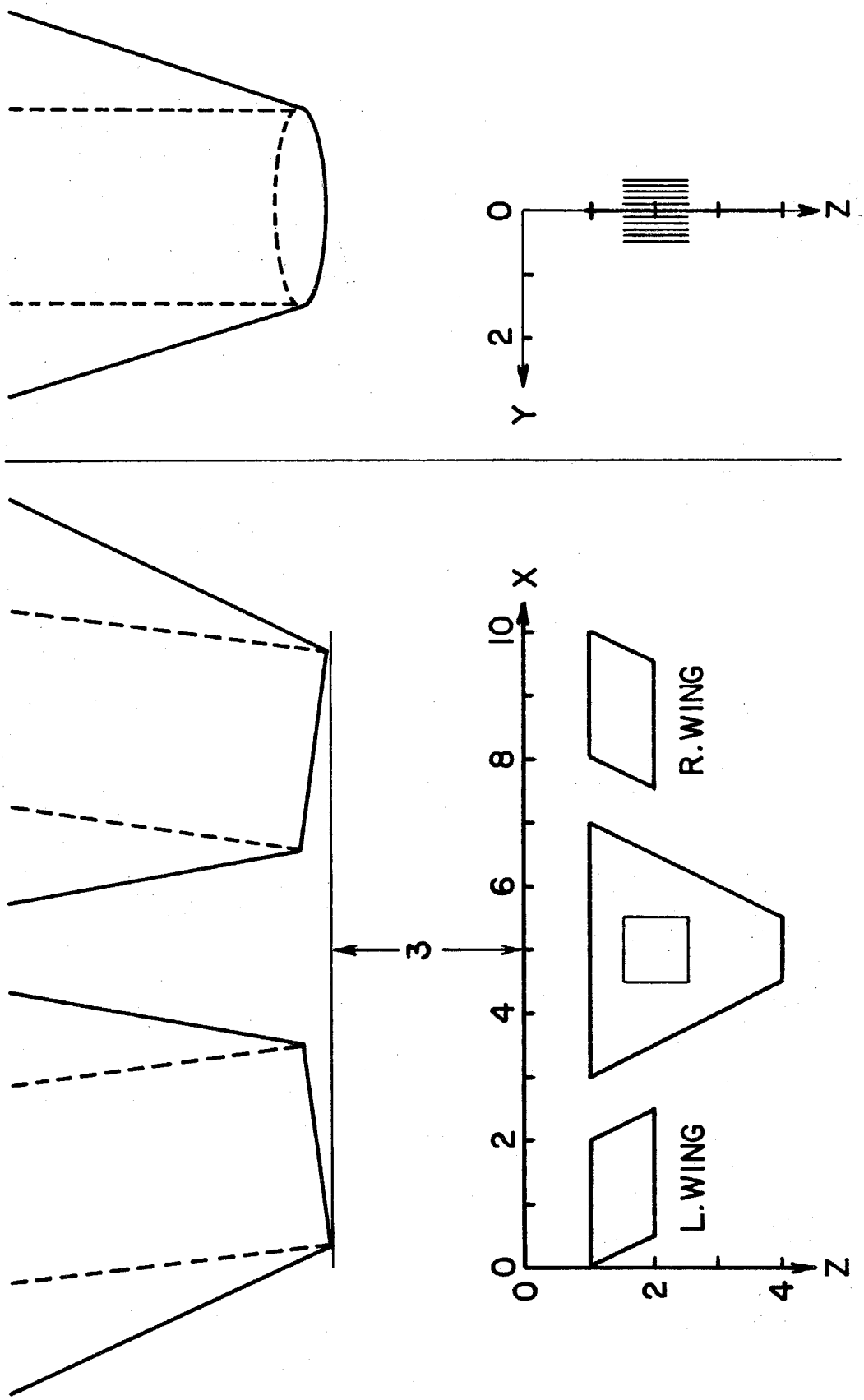

Fig. 4.2 The Measurement Region

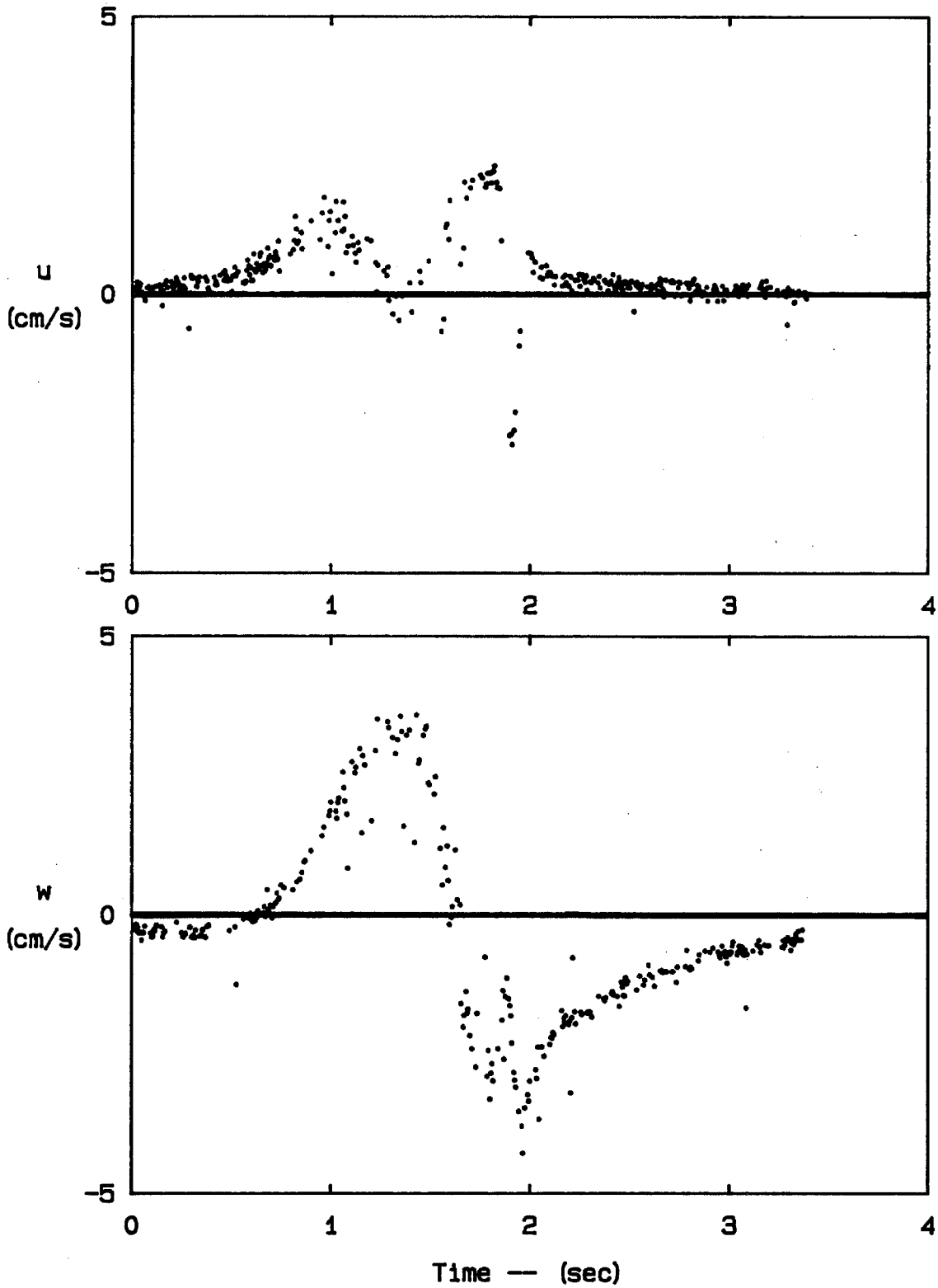

Fig. 5.1 Typical Unfiltered Velocity Traces

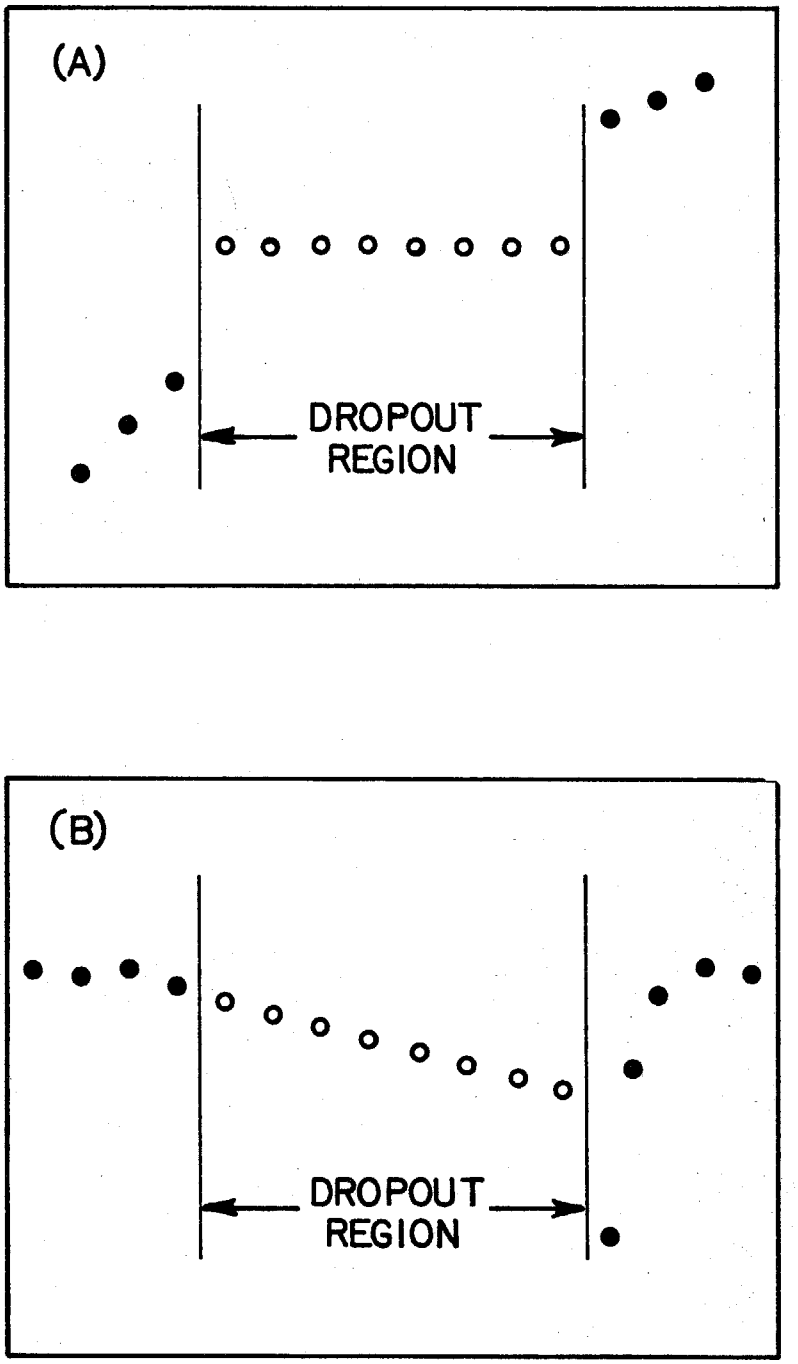

Fig. 5.2 Pitfalls in Filling in Dropouts

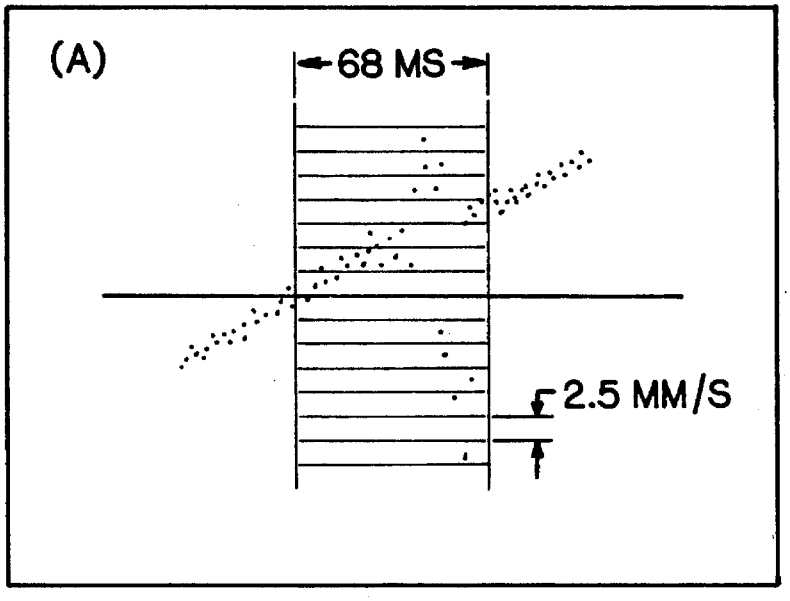

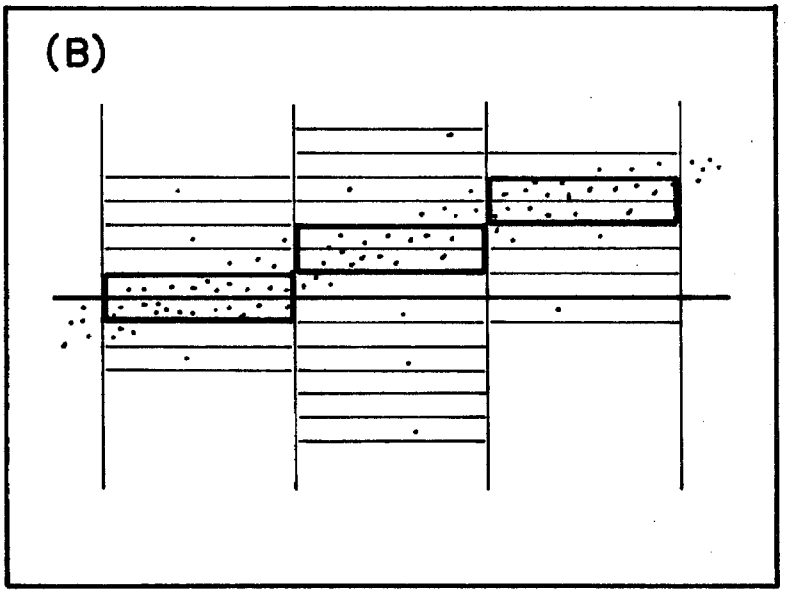

Fig. 5.3 Screening the Velocity Data

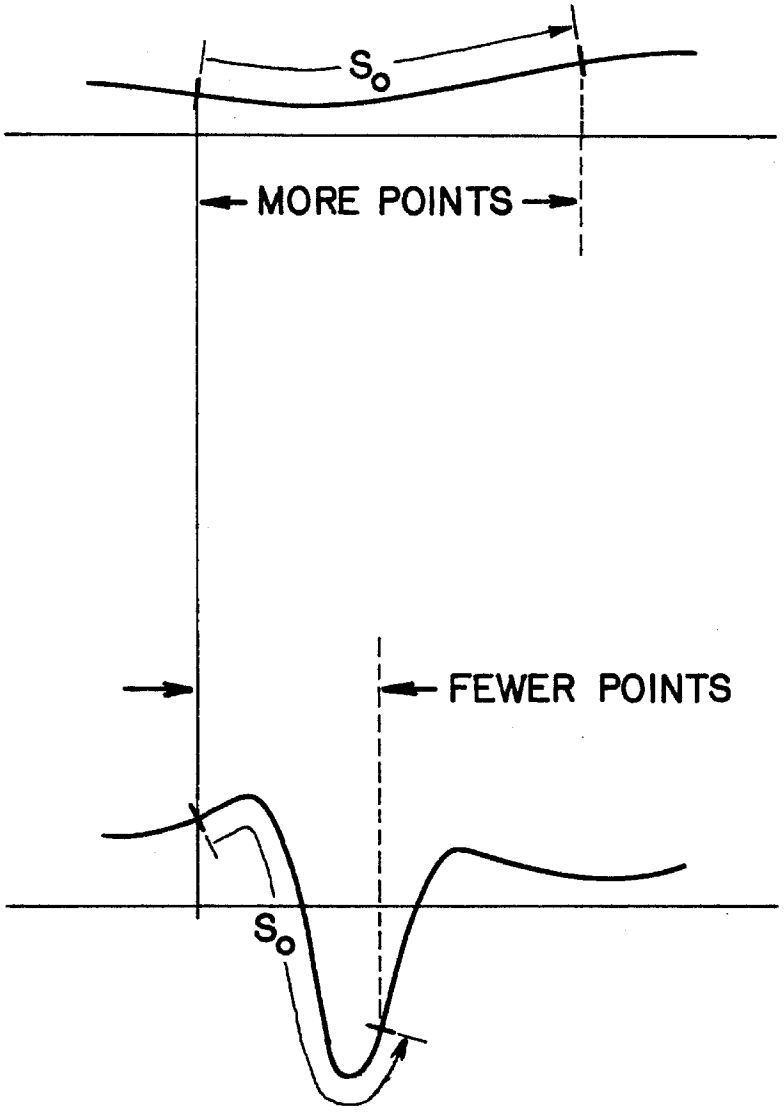

Fig. 5.4 Self-adjusting Curve Fit

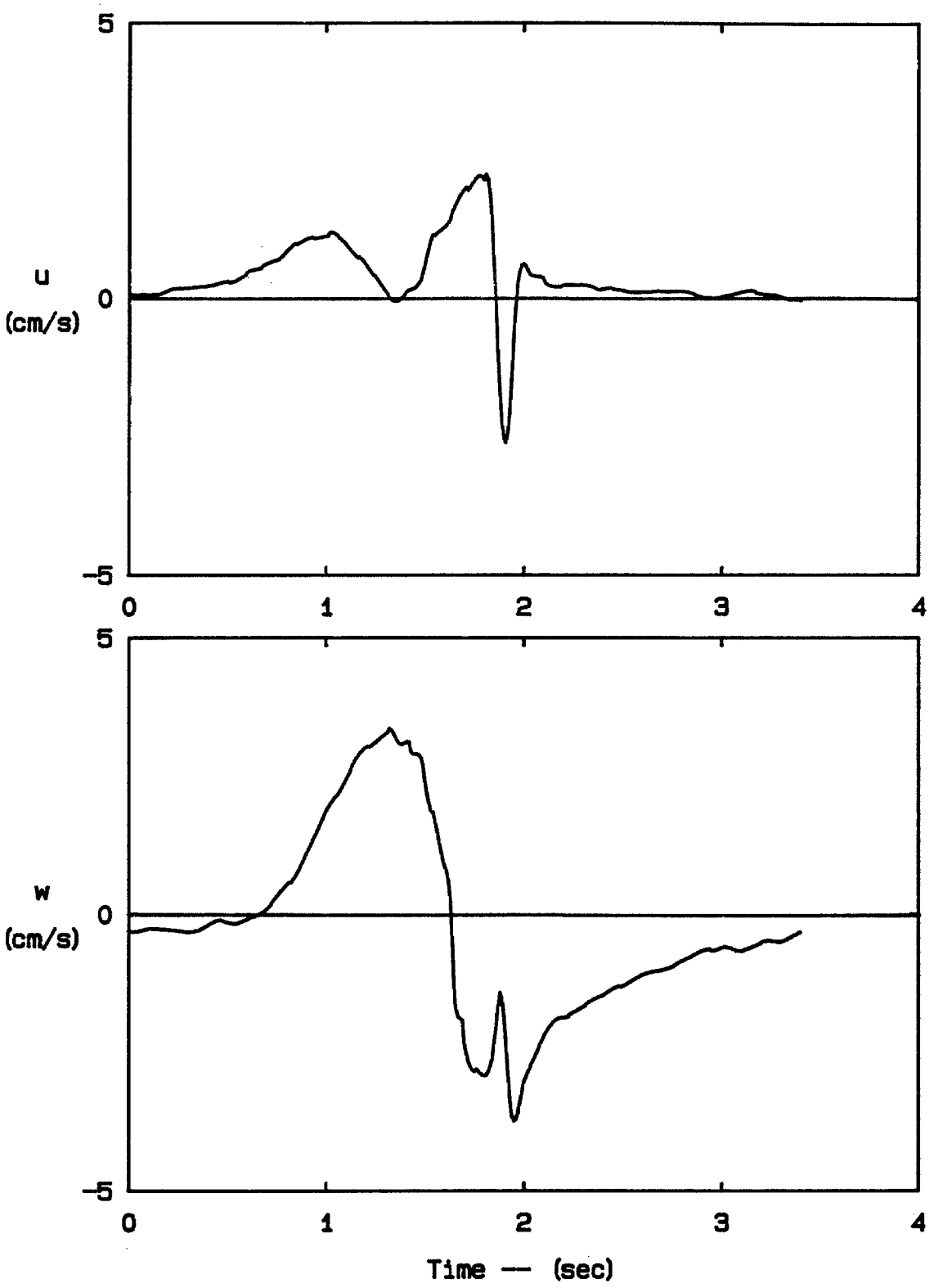

Fig. 5.5 Data from Fig. 5.1 after Smoothing

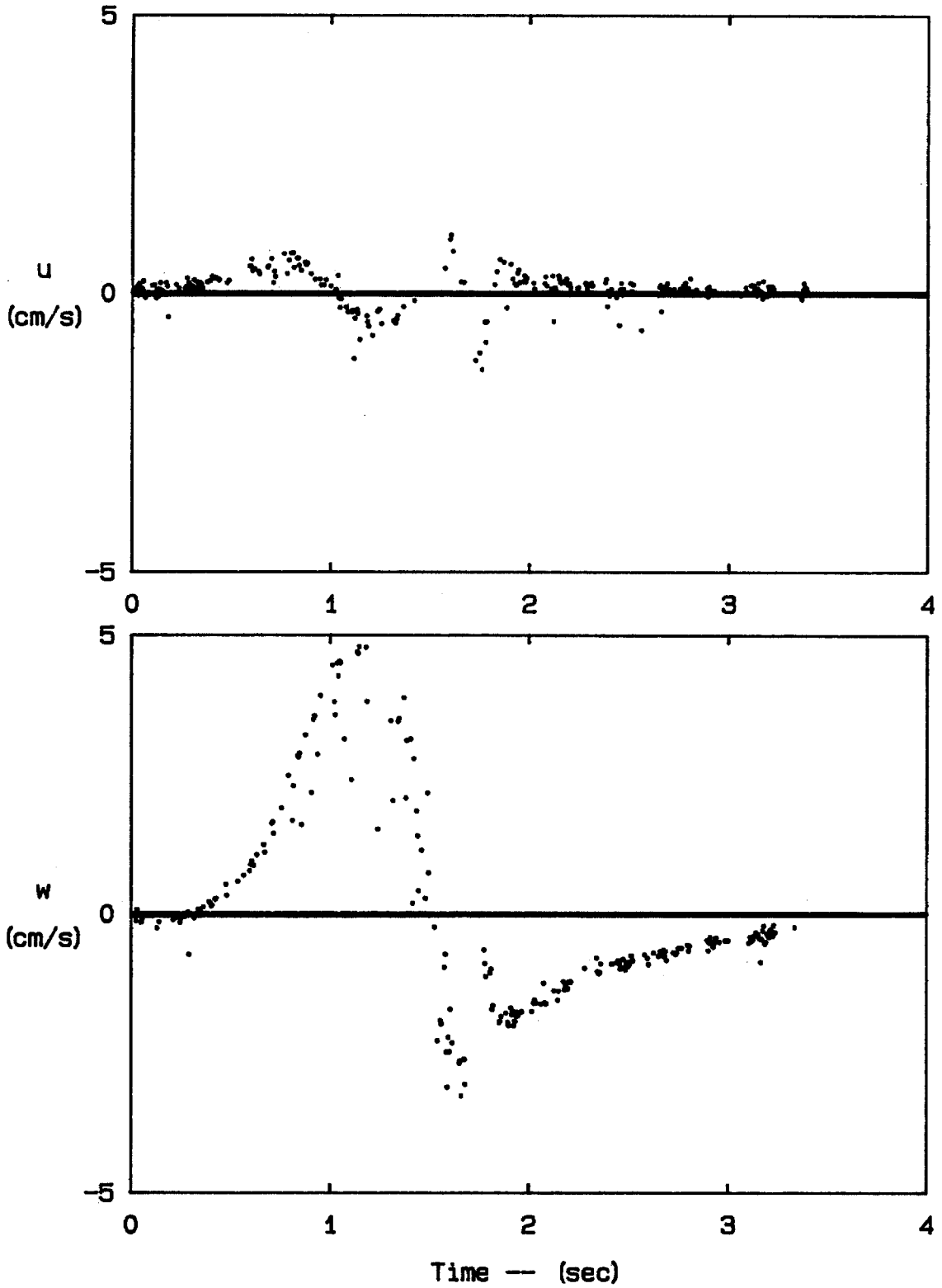

Fig. 5.6 Unsmoothed Data near Collision Area

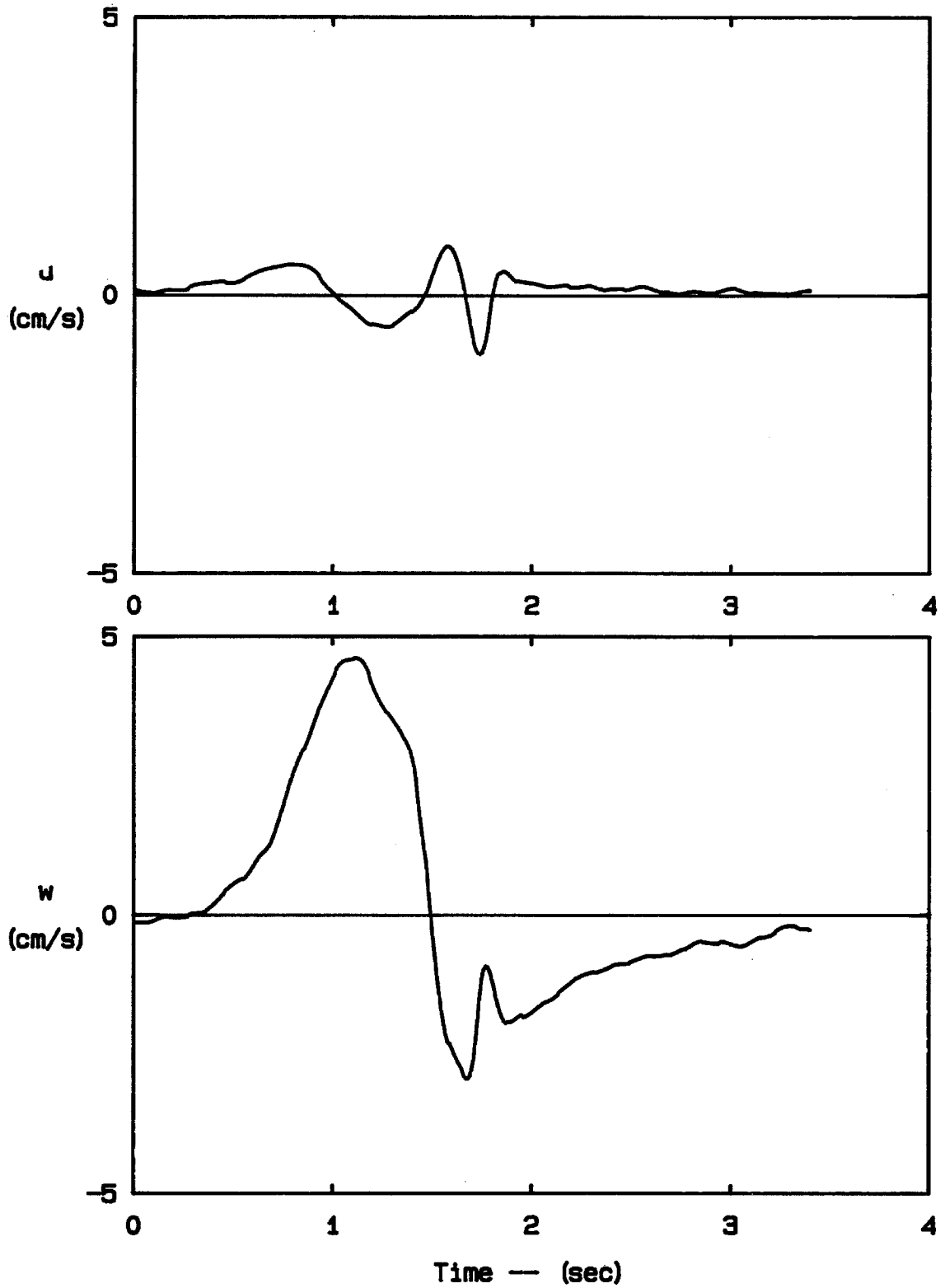

Fig. 5.7 Data from Fig. 5.6 after Smoothing

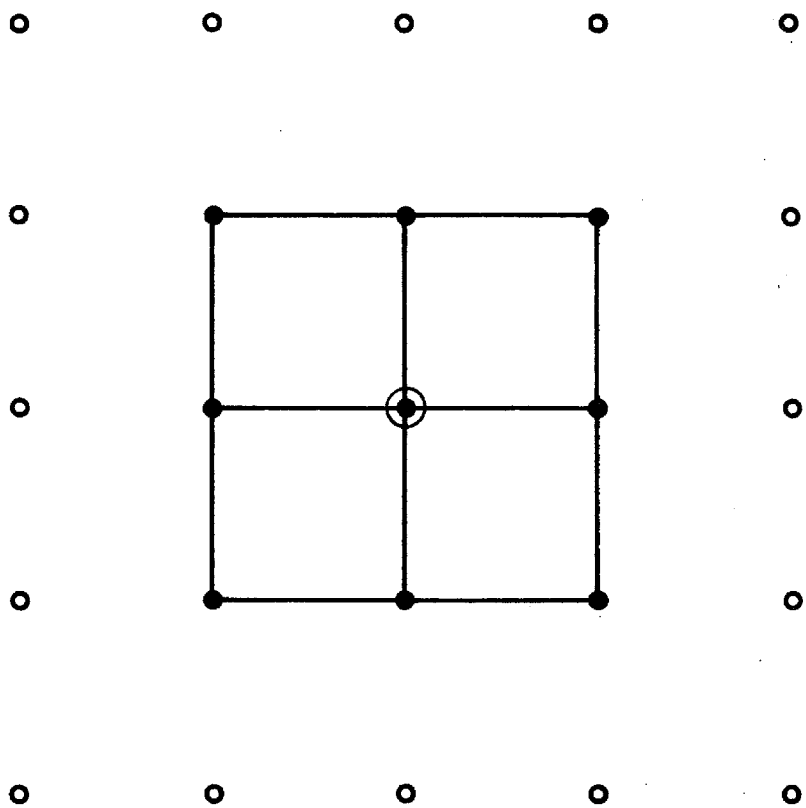

Fig. 5.8 Spatial Averaging Scheme

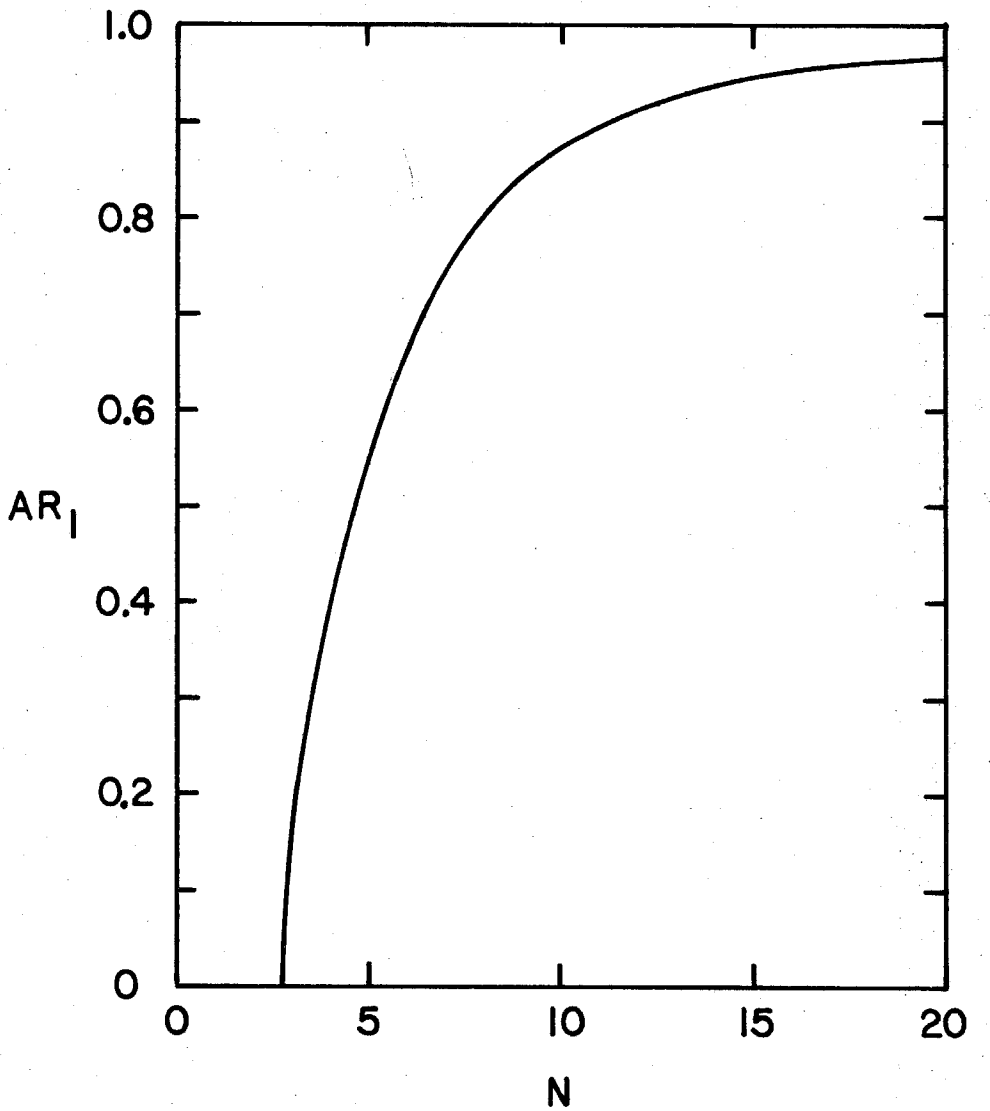

Fig. 5.9 Amplitude Response of 1-D Digital Filter

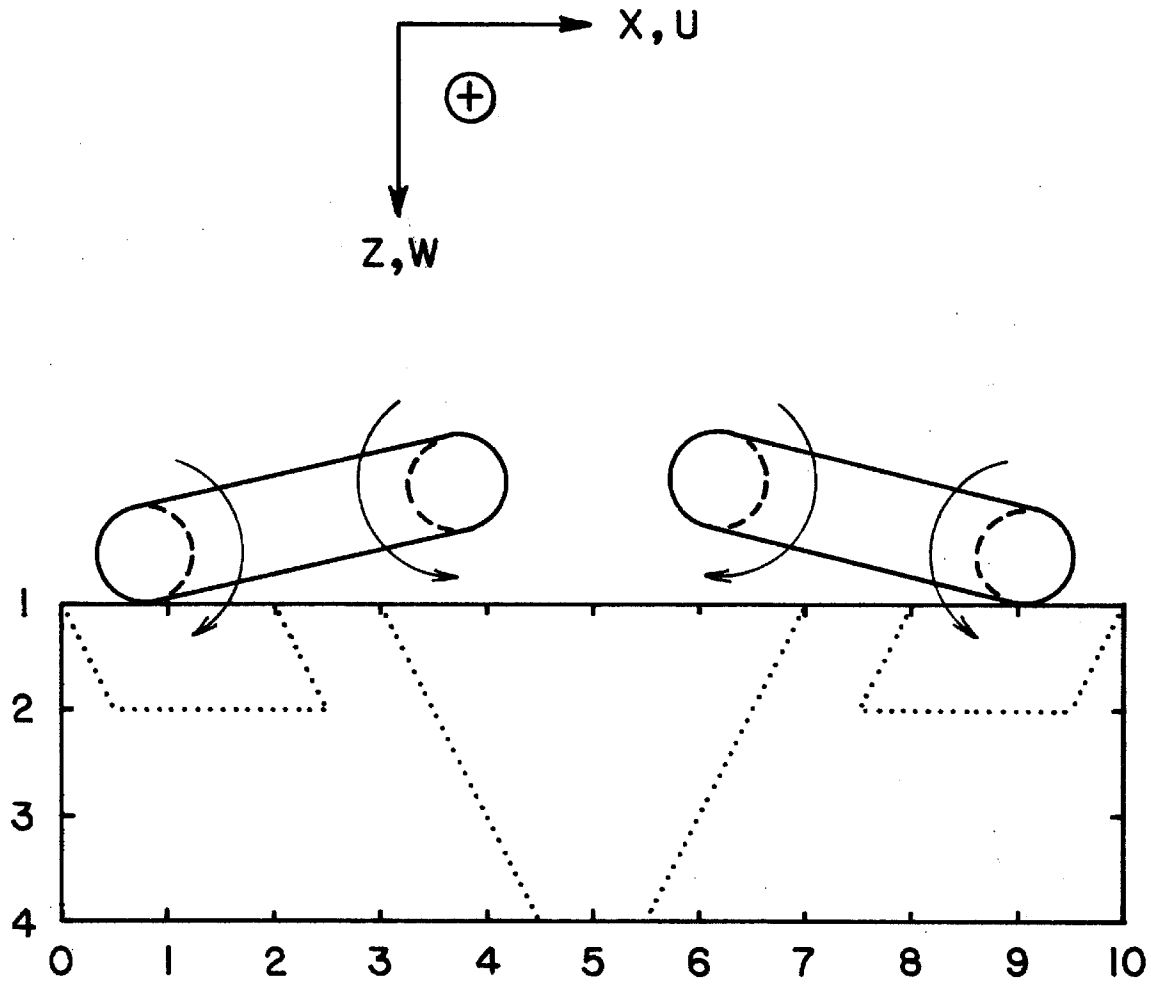

Fig. 6.1 Initial Vortex Locations

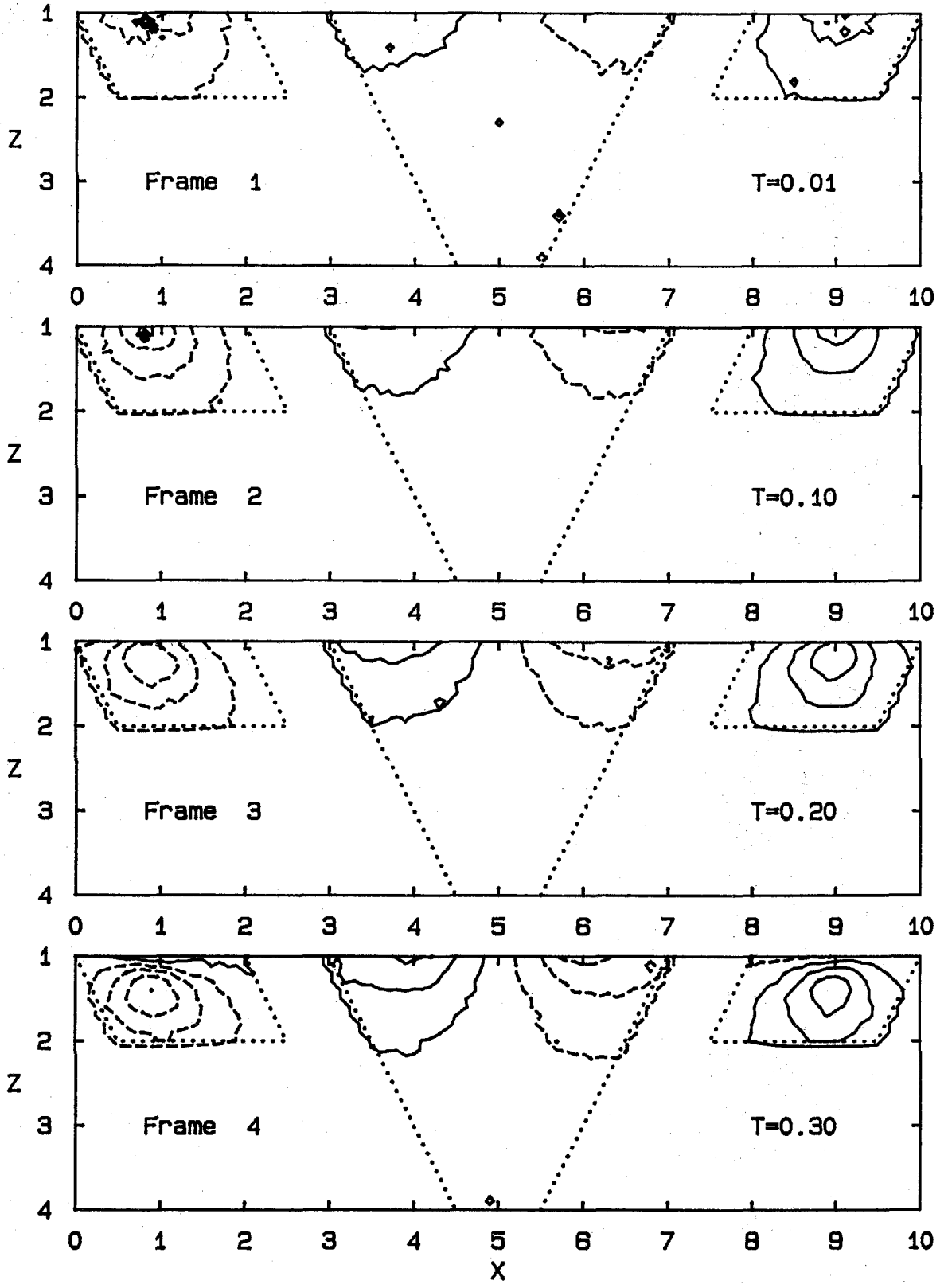

Fig. 8.2 Velocity Contours in the X-Z Plane; u-component (unsmoothed)

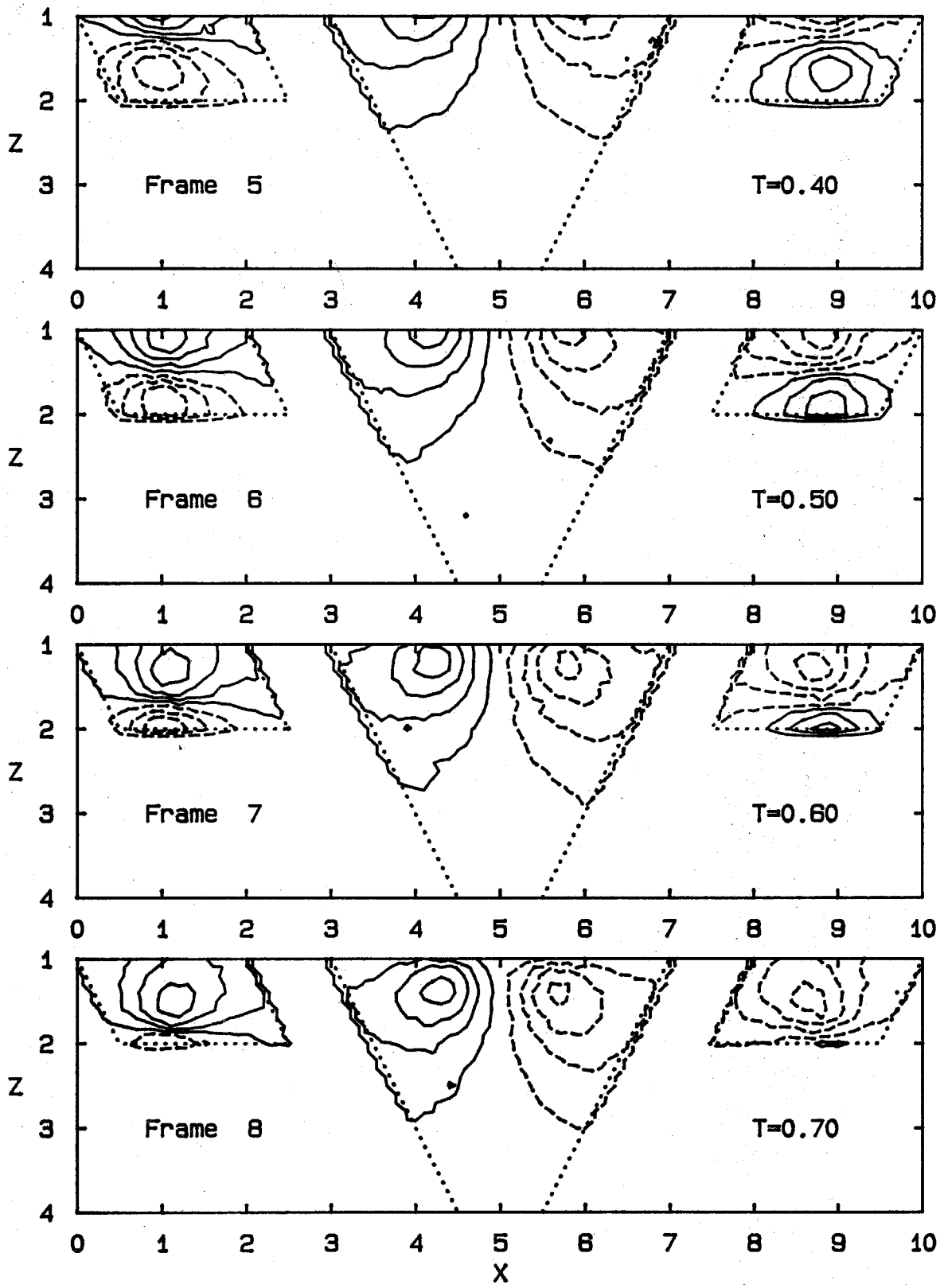

Fig. 6.2 Velocity Contours in the X-Z Plane; u-component (unsmoothed)

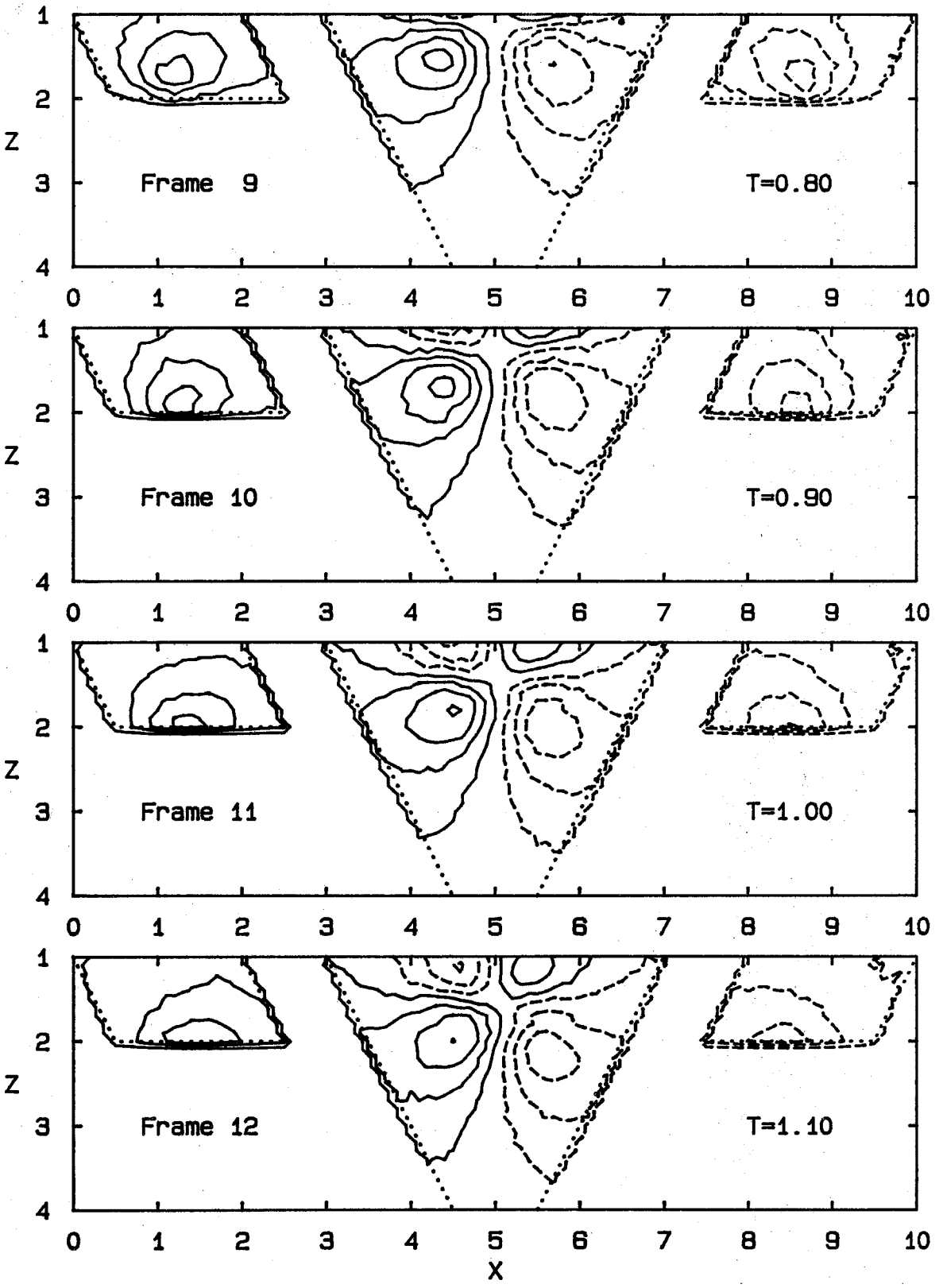

Fig. 6.2 Velocity Contours in the X-Z Plane; u-component (unsmoothed)

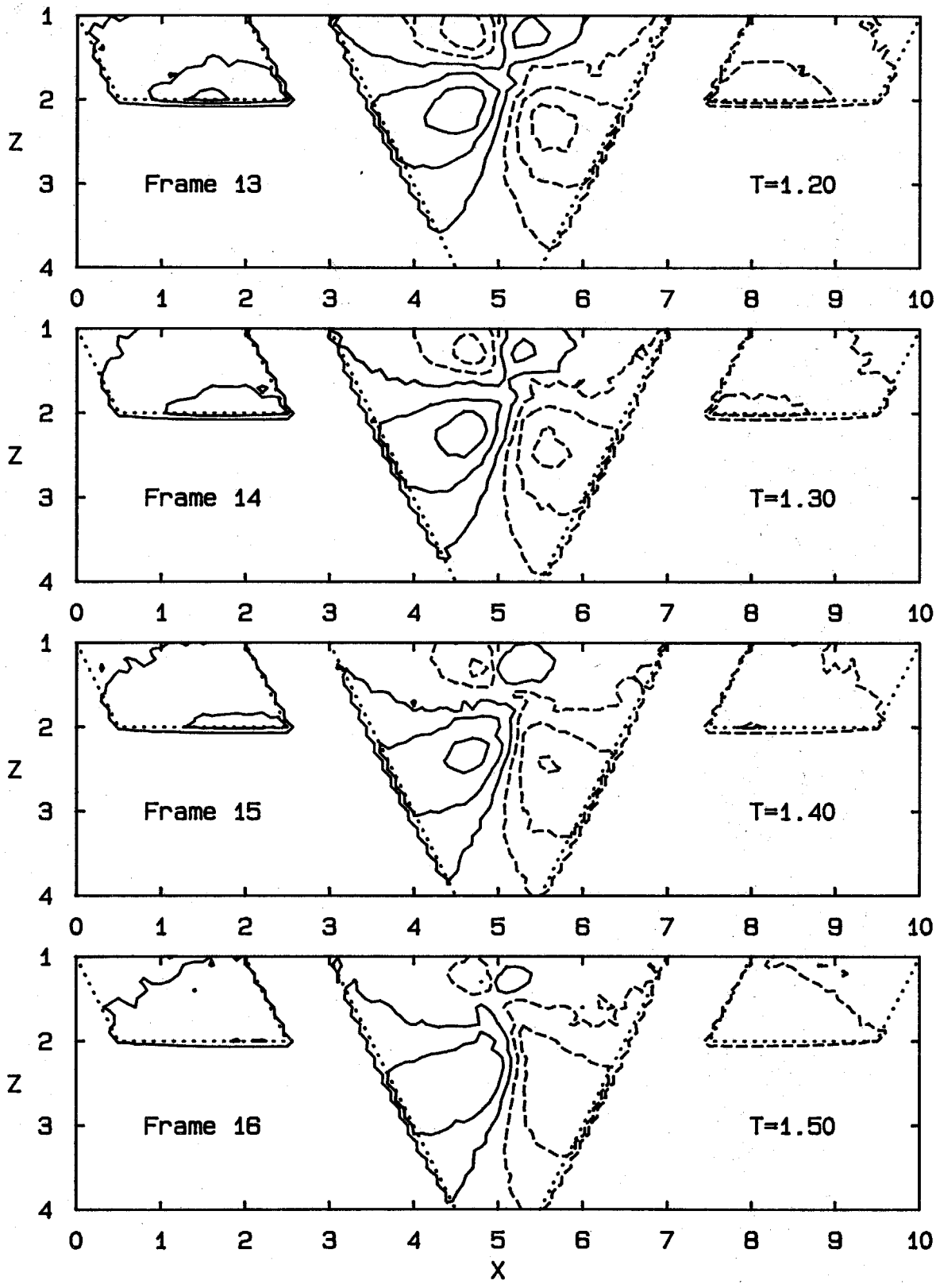

Fig. 6.2 Velocity Contours in the X-Z Plane; u-component (unsmoothed)

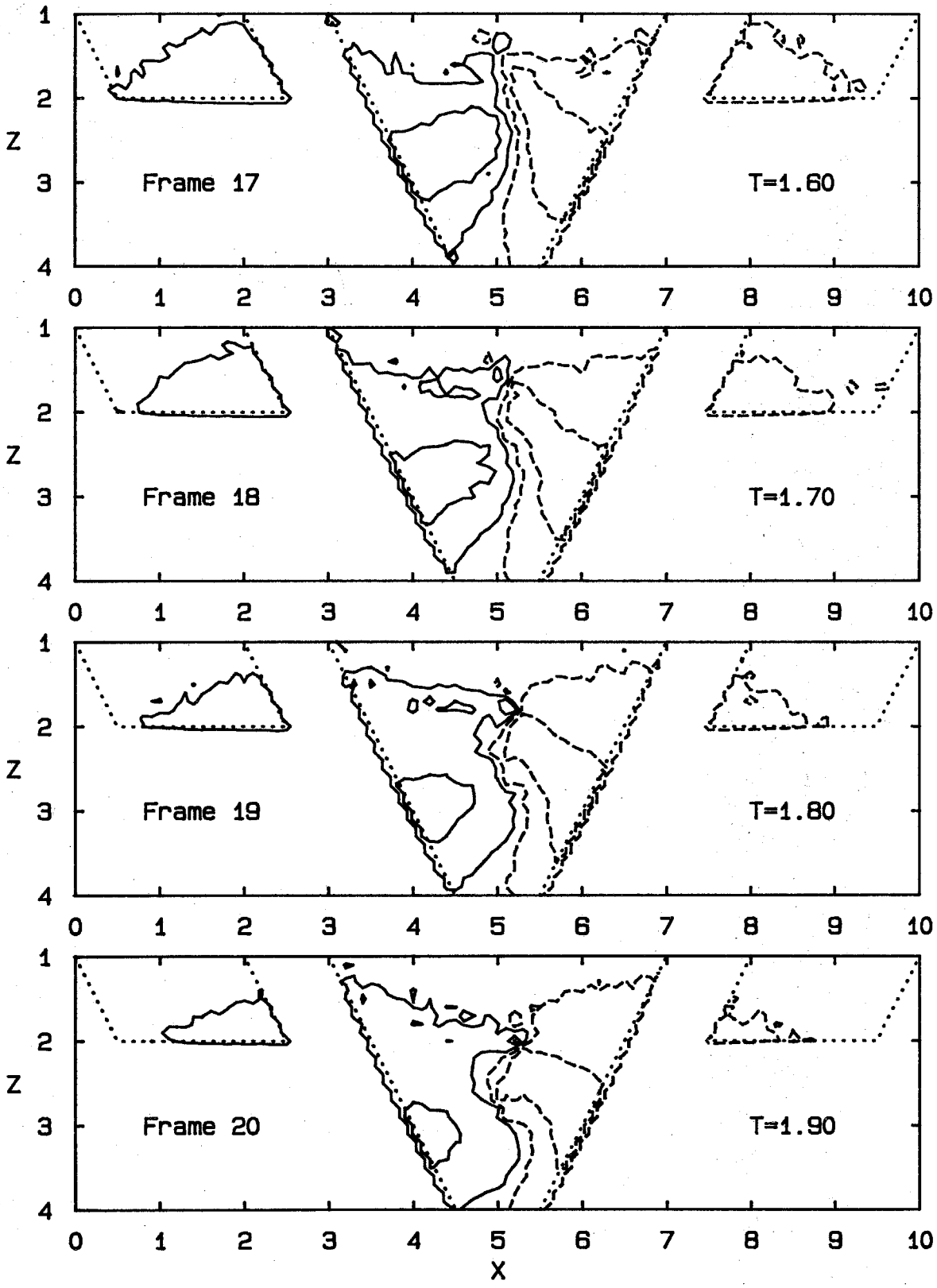

Fig. 6.2 Velocity Contours in the X-Z Plane; u-component (unsmoothed)

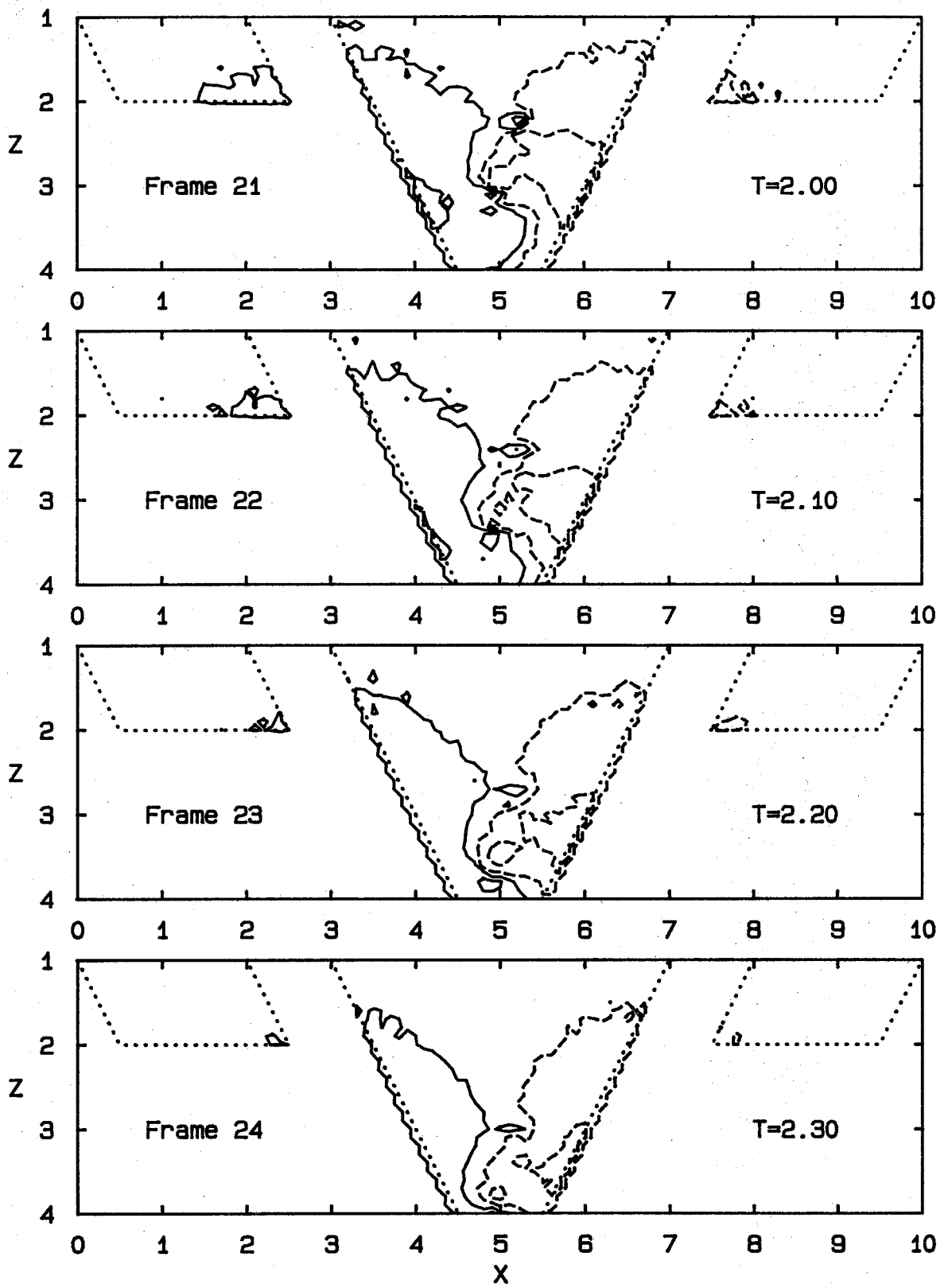

Fig. 6.2 Velocity Contours in the X-Z Plane; u-component (unsmoothed)

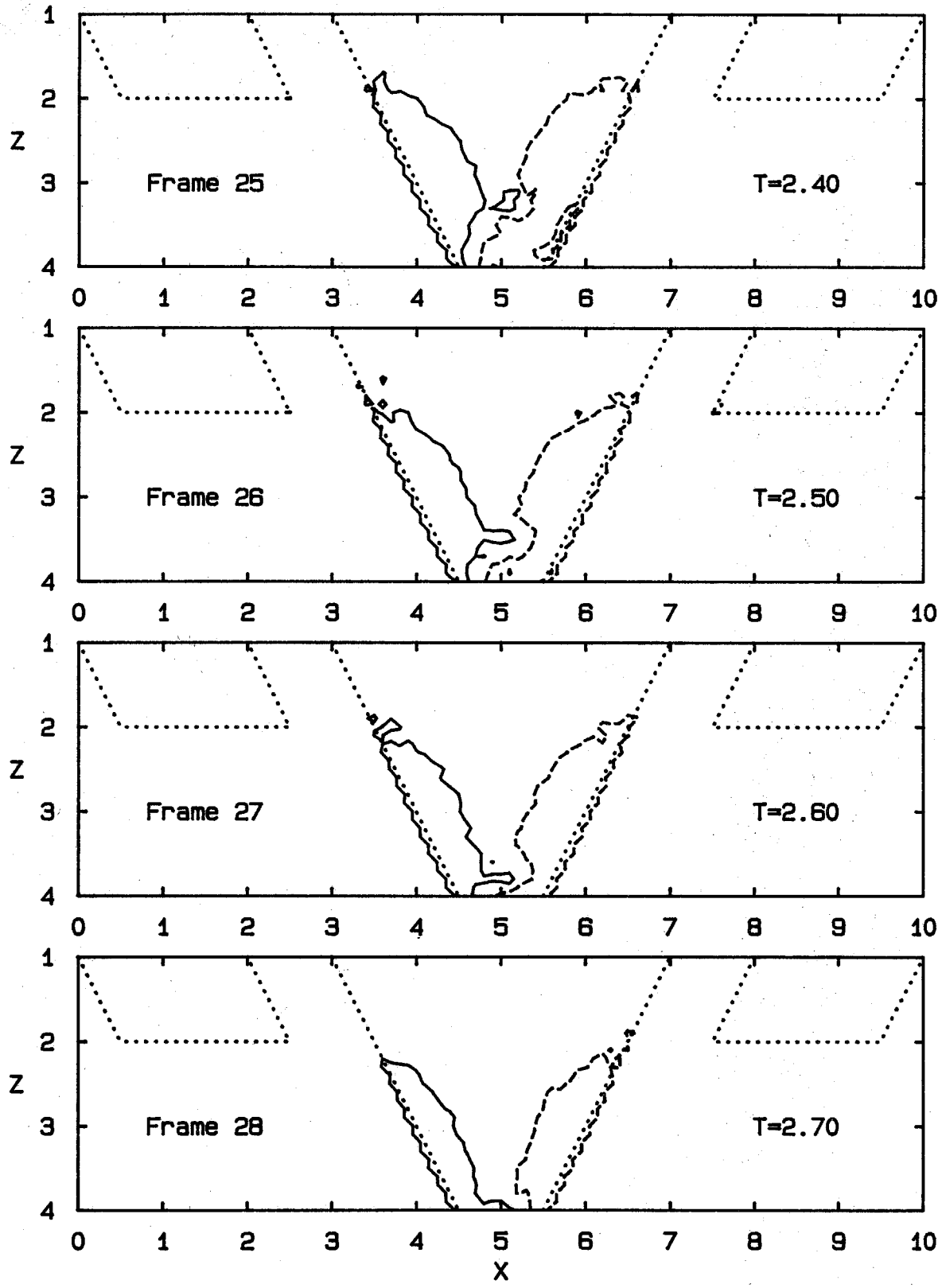

Fig. 6.2 Velocity Contours in the X-Z Plane; u-component (unsmoothed)

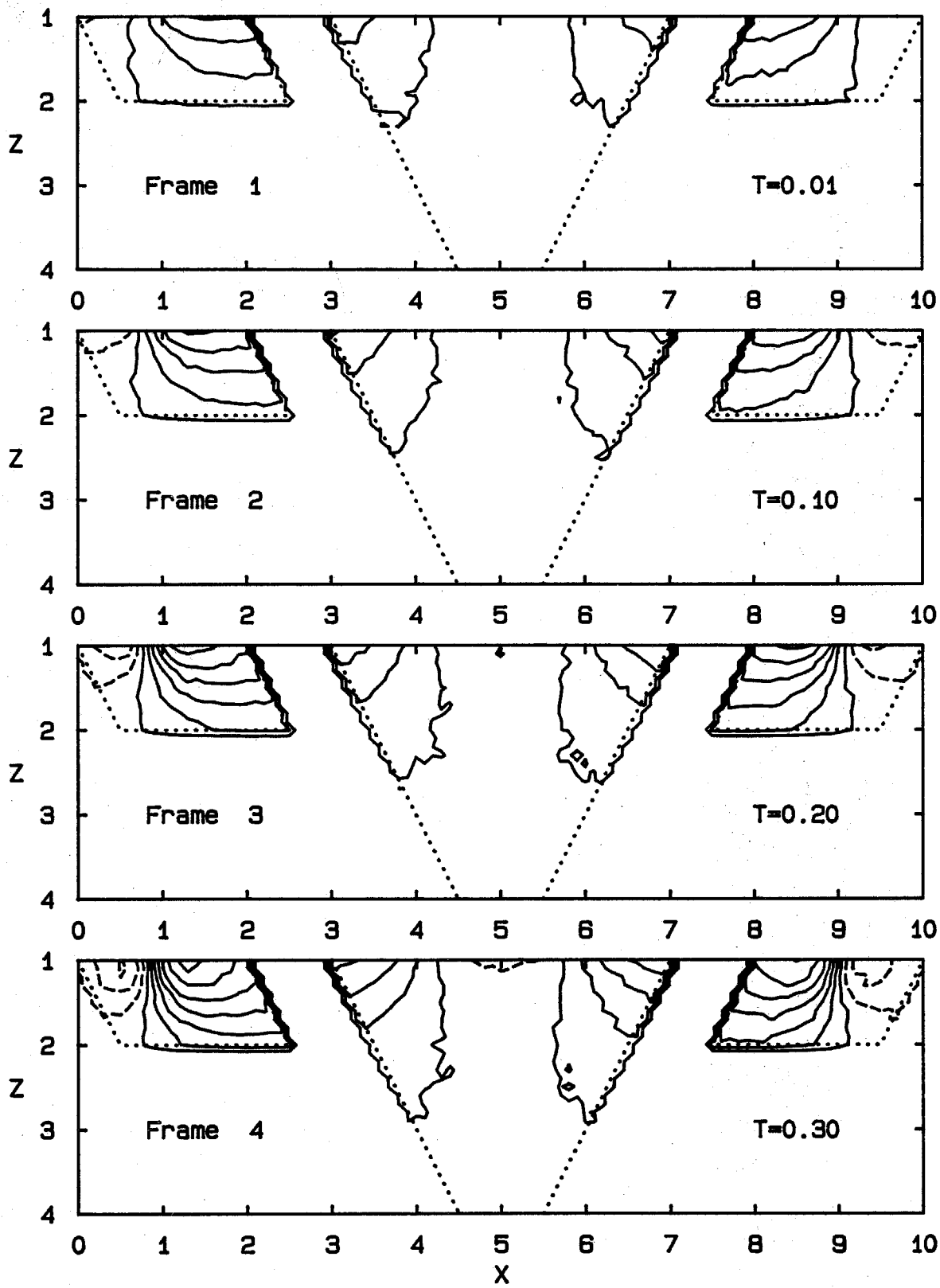

Fig. 6.3 Velocity Contours in the X-Z Plane; w-component (unsmoothed)

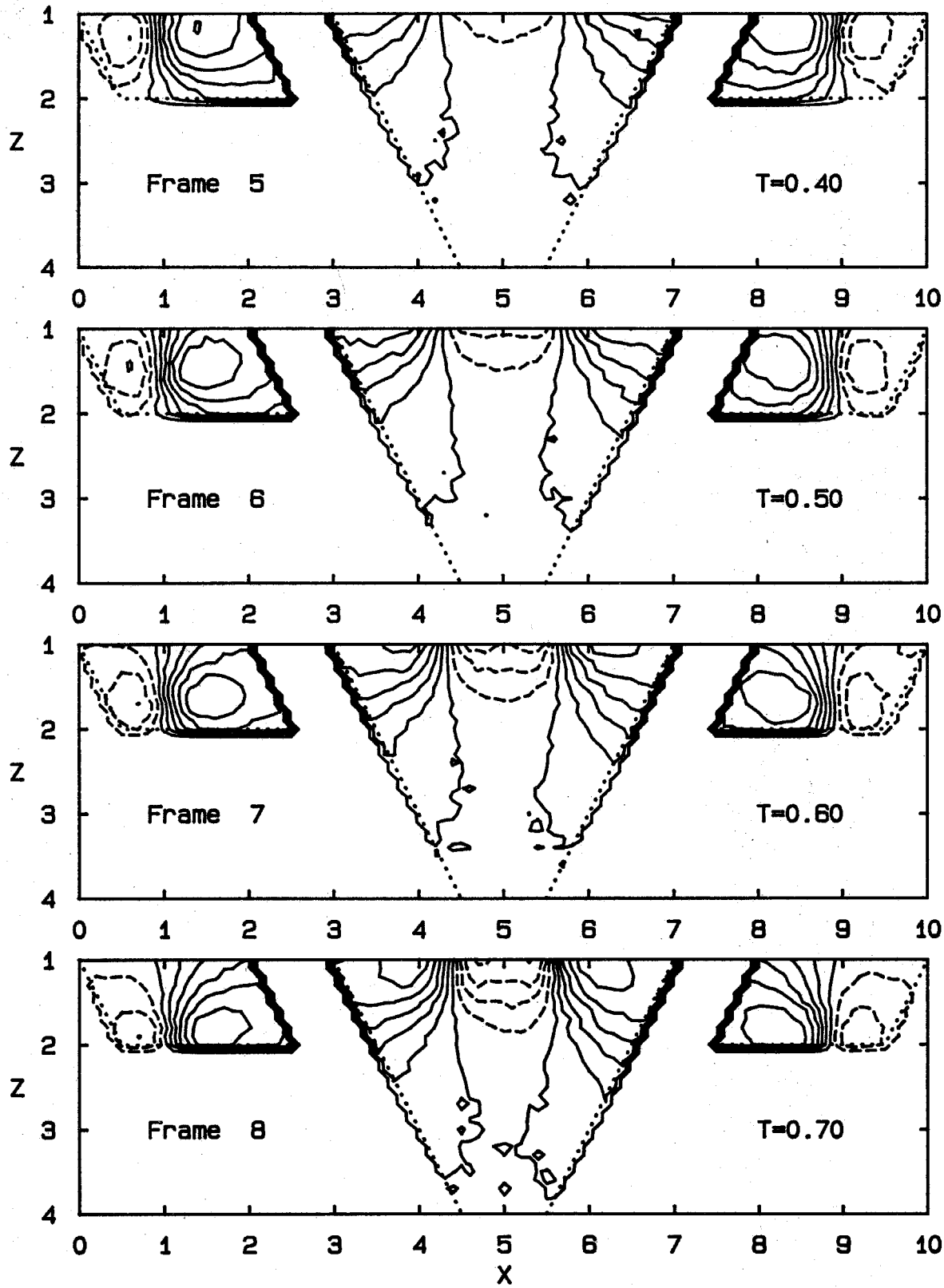

Fig. 6.3 Velocity Contours in the X-Z Plane; w-component (unsmoothed)

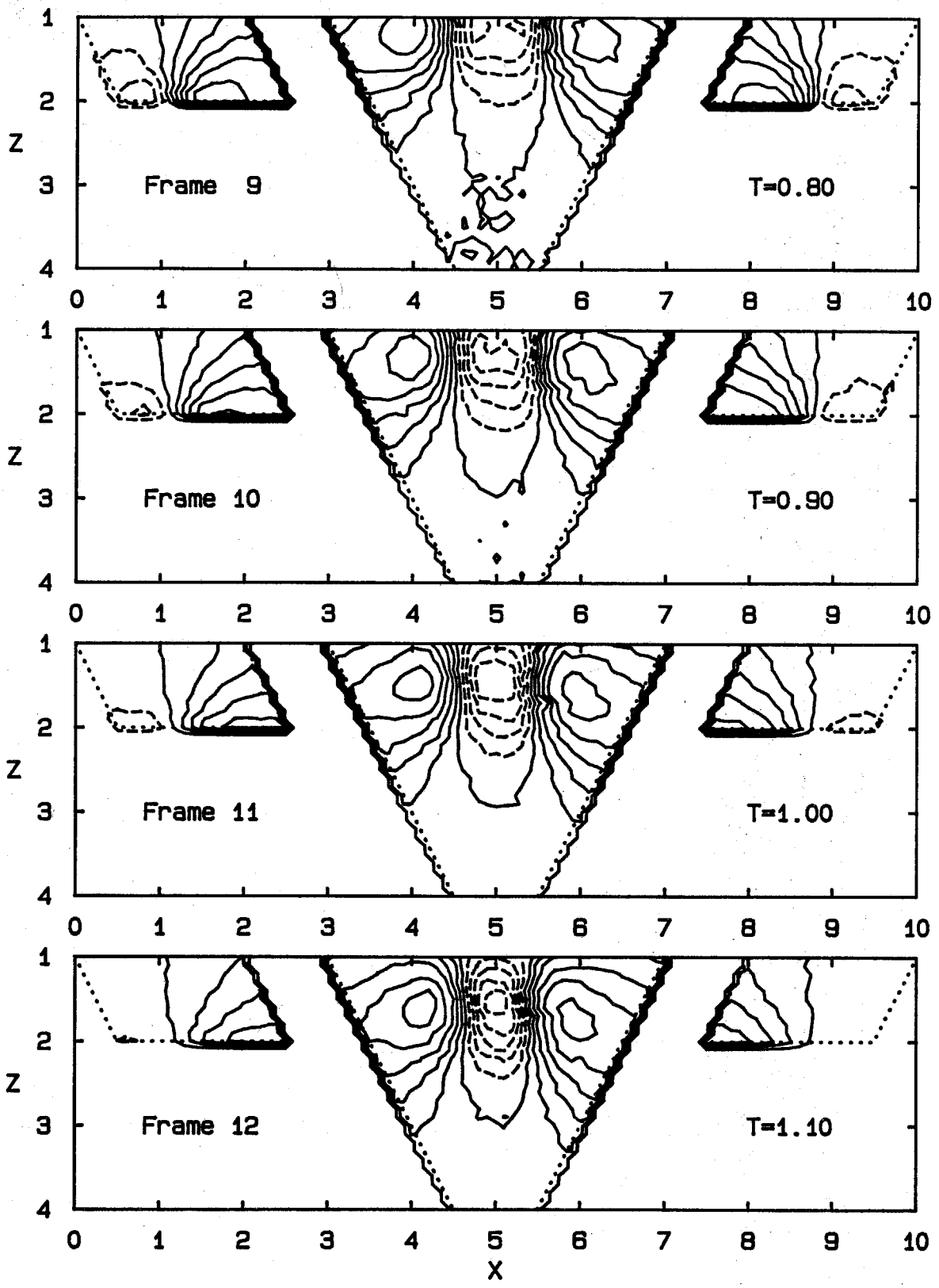

Fig. 6.3 Velocity Contours in the X-Z Plane; w-component (unsmoothed)

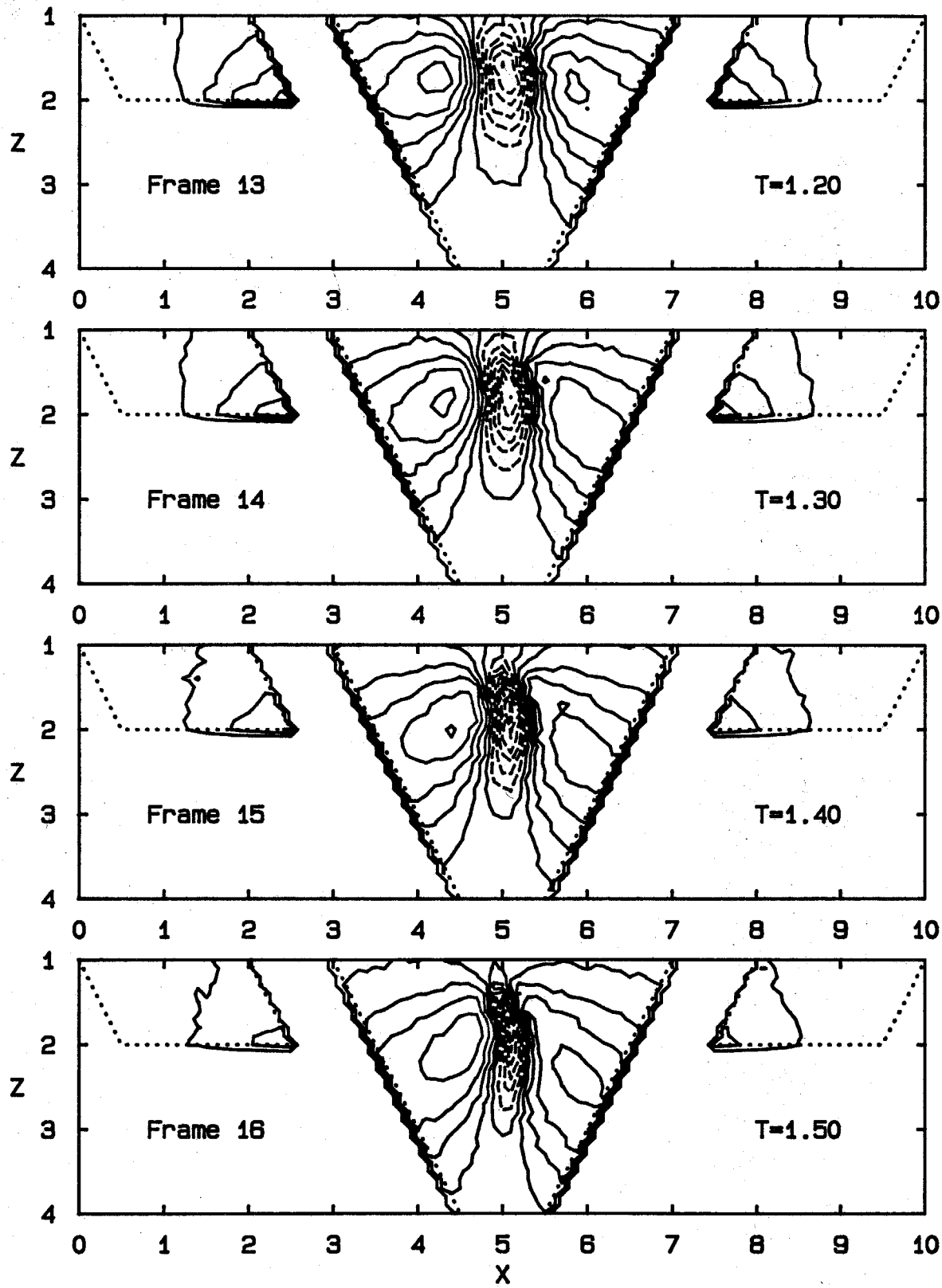

Fig. 6.3 Velocity Contours in the X-Z Plane; w-component (unsmoothed)

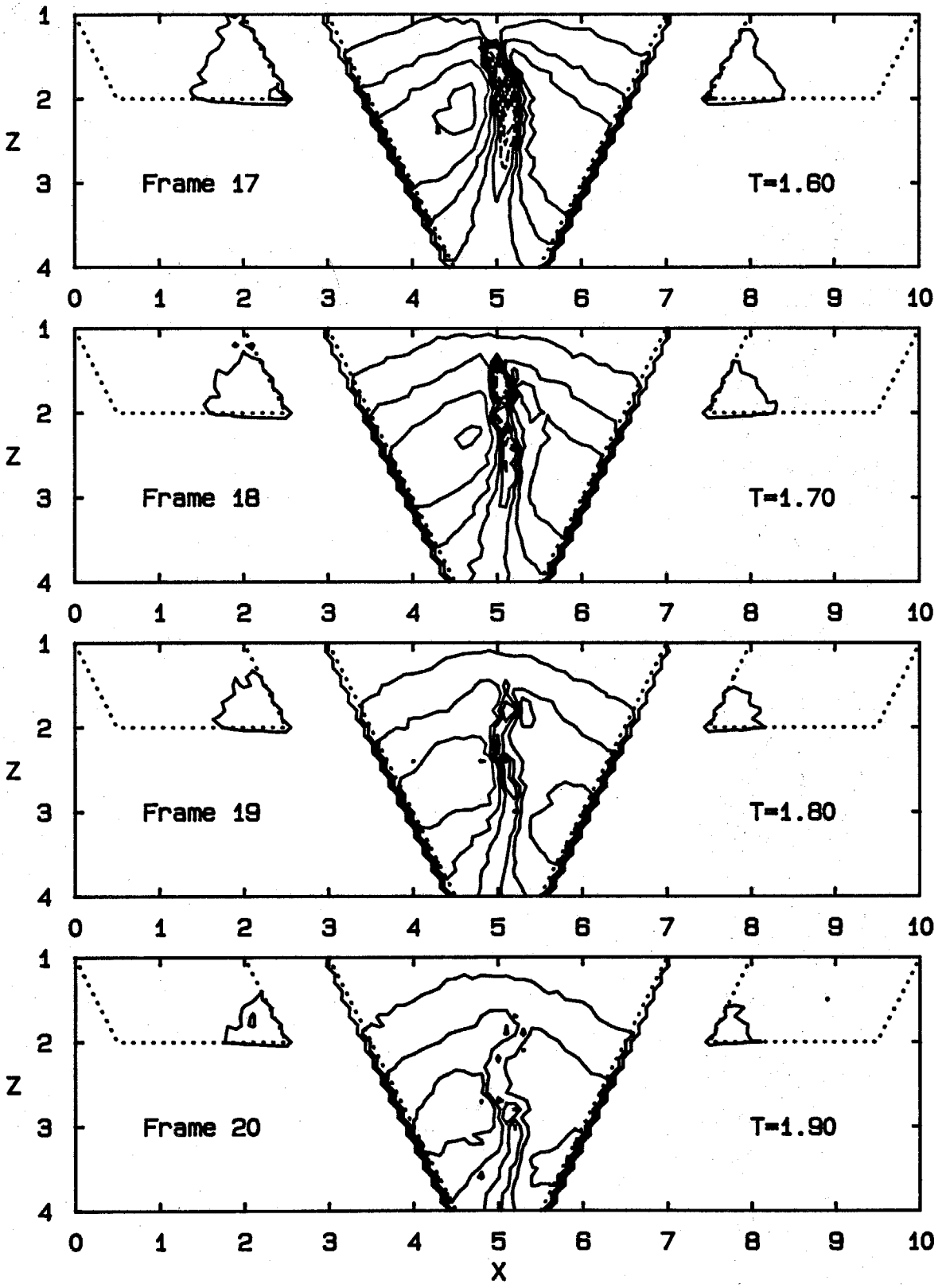

Fig. 6.3 Velocity Contours in the X-Z Plane; w-component (unsmoothed)

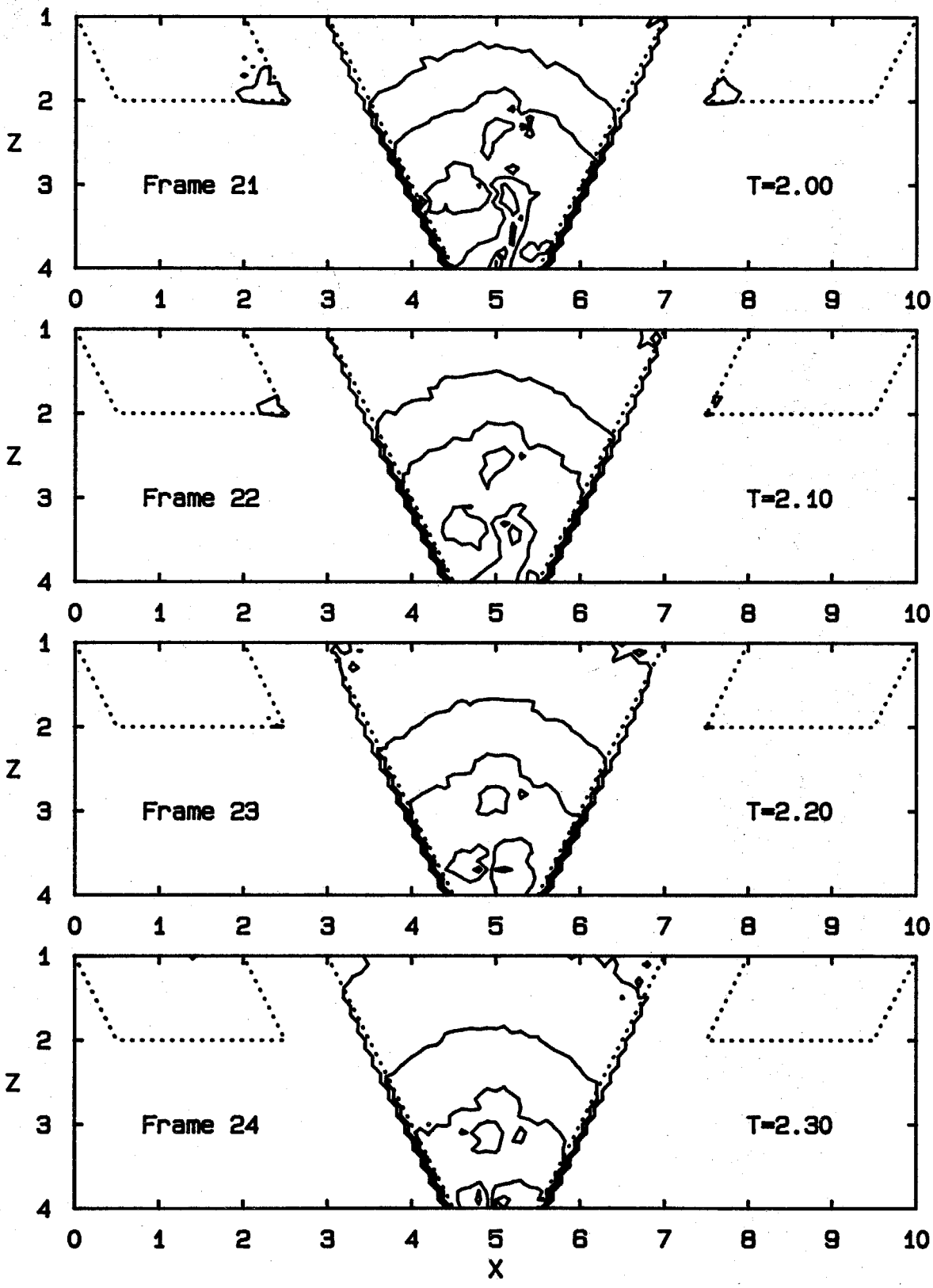

Fig. 6.3 Velocity Contours in the X-Z Plane; w-component (unsmoothed)

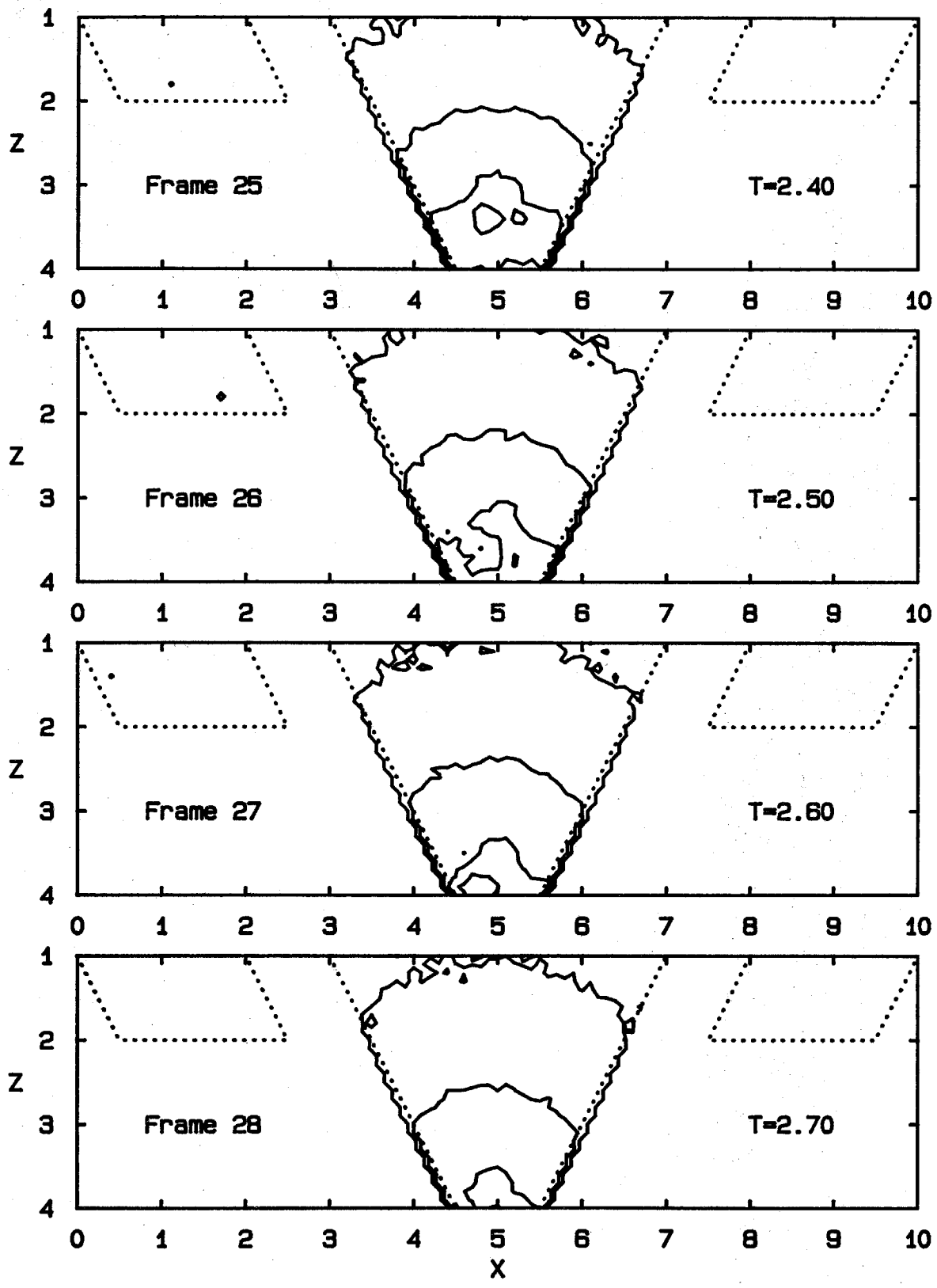

Fig. 6.3 Velocity Contours in the X-Z Plane; w-component (unsmoothed)

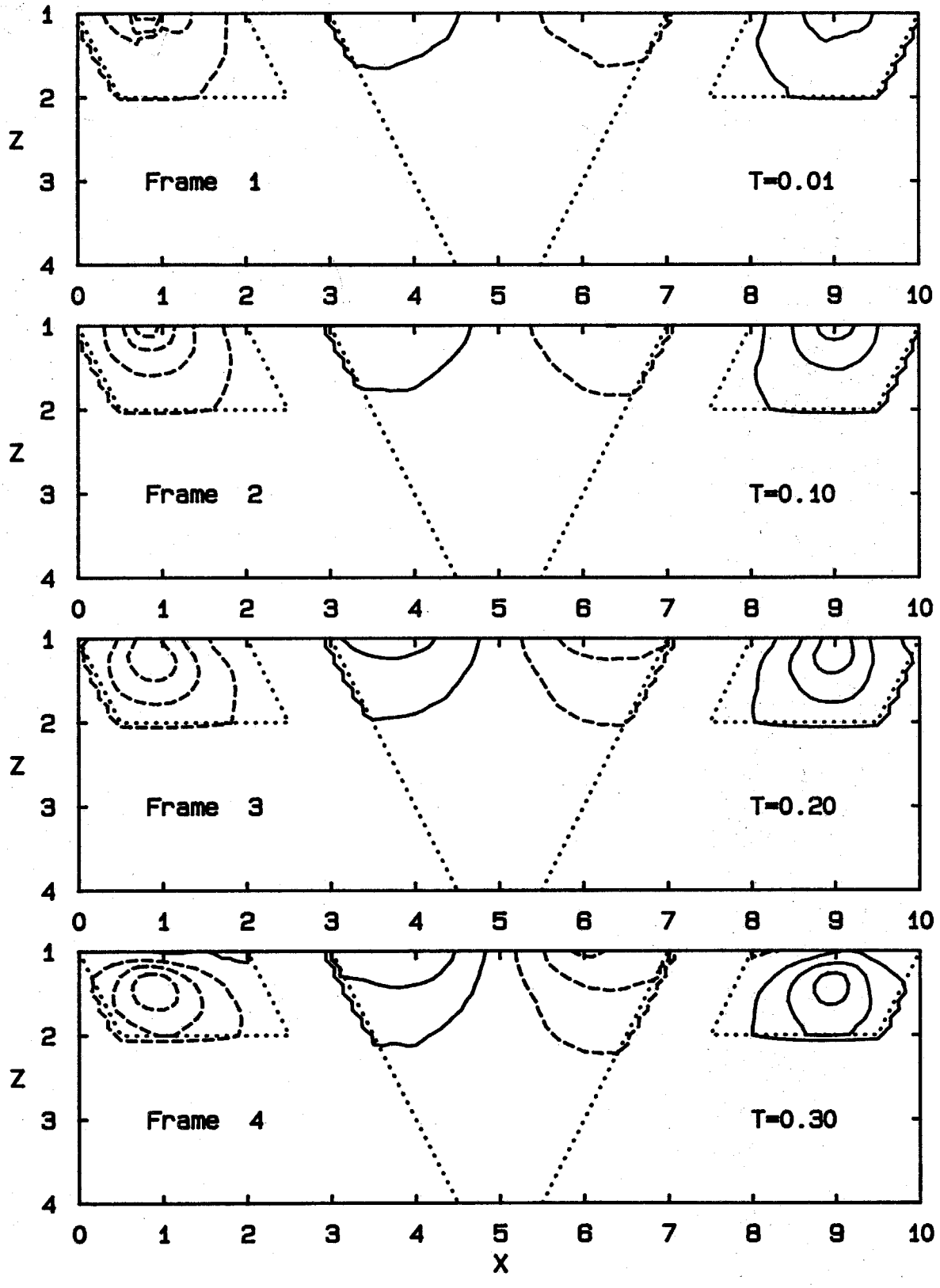

Fig. 6.4 Velocity Contours in the X-Z plane; u-component (smoothed)

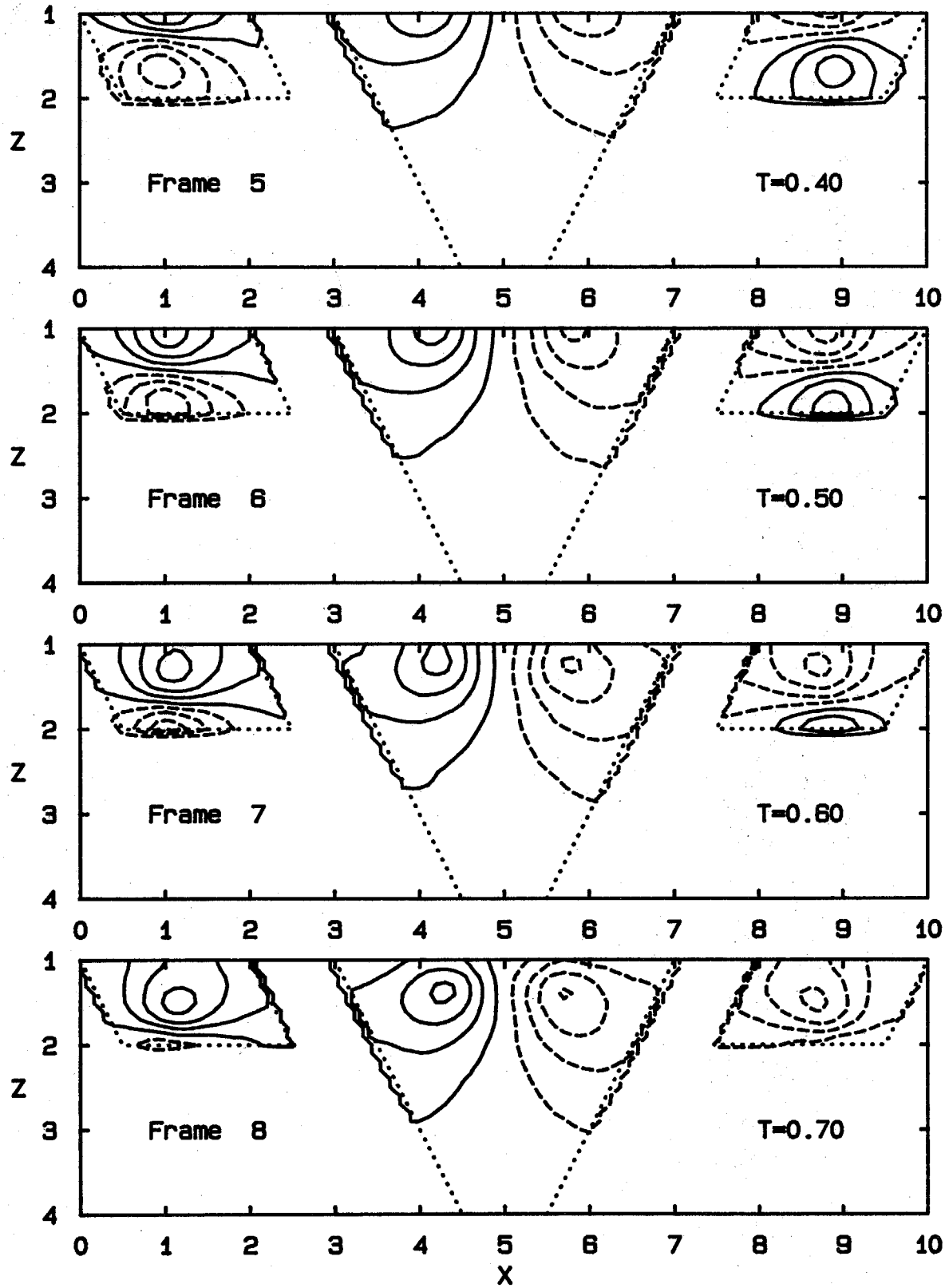

Fig. 6.4 Velocity Contours in the X-Z plane; u-component (smoothed)

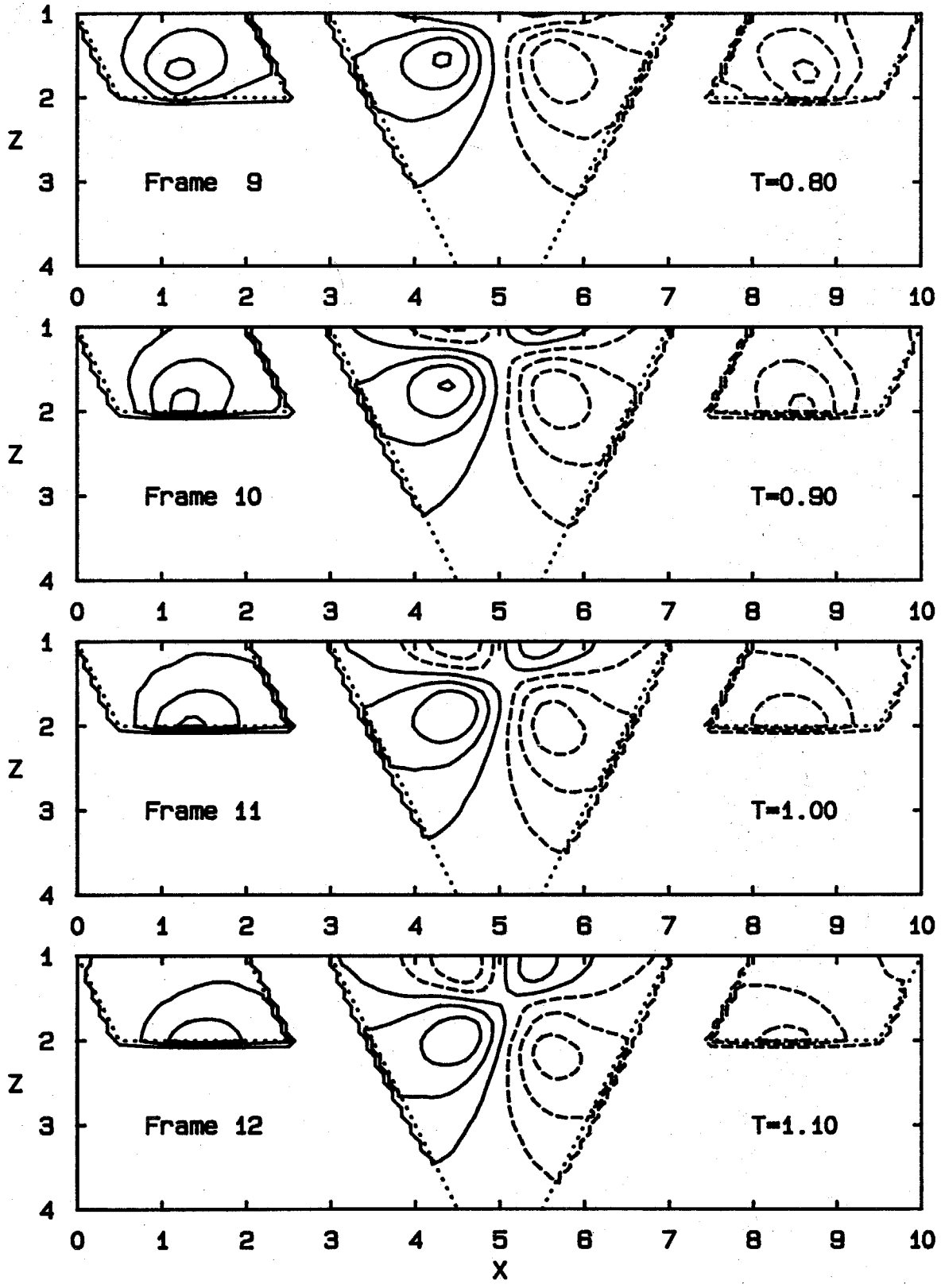

Fig. 6.4 Velocity Contours in the X-Z plane; u-component (smoothed)

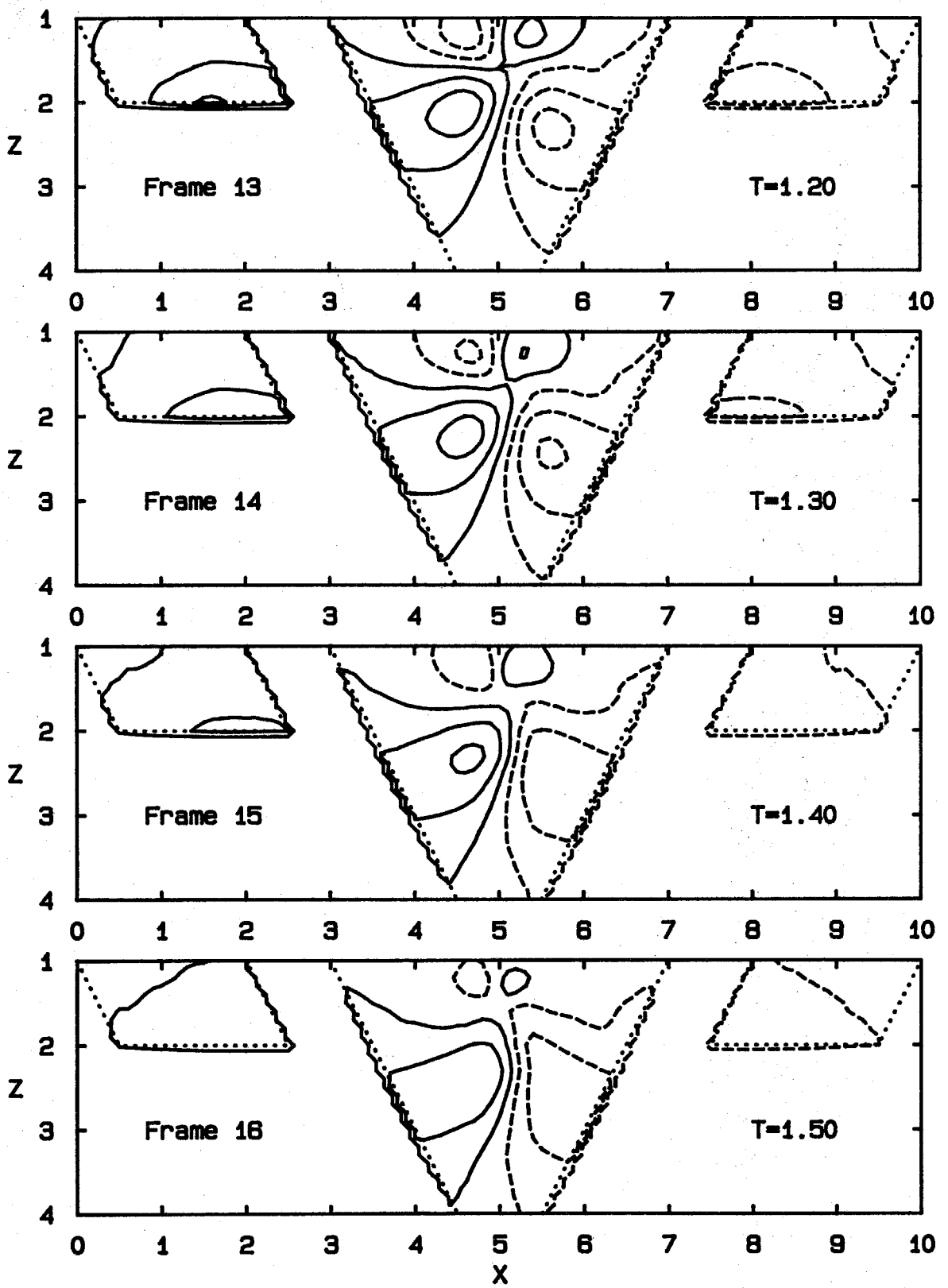

Fig. 6.4 Velocity Contours in the X-Z plane; u-component (smoothed)

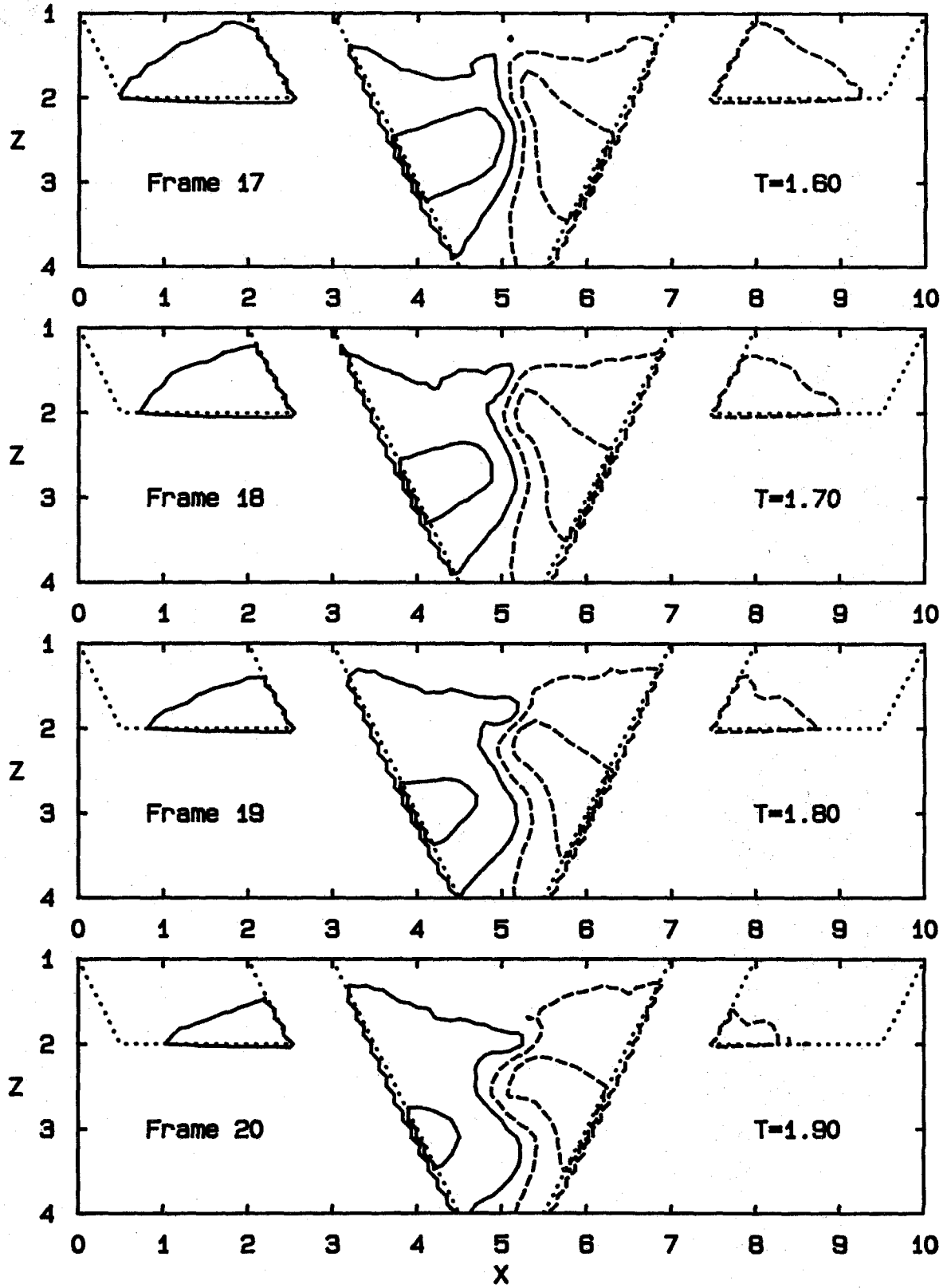

Fig. 6.4 Velocity Contours in the X-Z plane; u-component (smoothed)

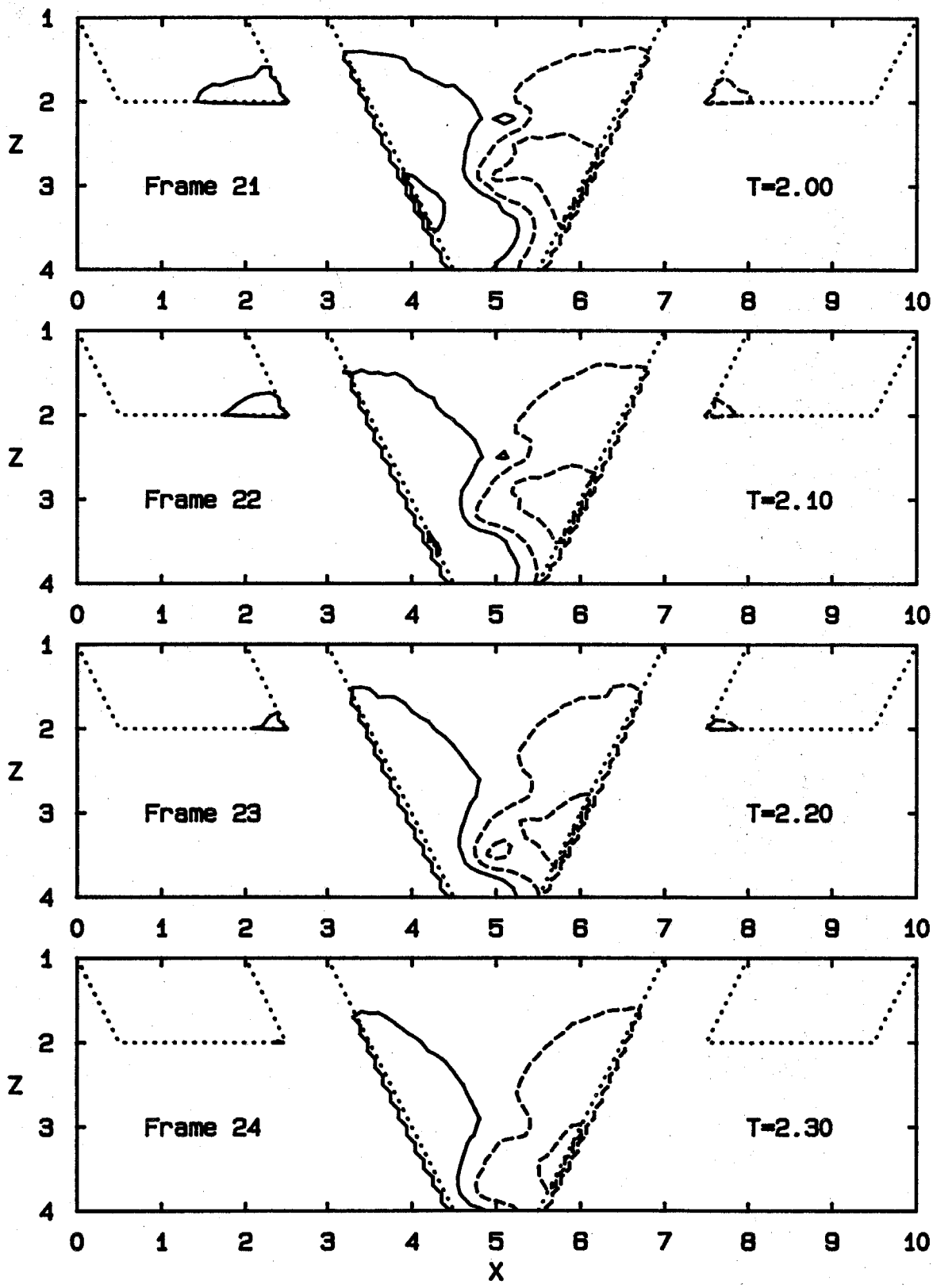

Fig. 6.4 Velocity Contours in the X-Z plane; u-component (smoothed)

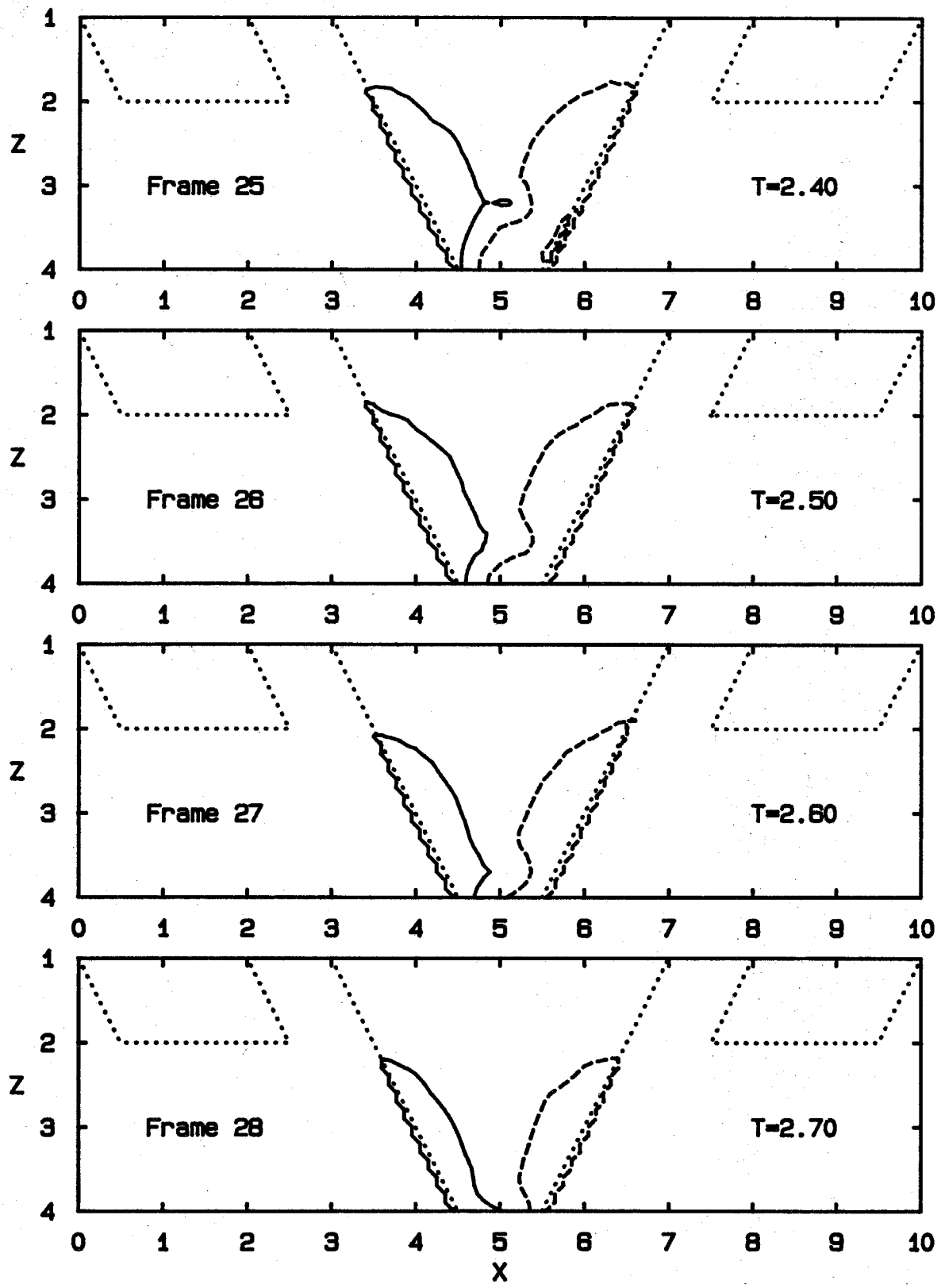

Fig. 6.4 Velocity Contours in the X-Z plane; u-component (smoothed)

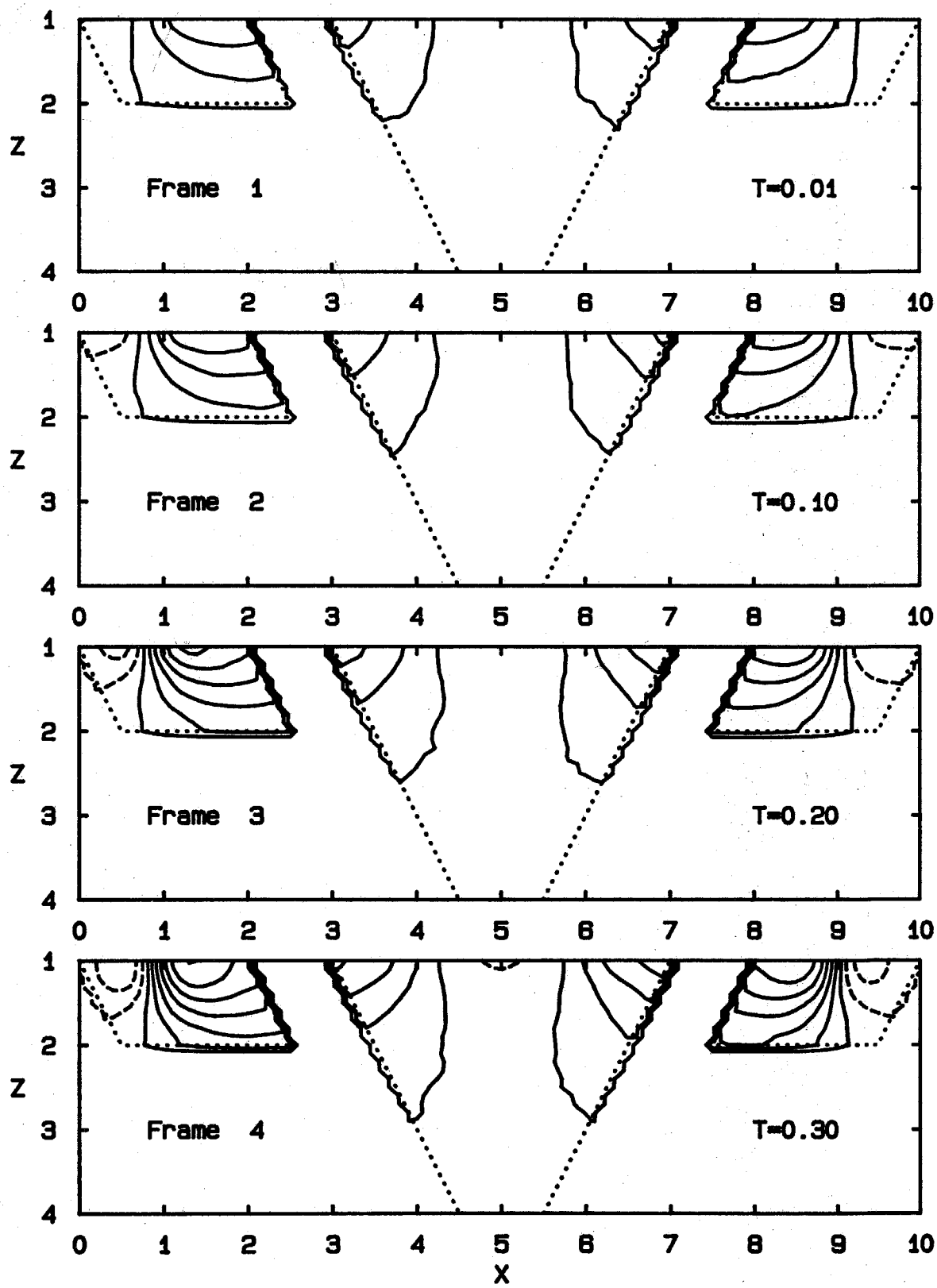

Fig. 6.5 Velocity Contours in the X-Z plane; w-component (smoothed)

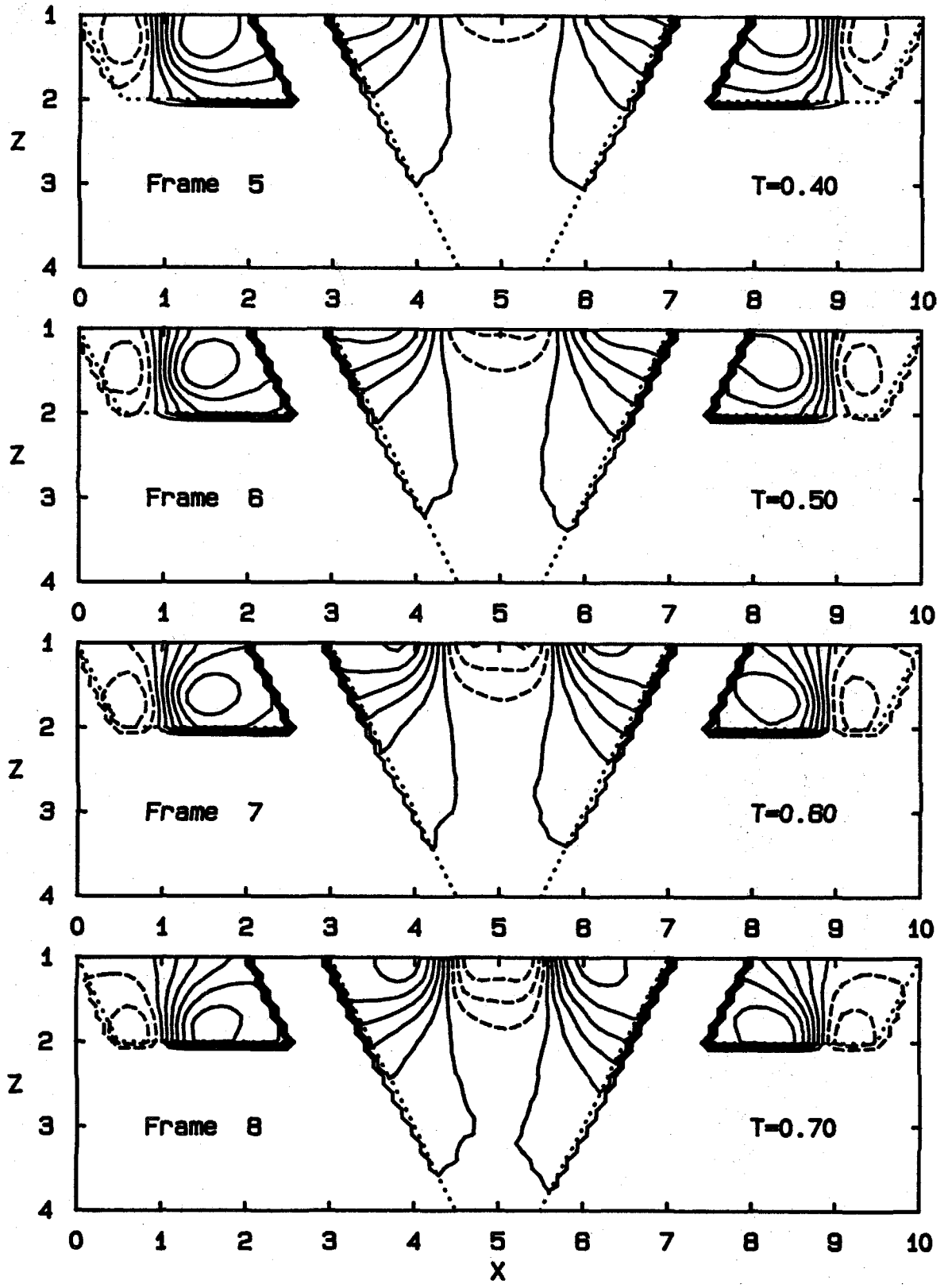

Fig. 6.5 Velocity Contours in the X-Z plane; w-component (smoothed)

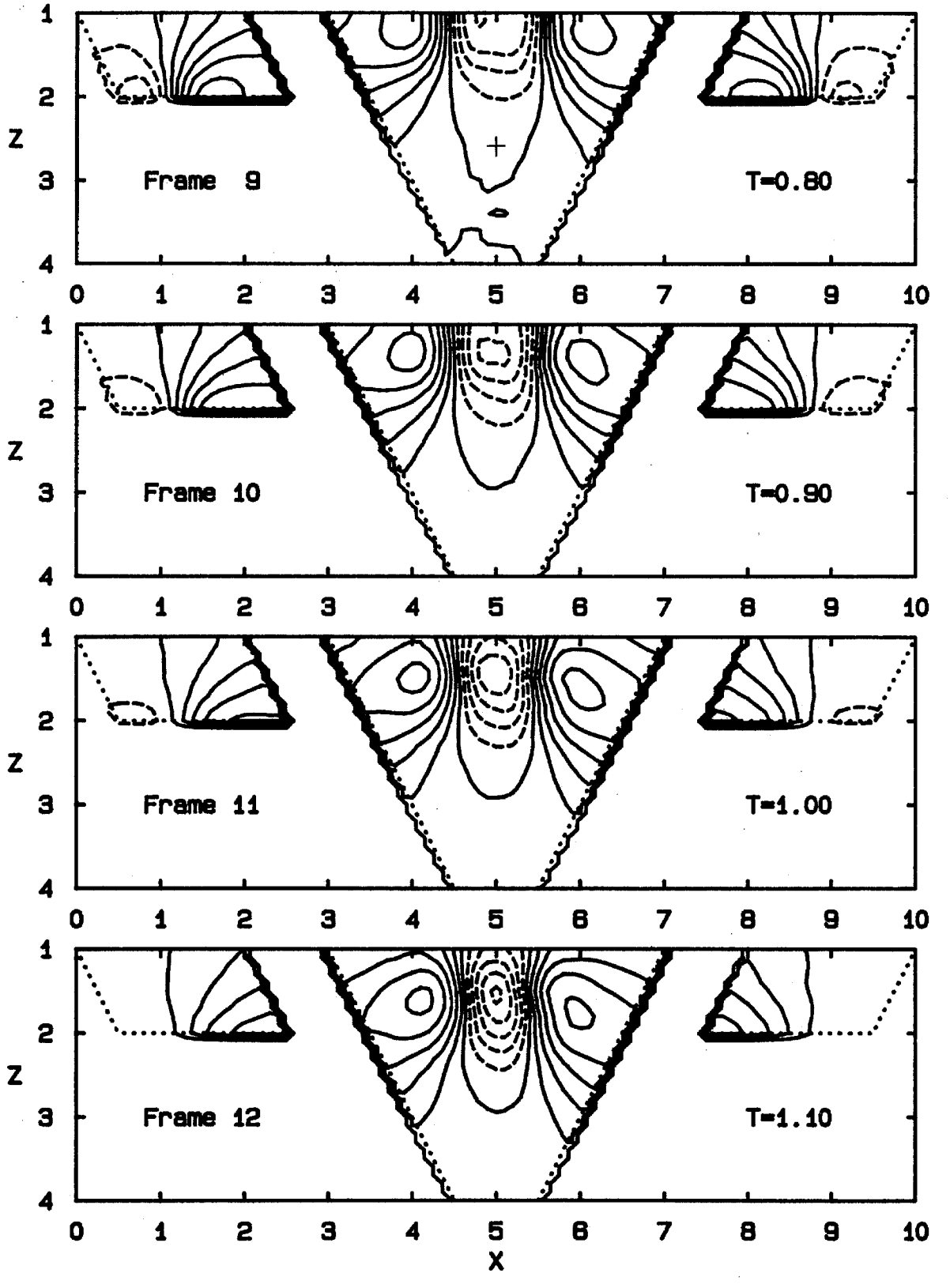

Fig. 6.5 Velocity Contours in the X-Z plane; w-component (smoothed)

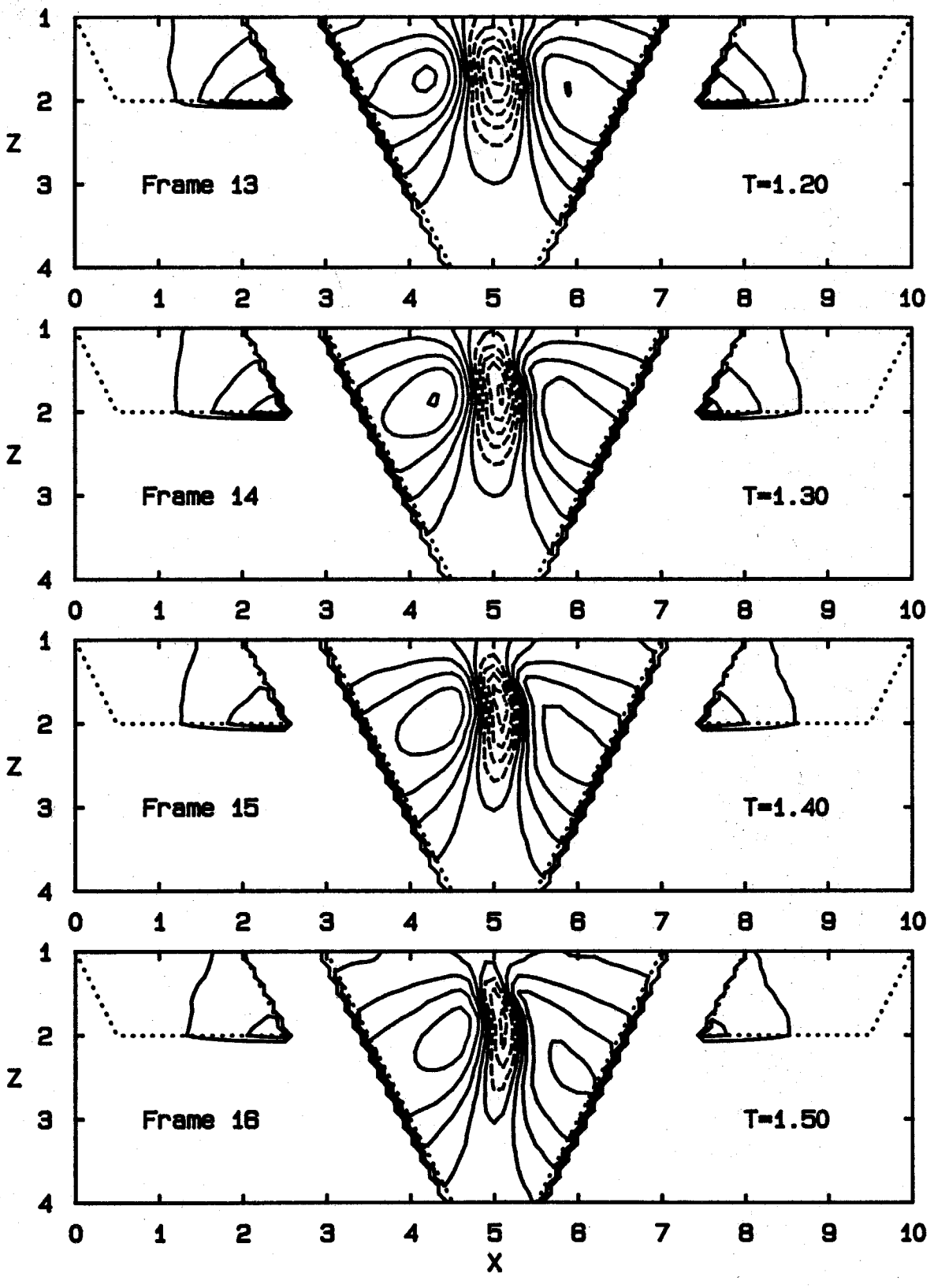

Fig. 8.5 Velocity Contours in the X-Z plane; w-component (smoothed)

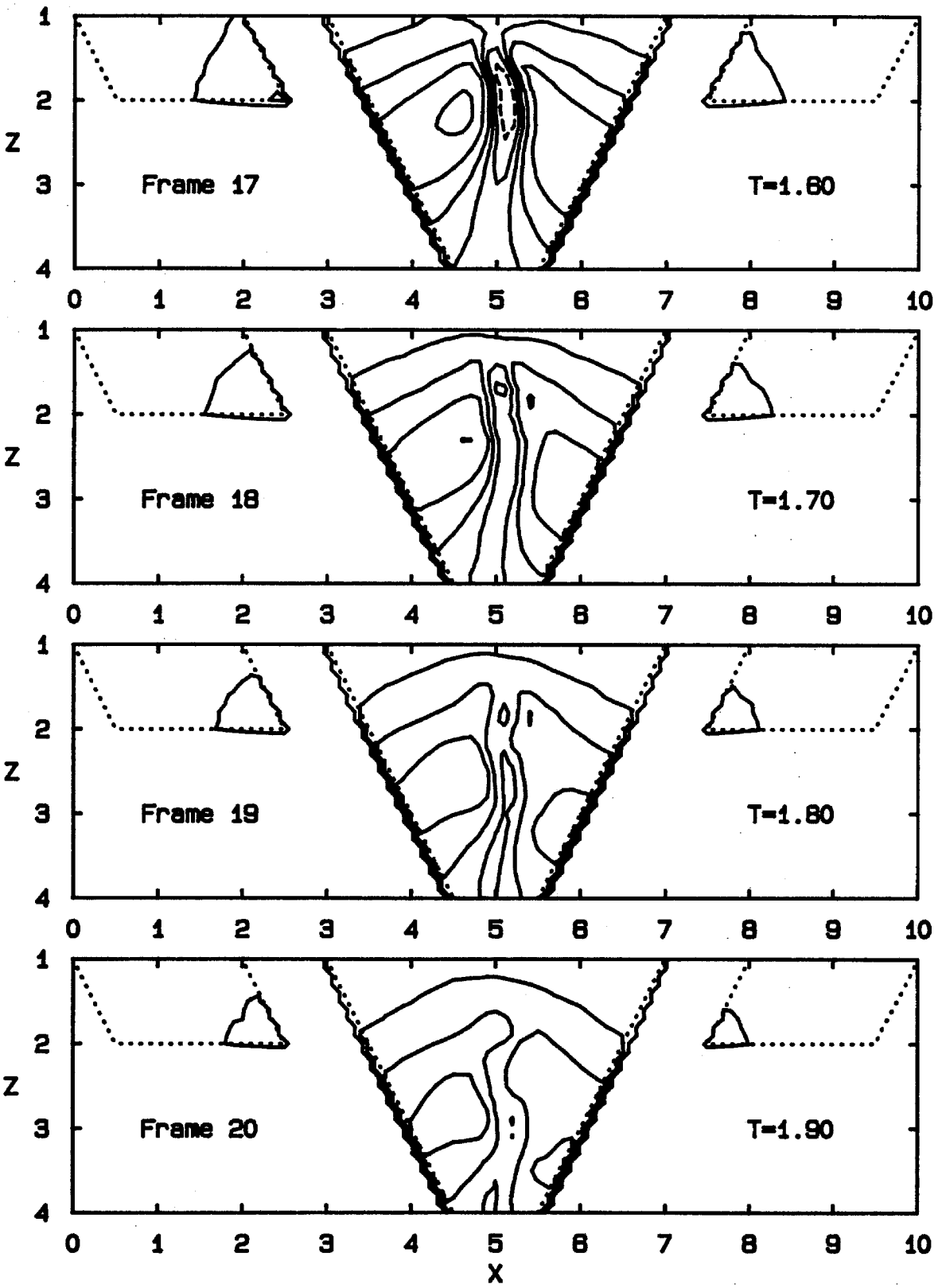

Fig. 8.5 Velocity Contours in the X-Z plane; w-component (smoothed)

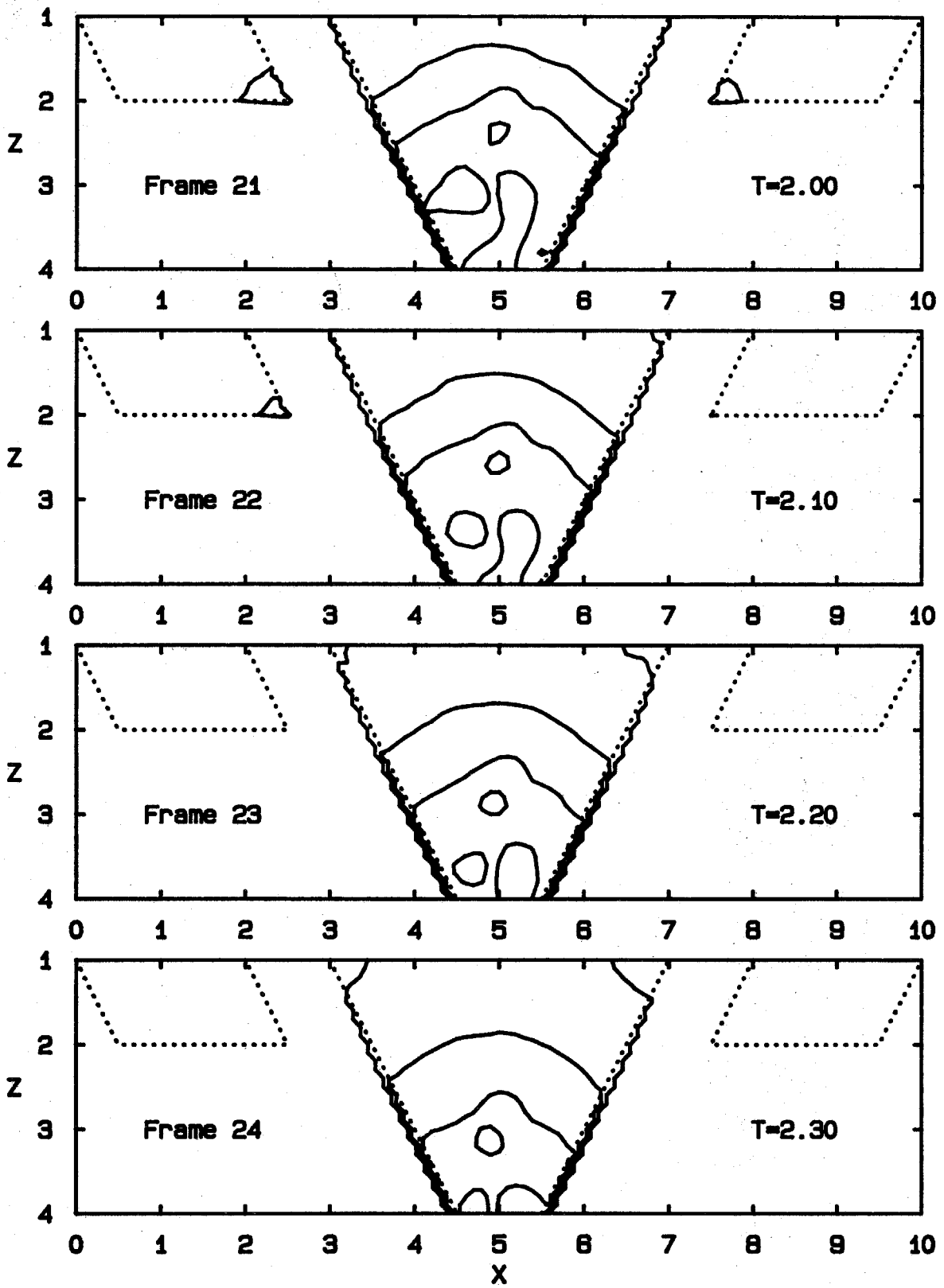

Fig. 6.5 Velocity Contours in the X-Z plane; w-component (smoothed)

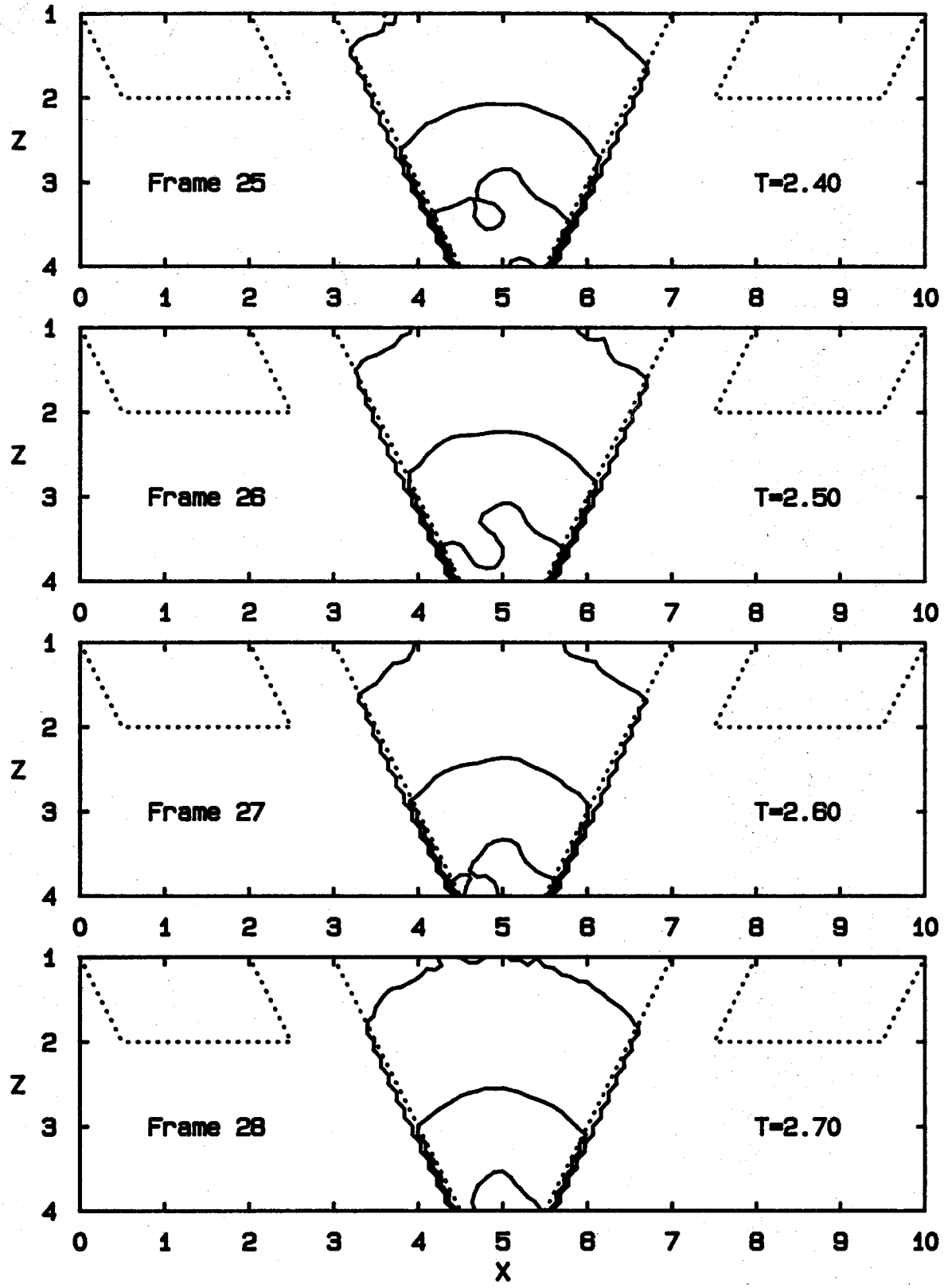

Fig. 6.5 Velocity Contours in the X-Z plane; w-component (smoothed)

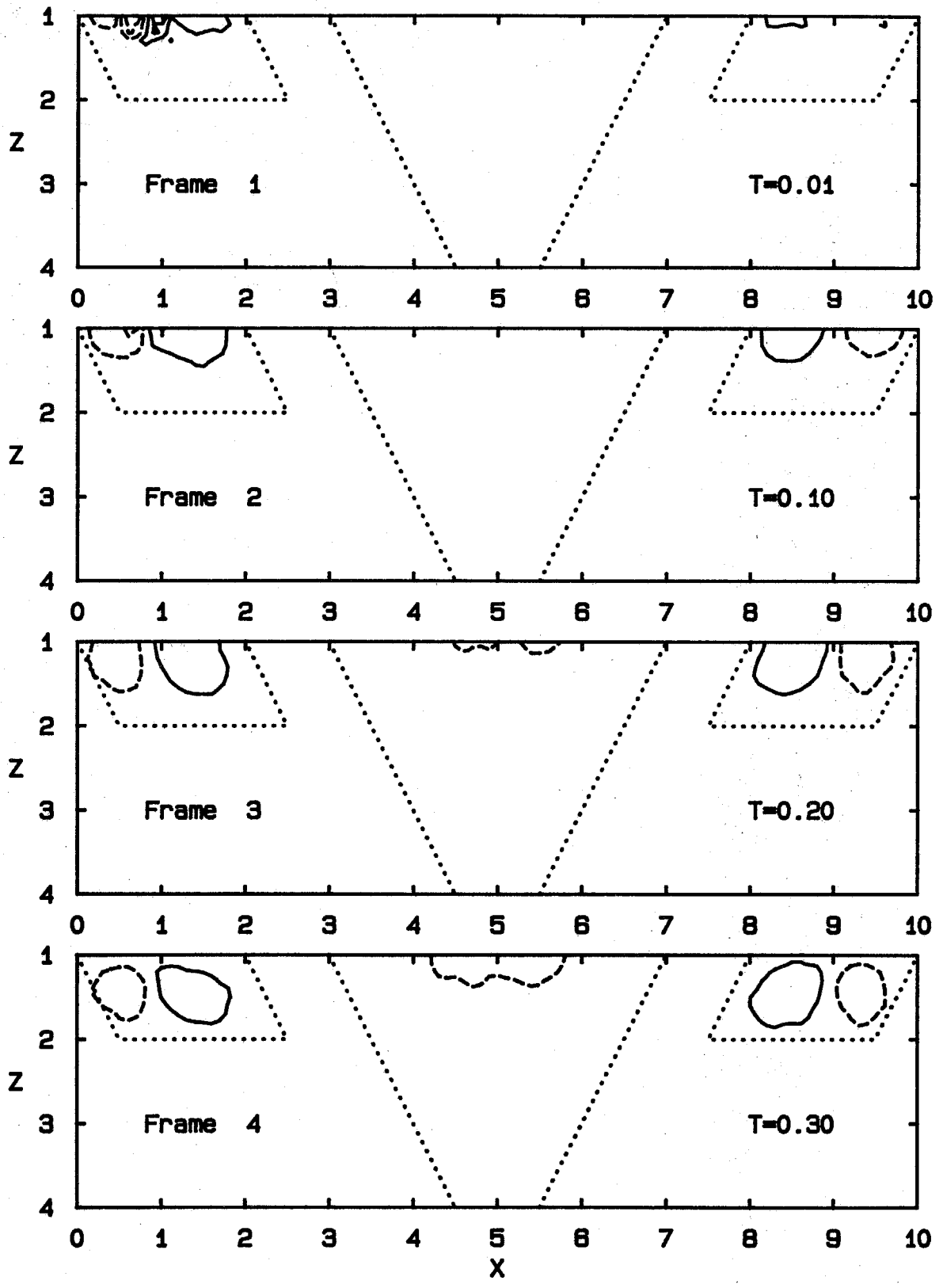

Fig. 6.6 Strain-rate Contours in the X-Z Plane; $\partial u/\partial x$

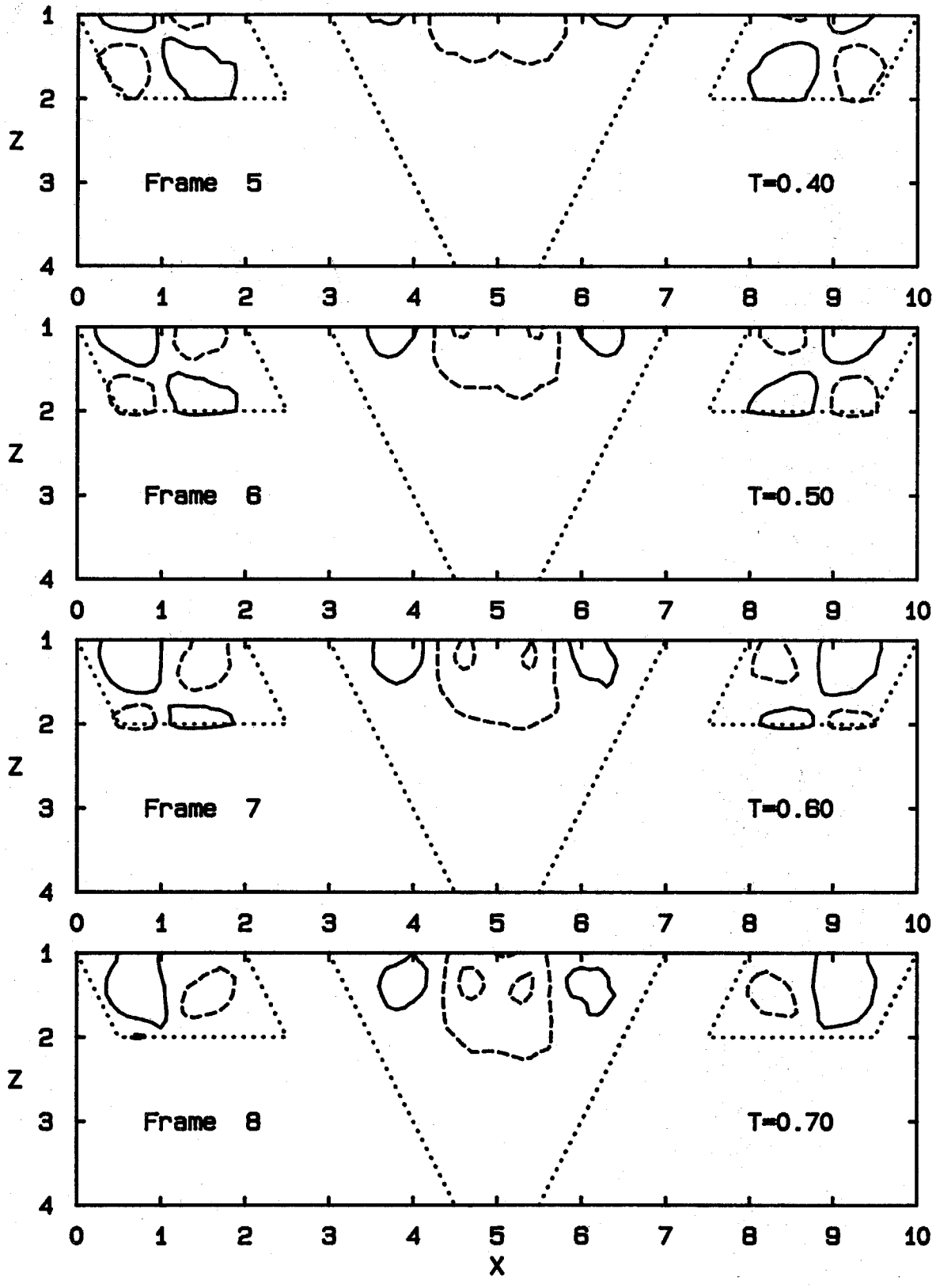

Fig. 6.6 Strain-rate Contours in the X-Z Plane; $\partial u/\partial x$

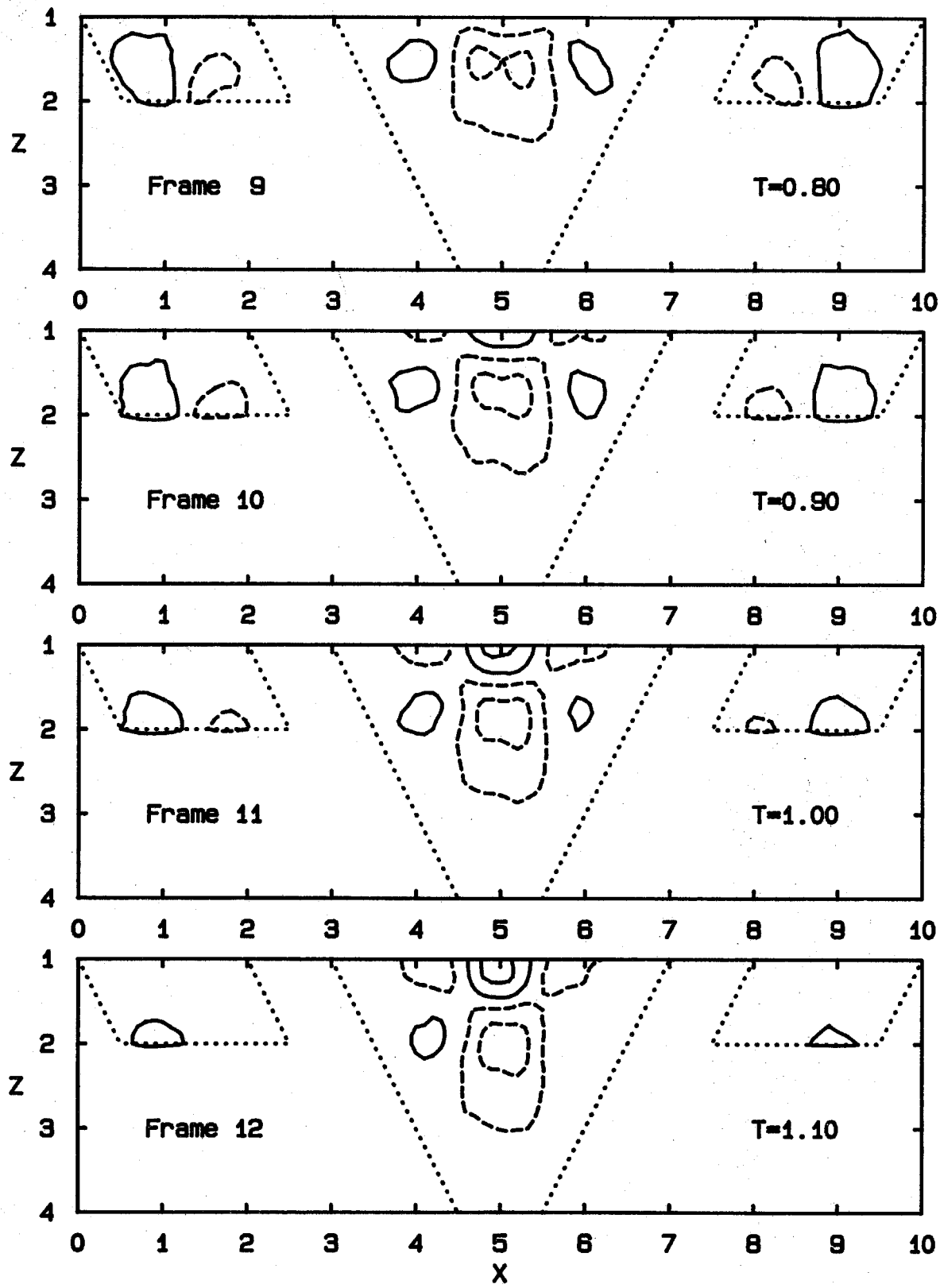

Fig. 6.6 Strain-rate Contours in the X-Z Plane; $\partial u/\partial x$

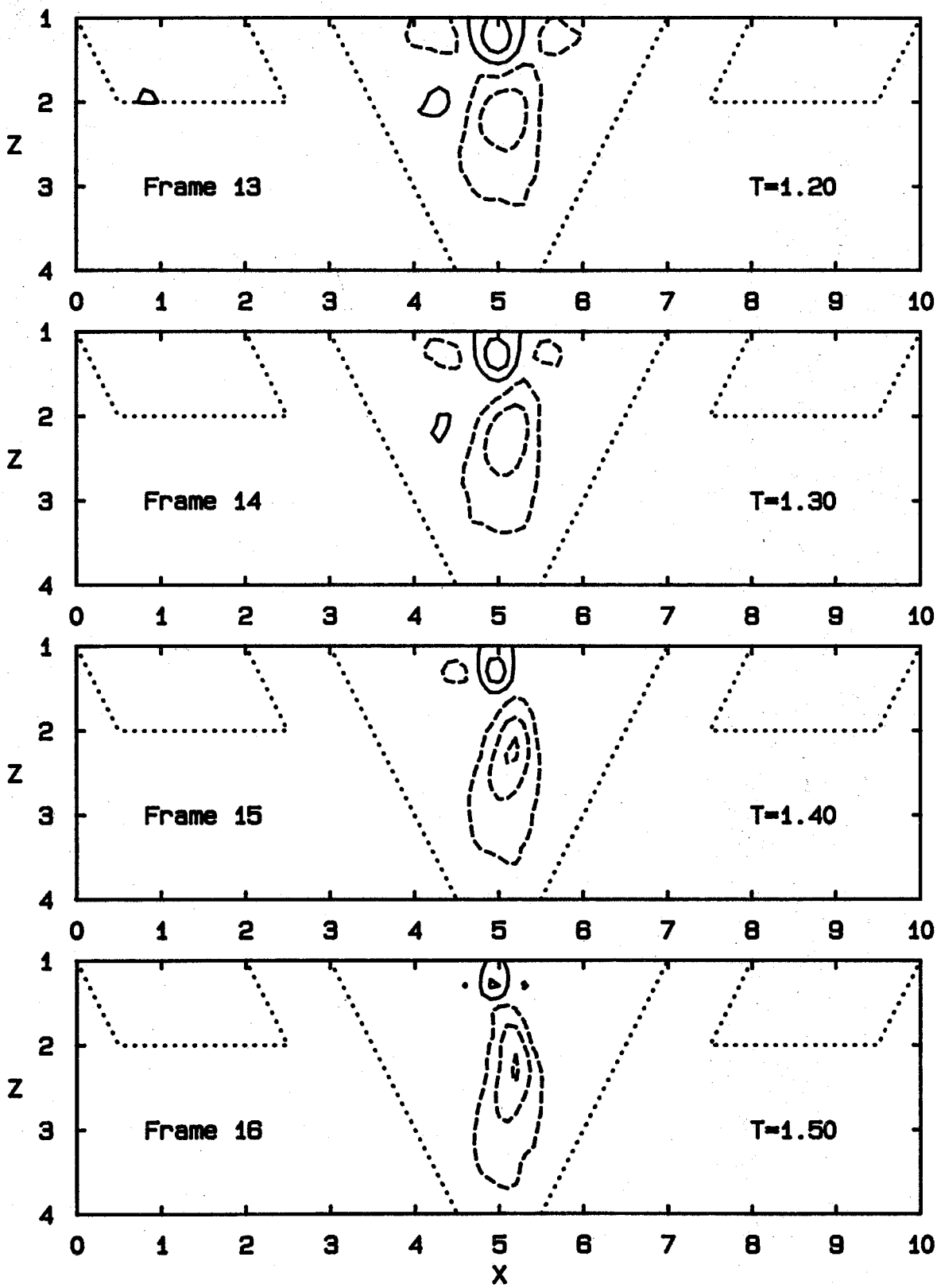

Fig. 6.6 Strain-rate Contours in the X-Z Plane; $\partial u/\partial x$

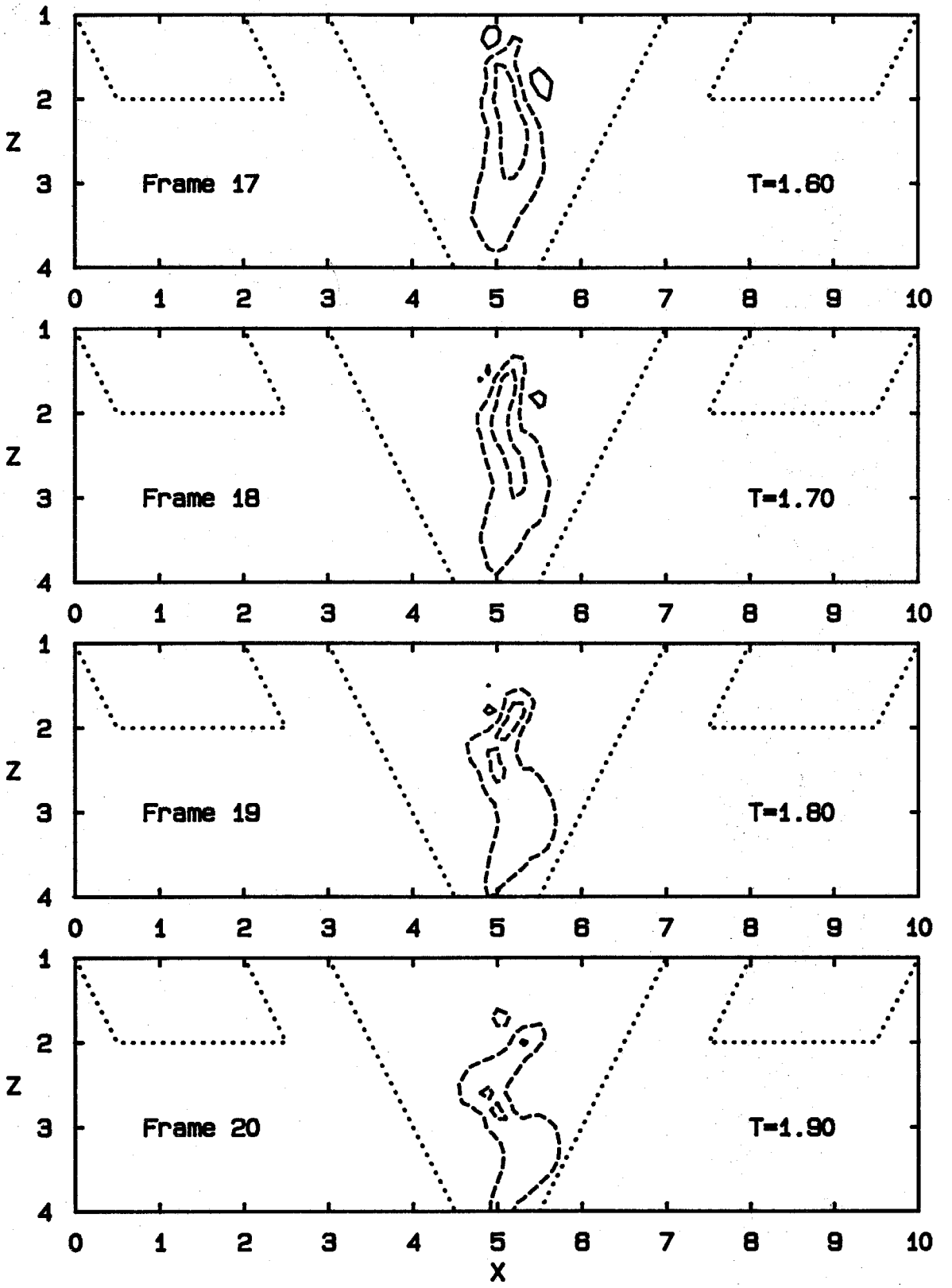

Fig. 6.6 Strain-rate Contours in the X-Z Plane; $\partial u/\partial x$

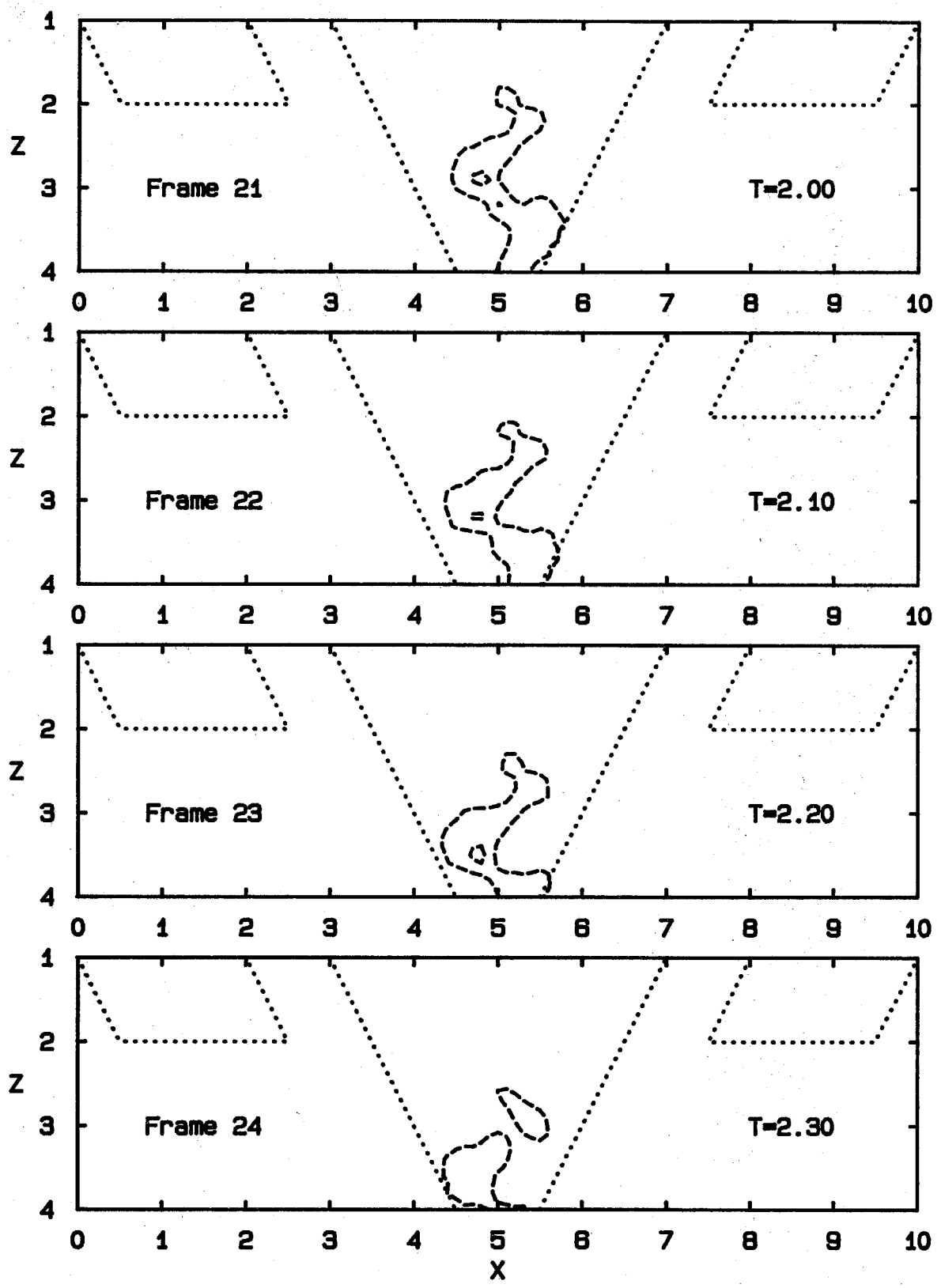

Fig. 6.6 Strain-rate Contours in the X-Z Plane; $\partial u/\partial x$

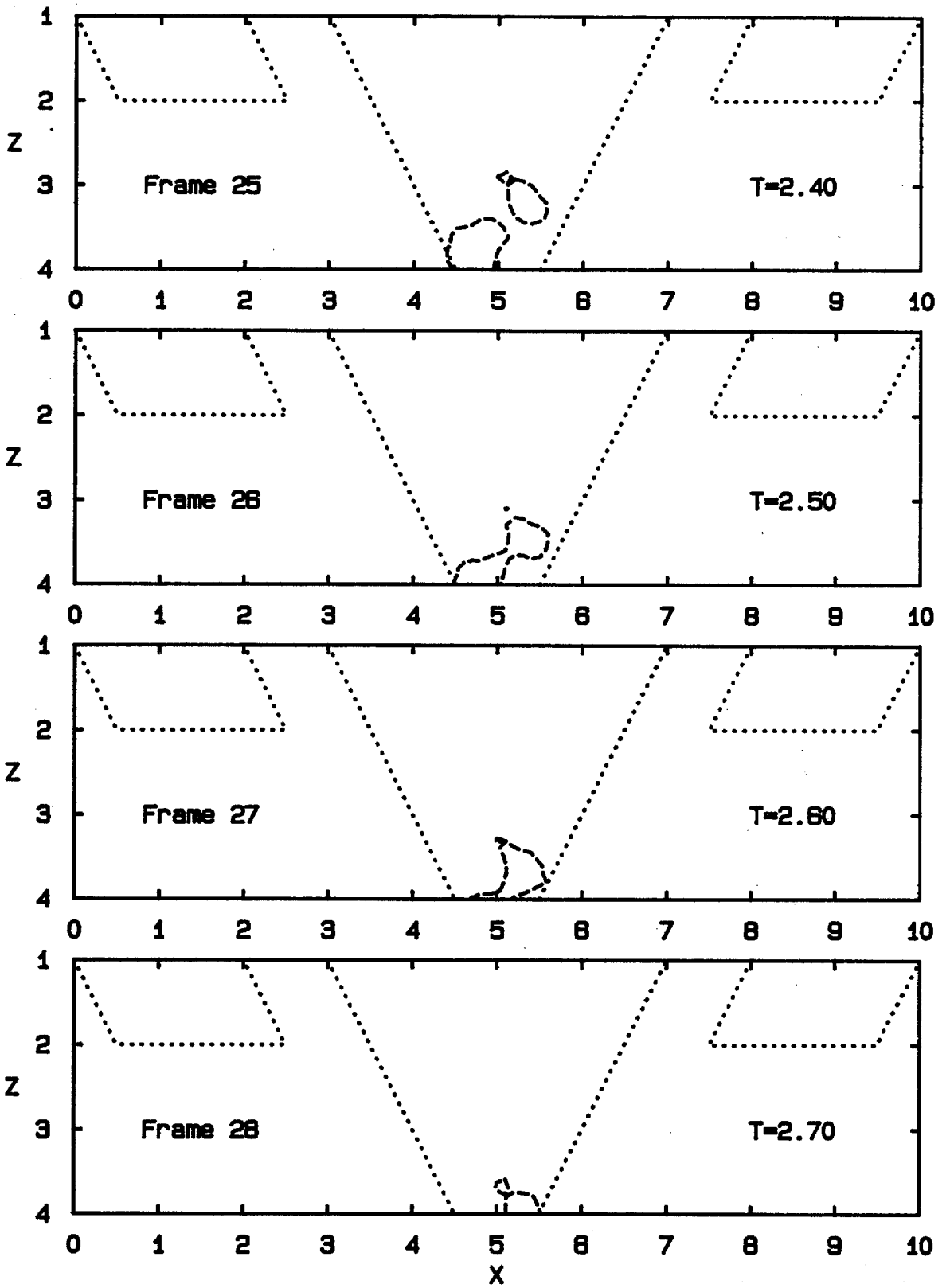

Fig. 6.6 Strain-rate Contours in the X-Z Plane; $\partial u/\partial x$

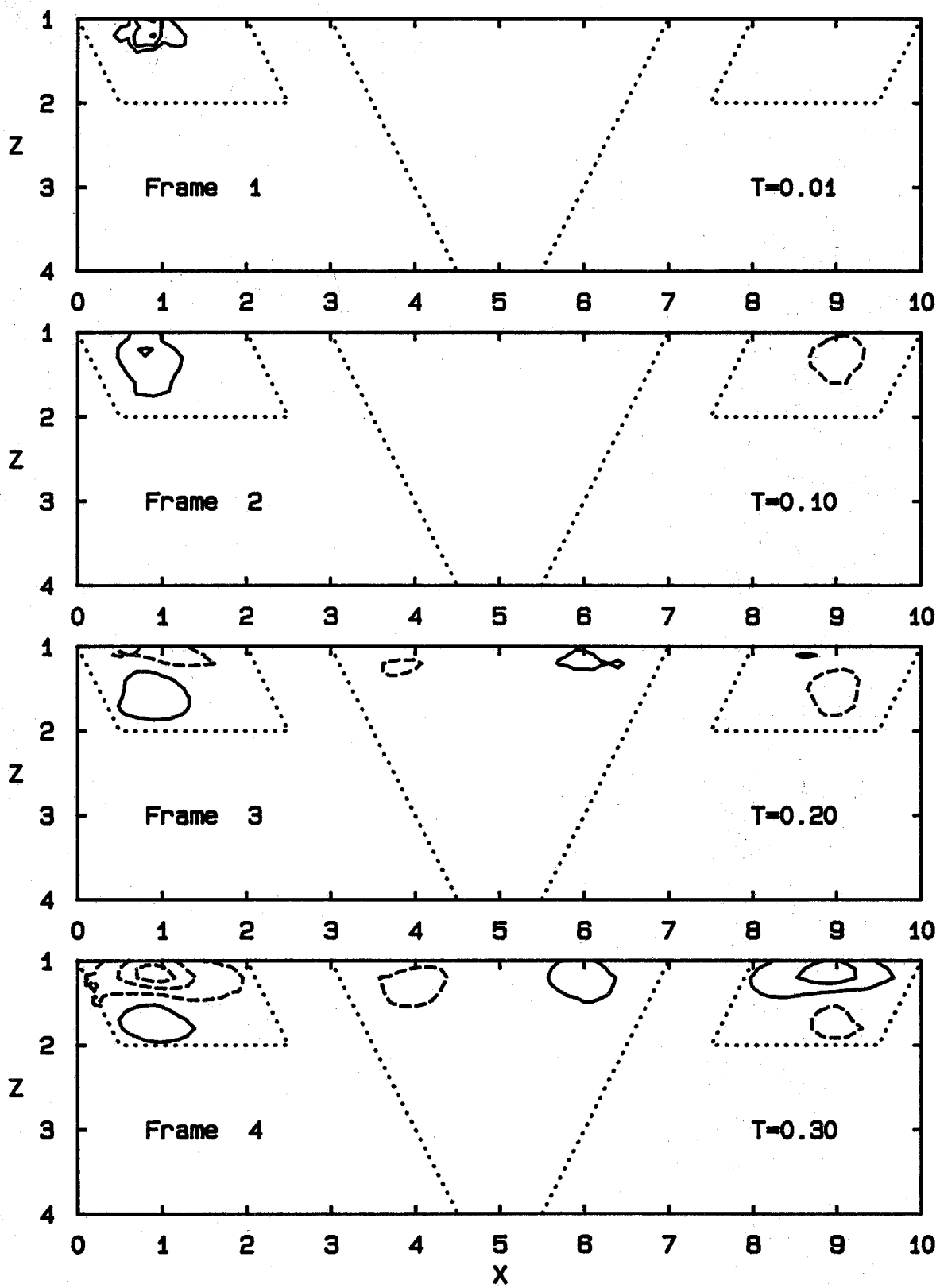

Fig. 6.7 Strain-rate Contours in the X-Z Plane; $\partial u/\partial z$

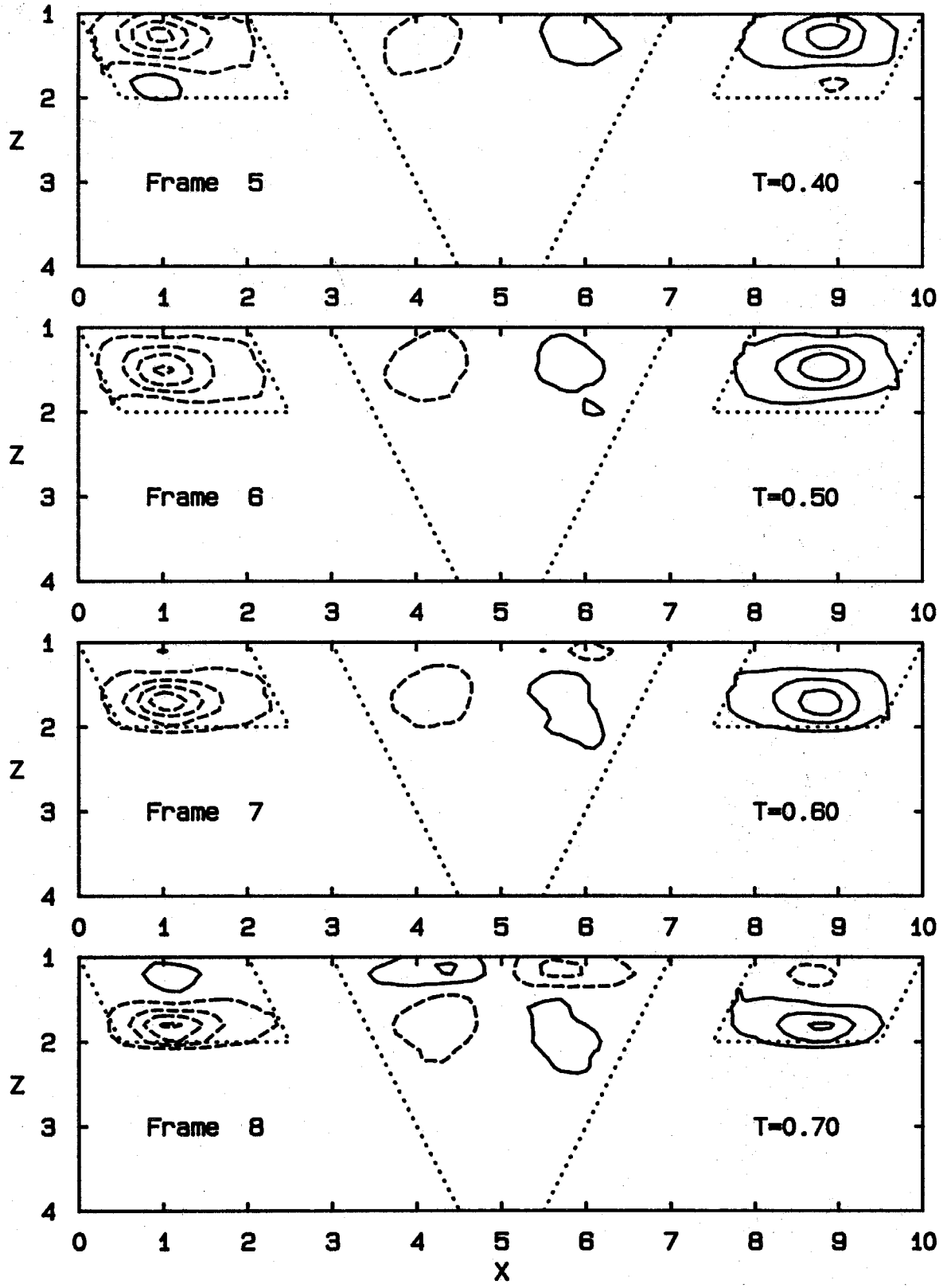

Fig. 6.7 Strain-rate Contours in the X-Z Plane; $\partial u/\partial z$

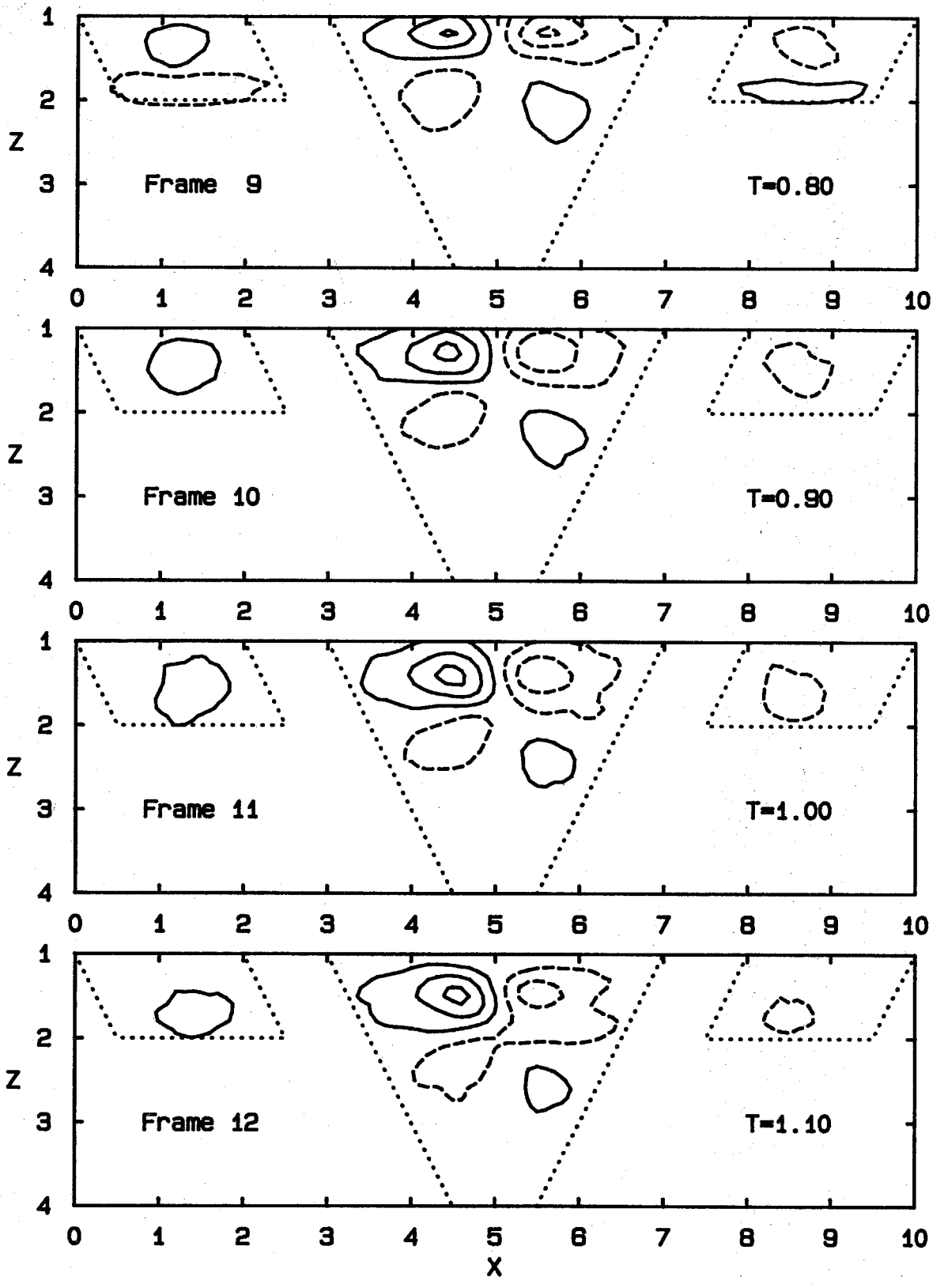

Fig. 6.7 Strain-rate Contours in the X-Z Plane; $\partial u/\partial z$

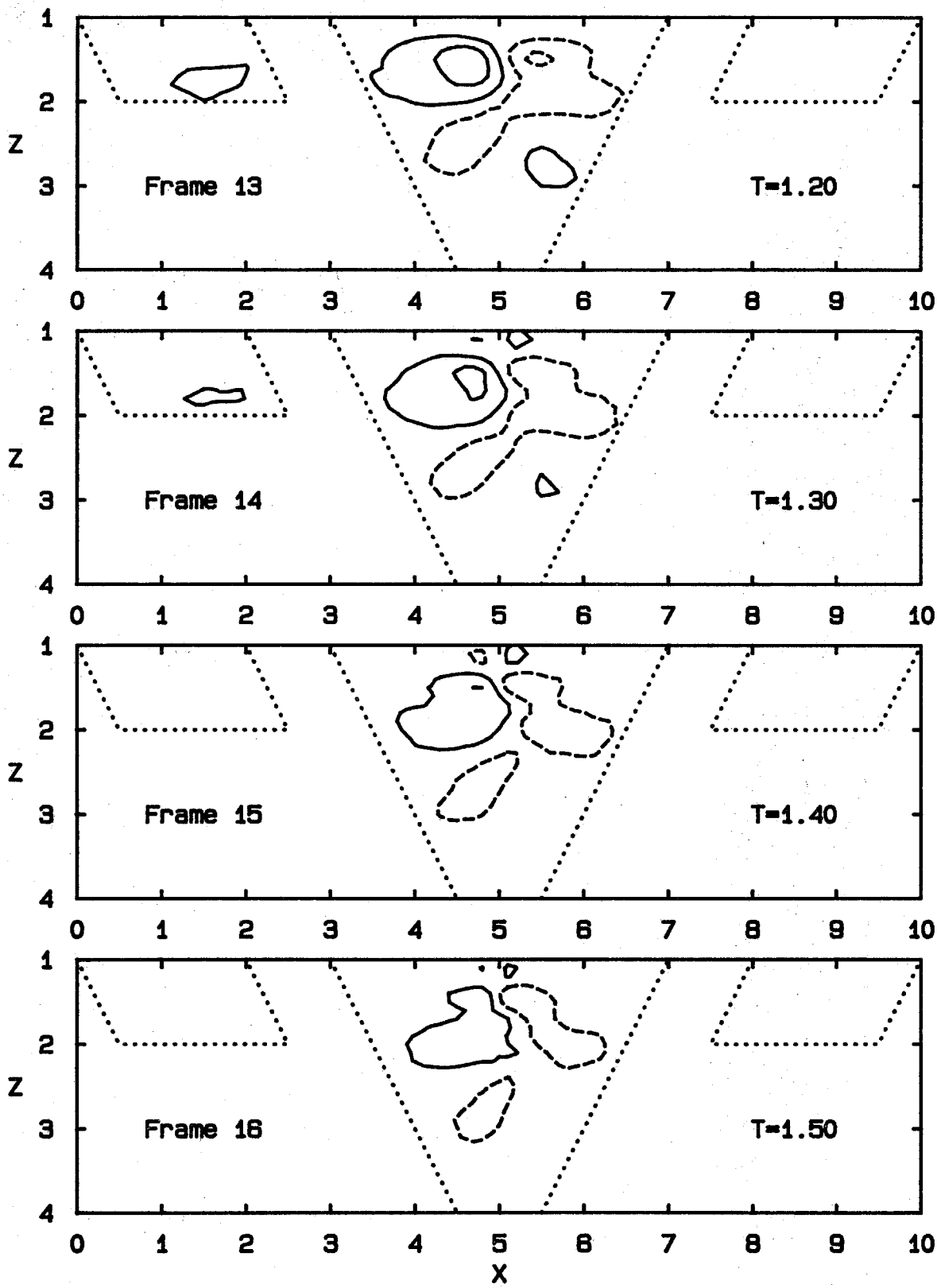

Fig. 6.7 Strain-rate Contours in the X-Z Plane; $\partial u/\partial z$

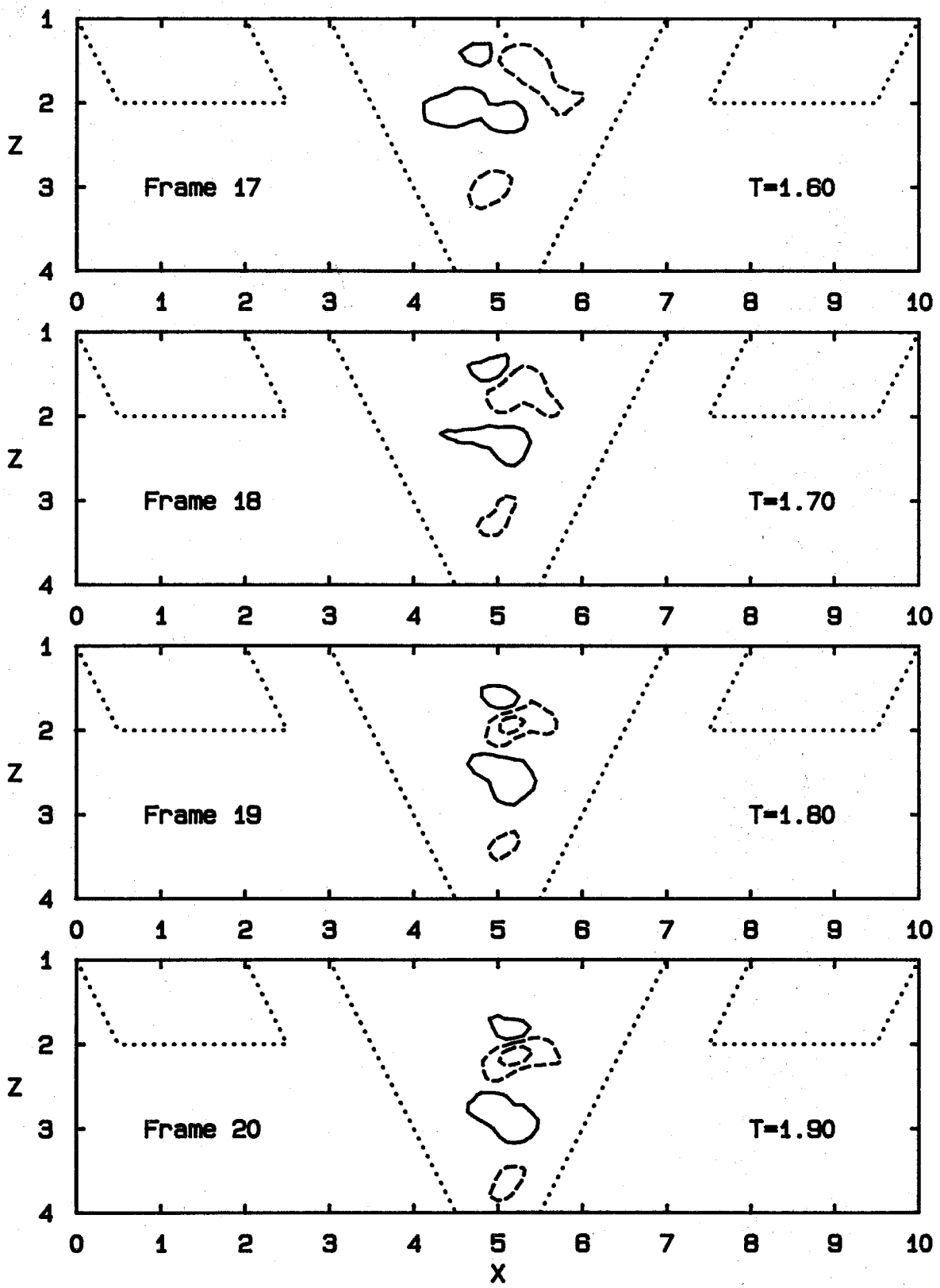

Fig. 6.7 Strain-rate Contours in the X-Z Plane; ∂u/∂z

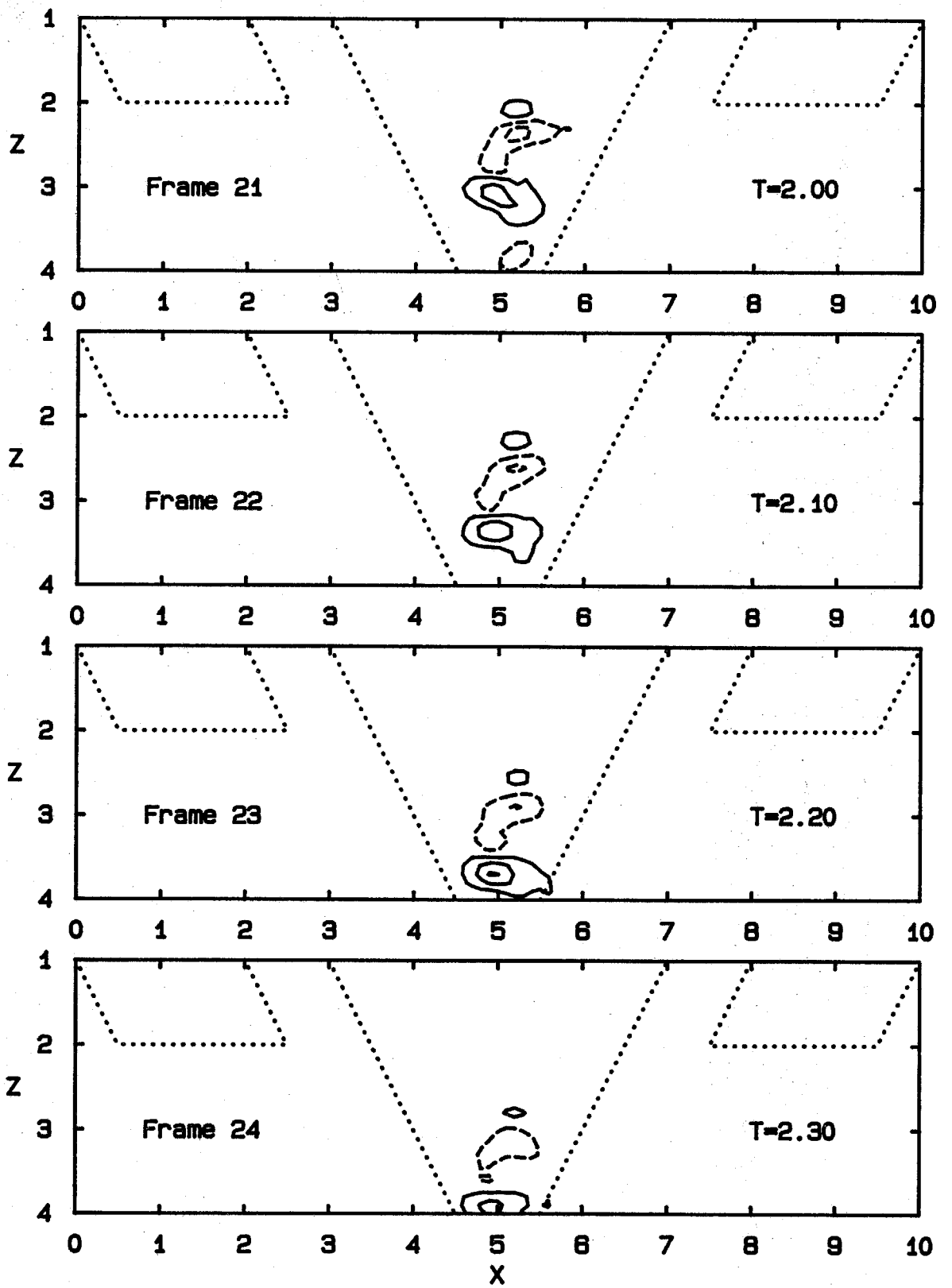

Fig. 6.7 Strain-rate Contours in the X-Z Plane; $\partial u/\partial z$

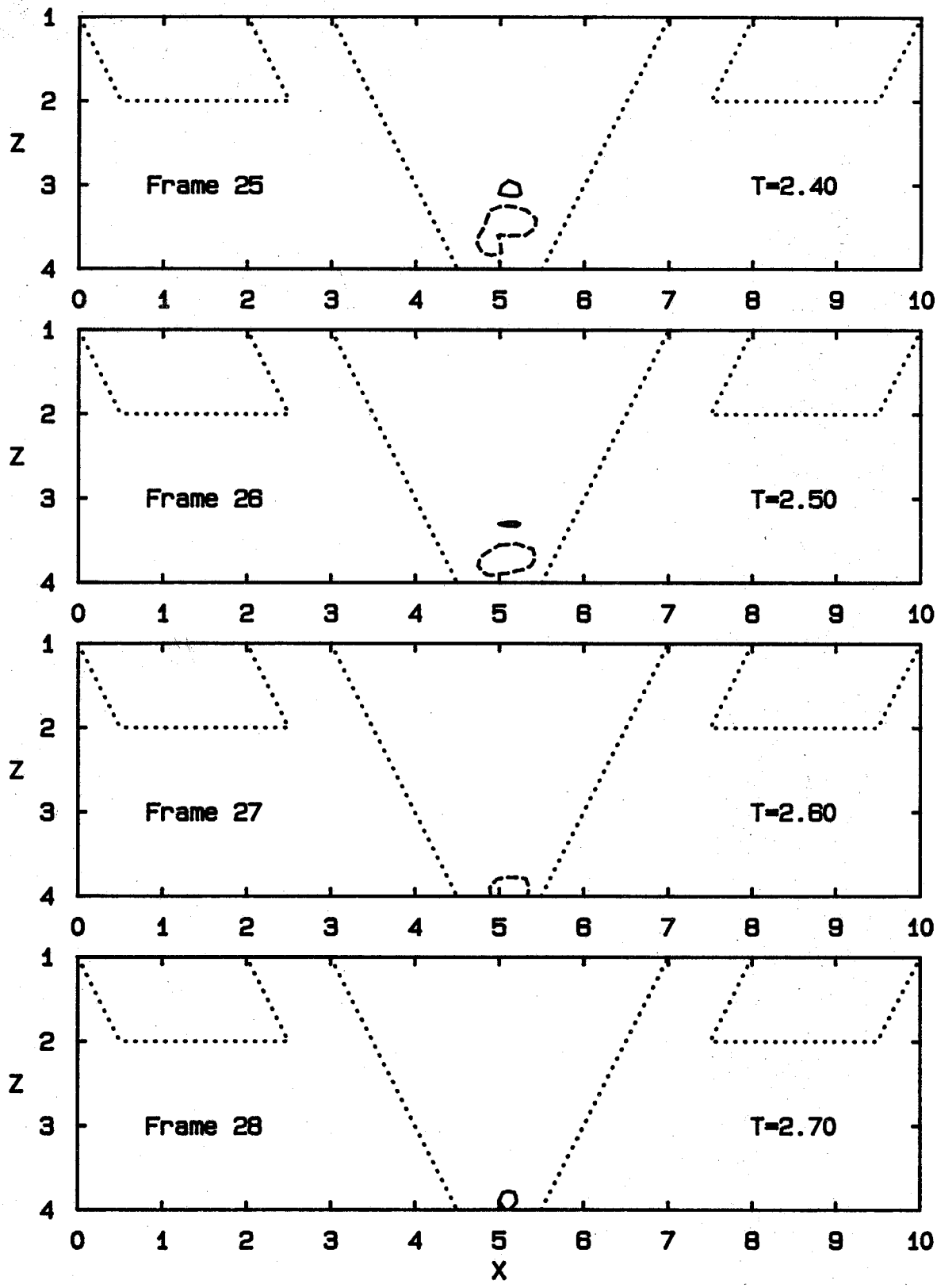

Fig. 6.7 Strain-rate Contours in the X-Z Plane; $\partial u/\partial z$

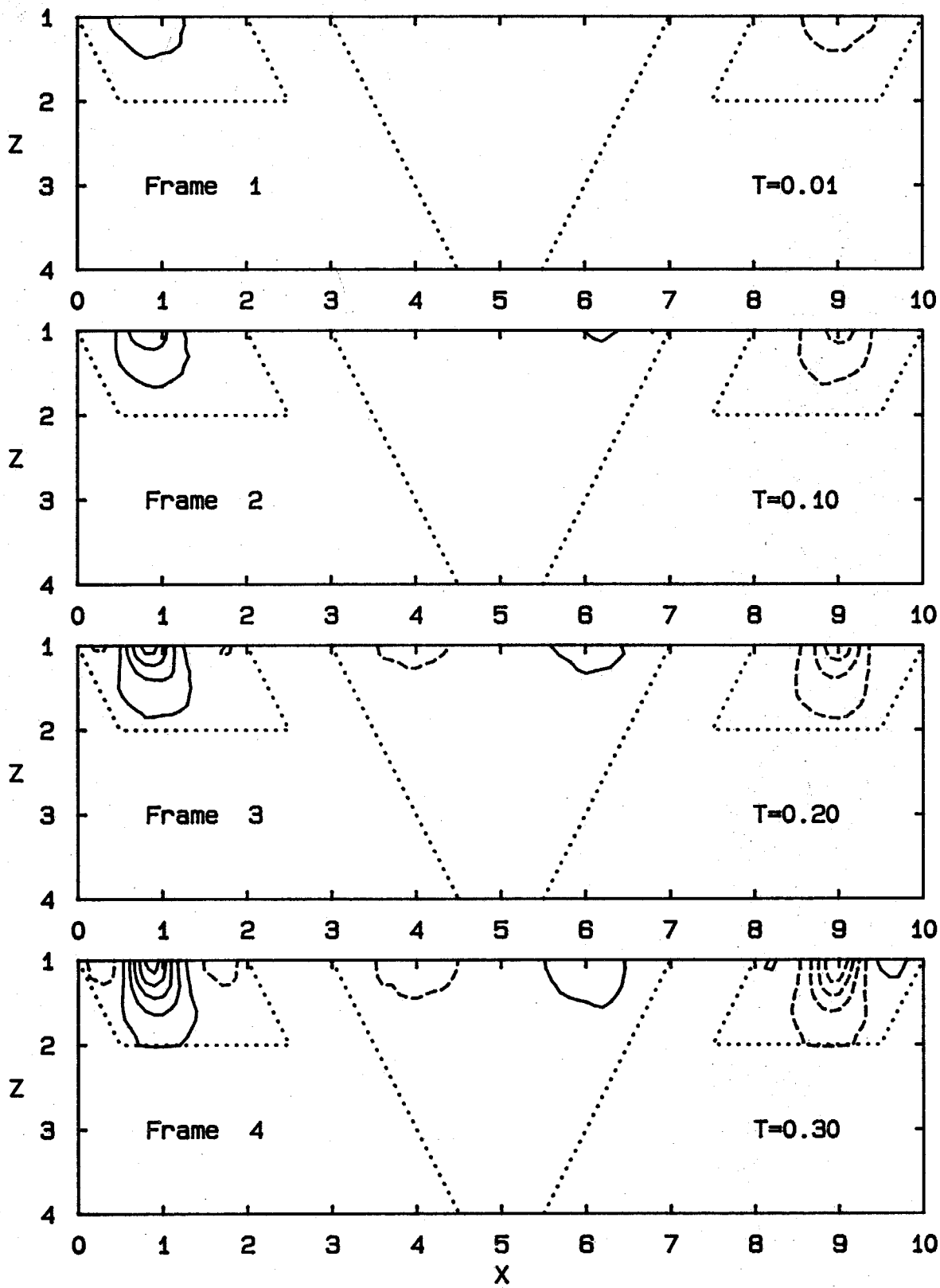

Fig. 6.8 Strain-rate Contours in the X-Z Plane; $\partial w/\partial x$

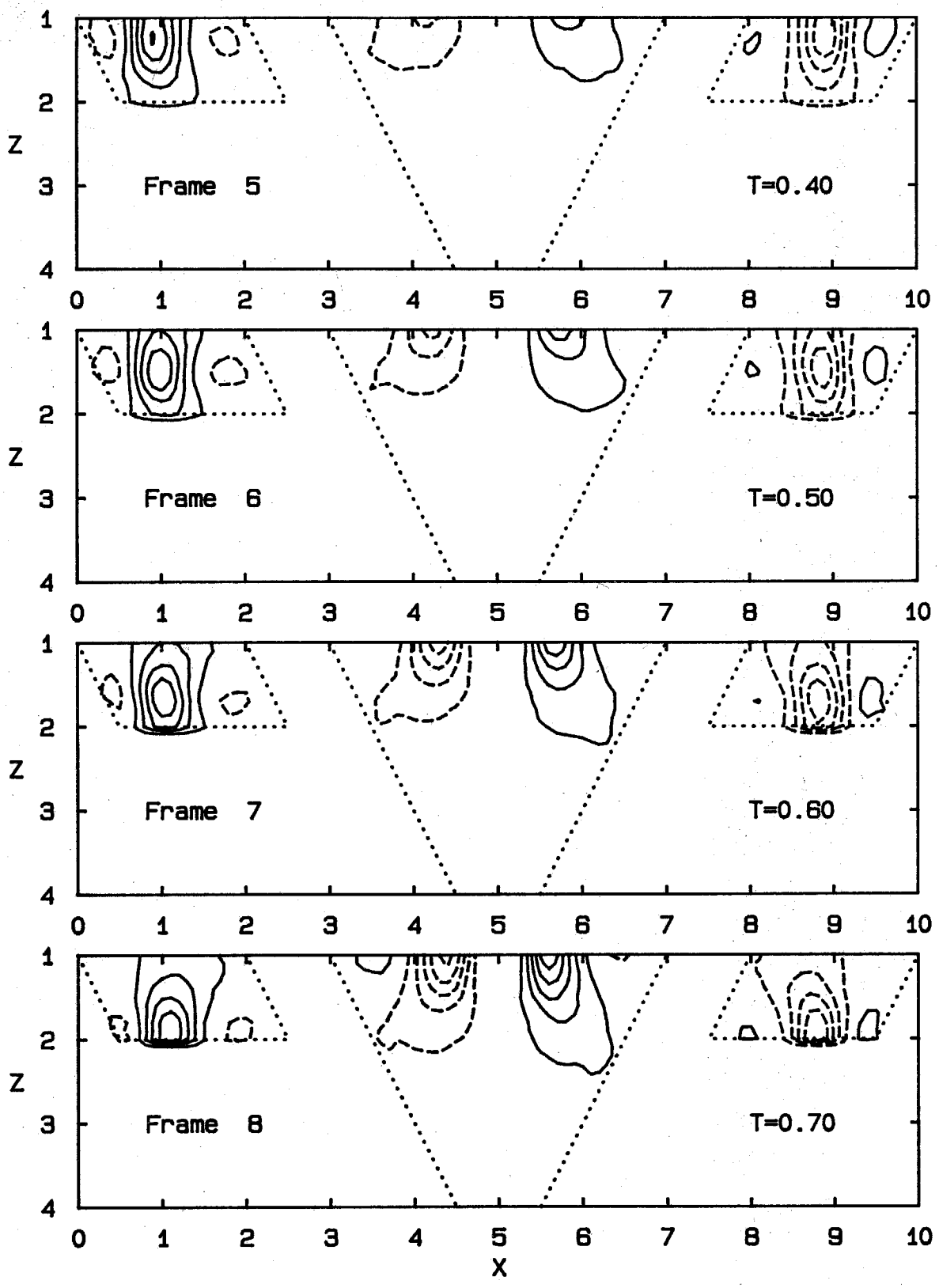

Fig. 6.8 Strain-rate Contours in the X-Z Plane; $\partial w/\partial x$

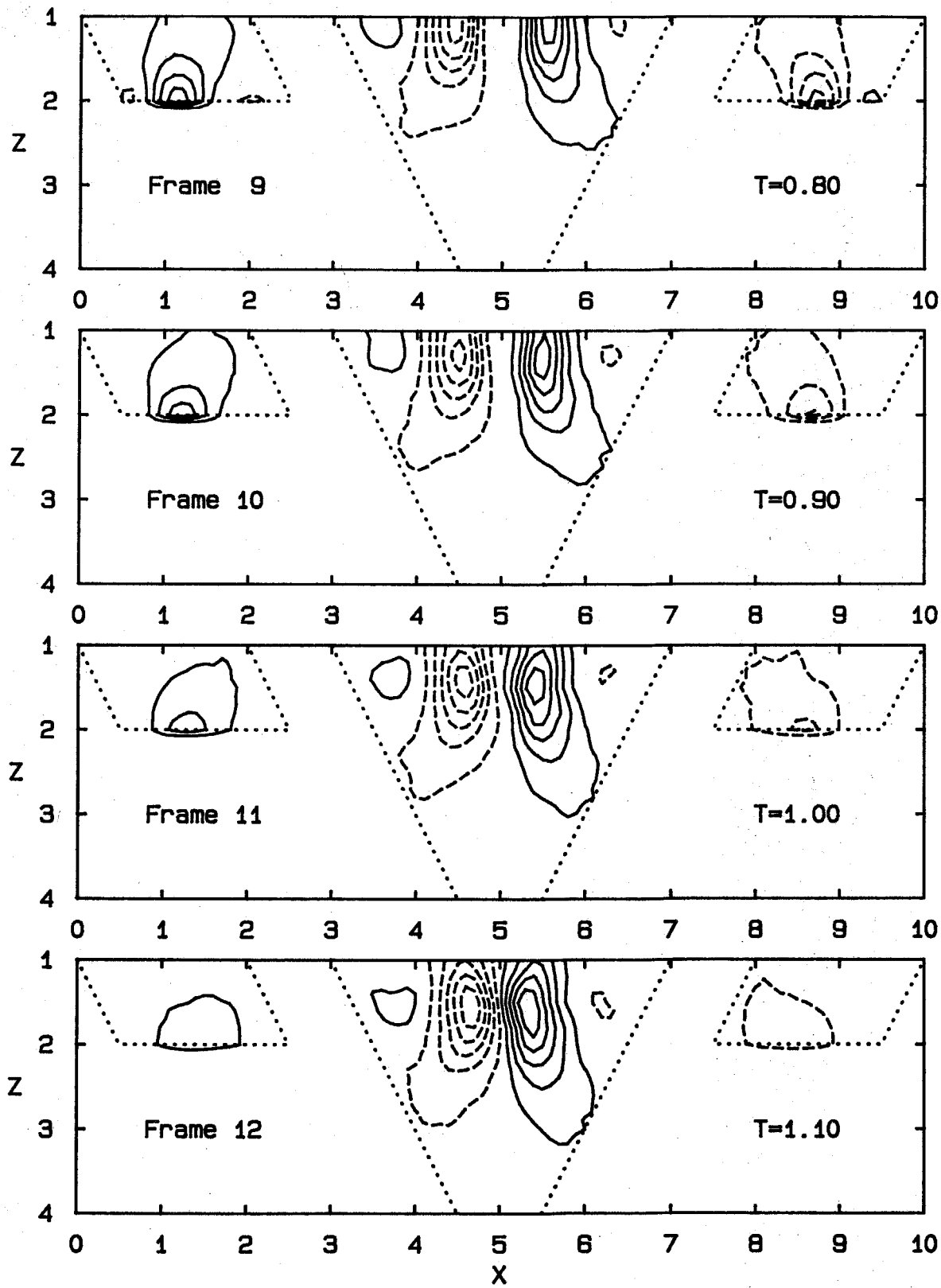

Fig. 6.8 Strain-rate Contours in the X-Z Plane; $\partial w/\partial x$

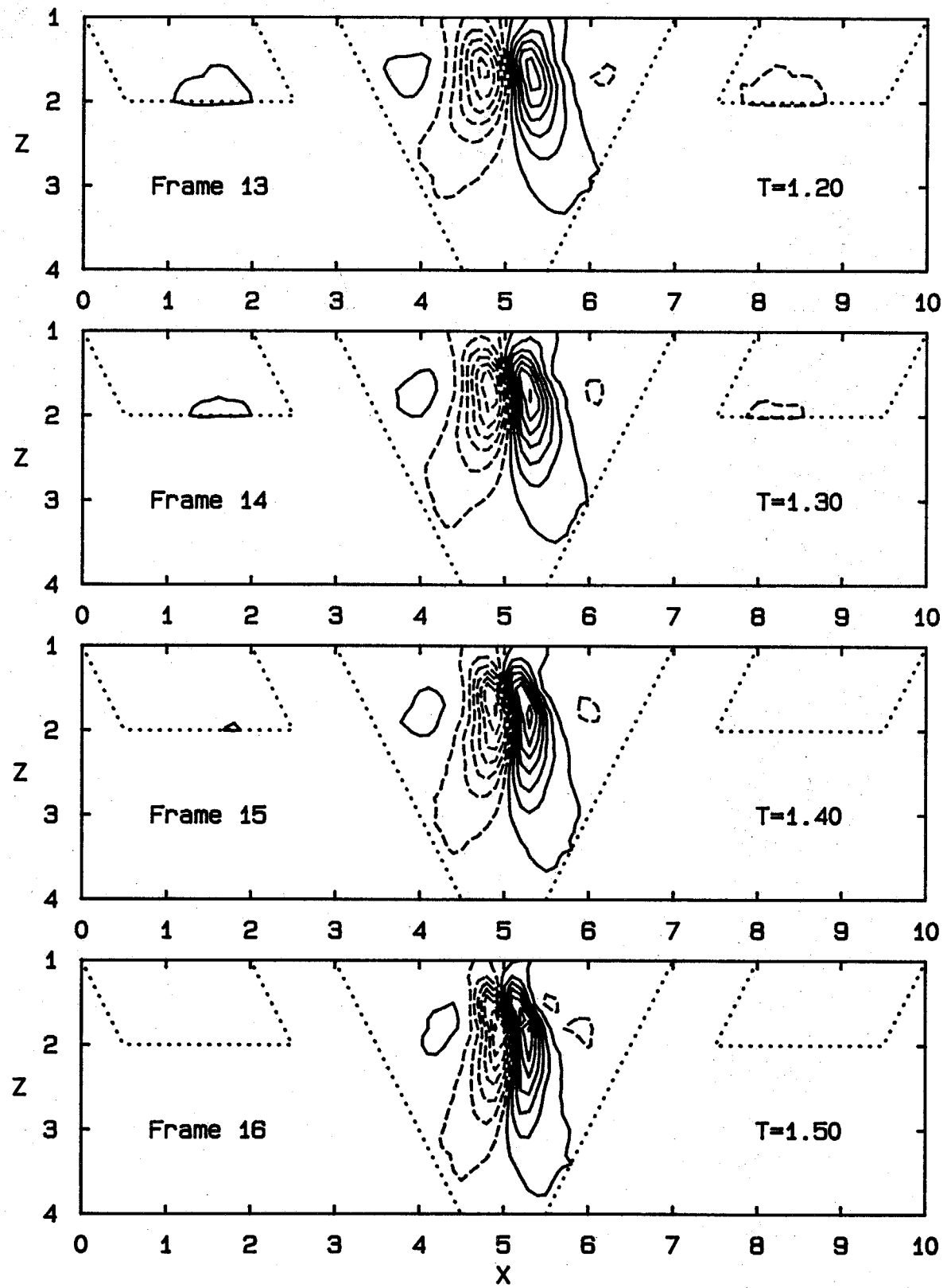

Fig. 6.8 Strain-rate Contours in the X-Z Plane; $\partial w/\partial x$

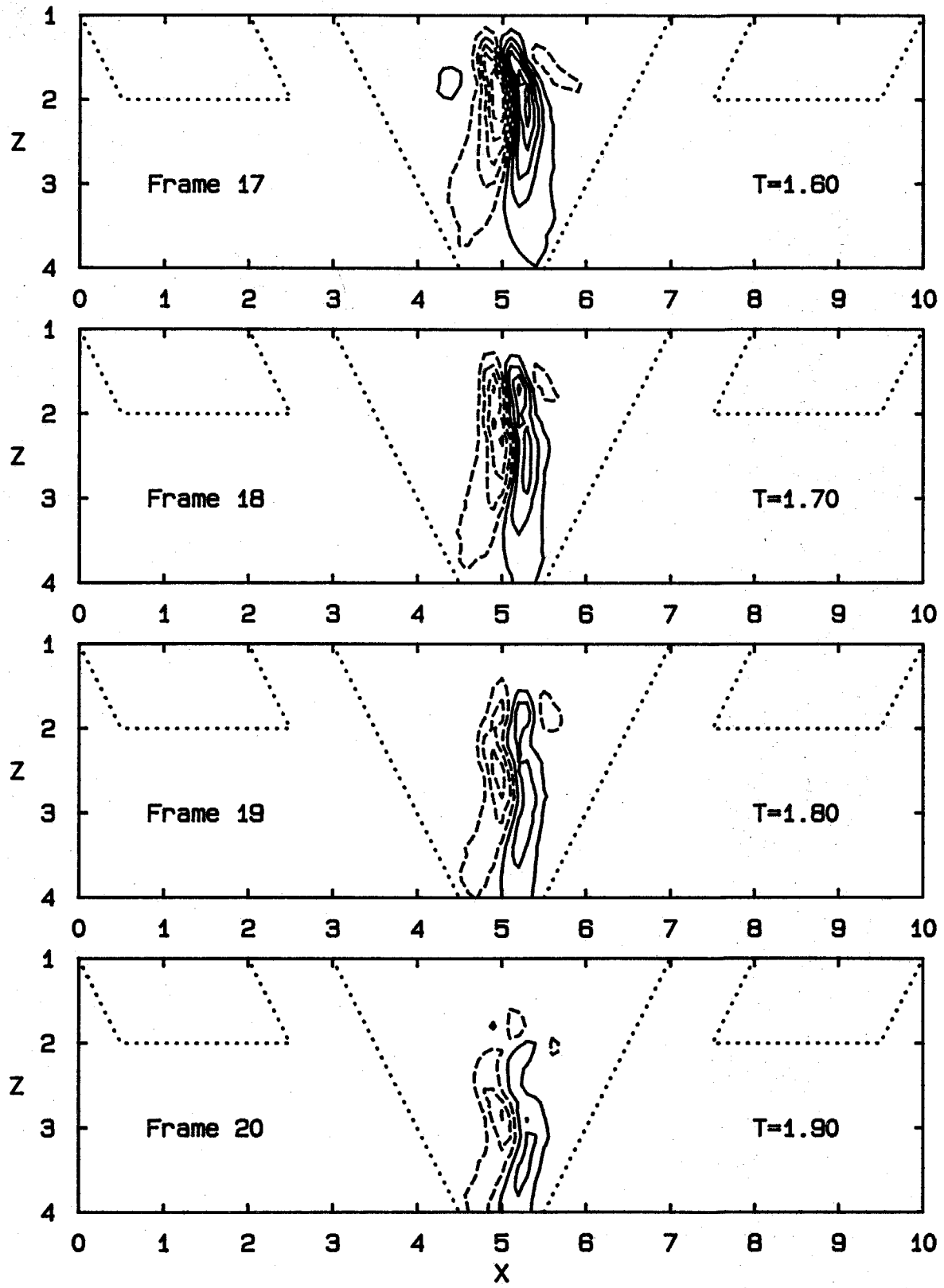

Fig. 6.8 Strain-rate Contours in the X-Z Plane; $\partial w/\partial x$

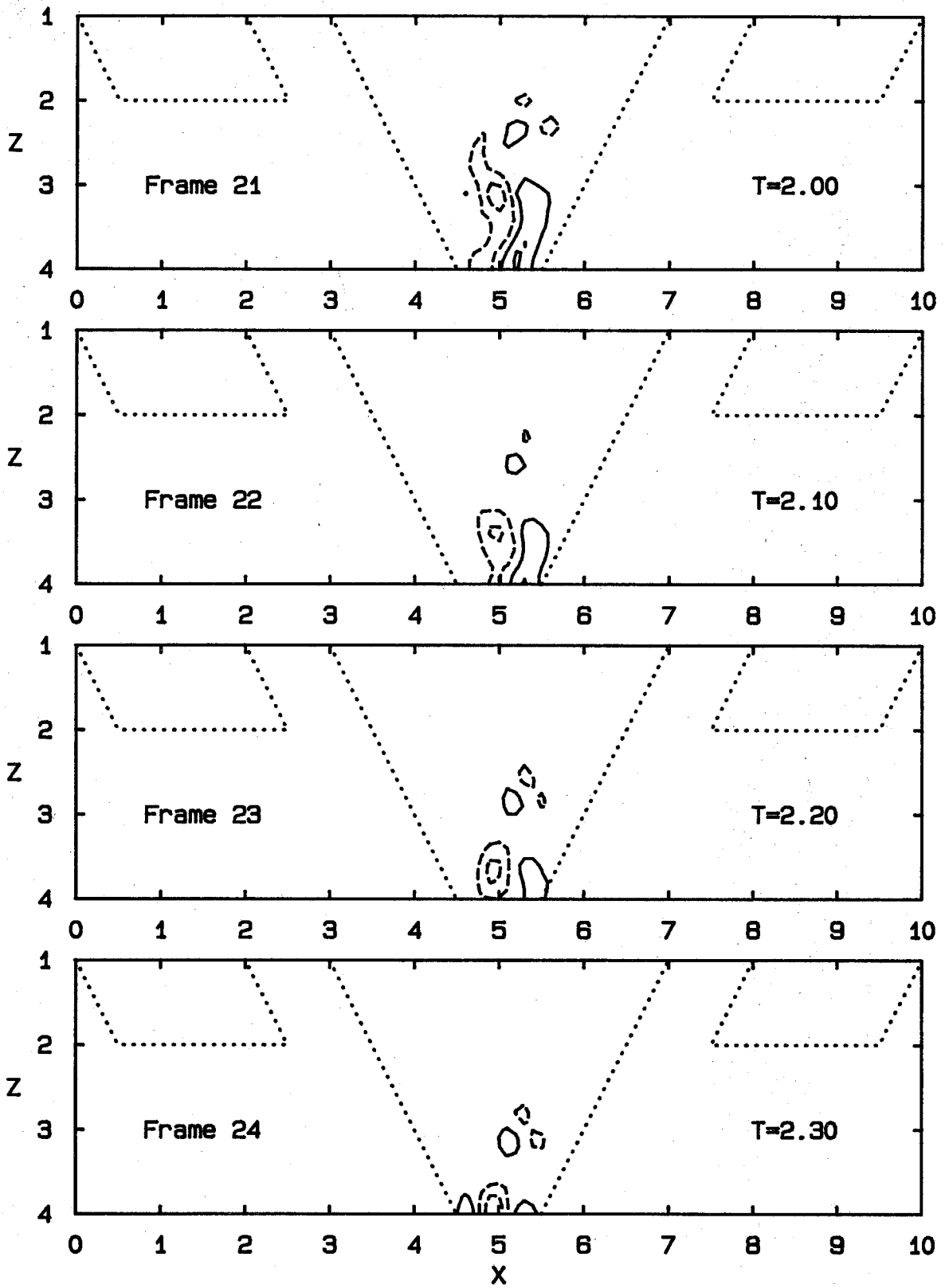

Fig. 6.8 Strain-rate Contours in the X-Z Plane; $\partial w/\partial x$

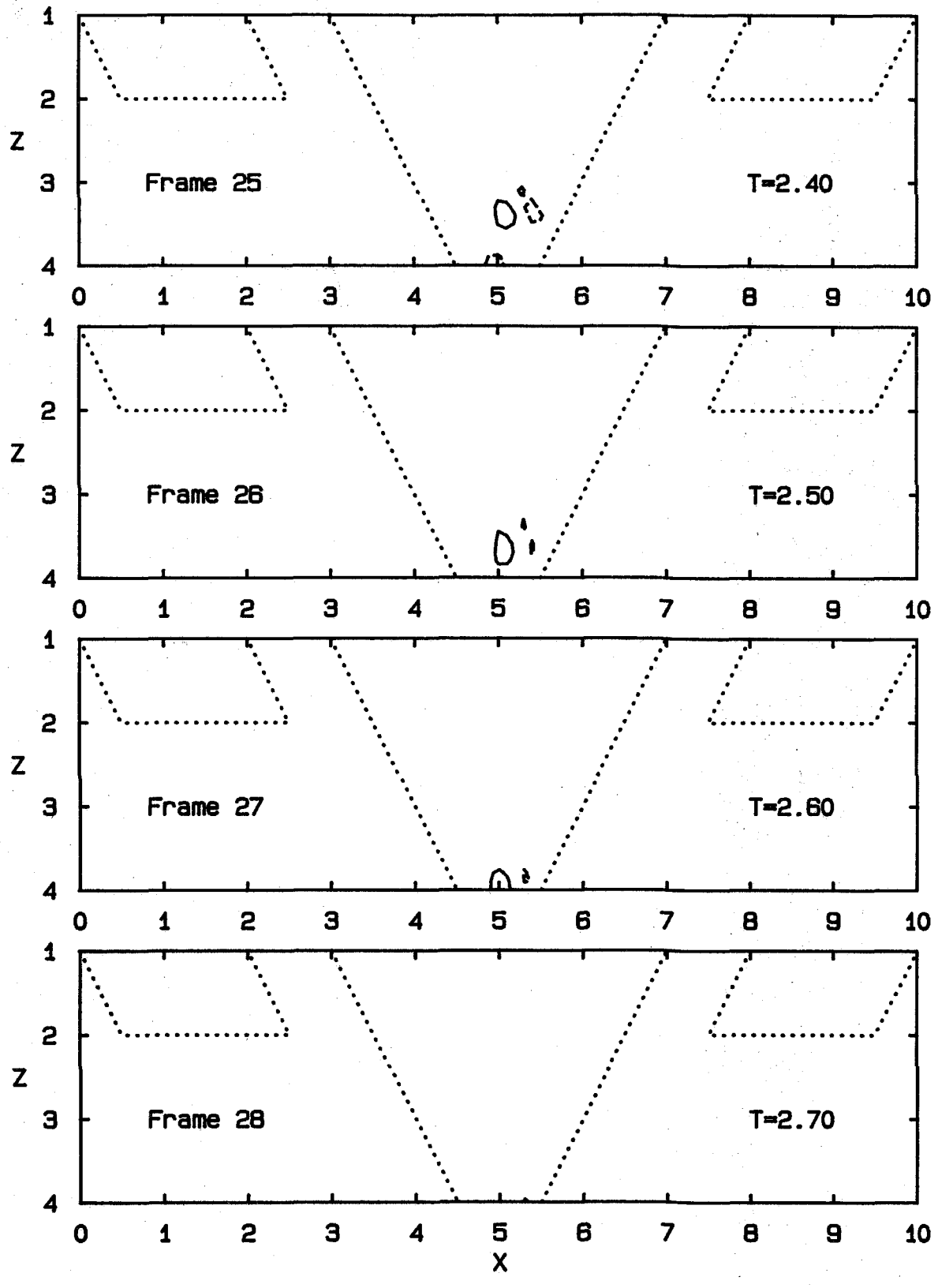

Fig. 6.8 Strain-rate Contours in the X-Z Plane; $\partial w/\partial x$

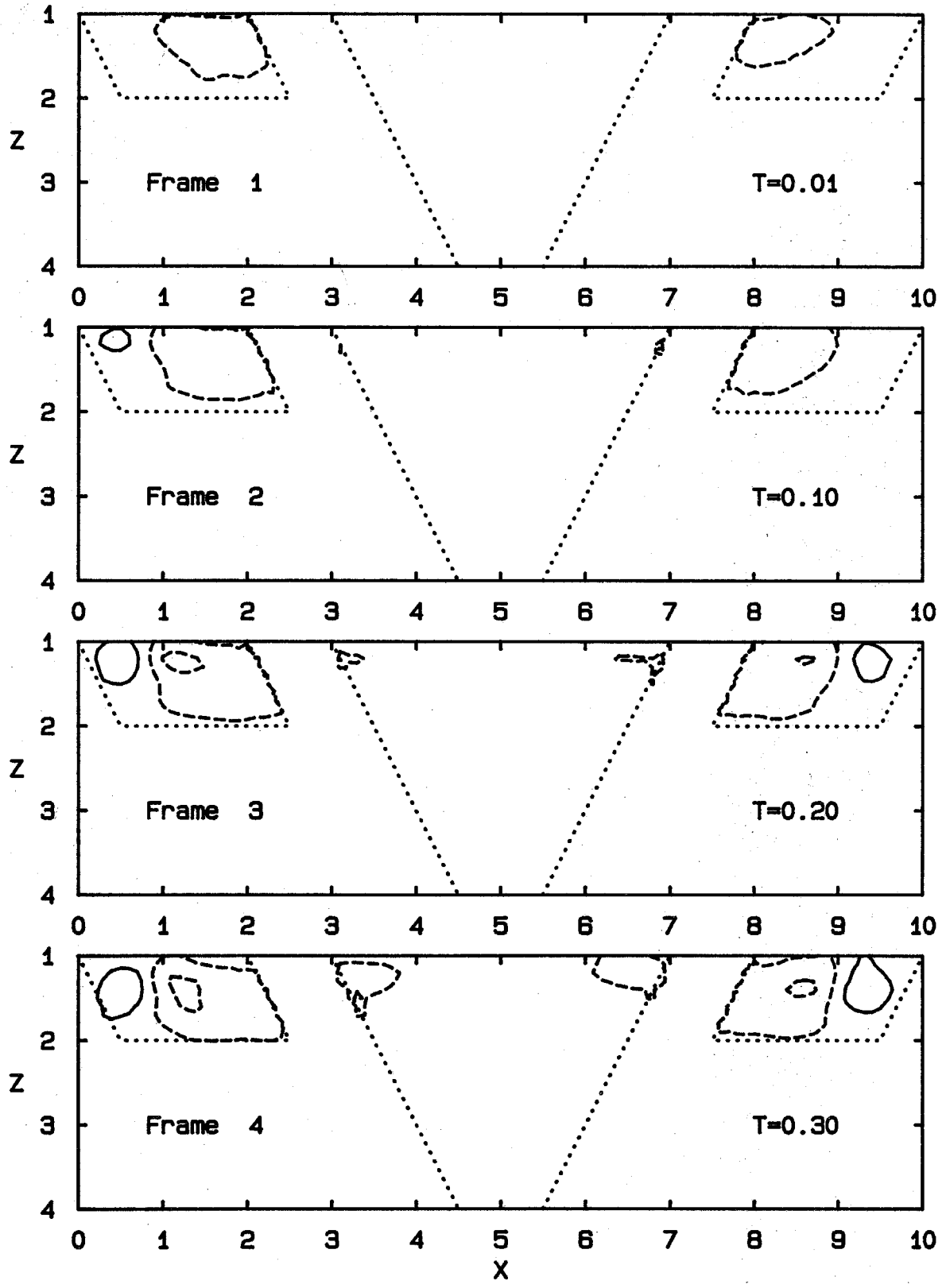

Fig. 6.9 Strain-rate Contours in the X-Z Plane; $\partial w/\partial z$

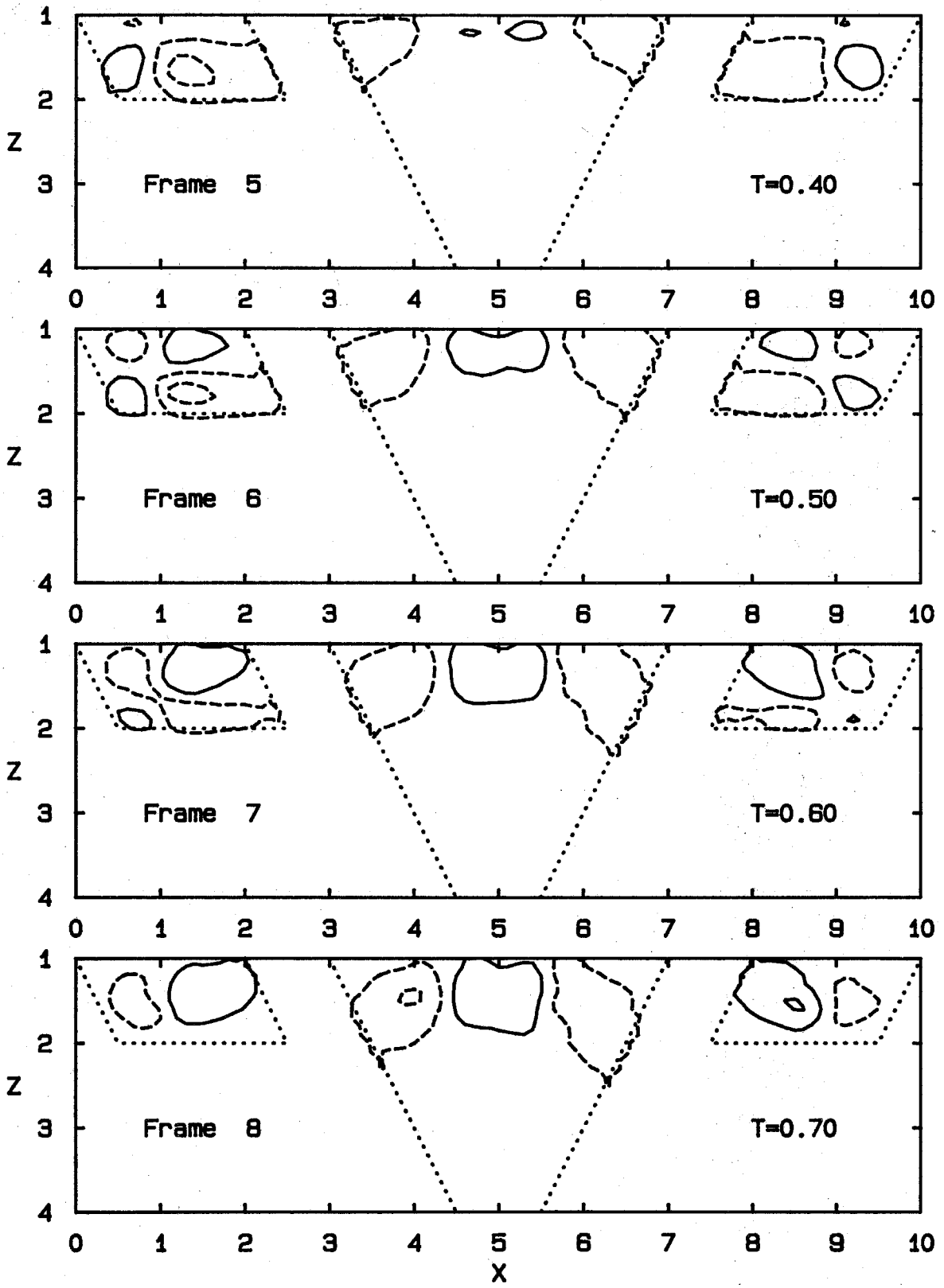

Fig. 6.9 Strain-rate Contours in the X-Z Plane; $\partial w/\partial z$

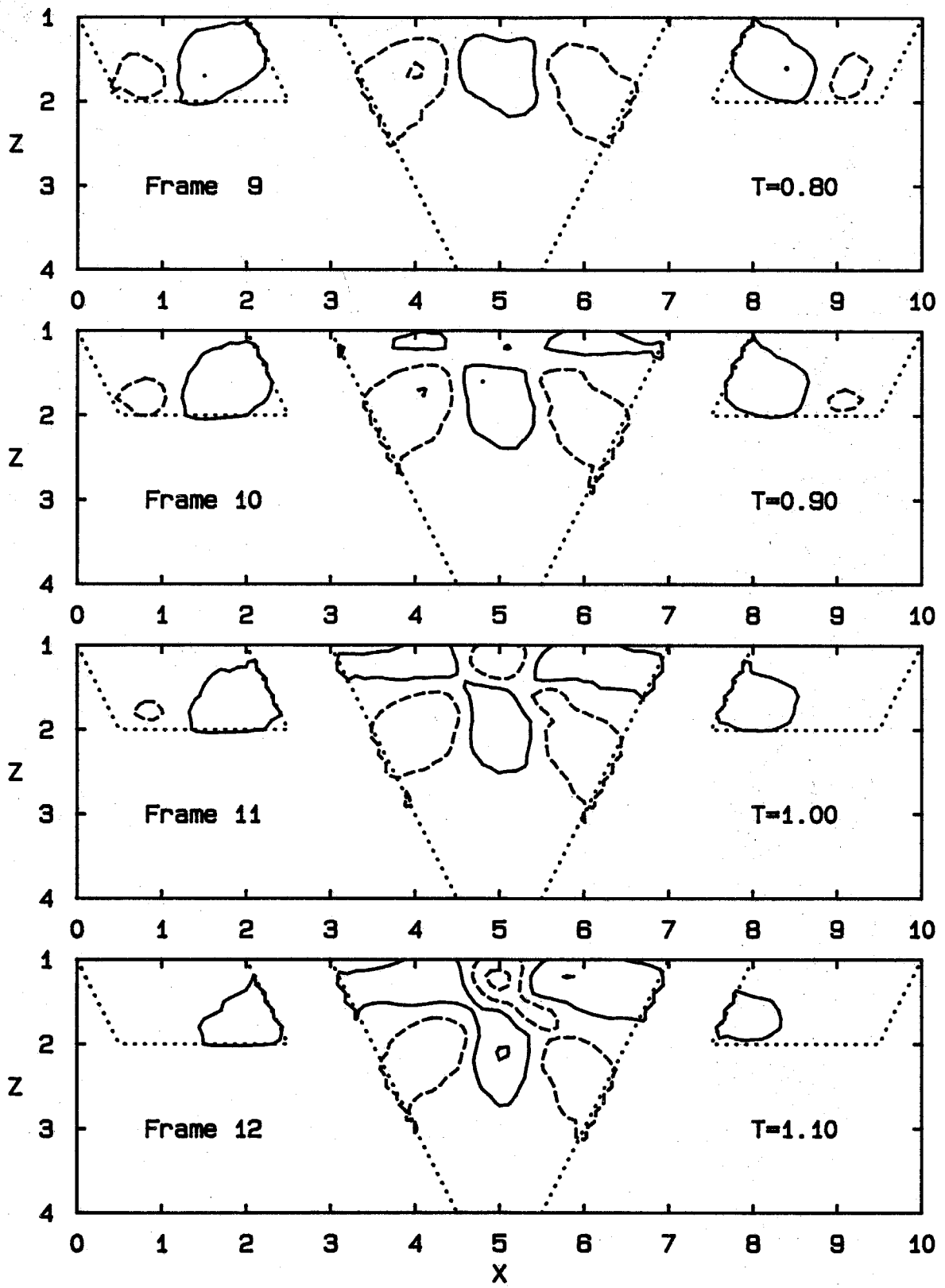

Fig. 6.9 Strain-rate Contours in the X-Z Plane; $\partial w/\partial z$

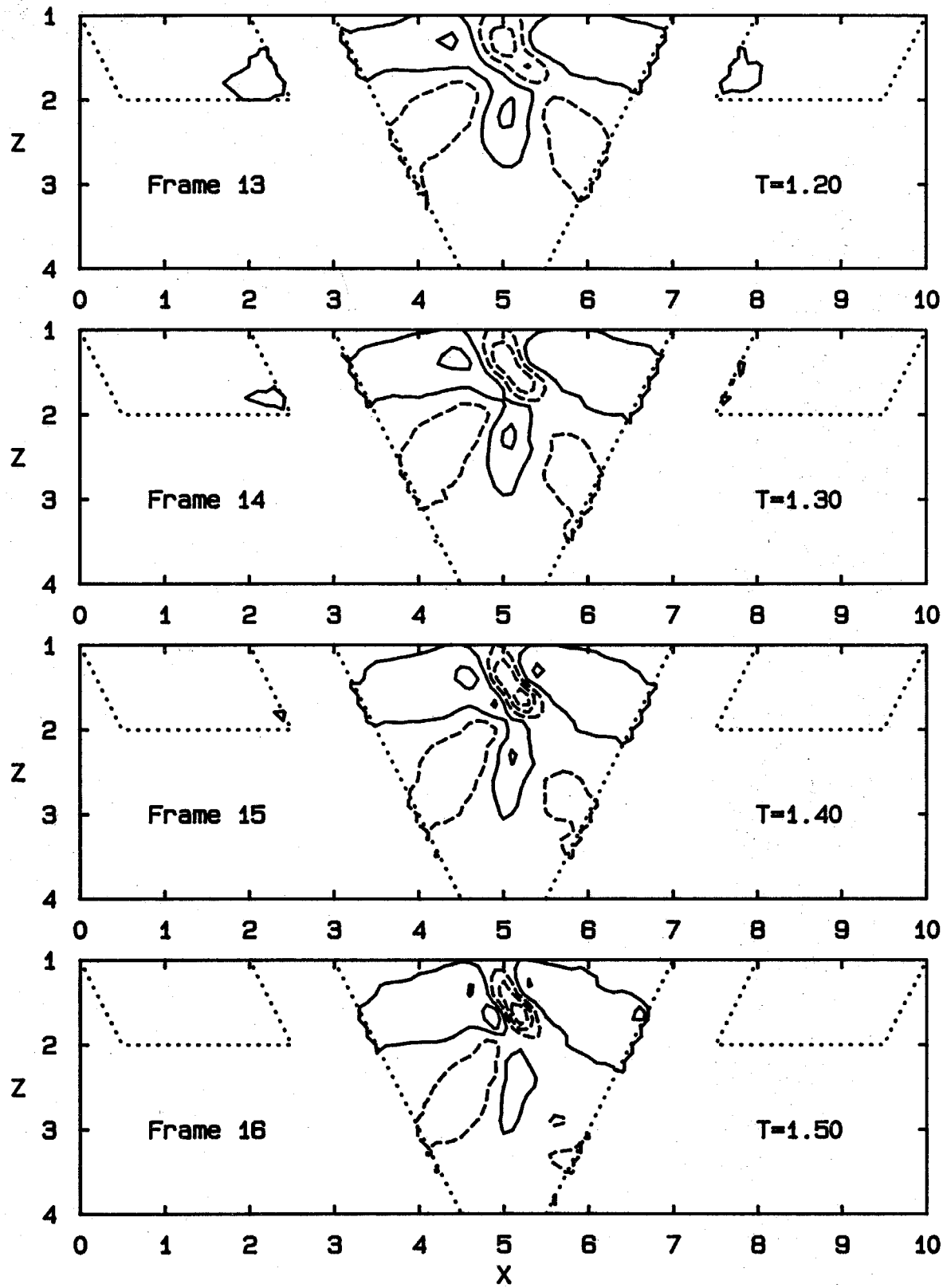

Fig. 6.9 Strain-rate Contours in the X-Z Plane; $\partial w/\partial z$

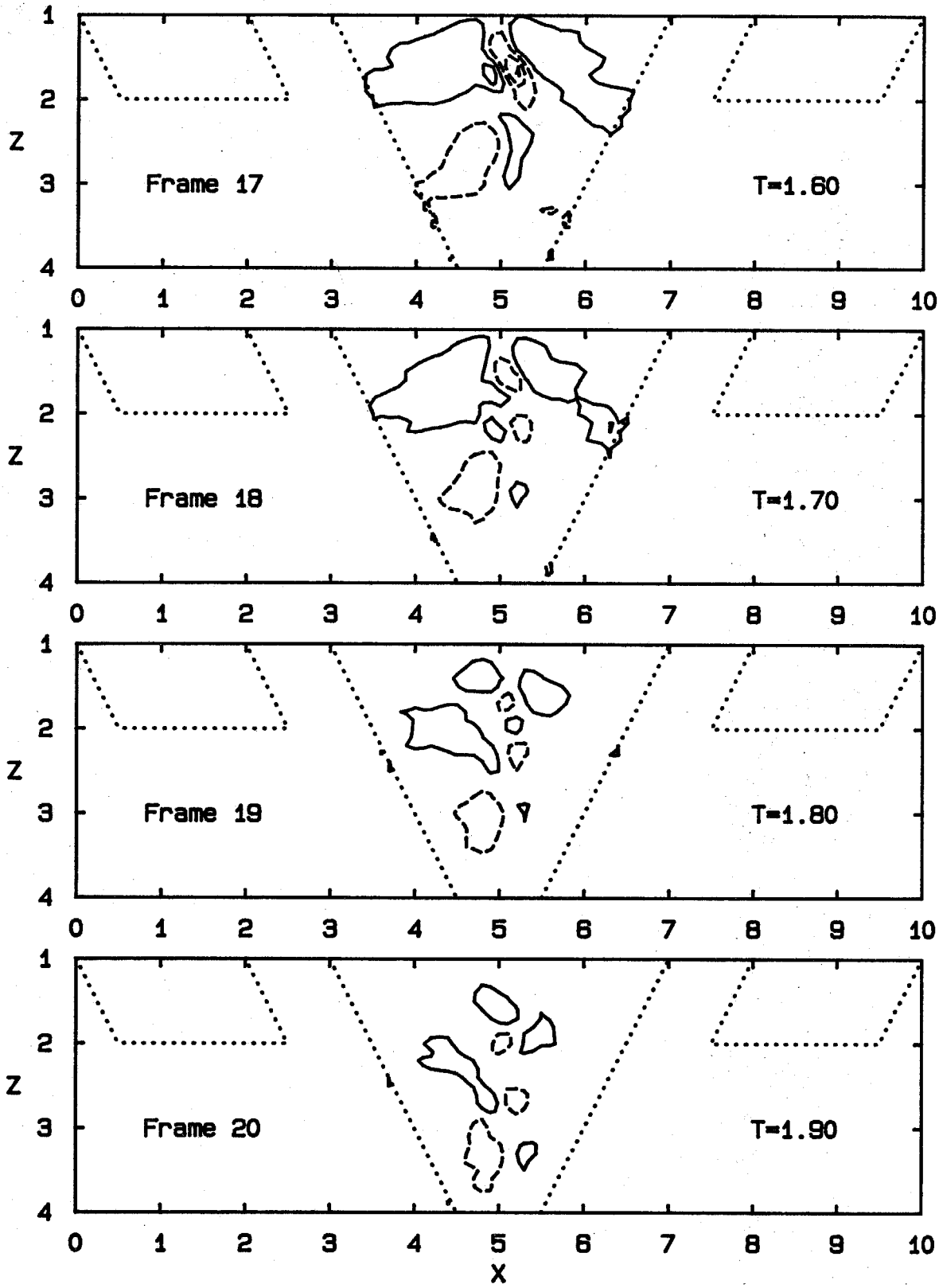

Fig. 6.9 Strain-rate Contours in the X-Z Plane; $\partial w/\partial z$

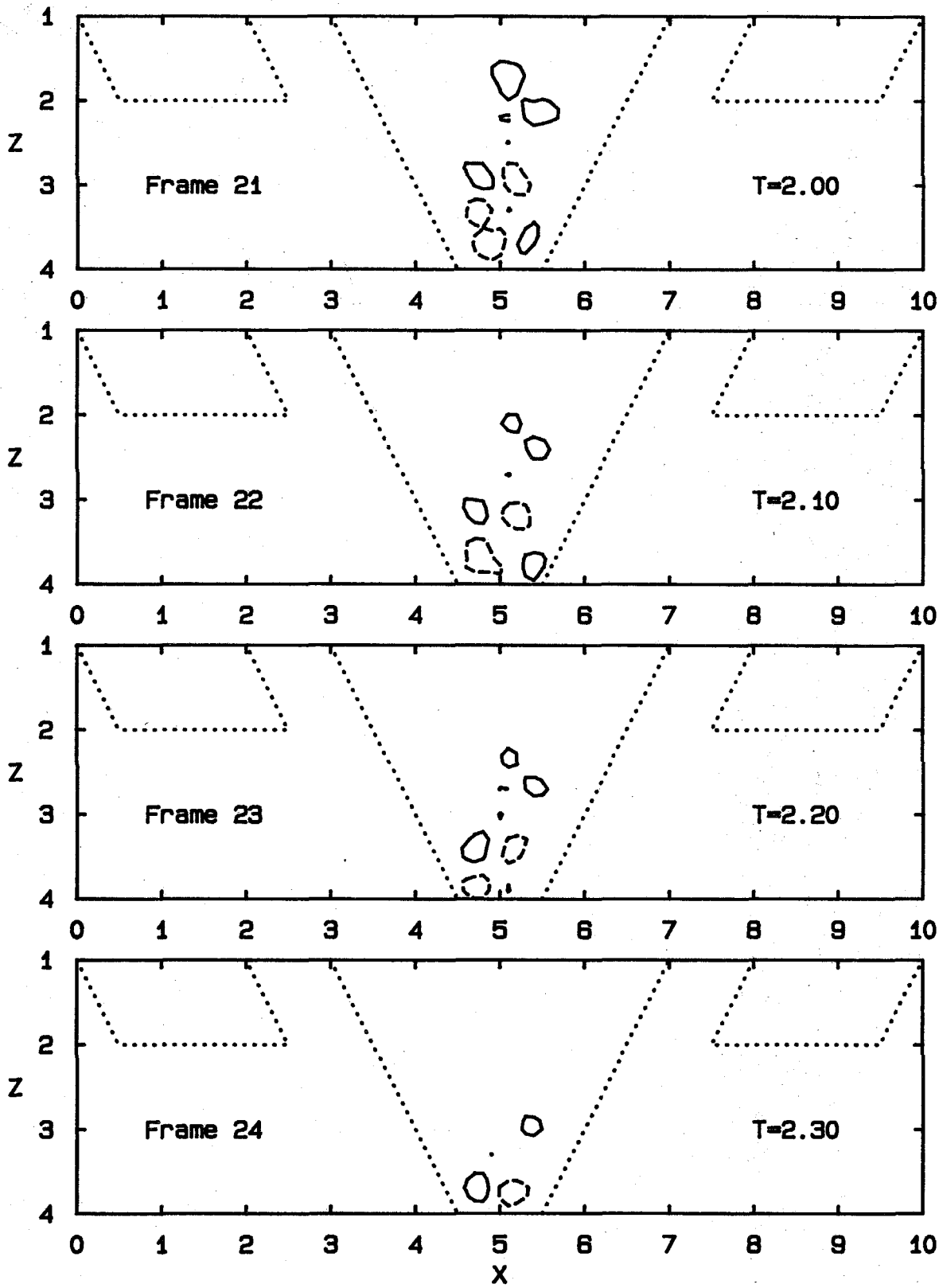

Fig. 6.9 Strain-rate Contours in the X-Z Plane; $\partial w/\partial z$

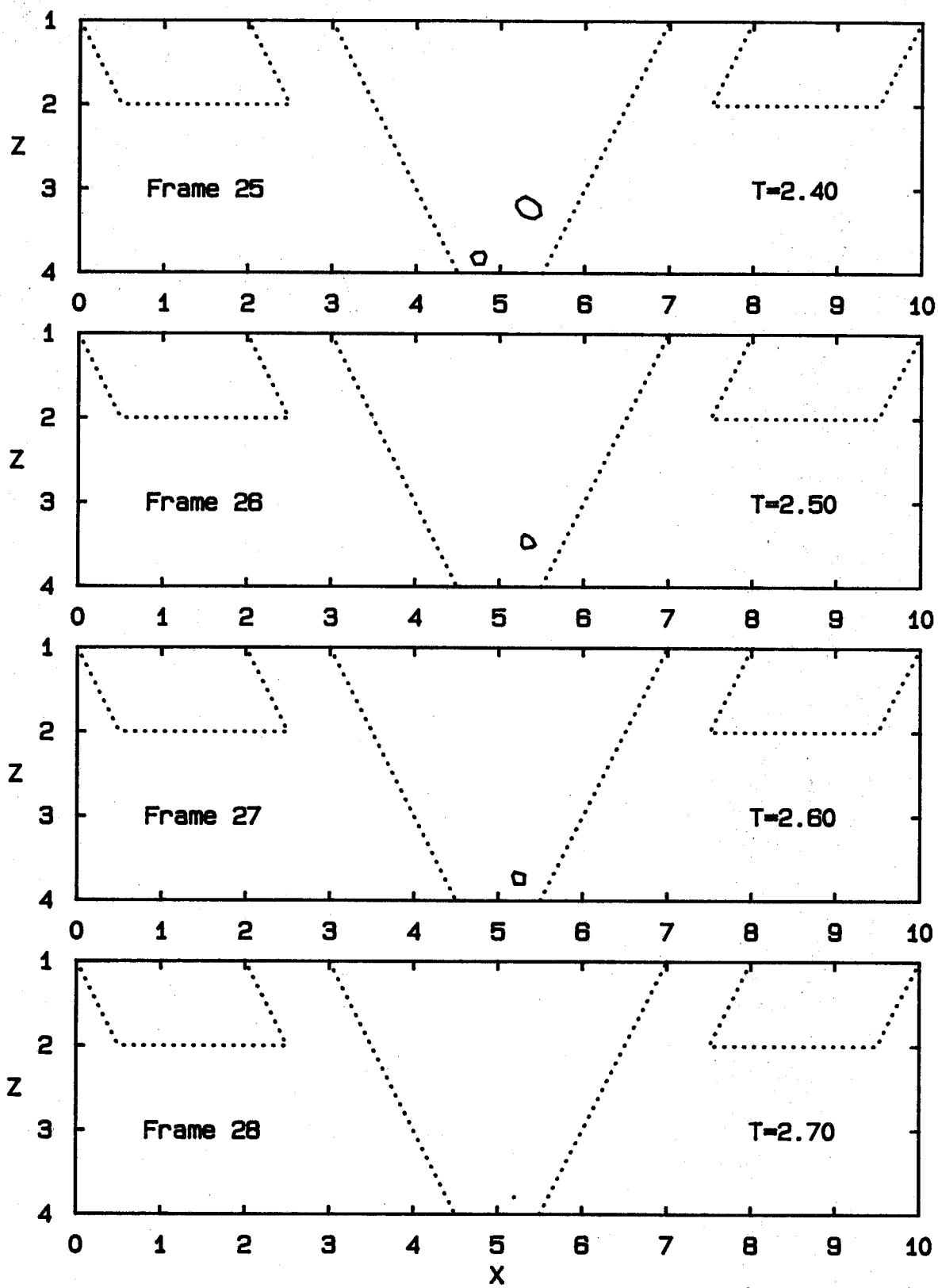

Fig. 6.9 Strain-rate Contours in the X-Z Plane; $\partial w/\partial z$

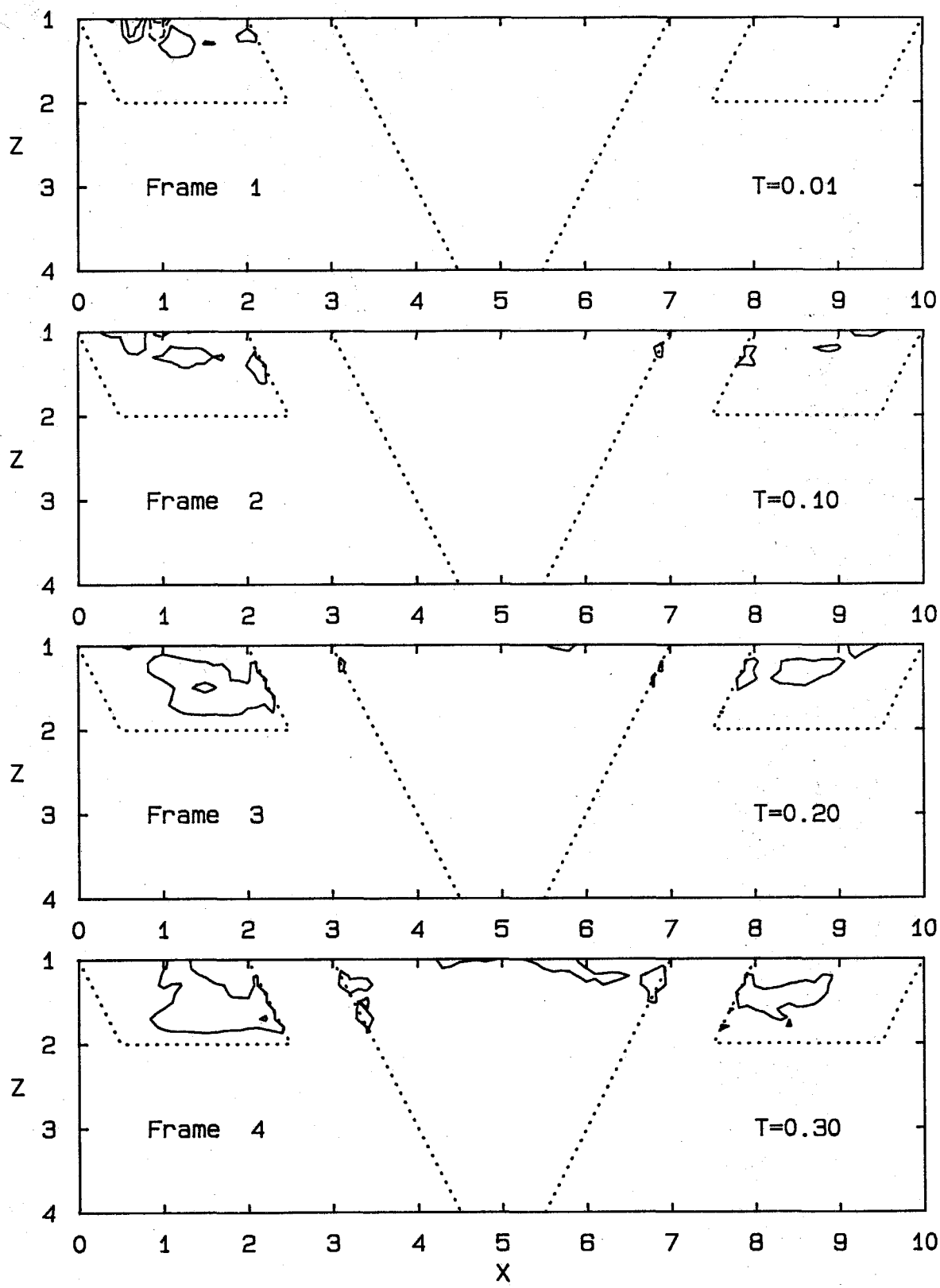

Fig. 6.10 Strain-rate Contours in the X-Z Plane; $\partial v/\partial y$

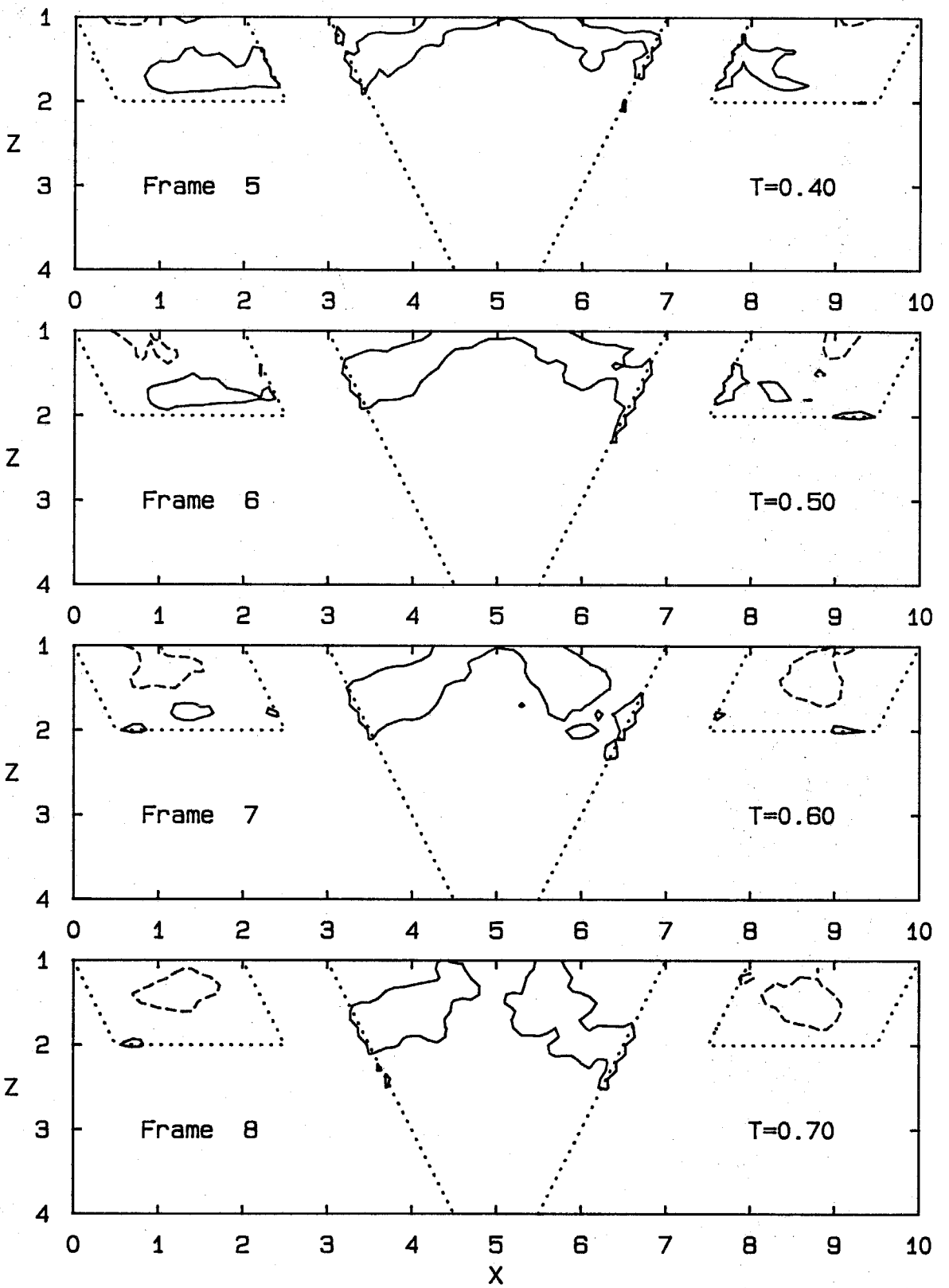

Fig. 6.10 Strain-rate Contours in the X-Z Plane; $\partial v/\partial y$

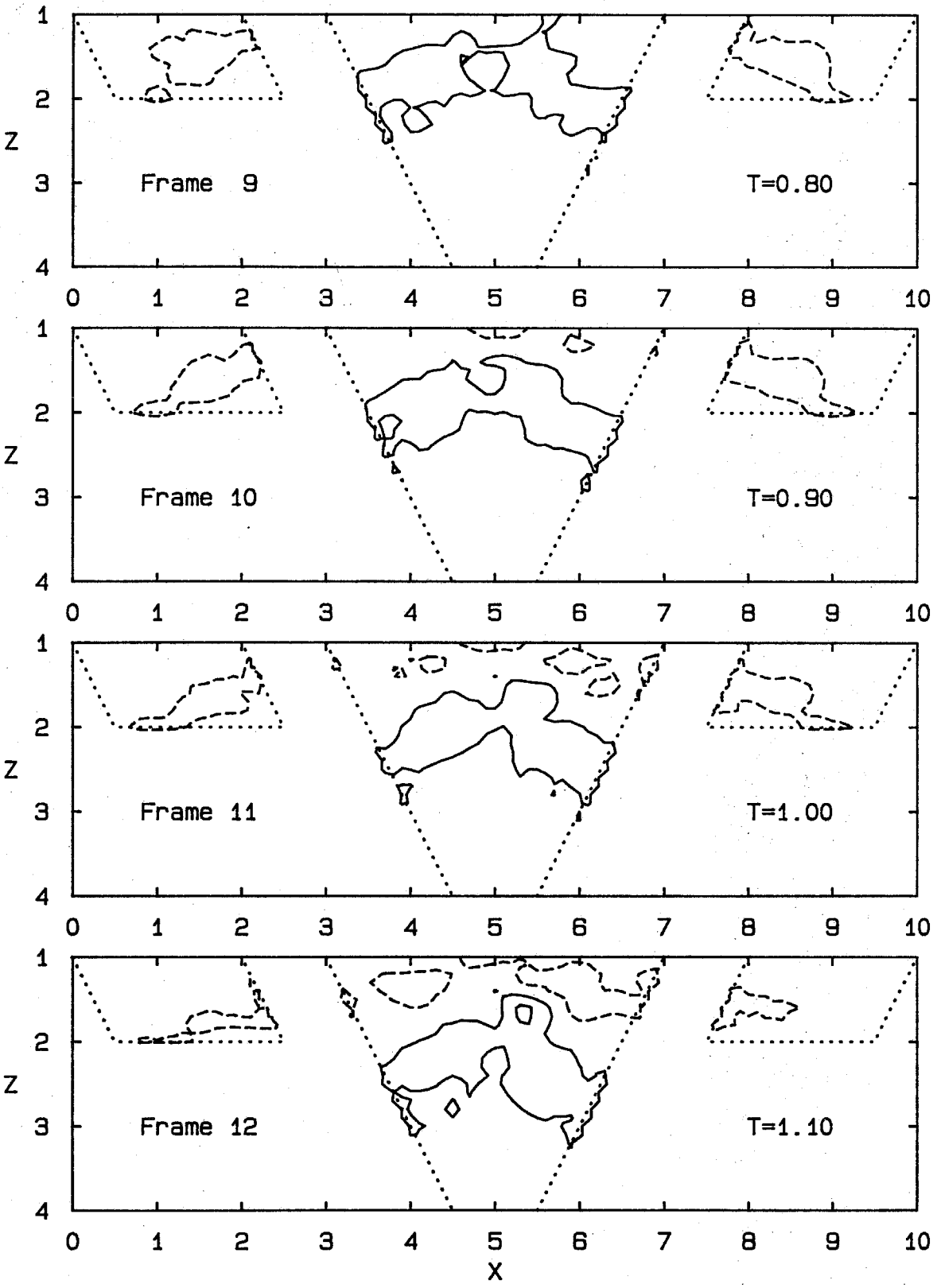

Fig. 6.10 Strain-rate Contours in the X-Z Plane; $\partial v/\partial y$

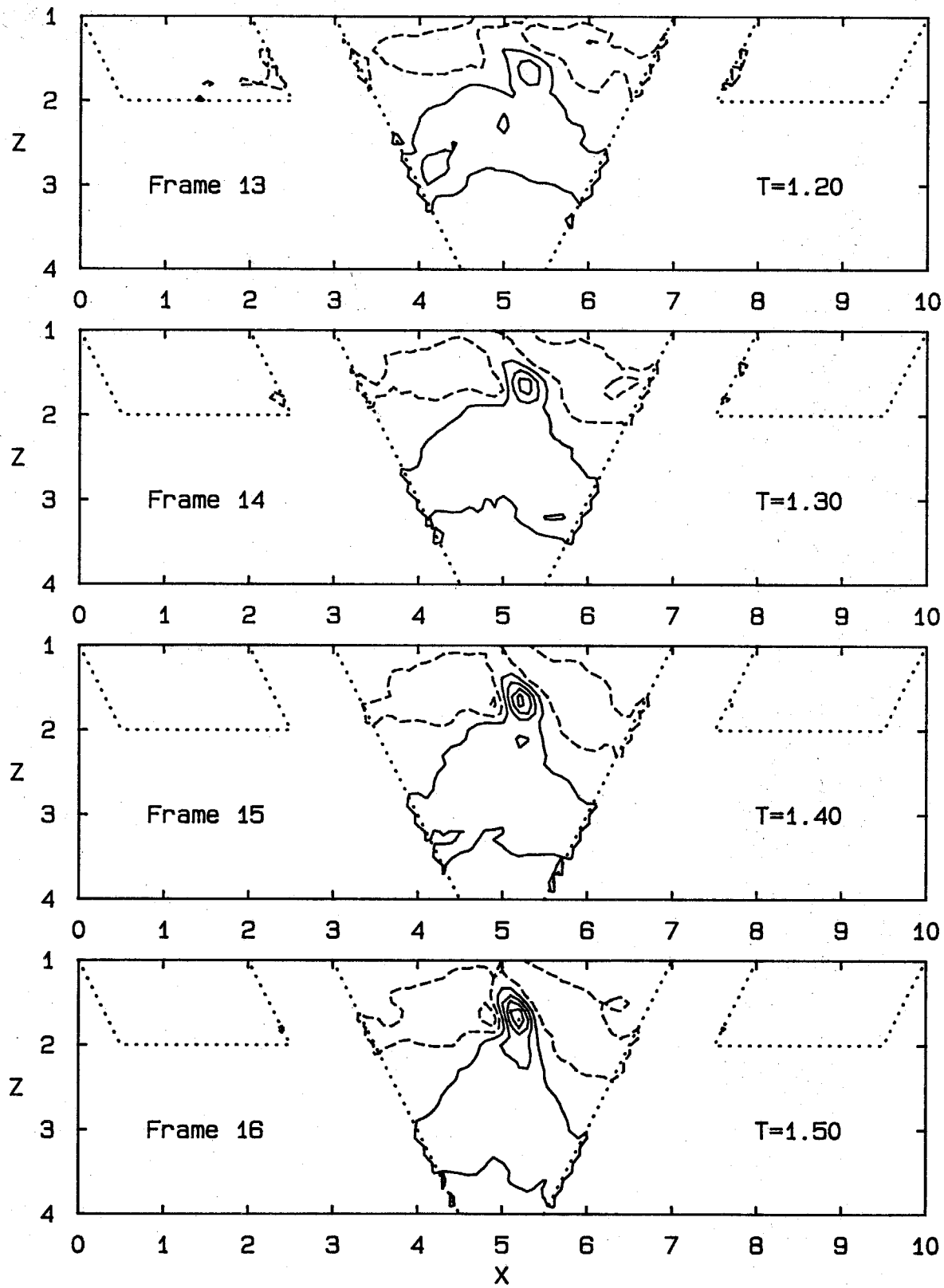

Fig. 6.10 Strain-rate Contours in the X-Z Plane; $\partial v/\partial y$

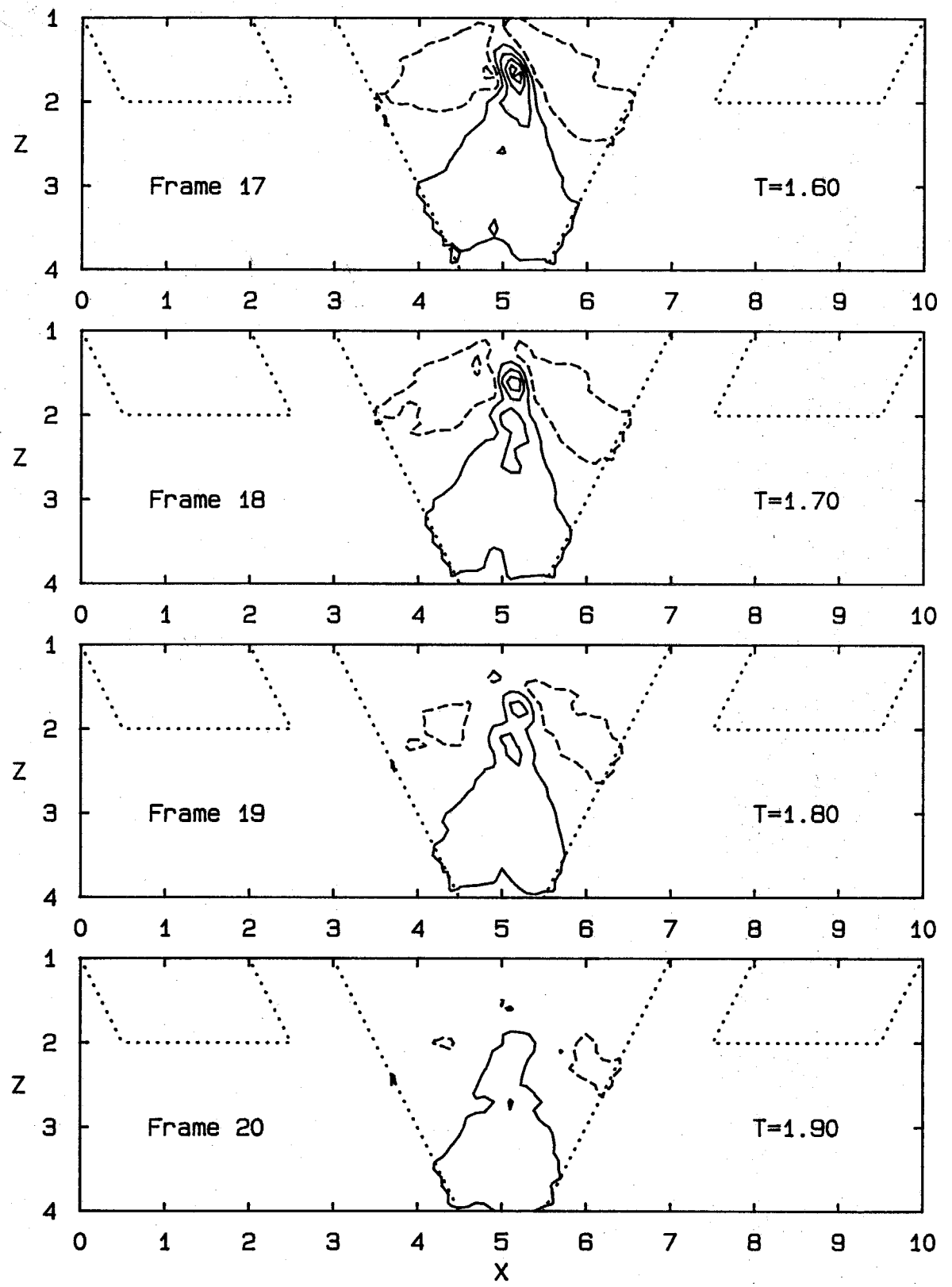

Fig. 6.10 Strain-rate Contours in the X-Z Plane; $\partial v/\partial y$

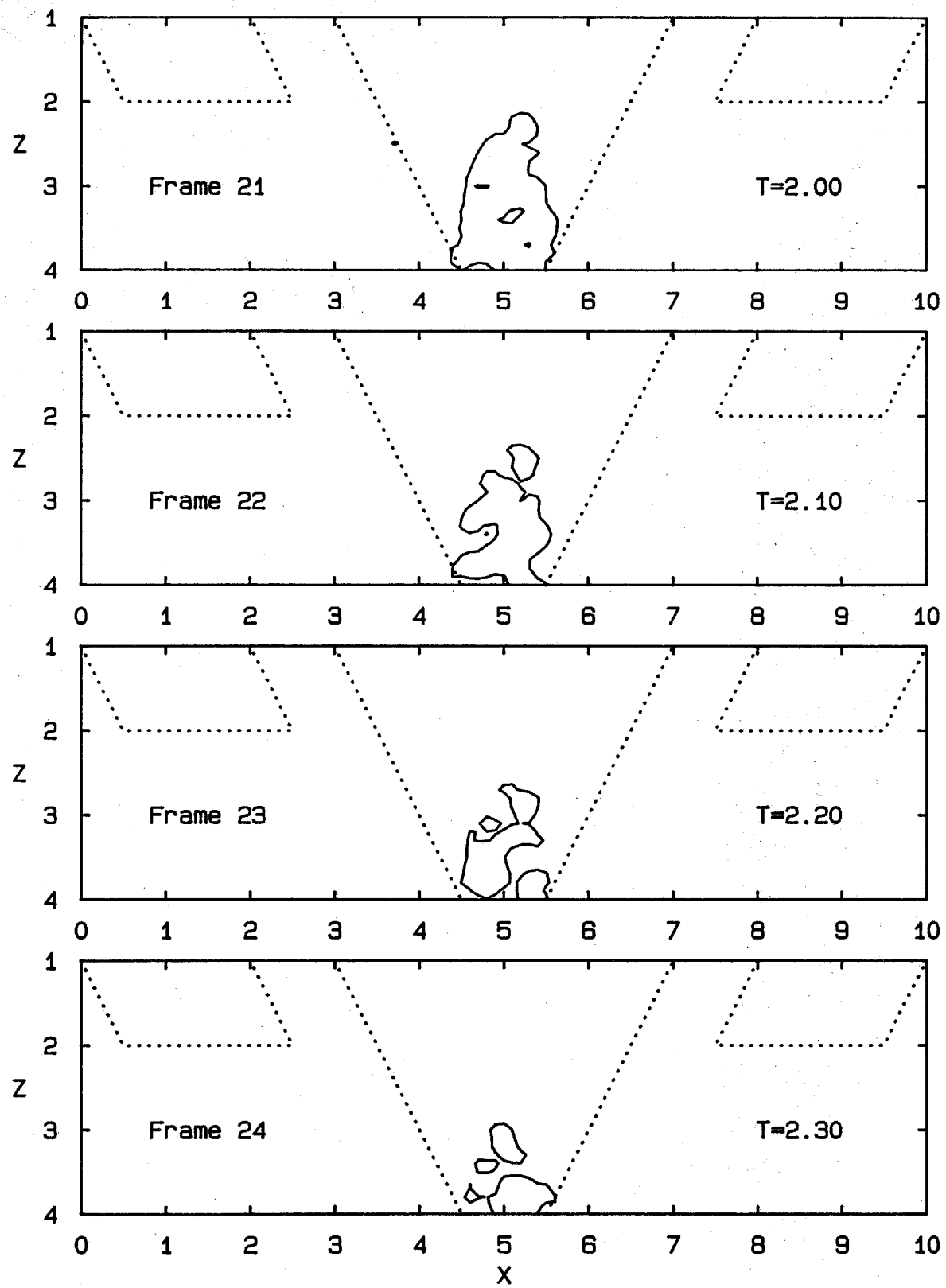

Fig. 6.10 Strain-rate Contours in the X-Z Plane; $\partial v/\partial y$

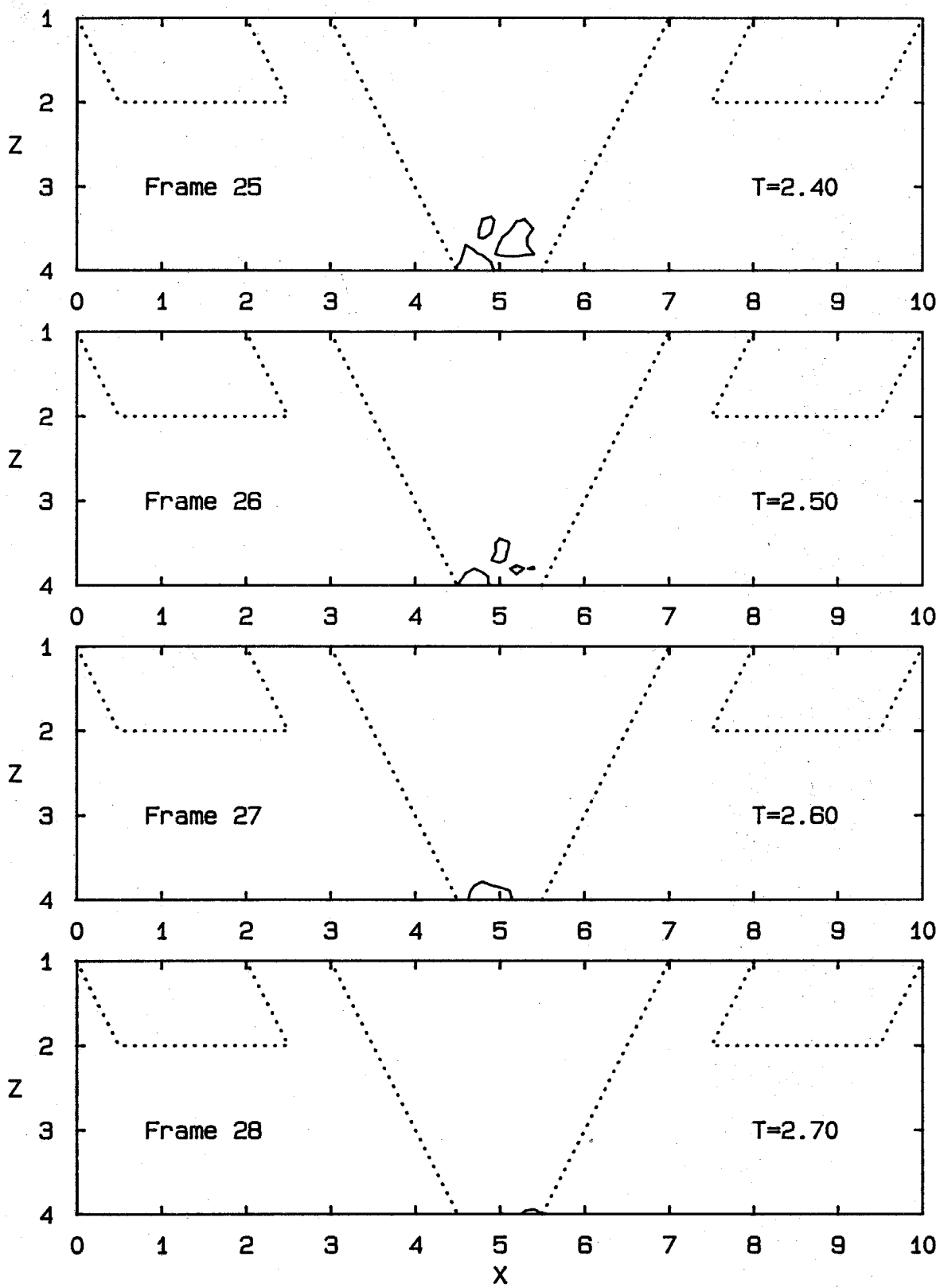

Fig. 6.10 Strain-rate Contours in the X-Z Plane; $\partial v/\partial y$

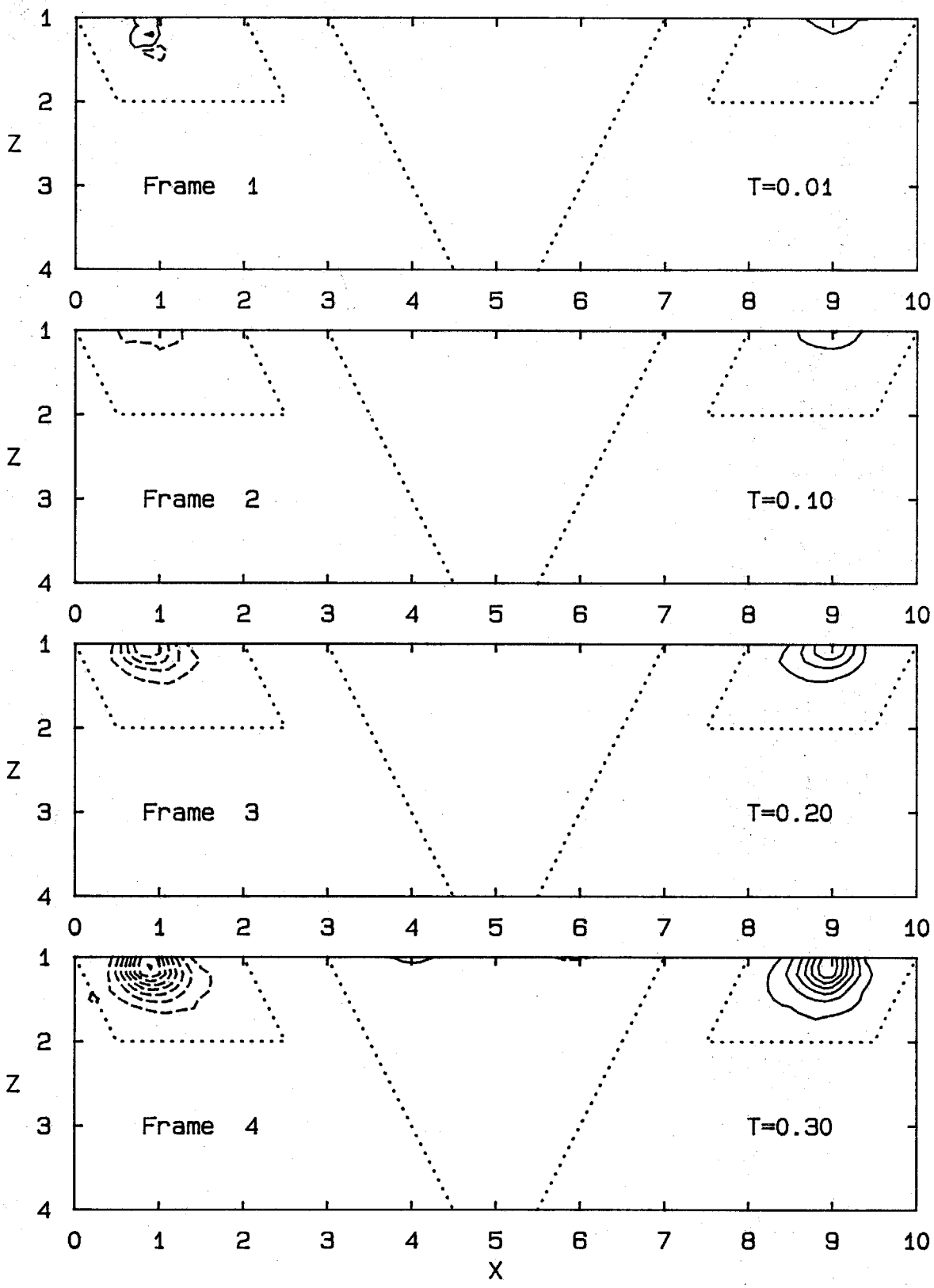

Fig. 6.11 Vorticity Contours in the X-Z Plane; ω_y

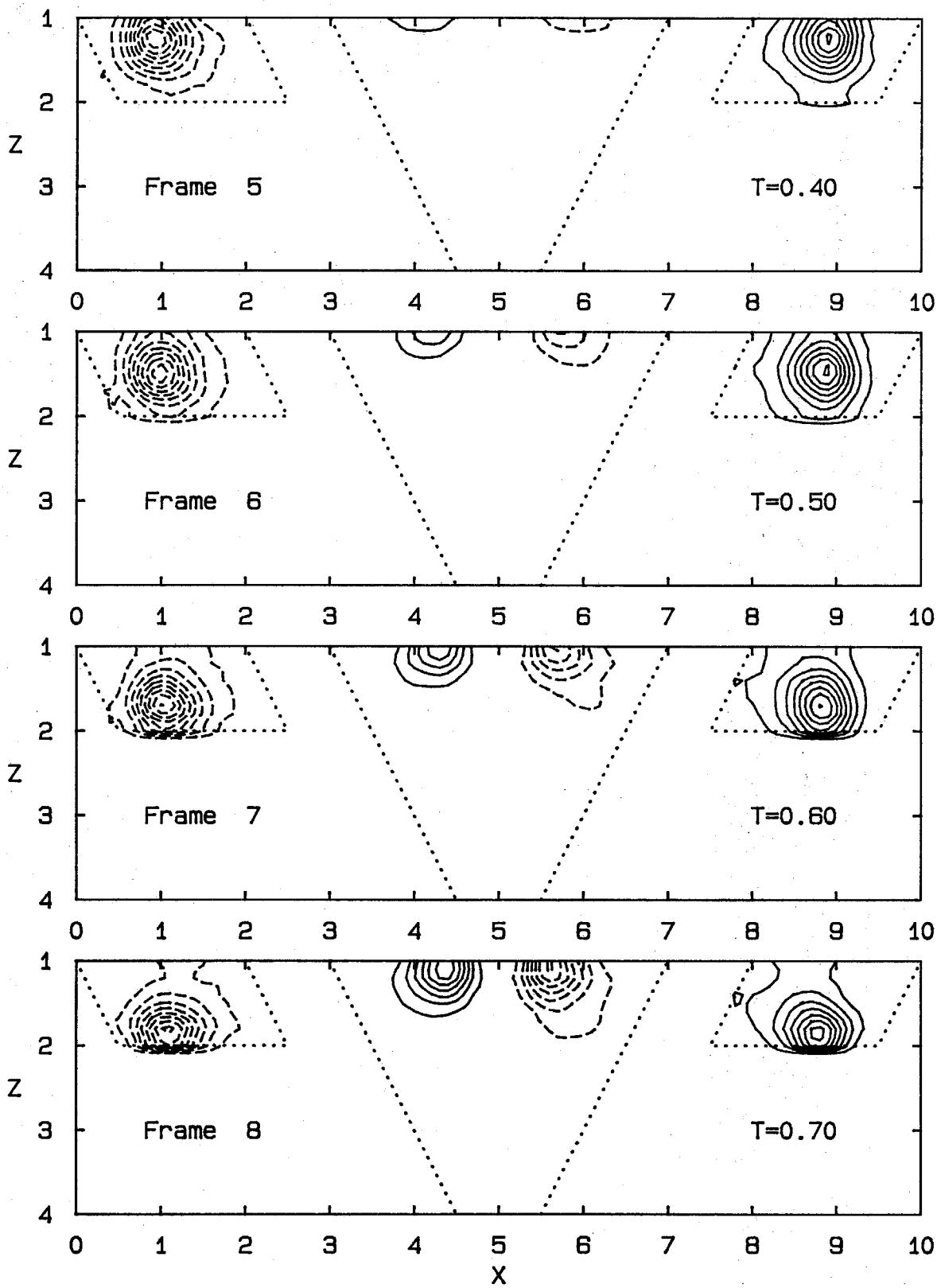

Fig. 6.11 Vorticity Contours in the X-Z Plane; ω_y

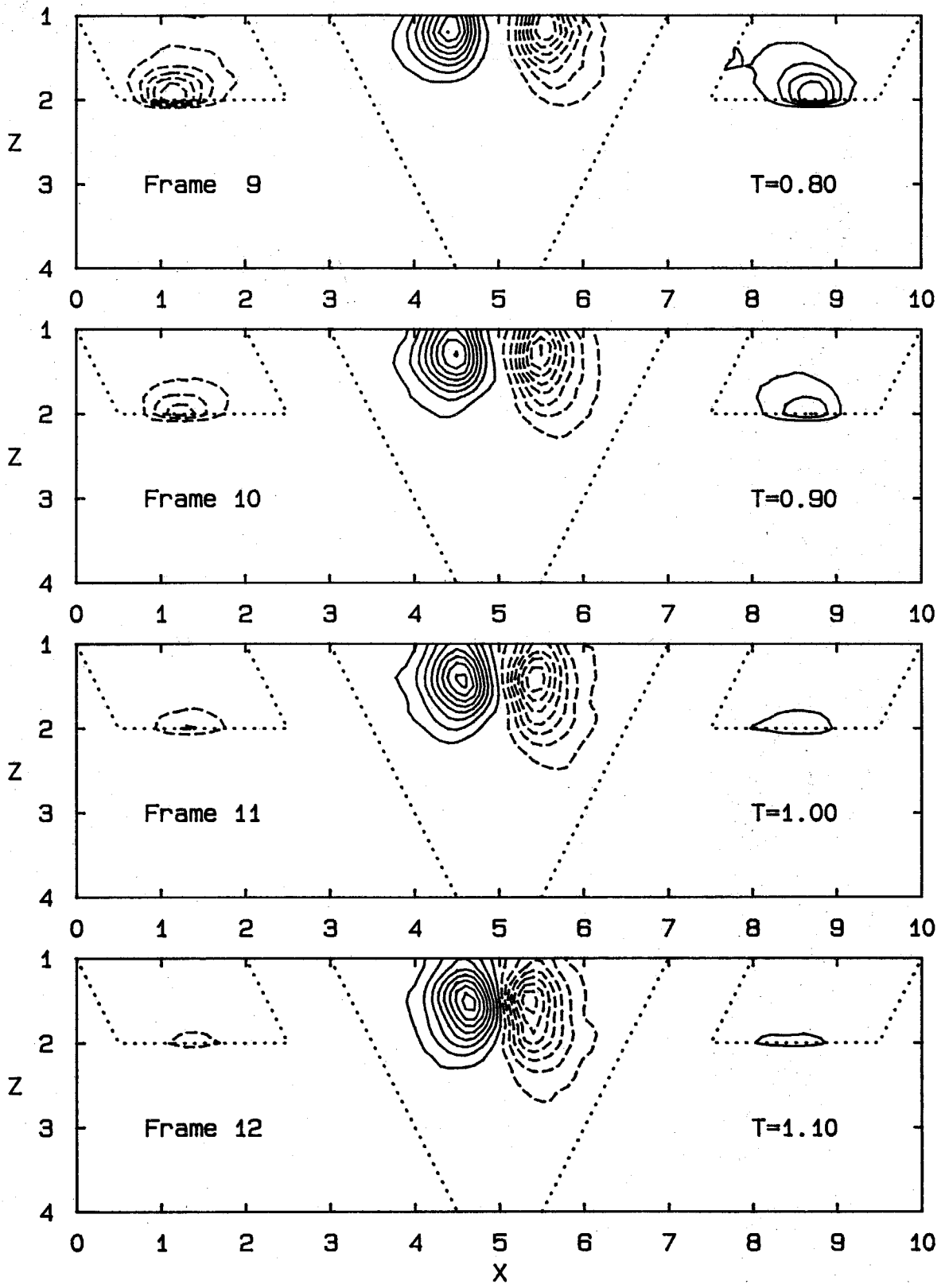

Fig. 6.11 Vorticity Contours in the X-Z Plane; ω_y

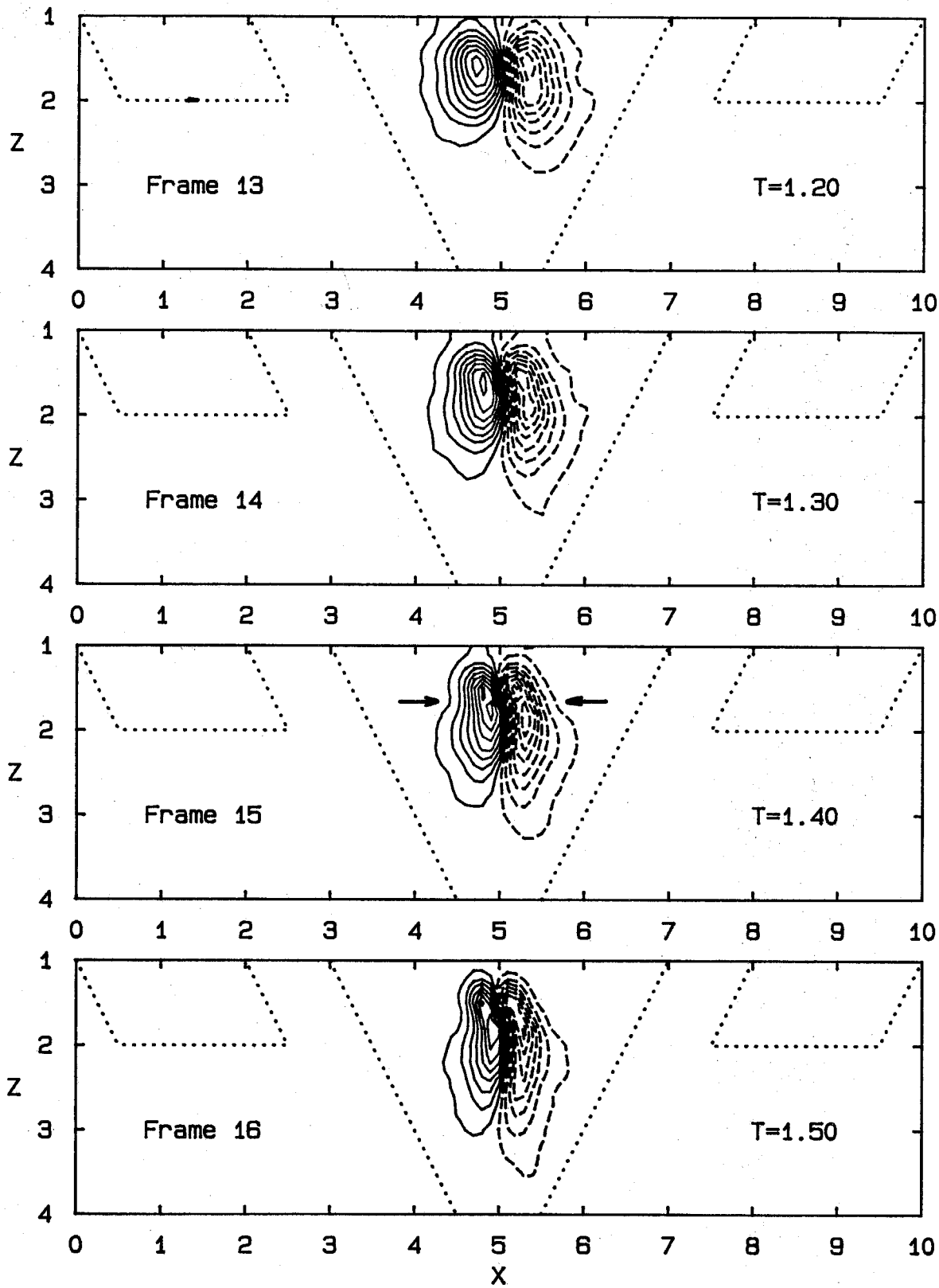

Fig. 6.11 Vorticity Contours in the X-Z Plane; ω_y

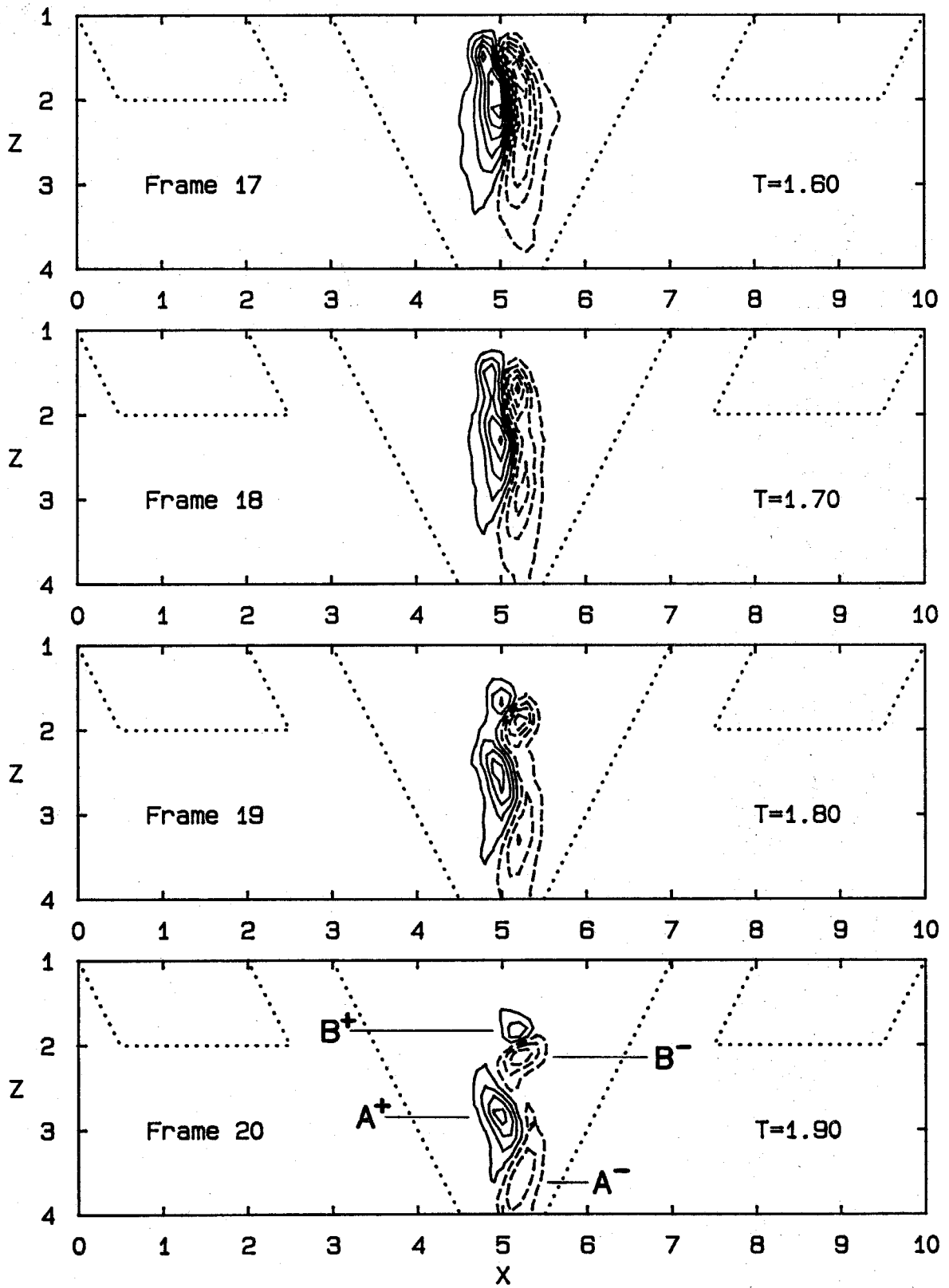

Fig. 6.11 Vorticity Contours in the X-Z Plane; ω_y

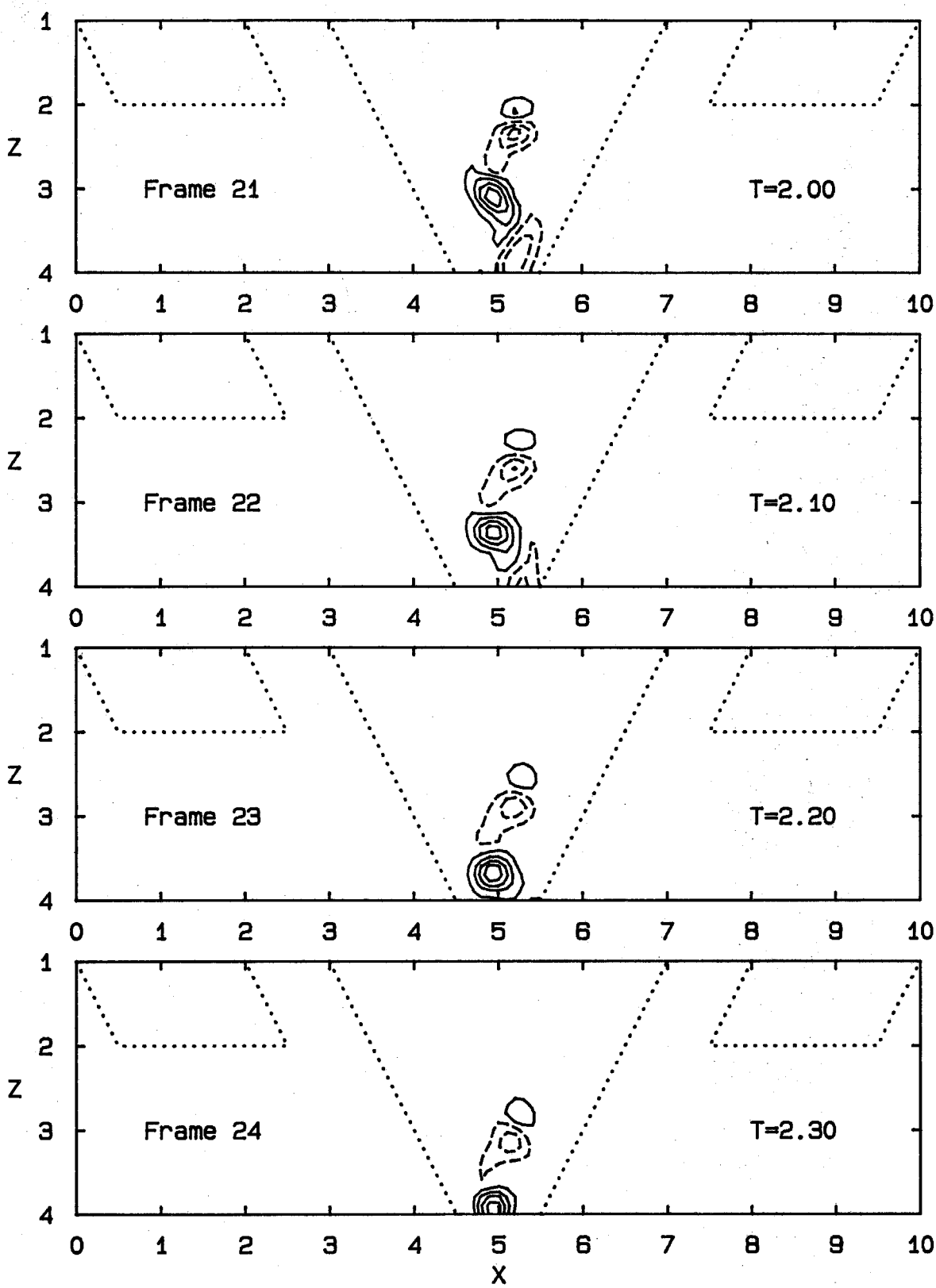

Fig. 6.11 Vorticity Contours in the X-Z Plane; ω_y

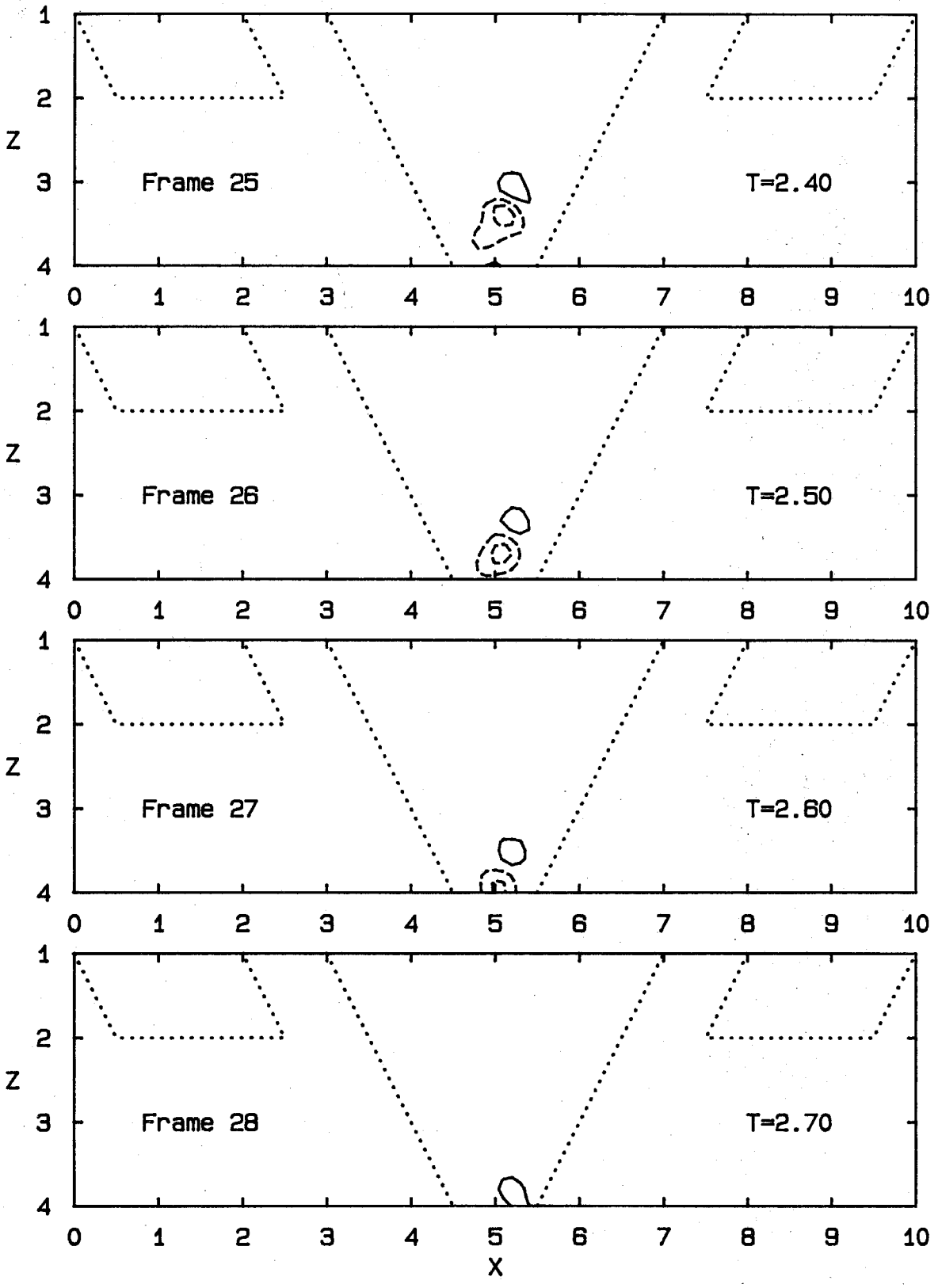

Fig. 6.11 Vorticity Contours in the X-Z Plane; ω_y

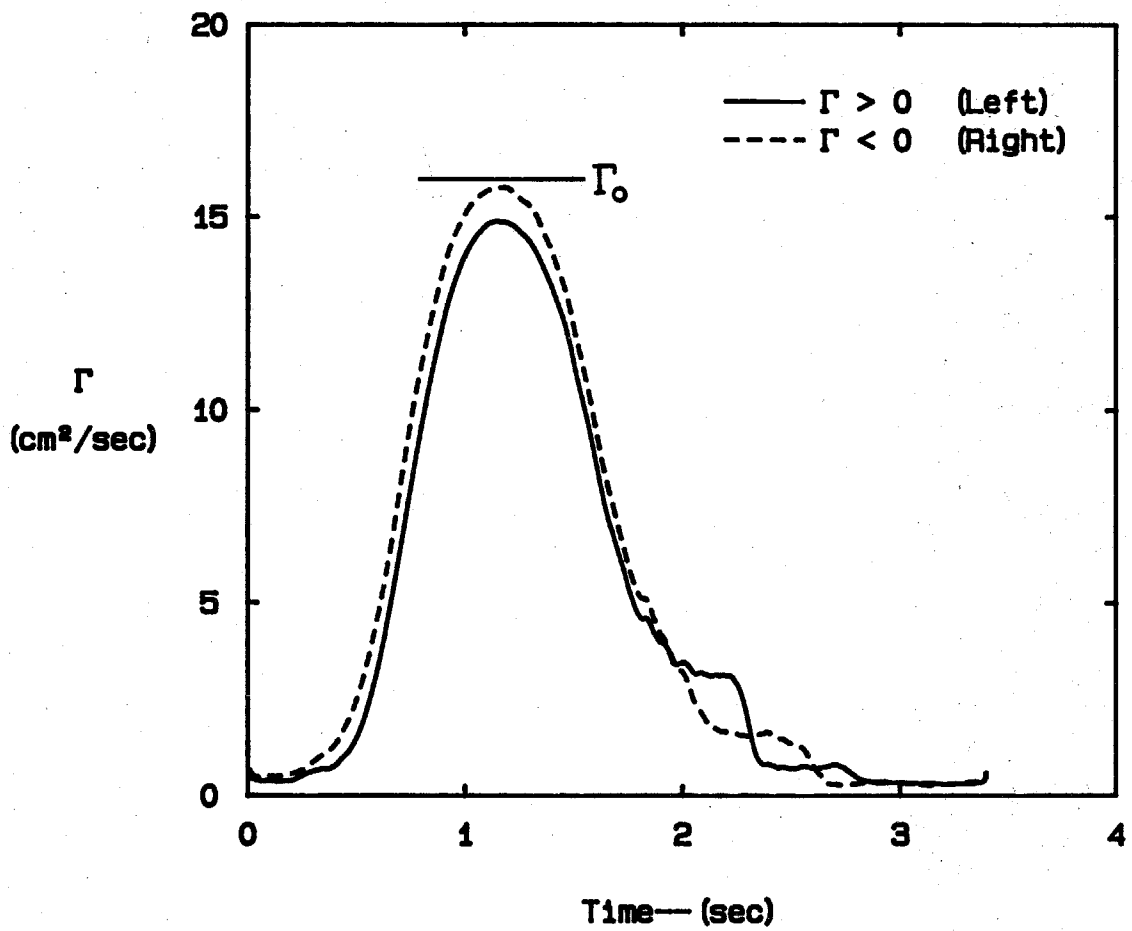

Fig. 6.12 Circulation in Central Measurement Region

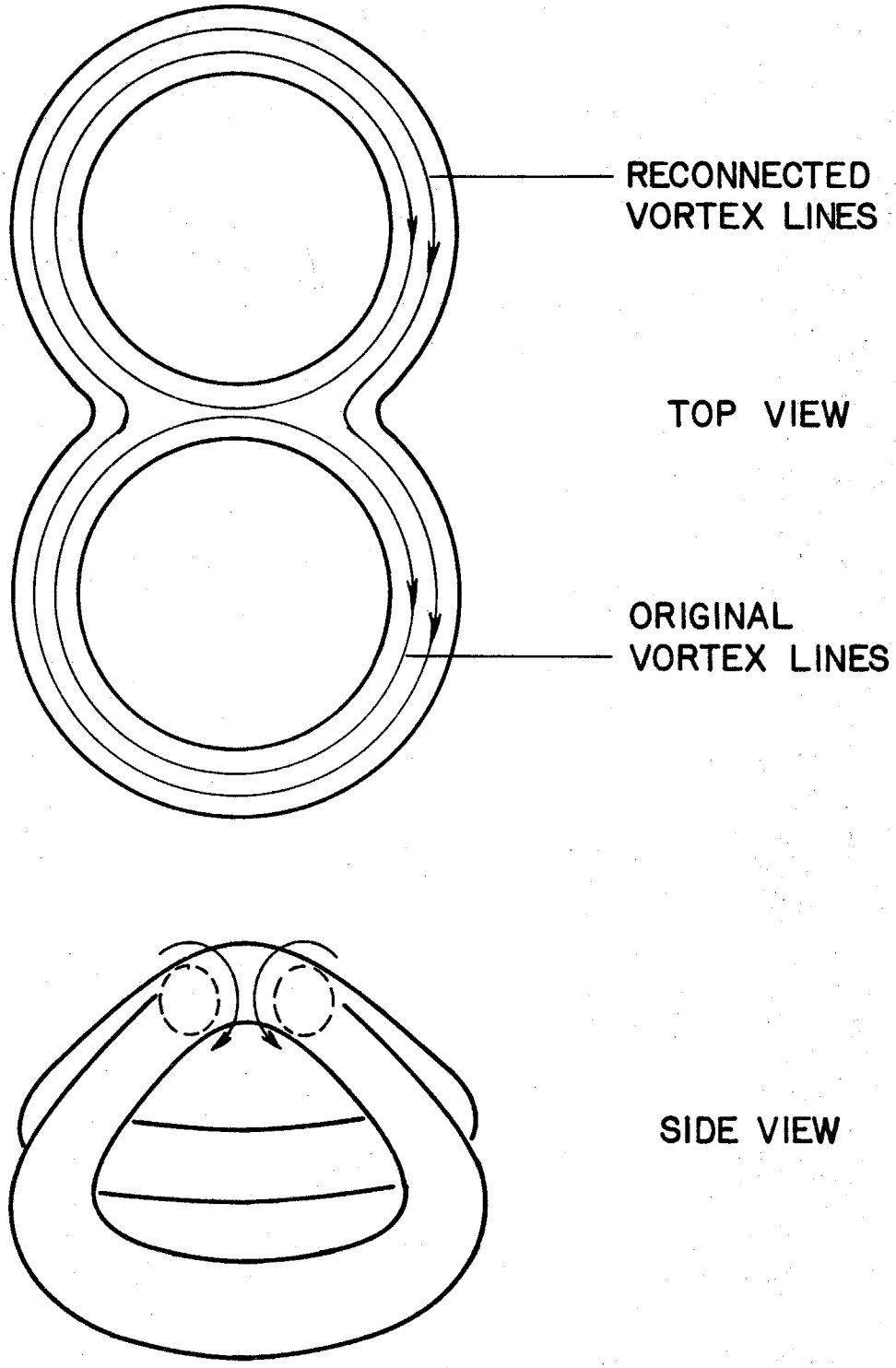

Fig. 6.13 Geometry of Reconnected Vorticity Field

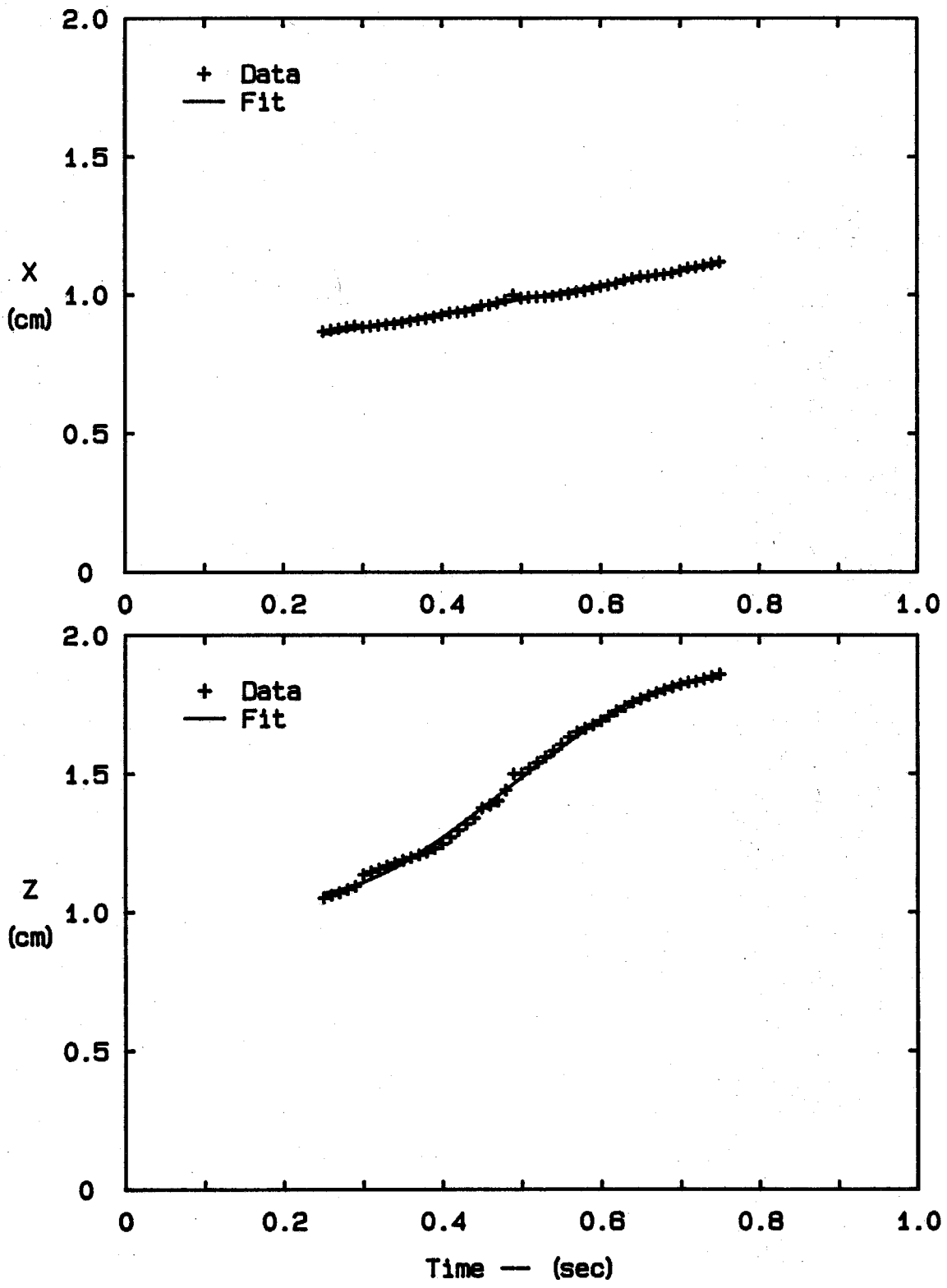

Fig. A.1 Core Trajectory Fit; Left Side

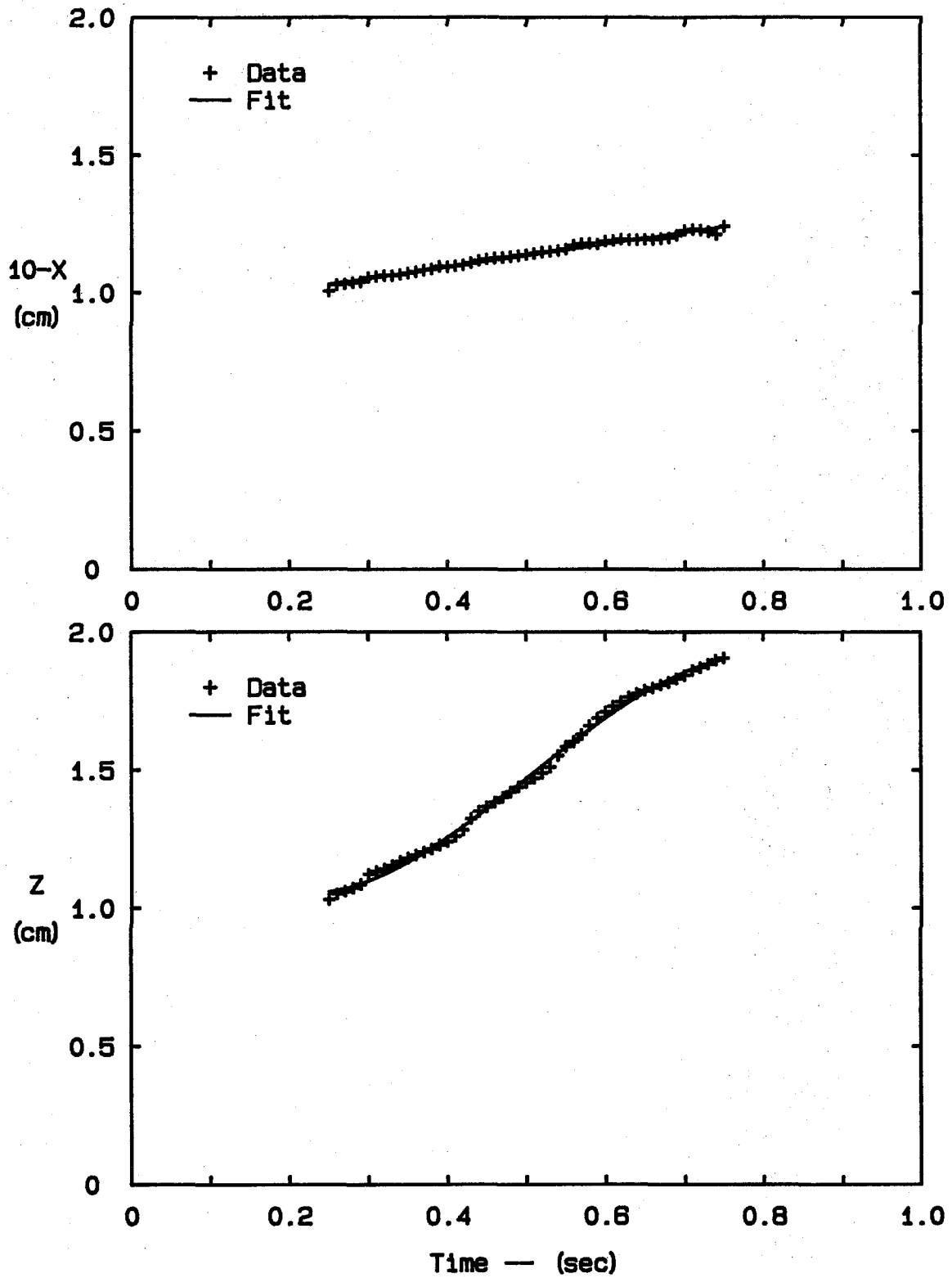

Fig. A.2 Core Trajectory Fit; Right Side

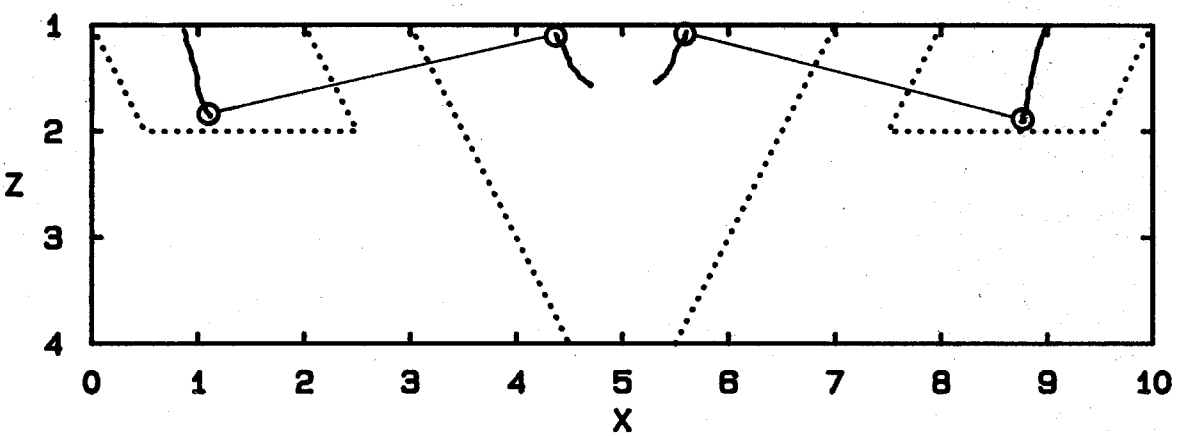

Fig. A.3 Paths of Vortex Cores

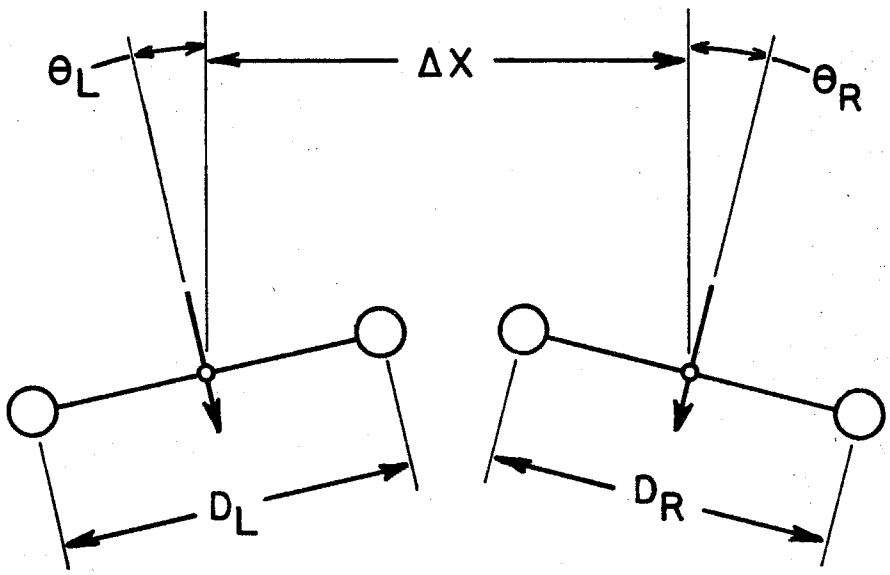

D_L=33.6 MM D_R=32.7 MM

θ_L=12.5° θ_R=14.1°

ΔX=44.6 MM

Fig. A.4 Recommended Starting Conditions

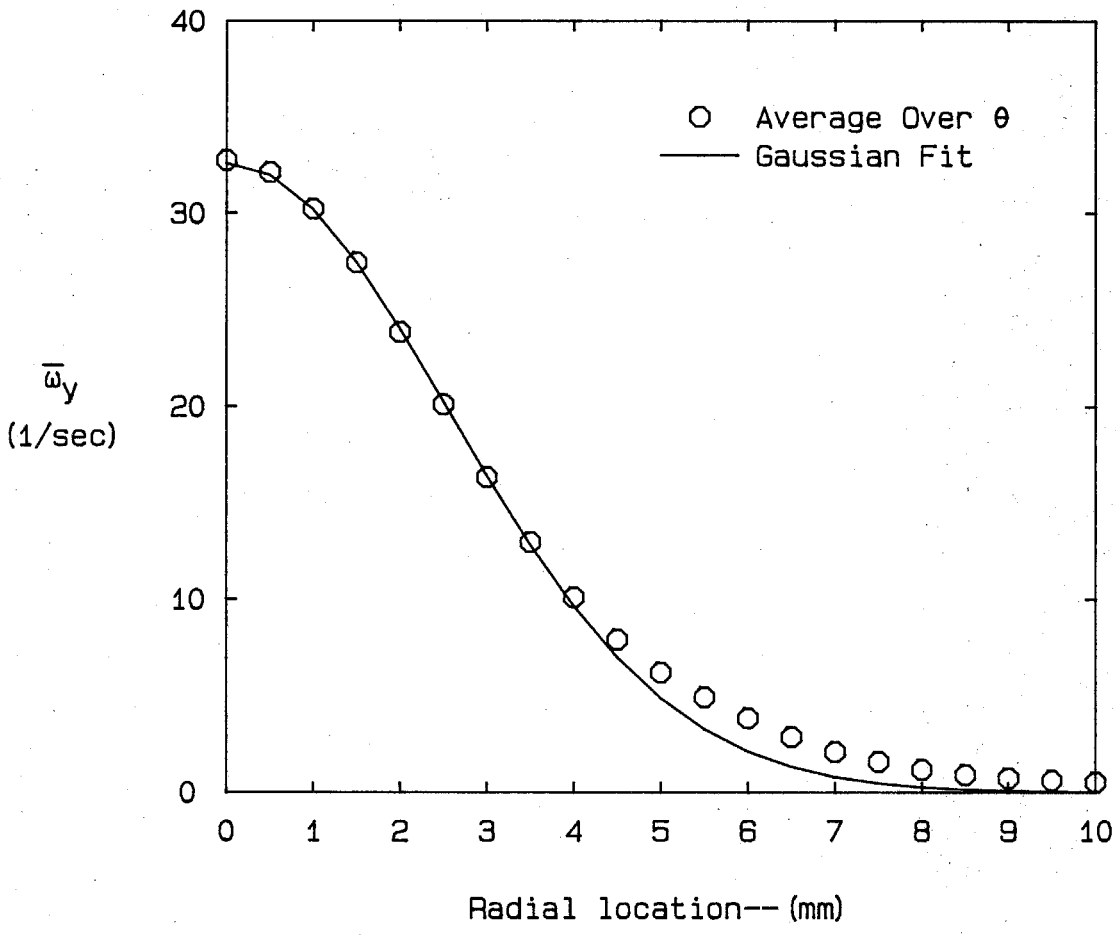

Fig. A.5 Averaged Vorticity Distribution; Left Side

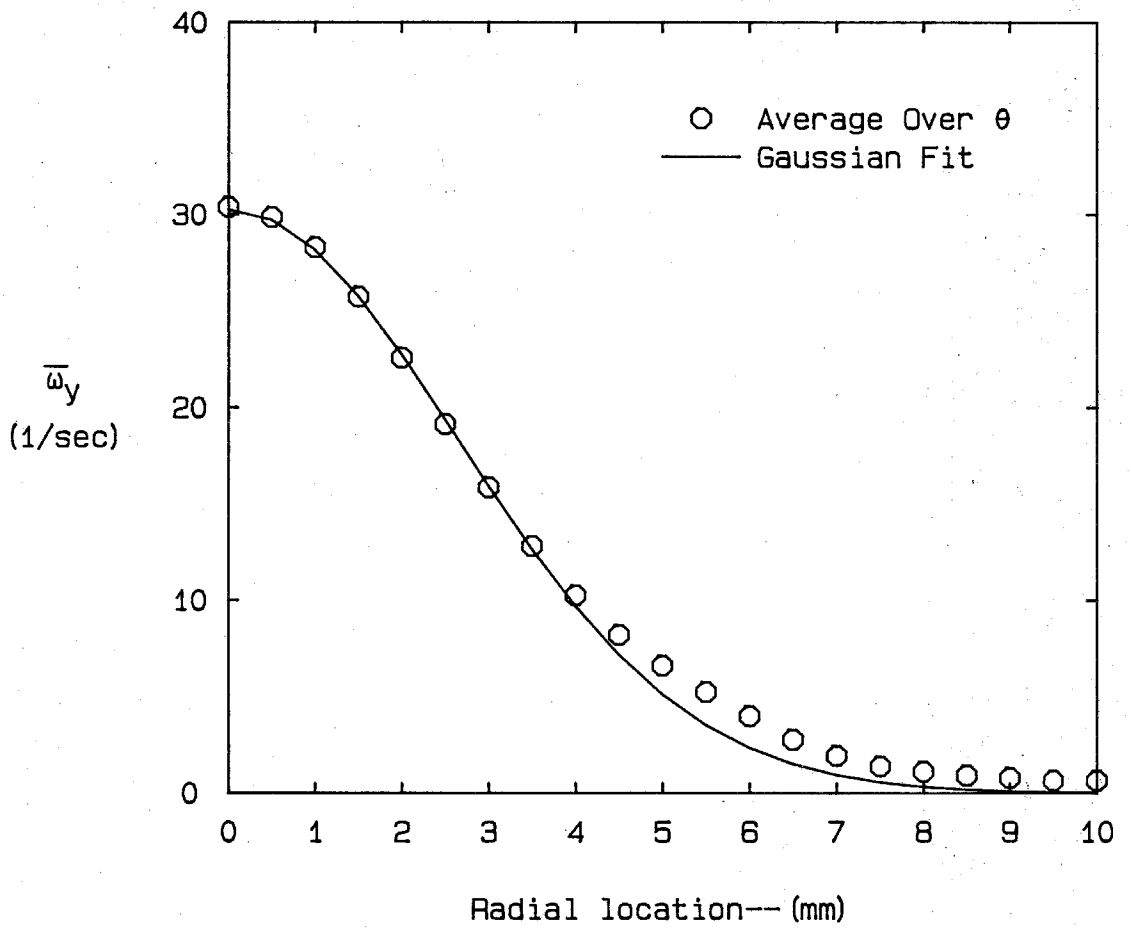

Fig. A.6 Averaged Vorticity Distribution; Right Side

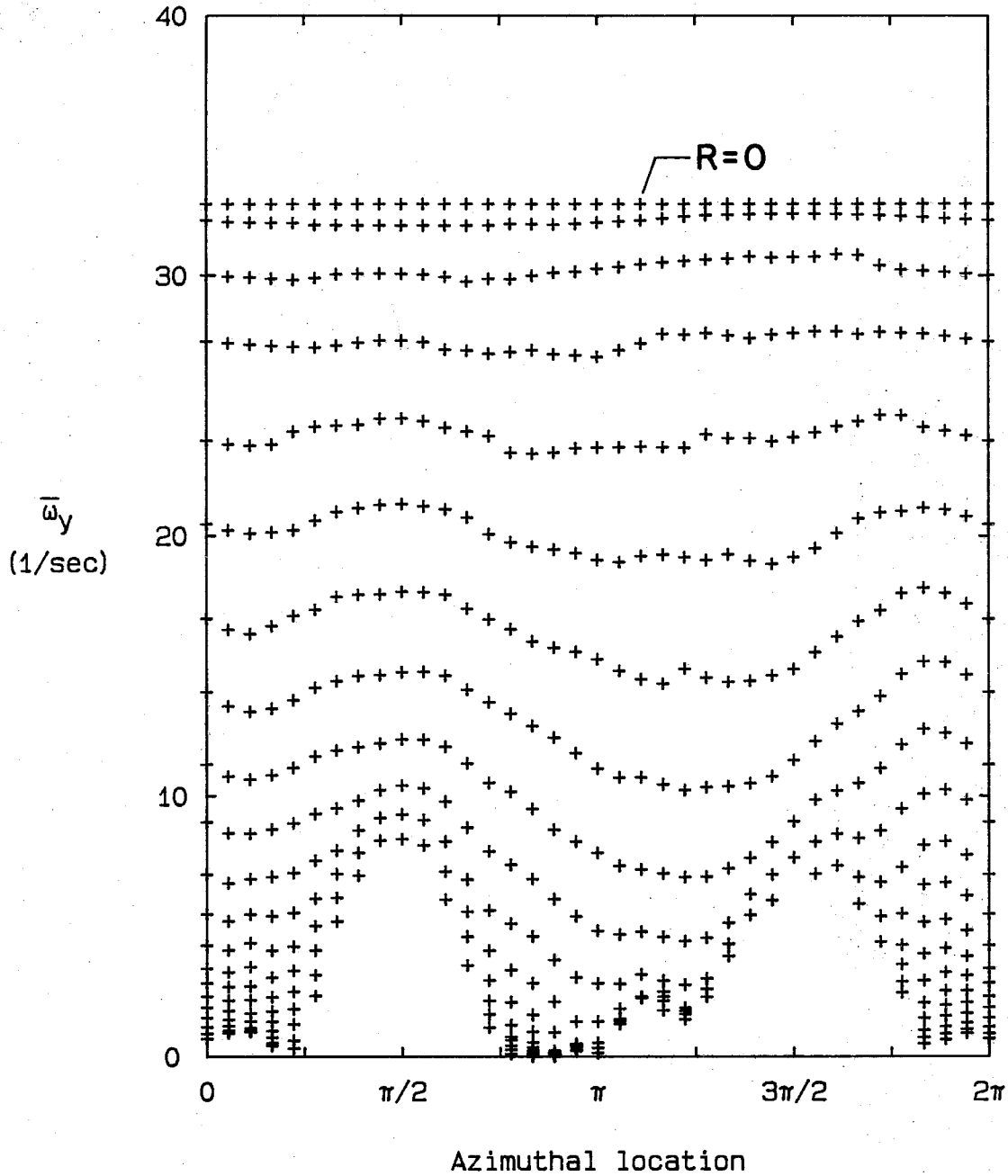

Fig. A.7 Detailed Vorticity Distribution; Left Side

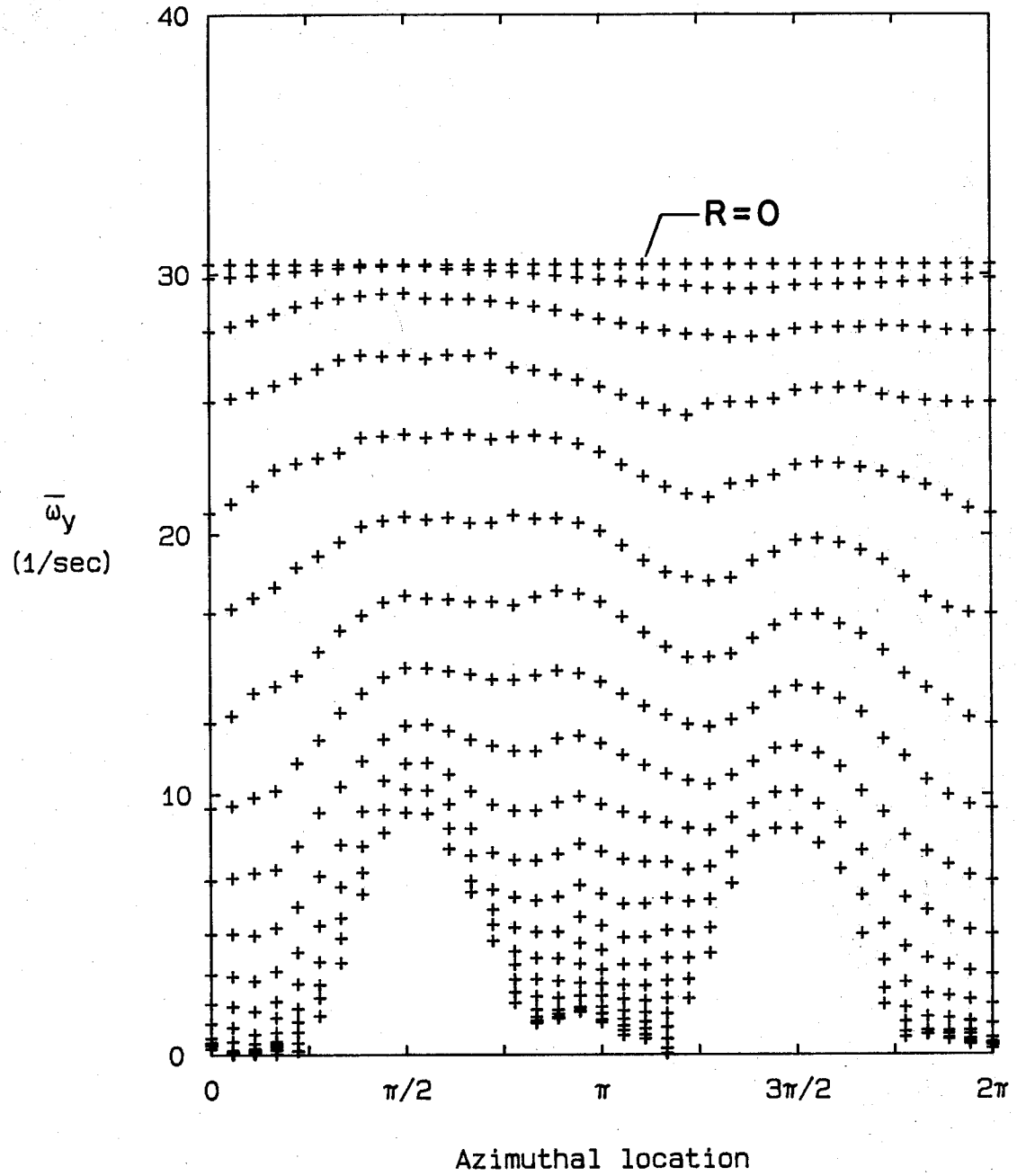

Fig. A.8 Detailed Vorticity Distribution; Right Side

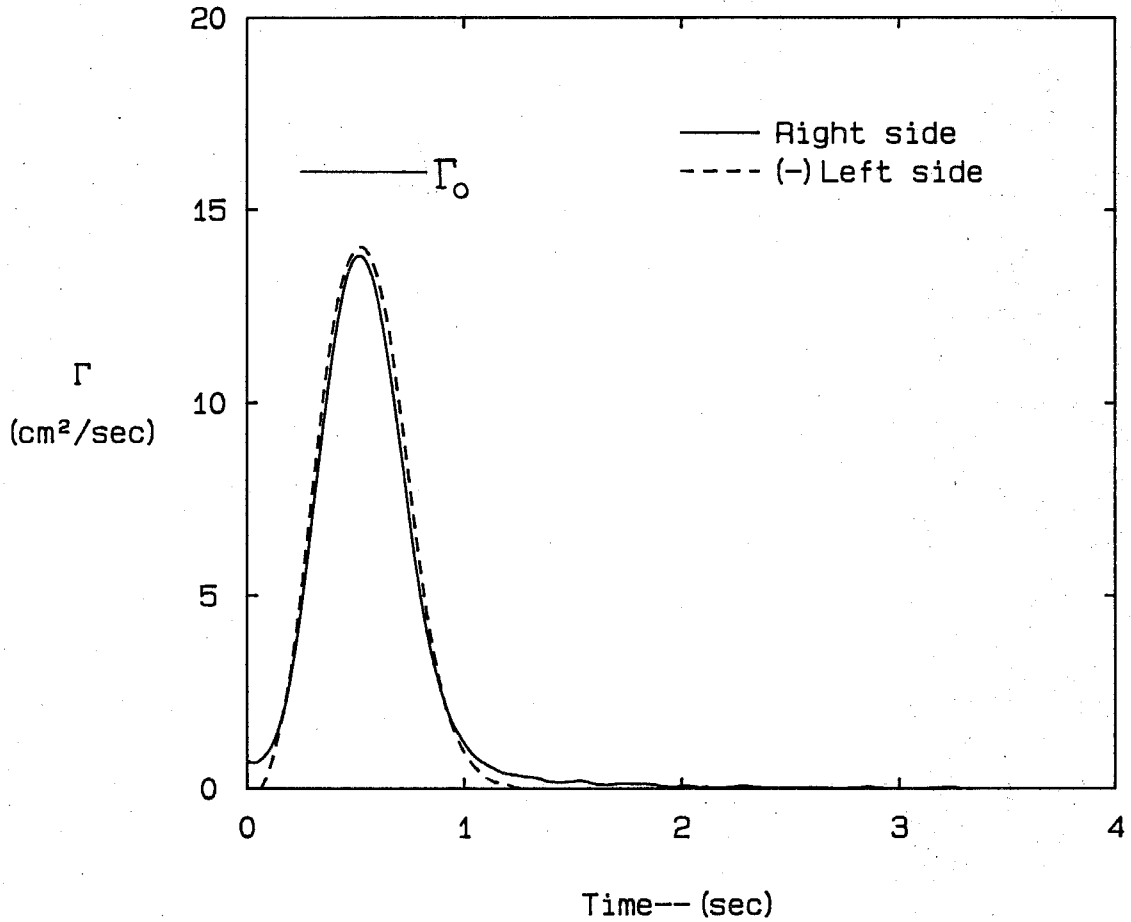

Fig. A.9 Circulation in Wings

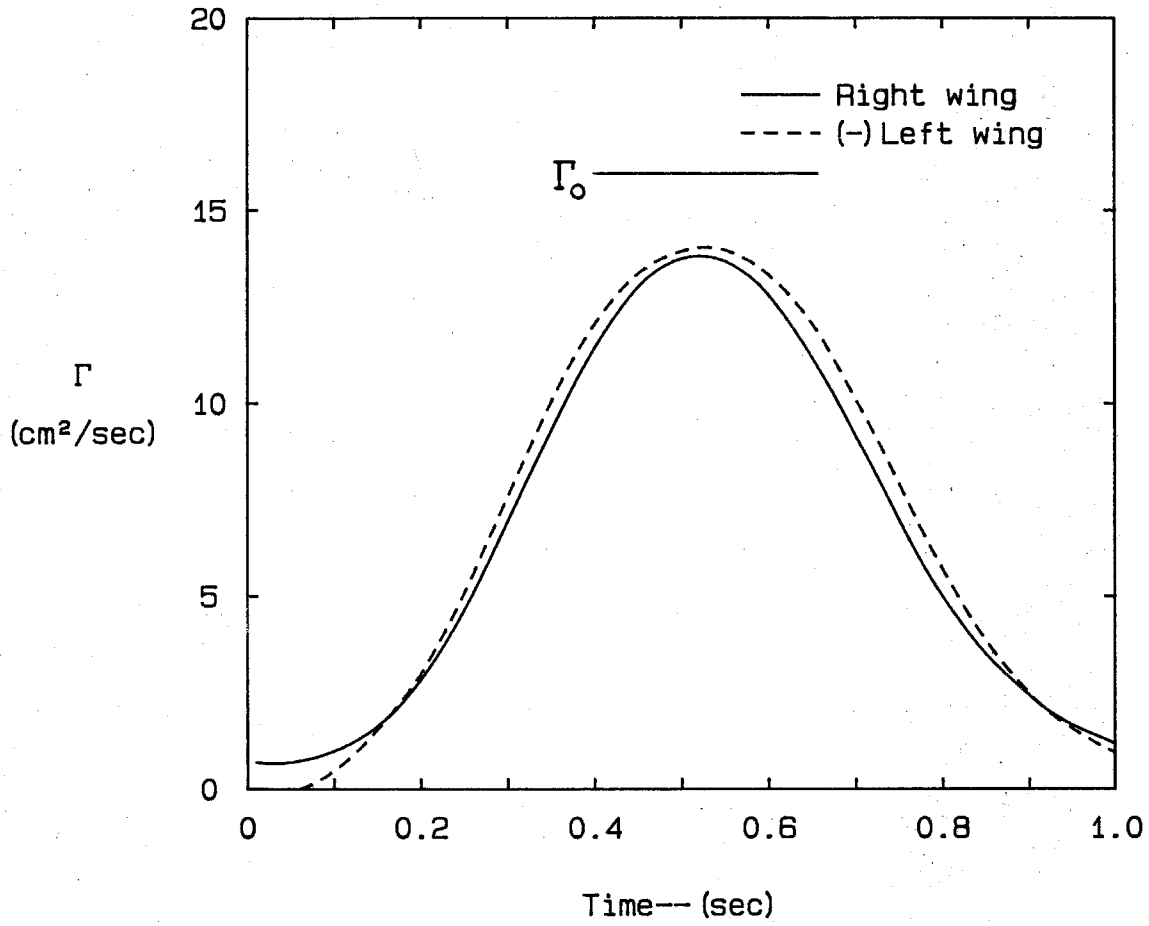

Fig. A.10 Circulation in Wings; Expanded Scale

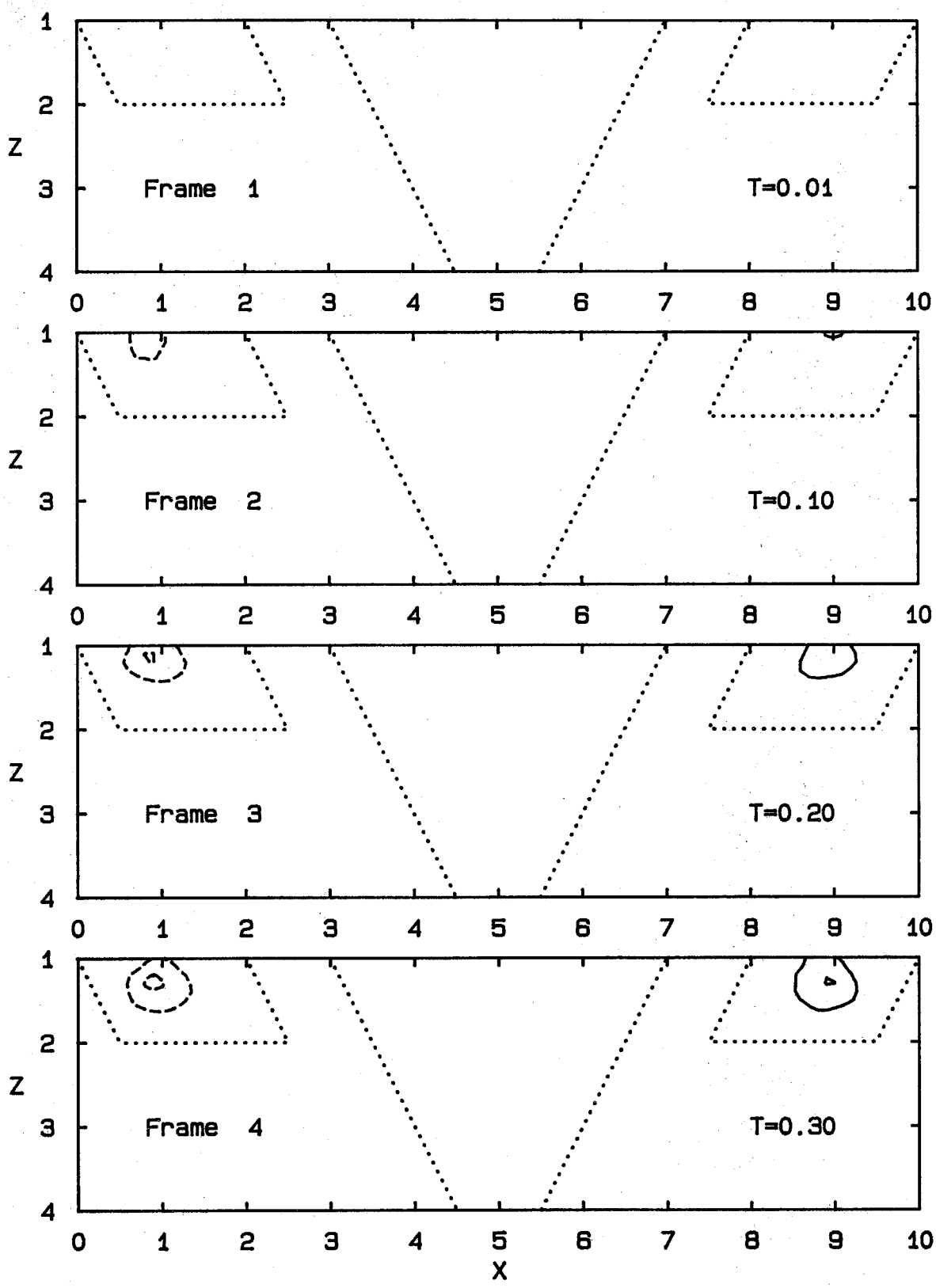

Fig. B.1 Components of Vorticity Equation; $\partial\omega_y/\partial t$

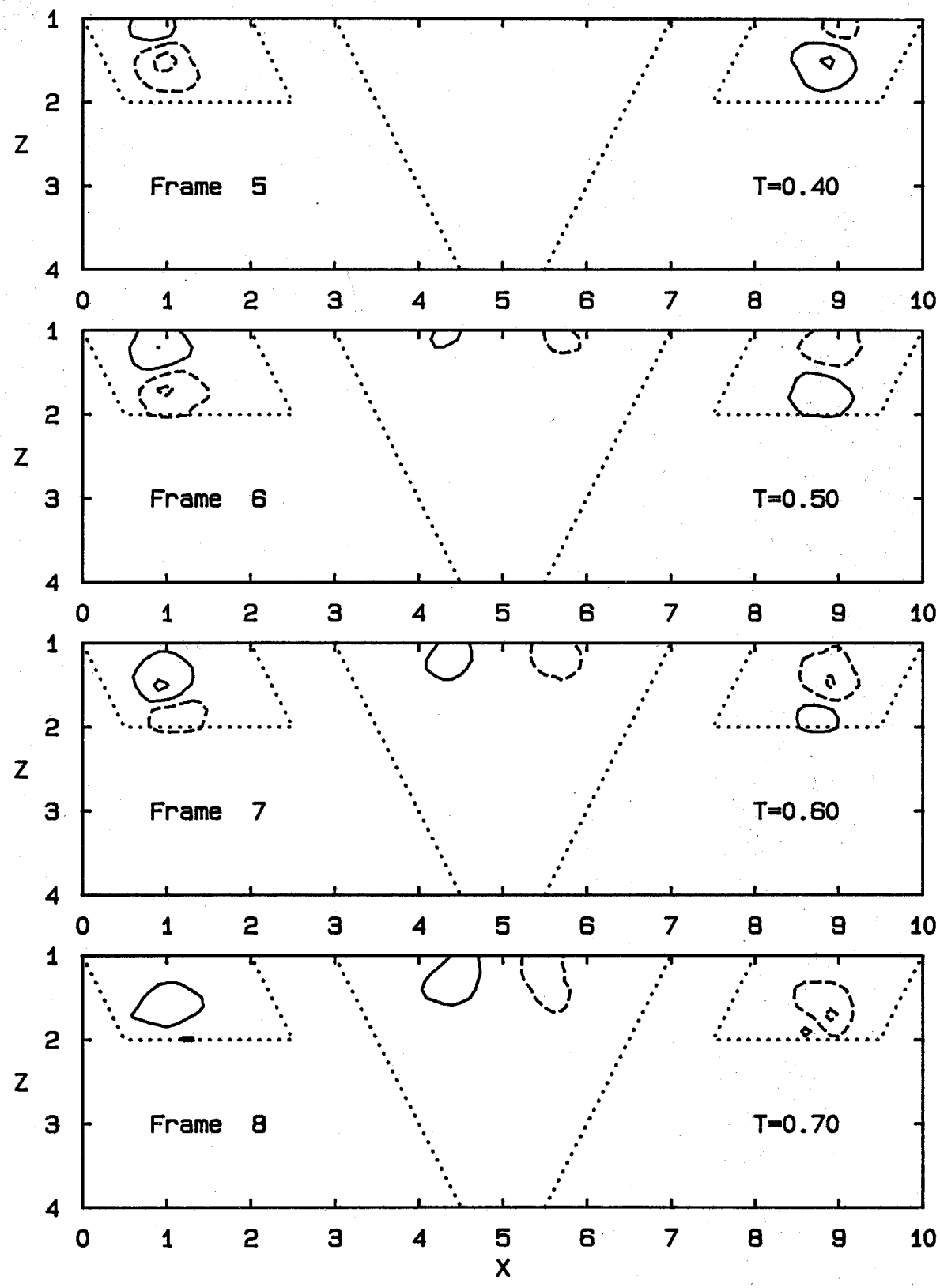

Fig. B.1 Components of Vorticity Equation; $\partial\omega_y/\partial t$

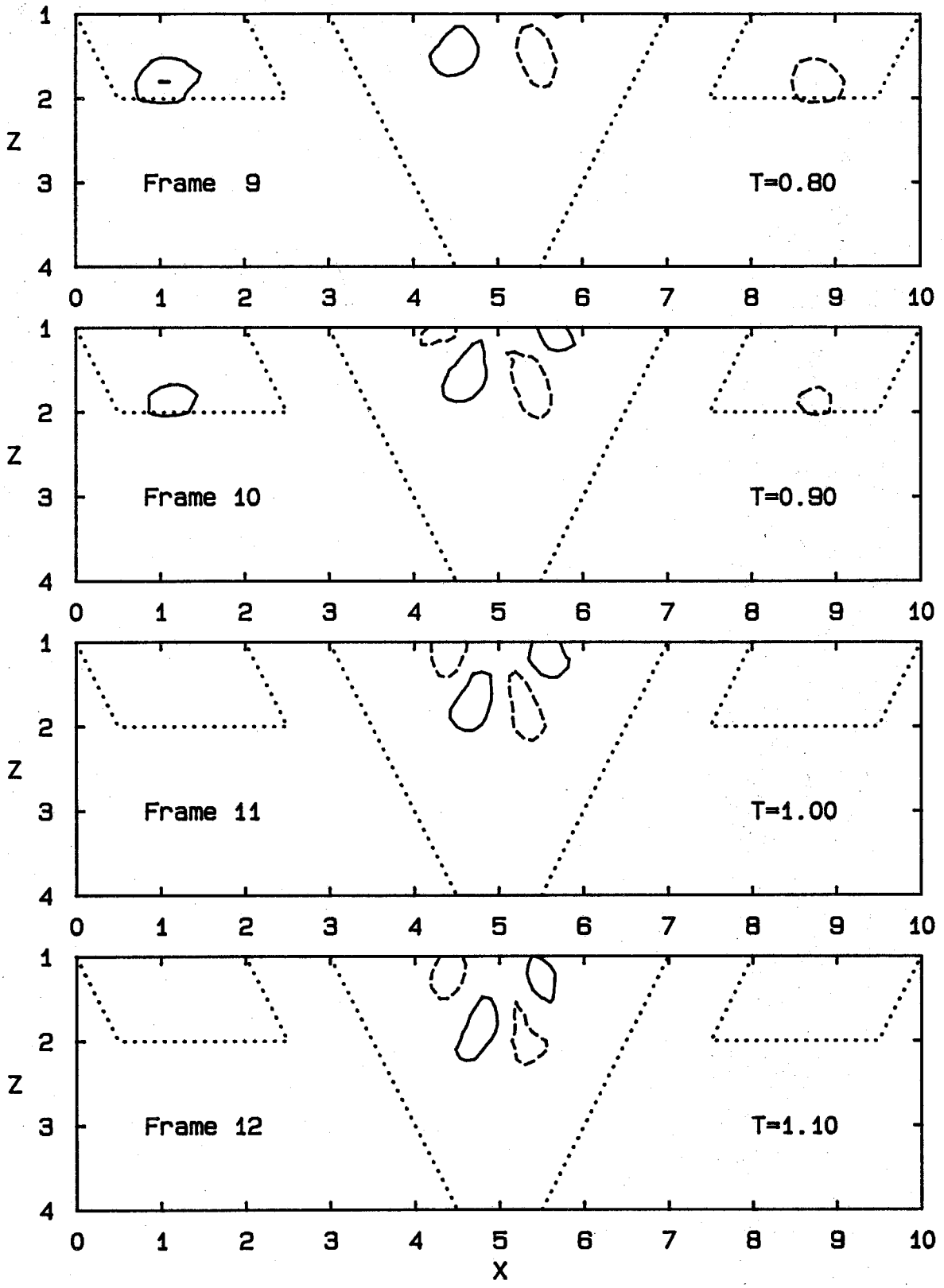

Fig. B.1 Components of Vorticity Equation; $\partial\omega_y/\partial t$

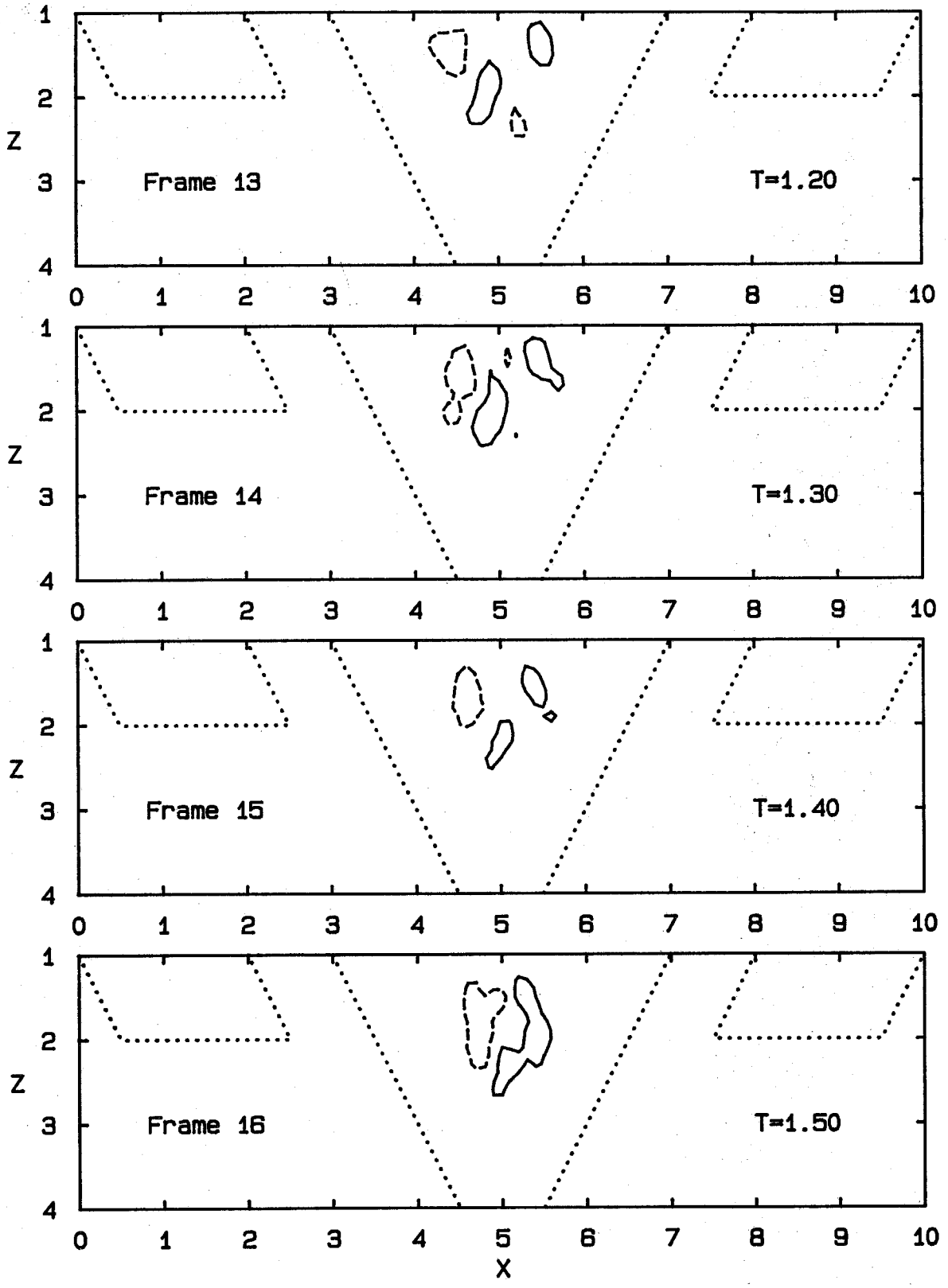

Fig. B.1 Components of Vorticity Equation; $\partial\omega_y/\partial t$

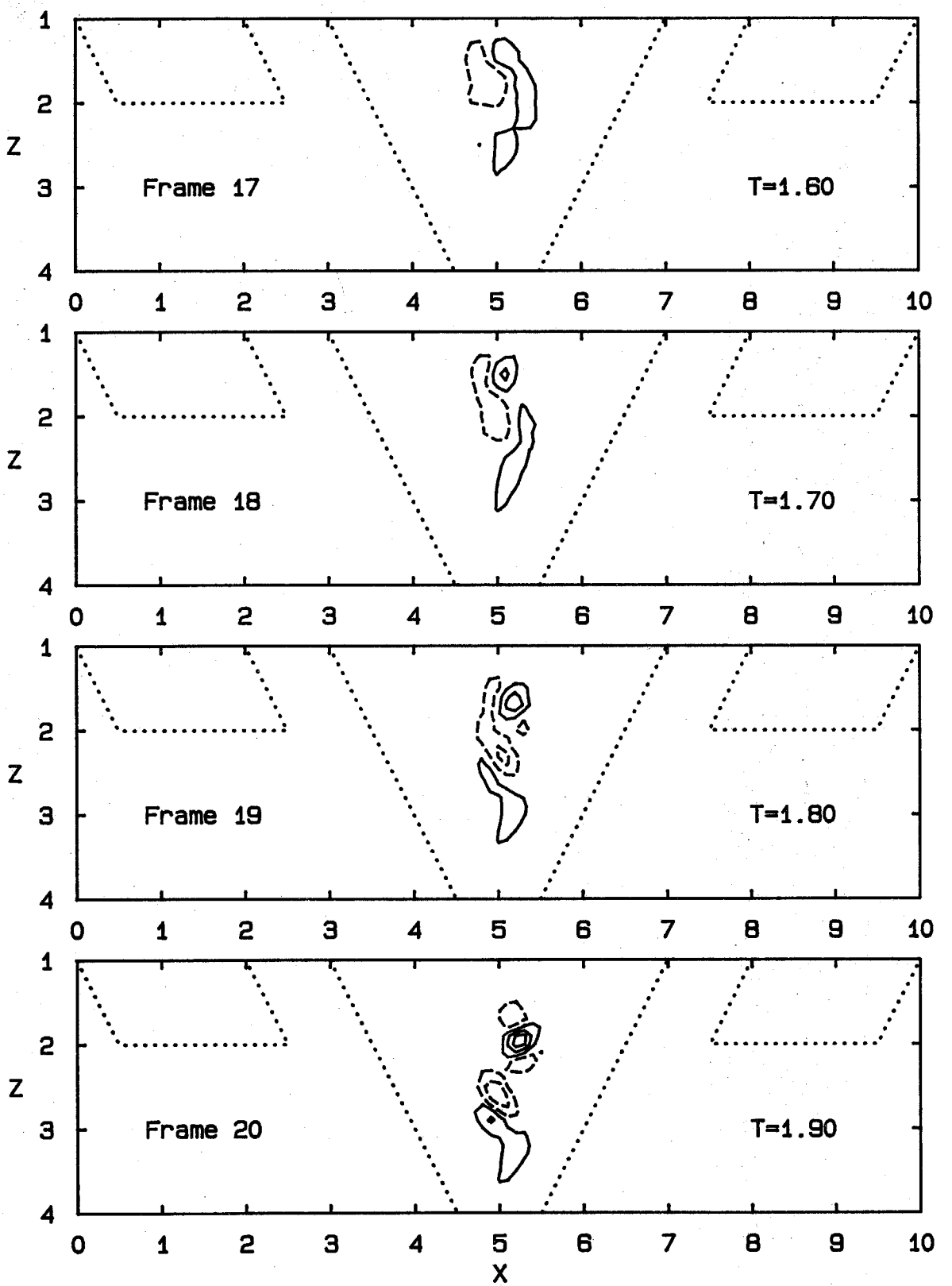

Fig. B.1 Components of Vorticity Equation; $\partial\omega_y/\partial t$

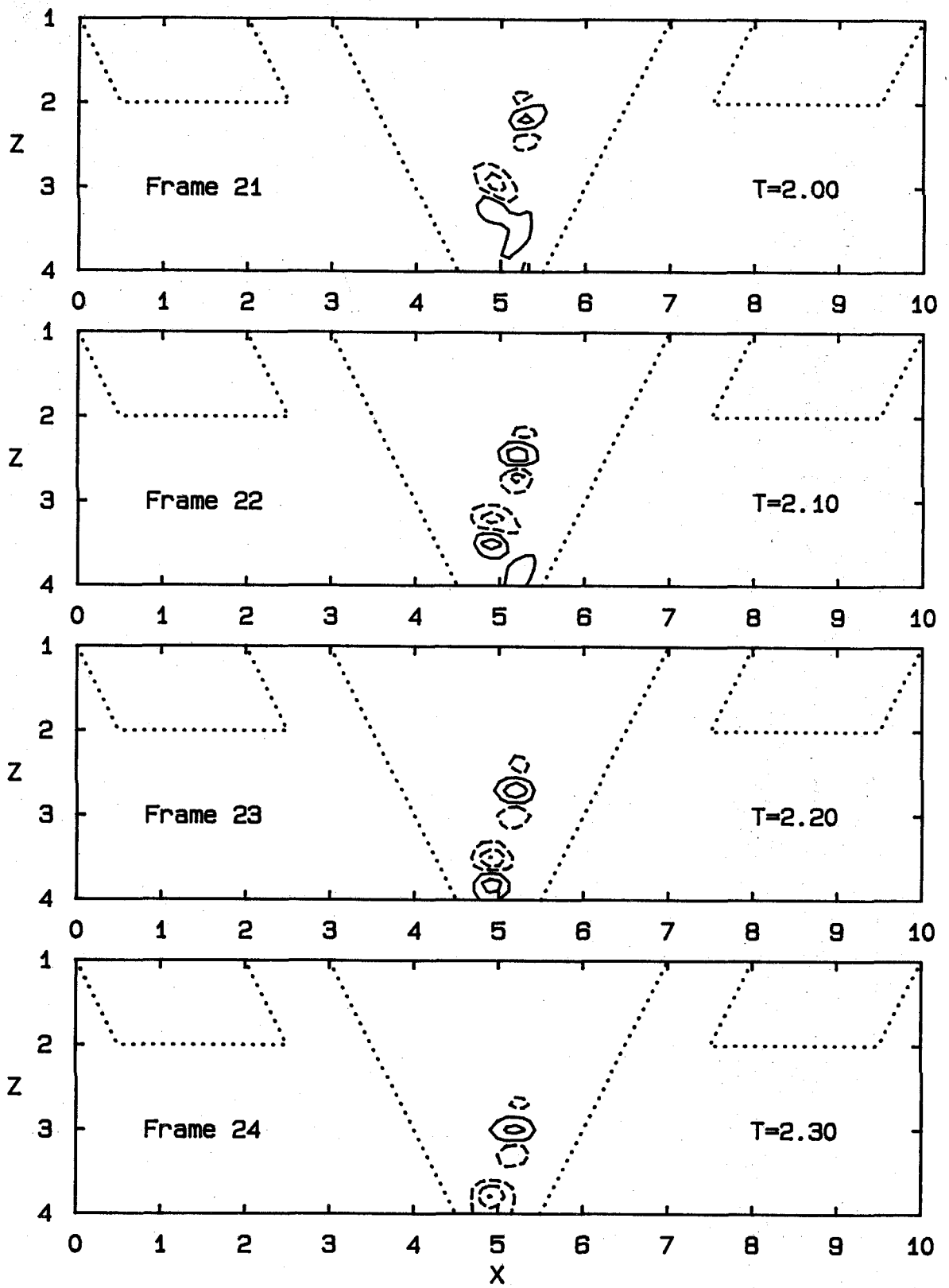

Fig. B.1 Components of Vorticity Equation; $\partial\omega_y/\partial t$

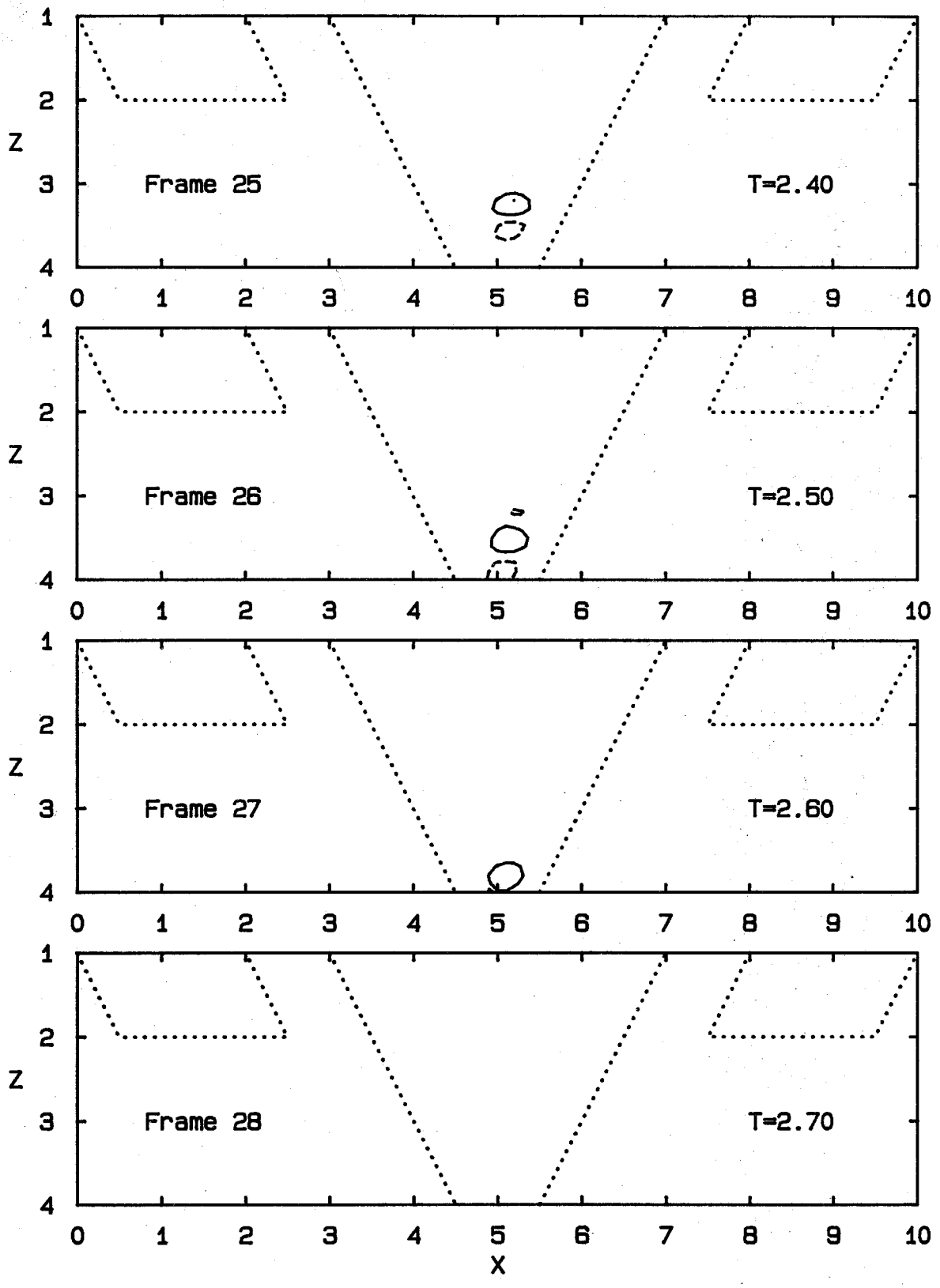

Fig. B.1 Components of Vorticity Equation; $\partial\omega_y/\partial t$

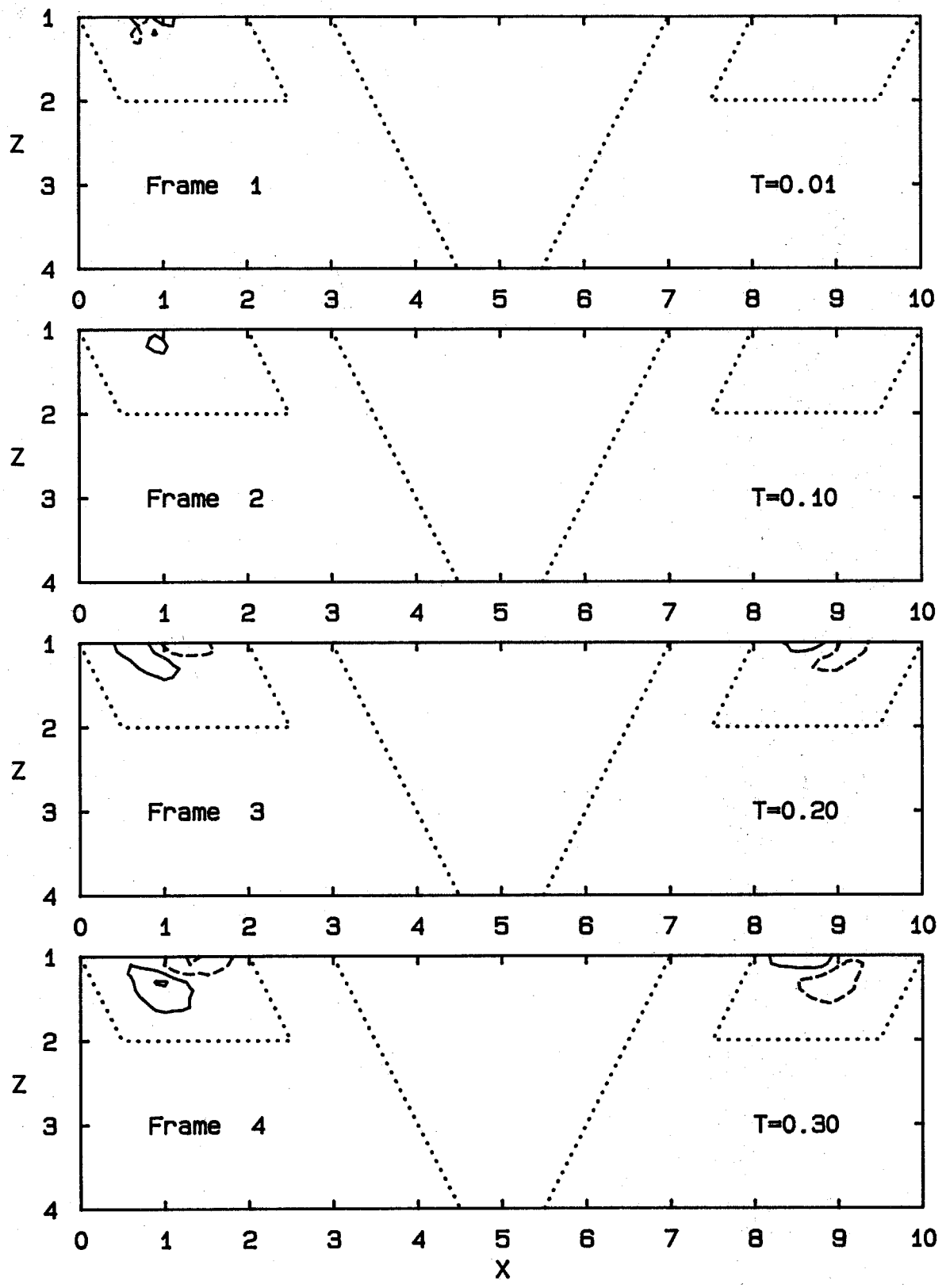

Fig. B.2 Components of Vorticity Equation; $(\vec{u}\cdot\nabla)\,\omega_y$

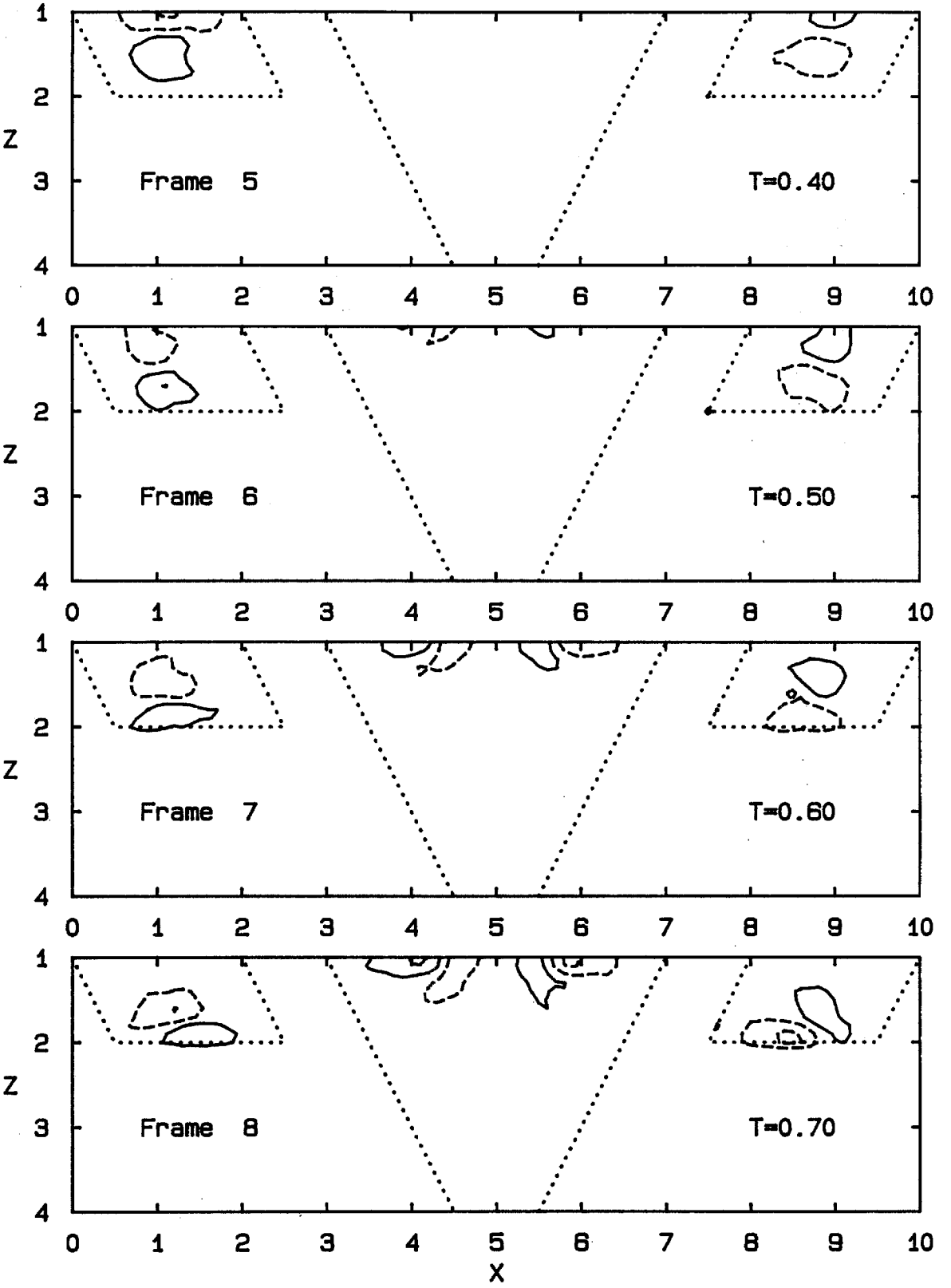

Fig. B.2 Components of Vorticity Equation; $(\vec{u}\cdot\nabla)\,\omega_y$

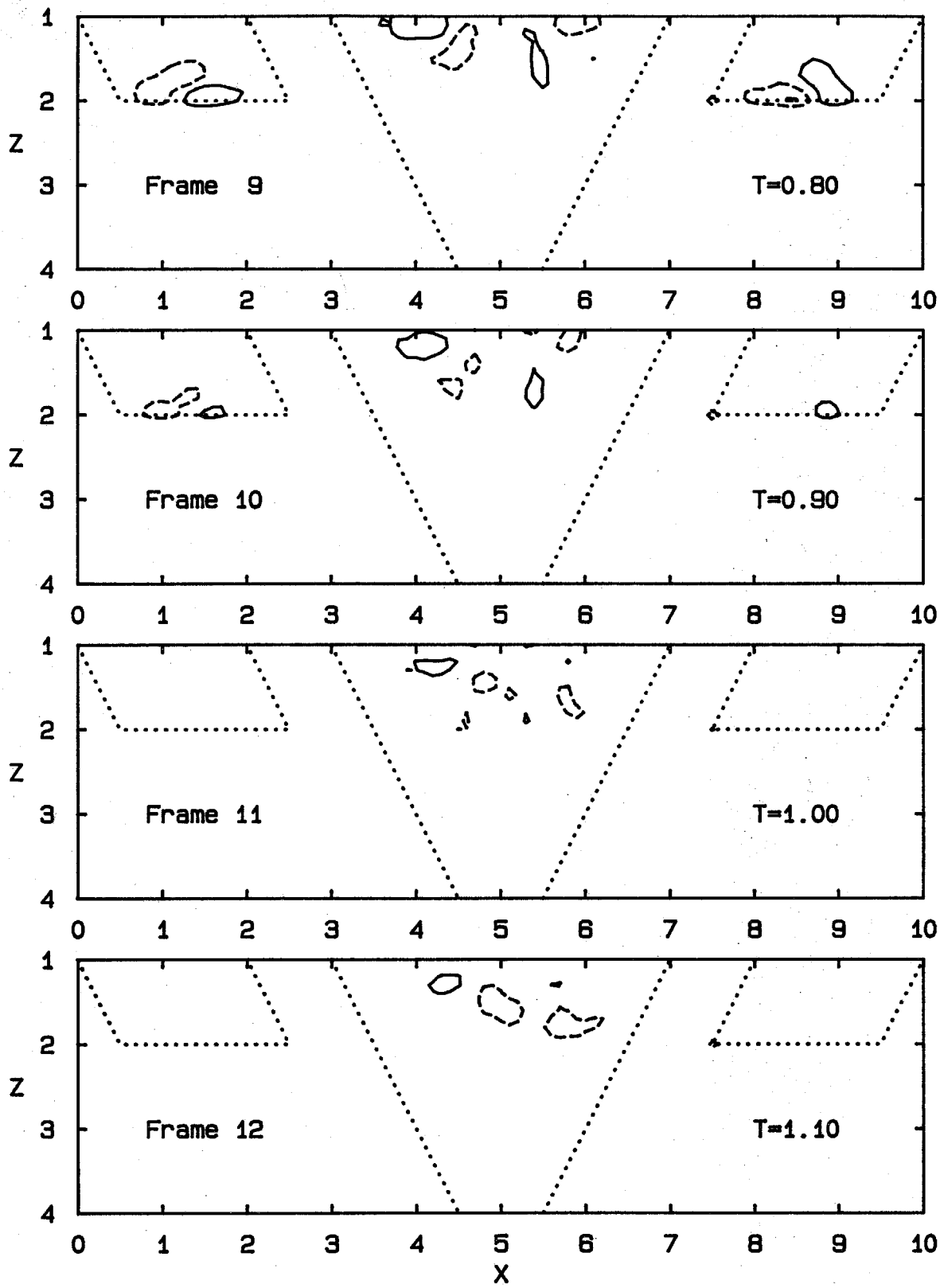

Fig. B.2 Components of Vorticity Equation; $(\tilde{u}\cdot\nabla)\,\omega_y$

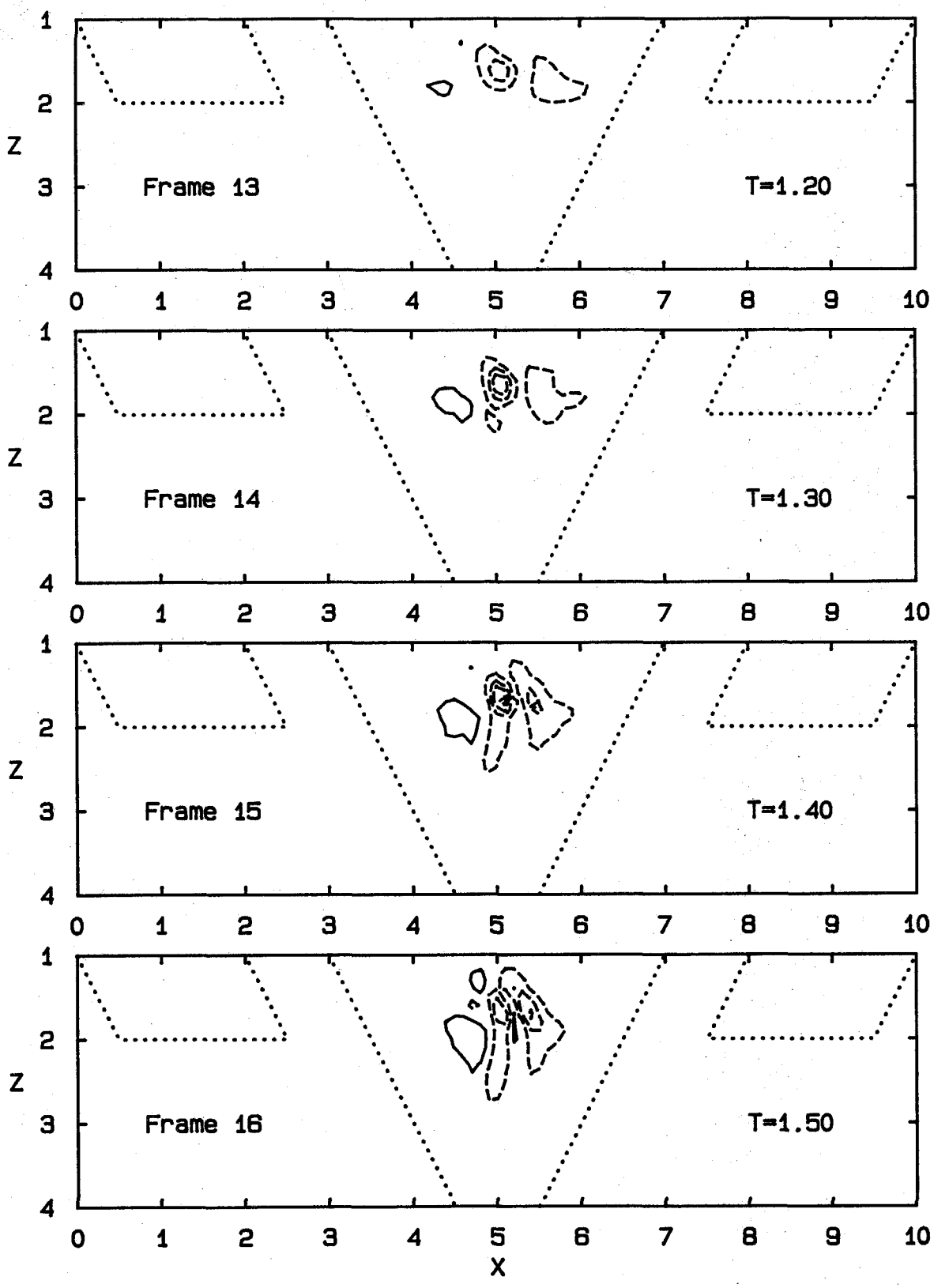

Fig. B.2 Components of Vorticity Equation; $(\vec{u}\cdot\nabla)\,\omega_y$

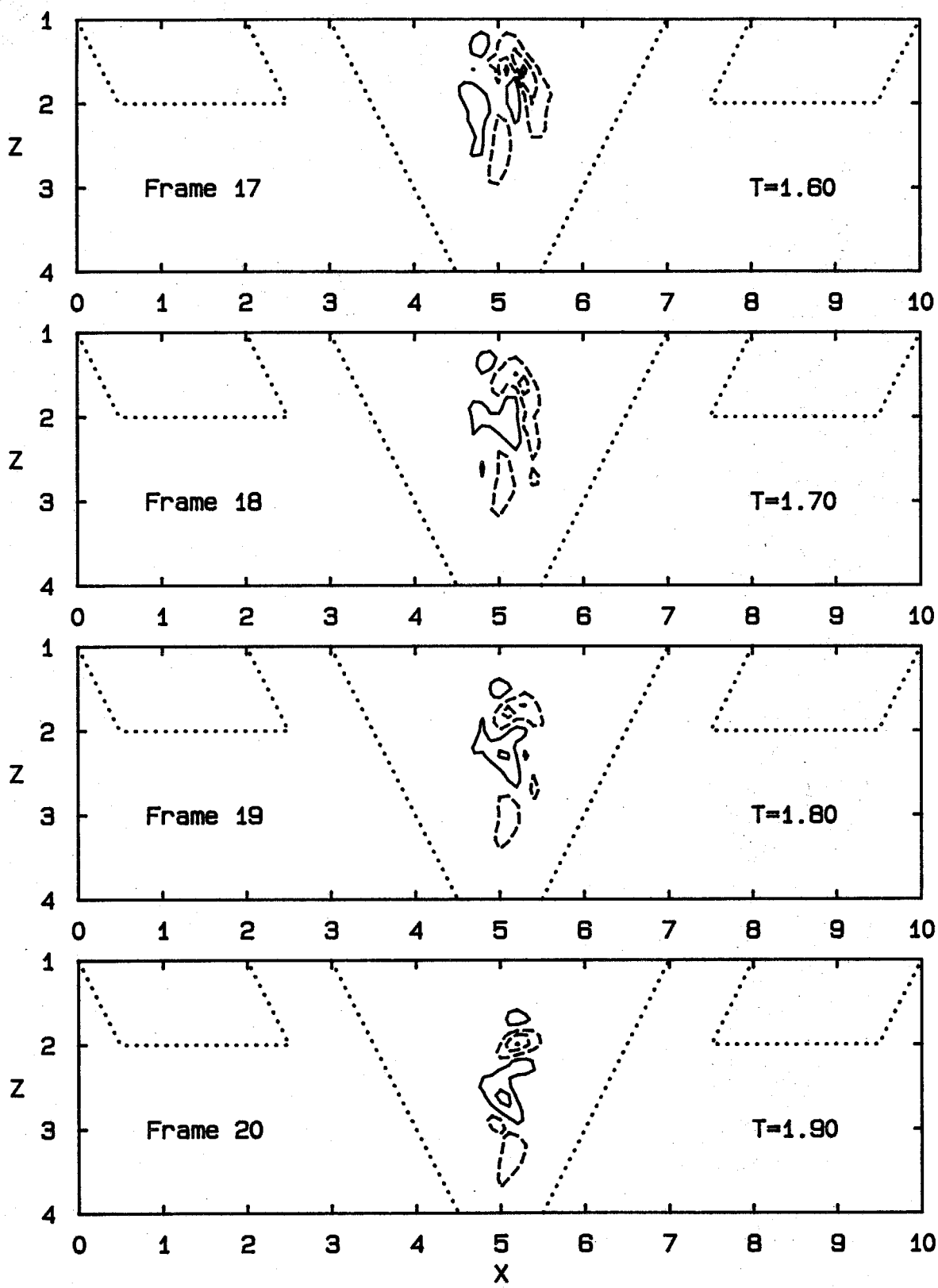

Fig. B.2 Components of Vorticity Equation; $(\vec{u}\cdot\nabla)\,\omega_y$

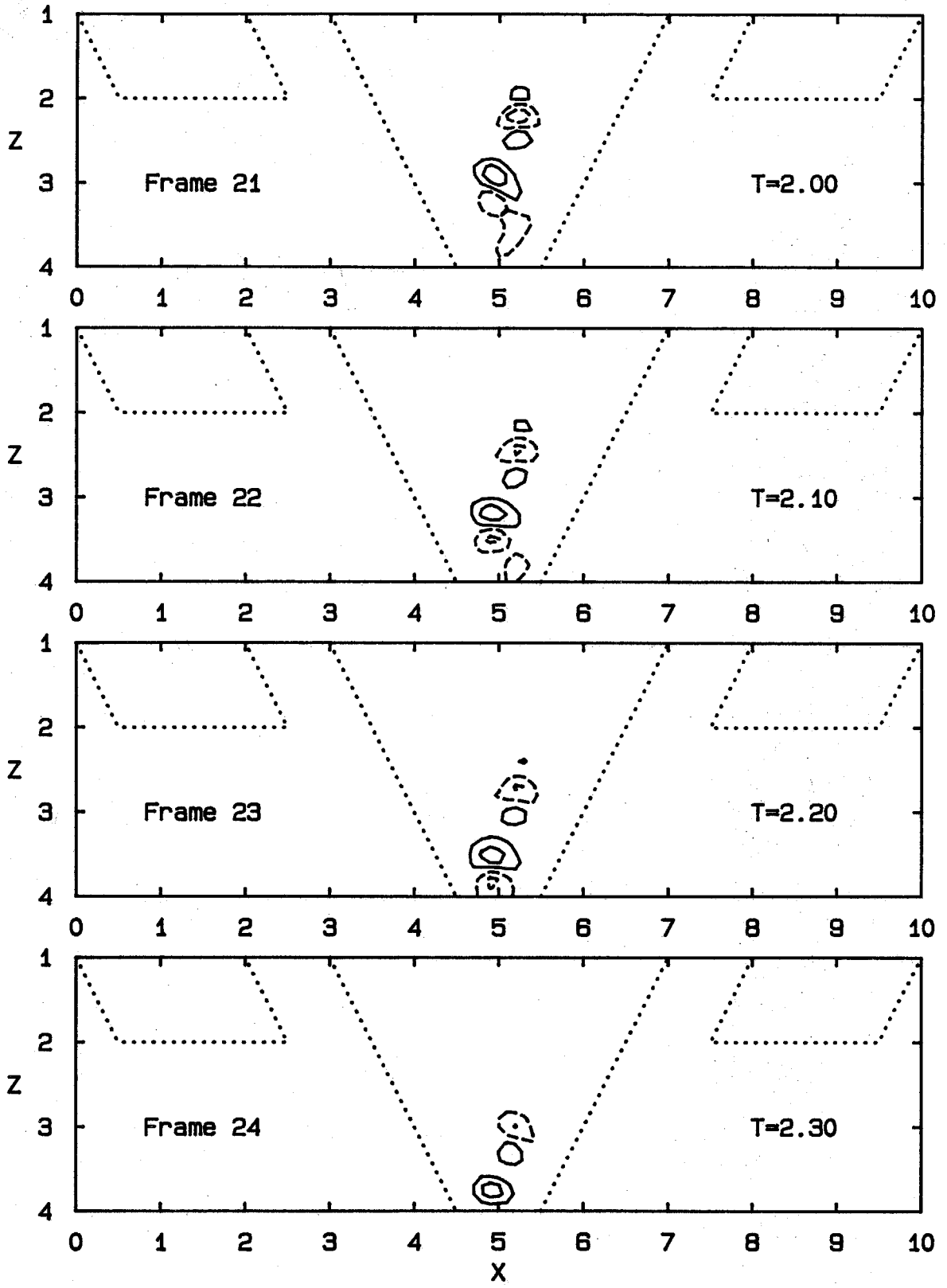

Fig. B.2 Components of Vorticity Equation; $(\vec{u}\cdot\nabla)\,\omega_y$

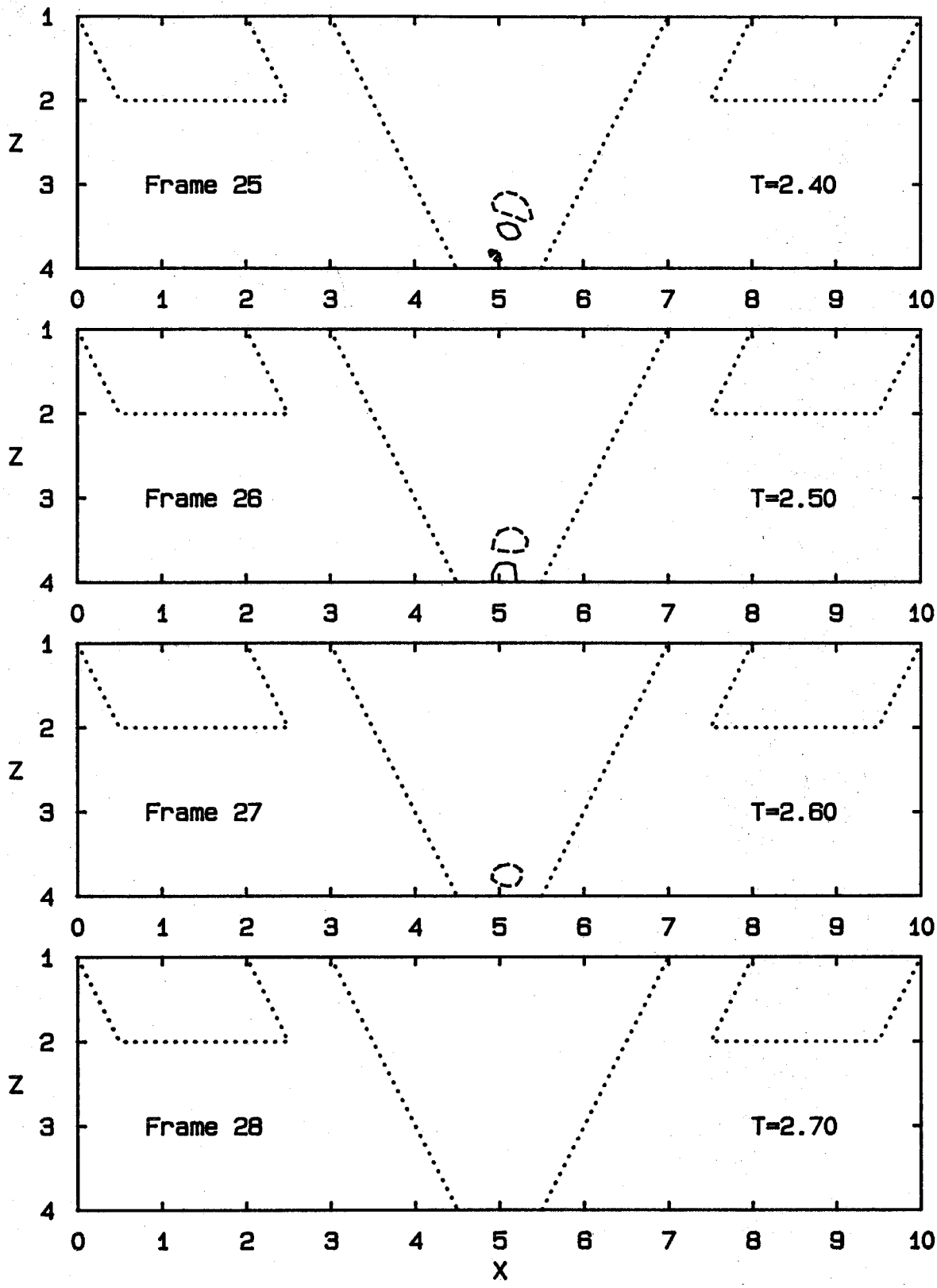

Fig. B.2 Components of Vorticity Equation; $(\vec{u}\cdot\nabla)\,\omega_y$

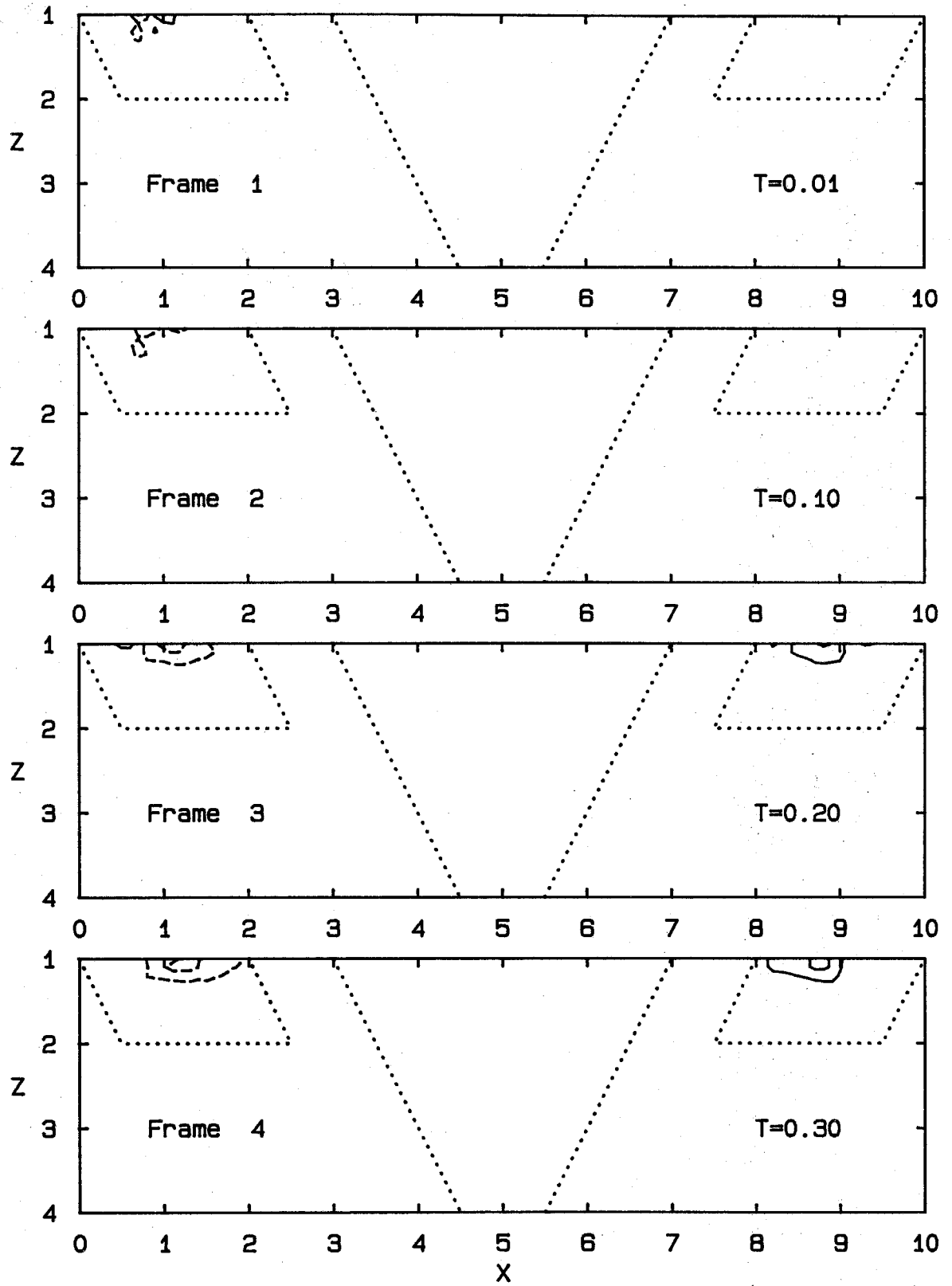

Fig. B.3 Components of Vorticity Equation; $D\omega_y/Dt$

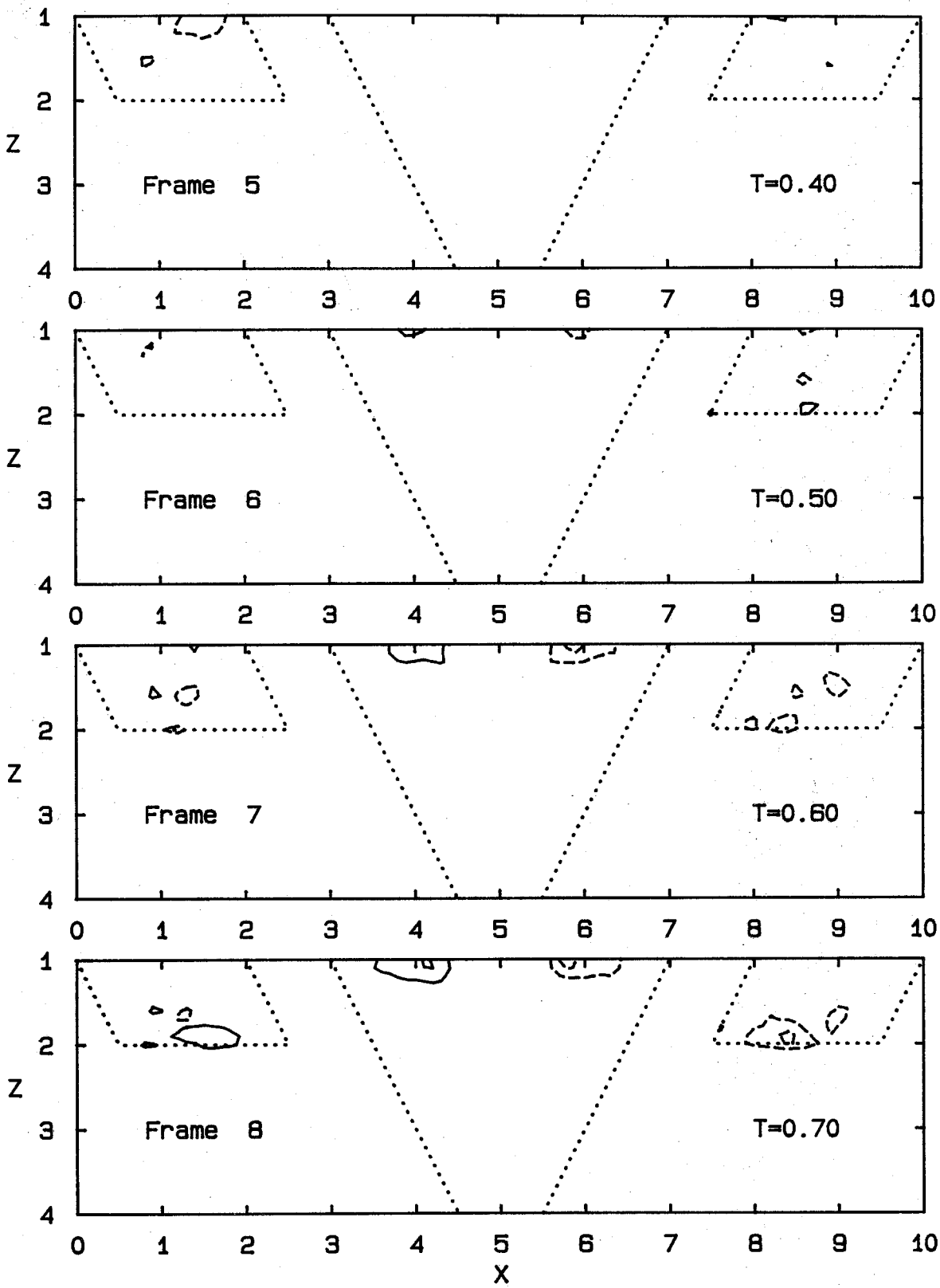

Fig. B.3 Components of Vorticity Equation: $D\omega_y/Dt$

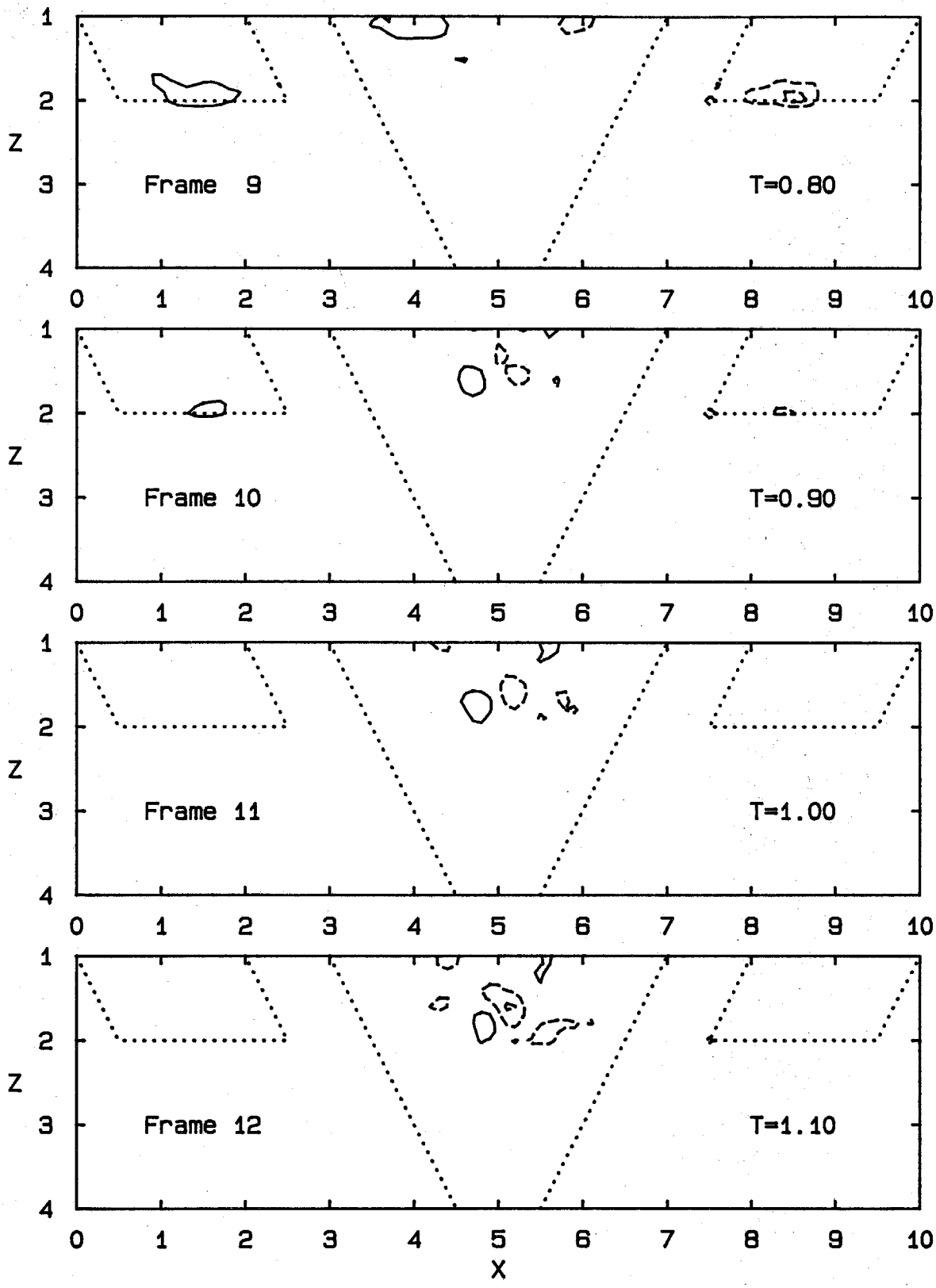

Fig. B.3 Components of Vorticity Equation; $D\omega_y/Dt$

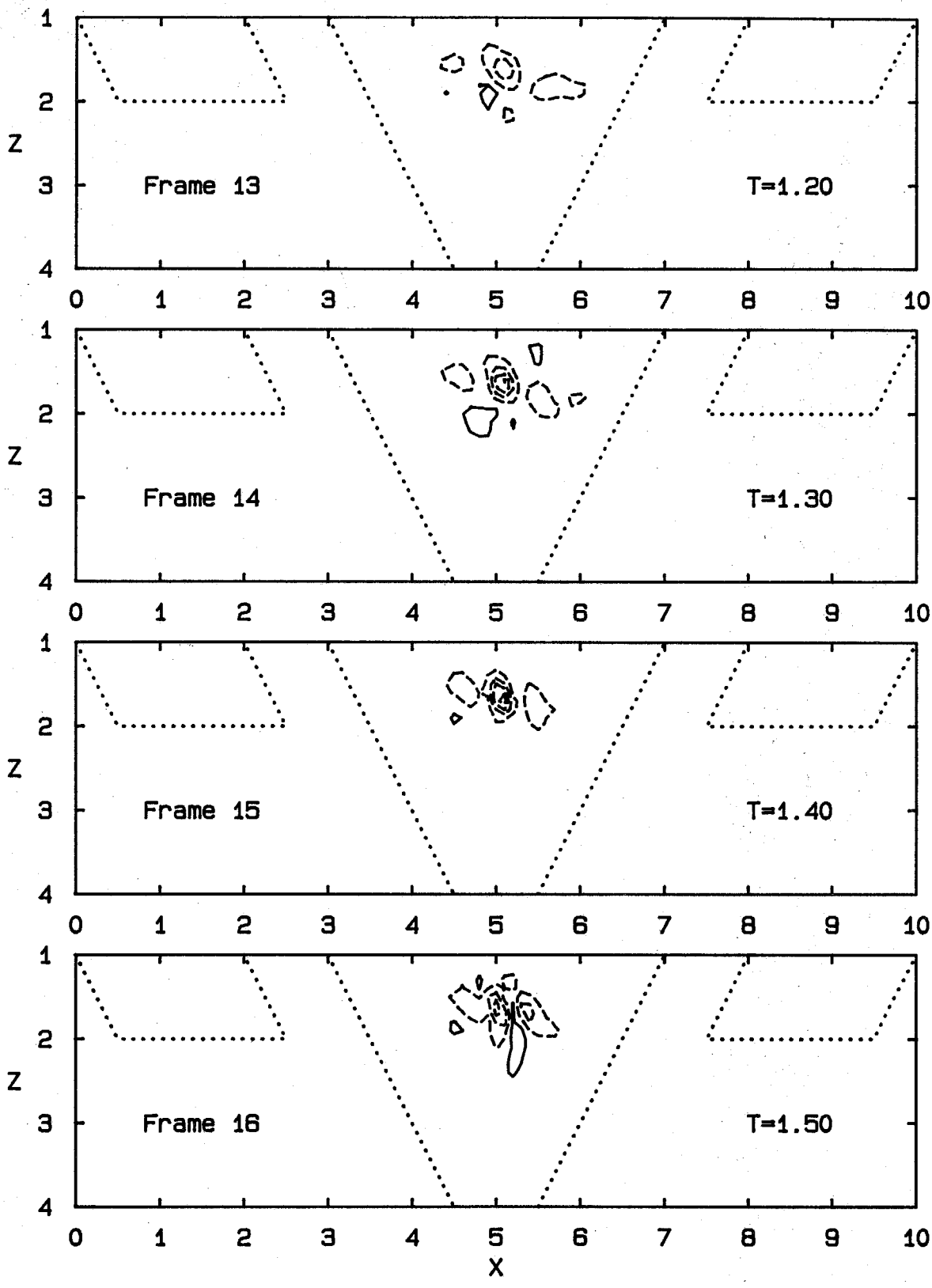

Fig. B.3 Components of Vorticity Equation: $D\omega_y/Dt$

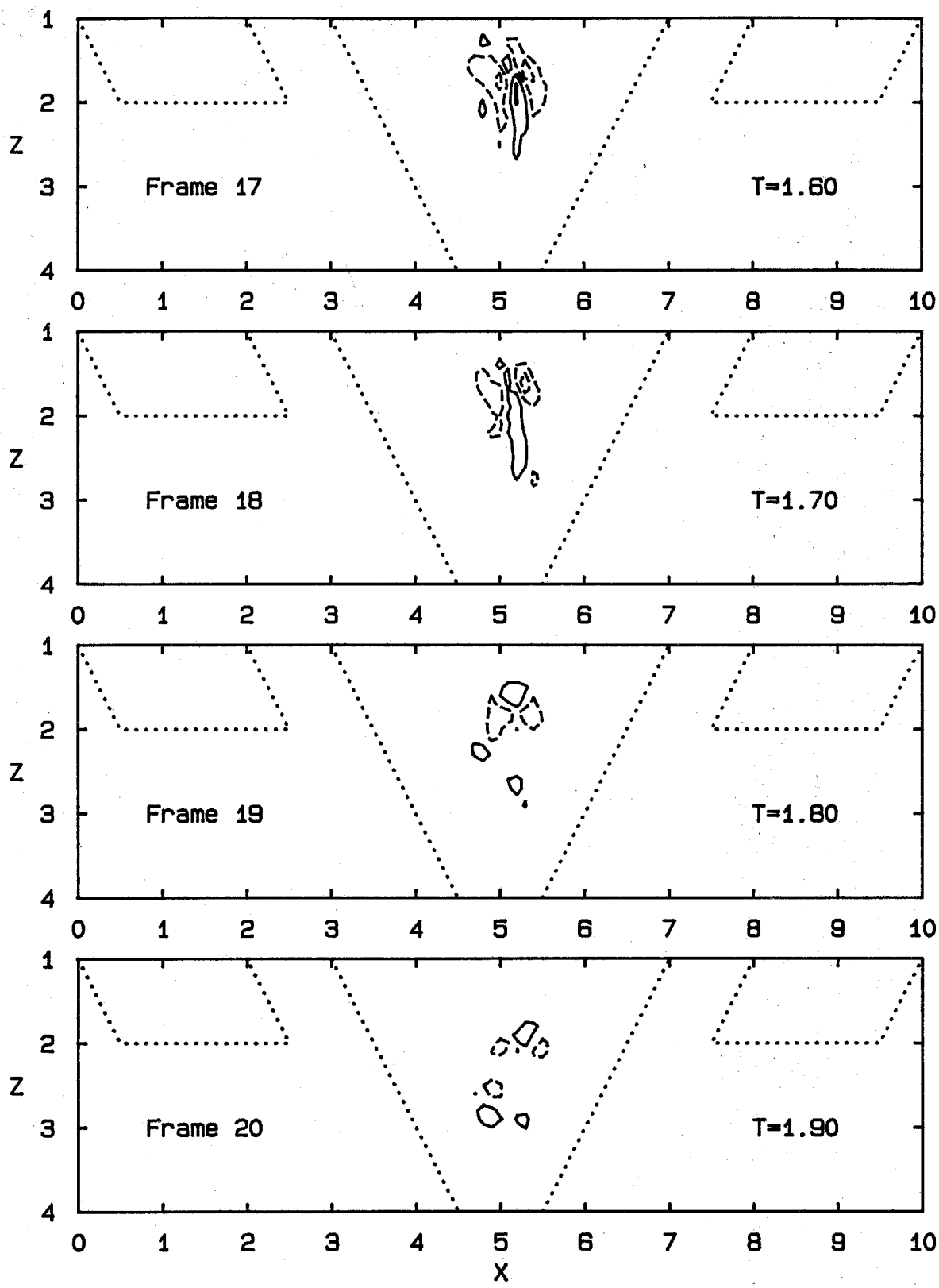

Fig. B.3 Components of Vorticity Equation; $D\omega_y/Dt$

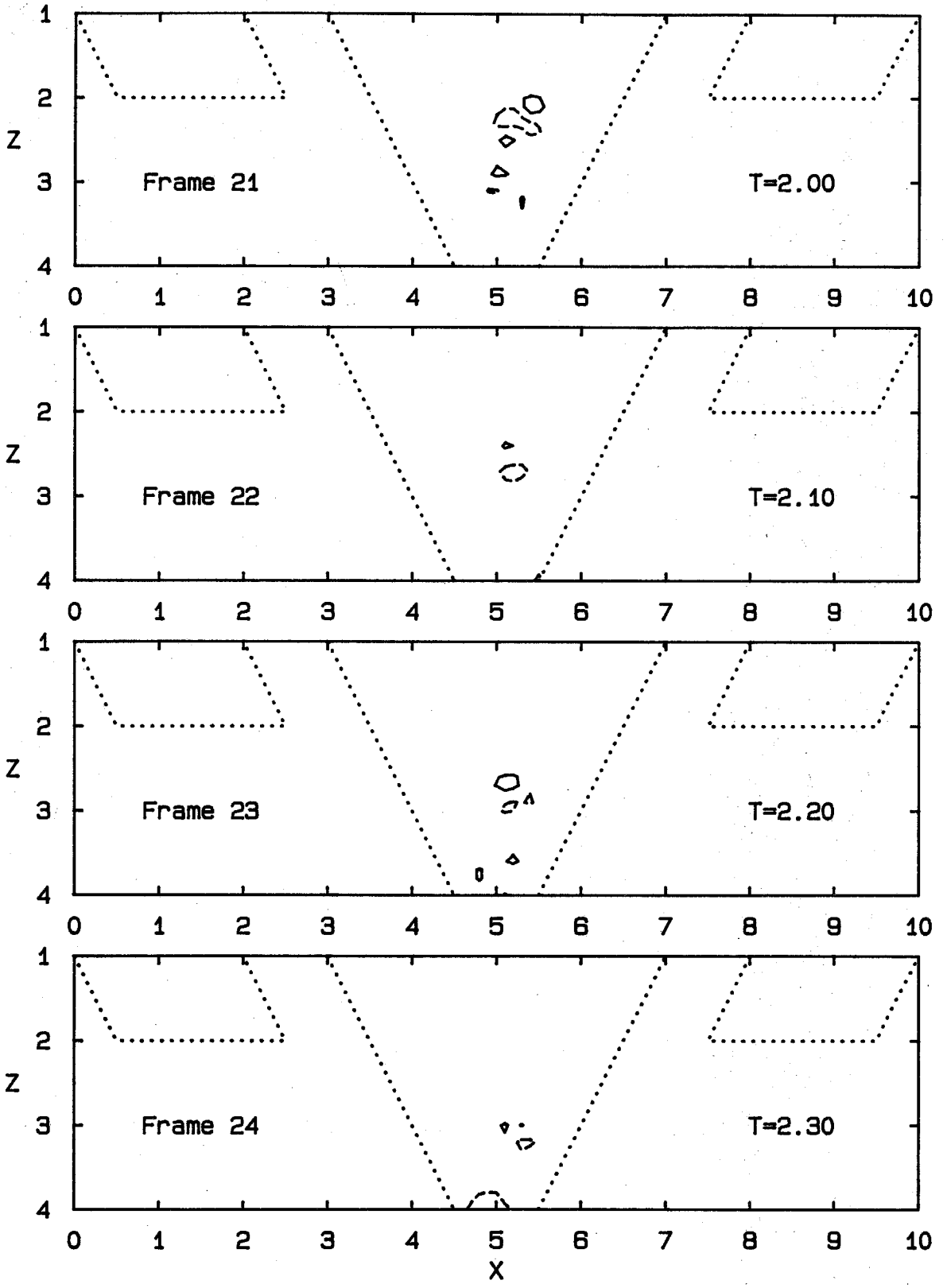

Fig. B.3 Components of Vorticity Equation; $D\omega_y/Dt$

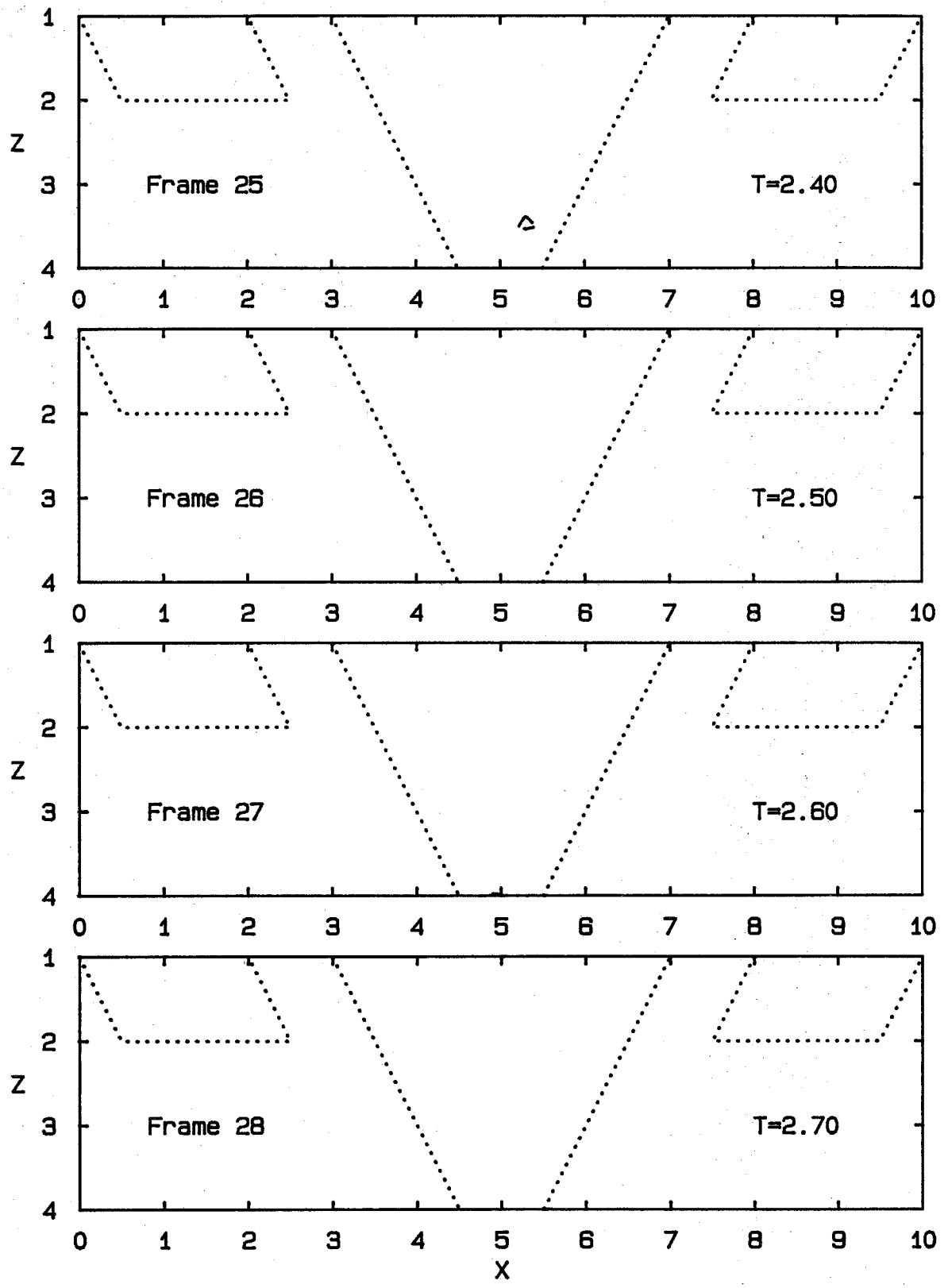

Fig. B.3 Components of Vorticity Equation; $D\omega_y/Dt$

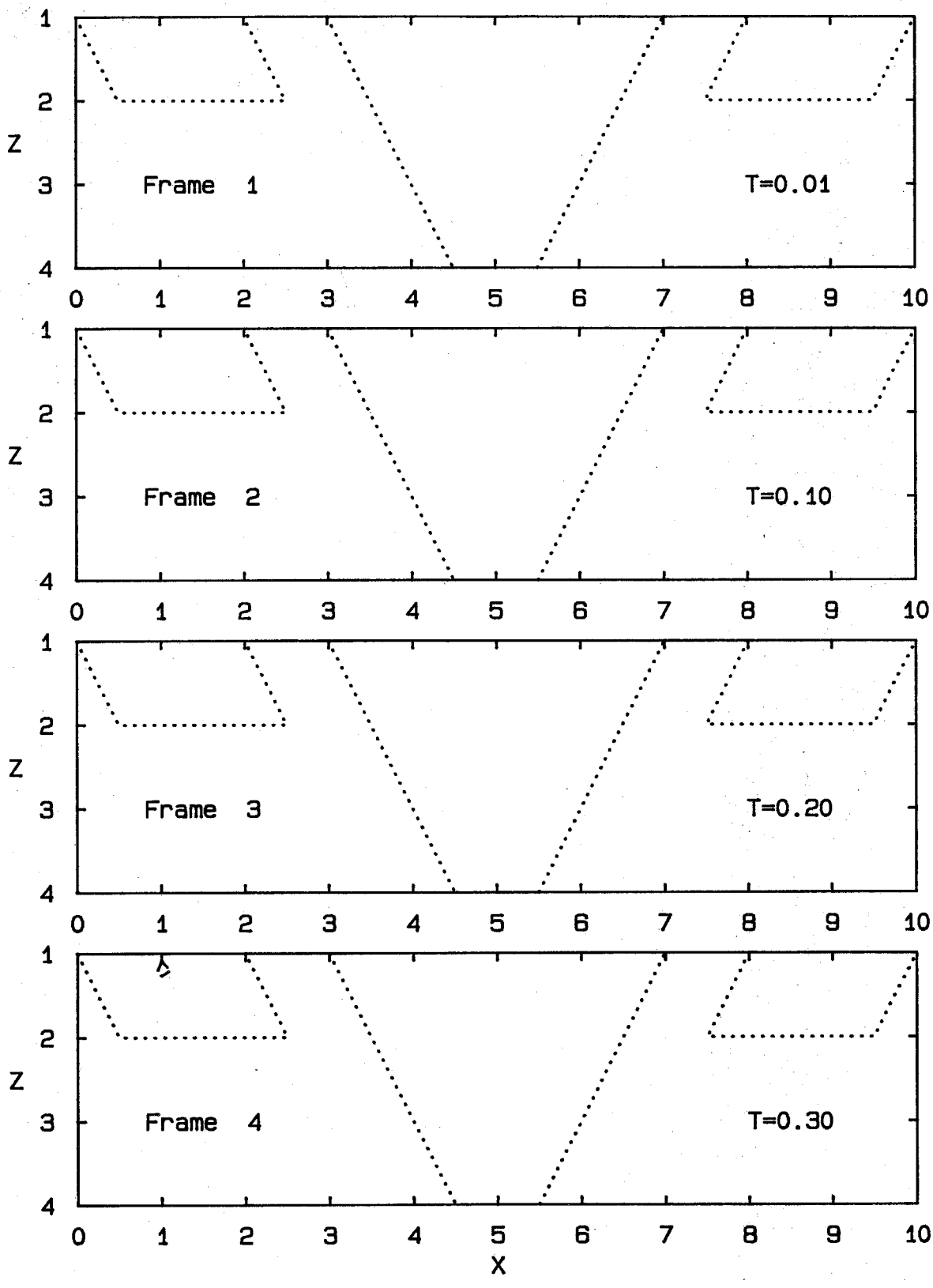

Fig. B.4 Components of Vorticity Equation; $\omega_y (\partial v/\partial y)$

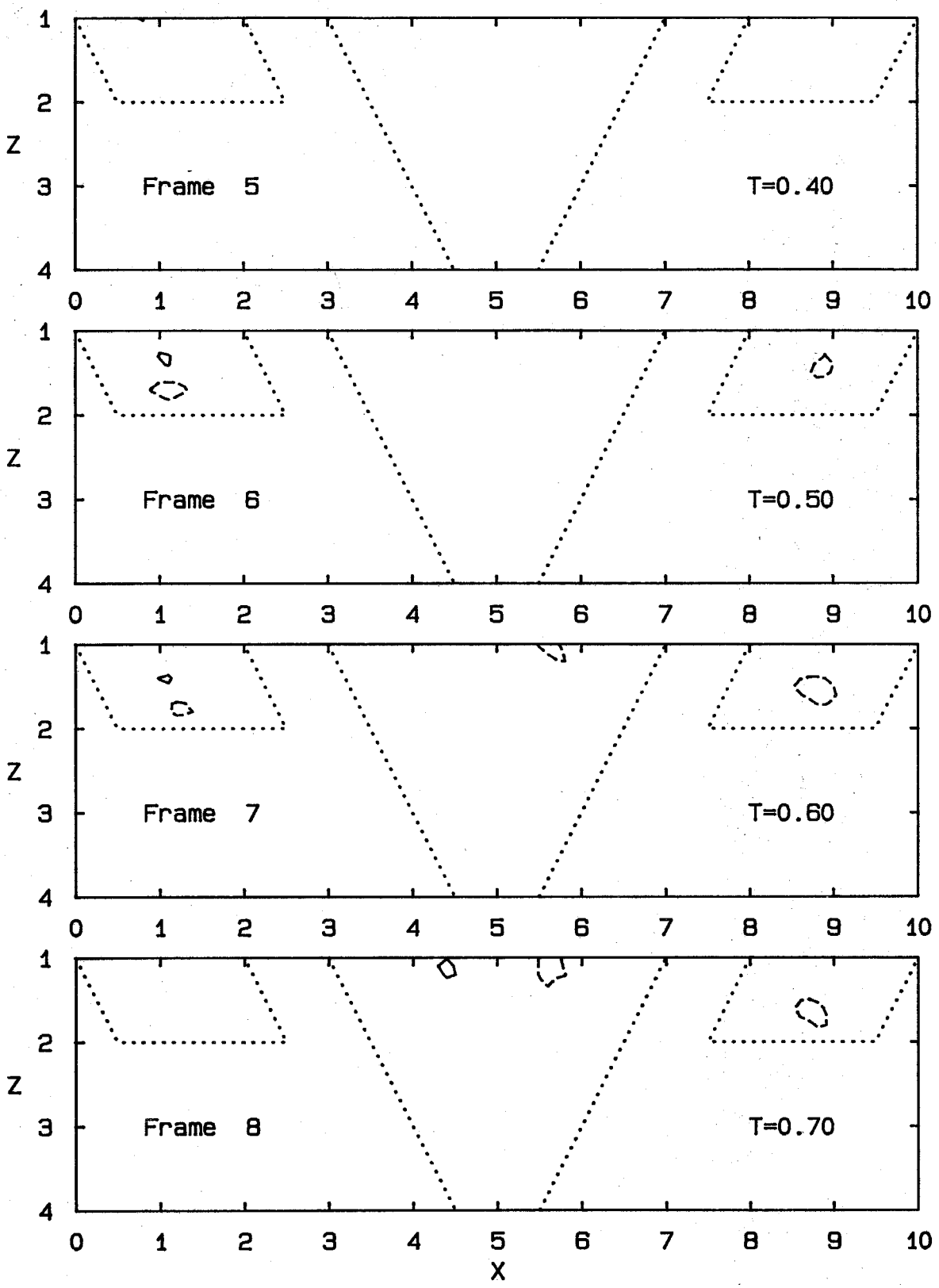

Fig. B.4 Components of Vorticity Equation; $\omega_y (\partial v/\partial y)$

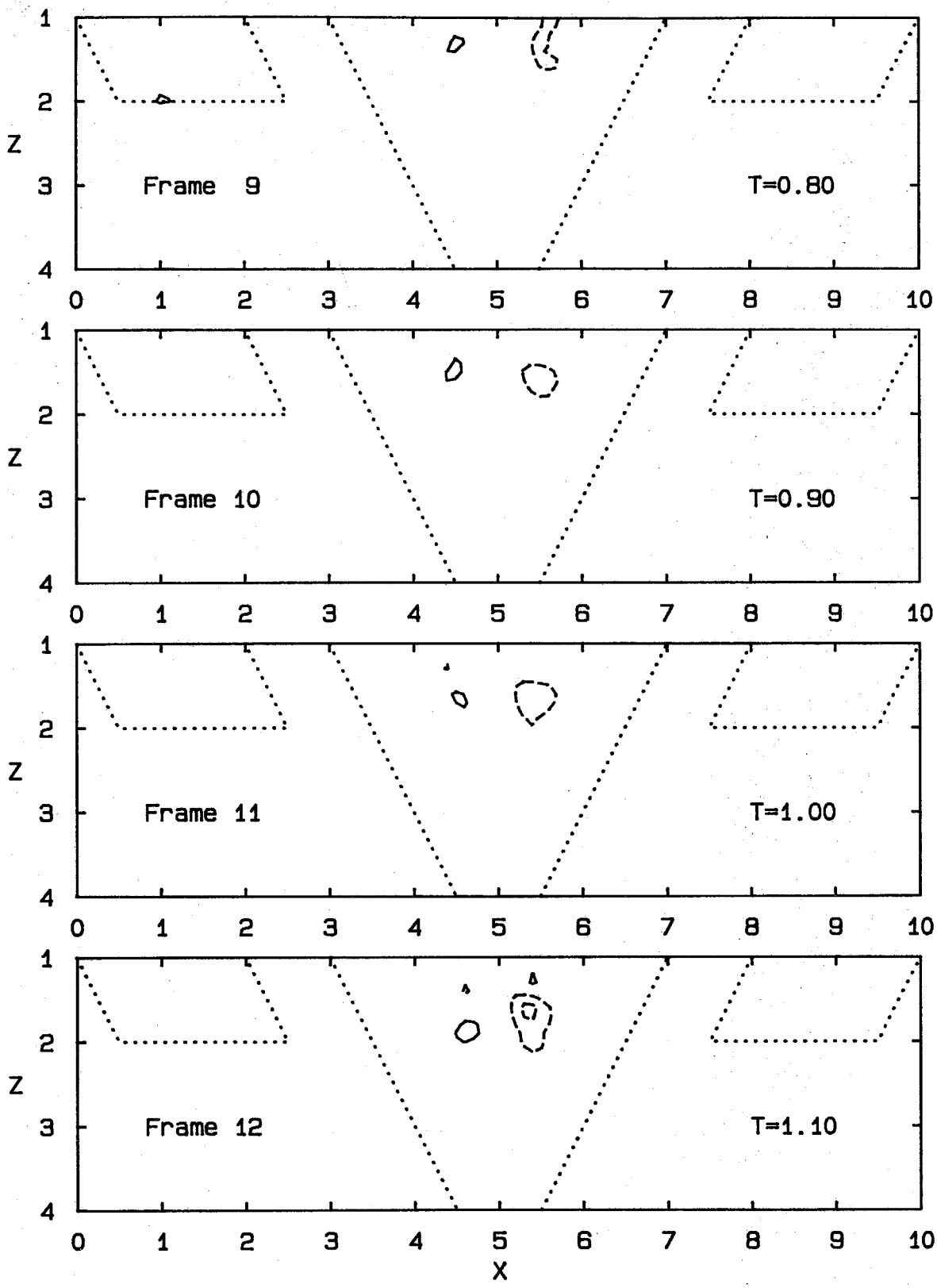

Fig. B.4 Components of Vorticity Equation; $\omega_y (\partial v/\partial y)$

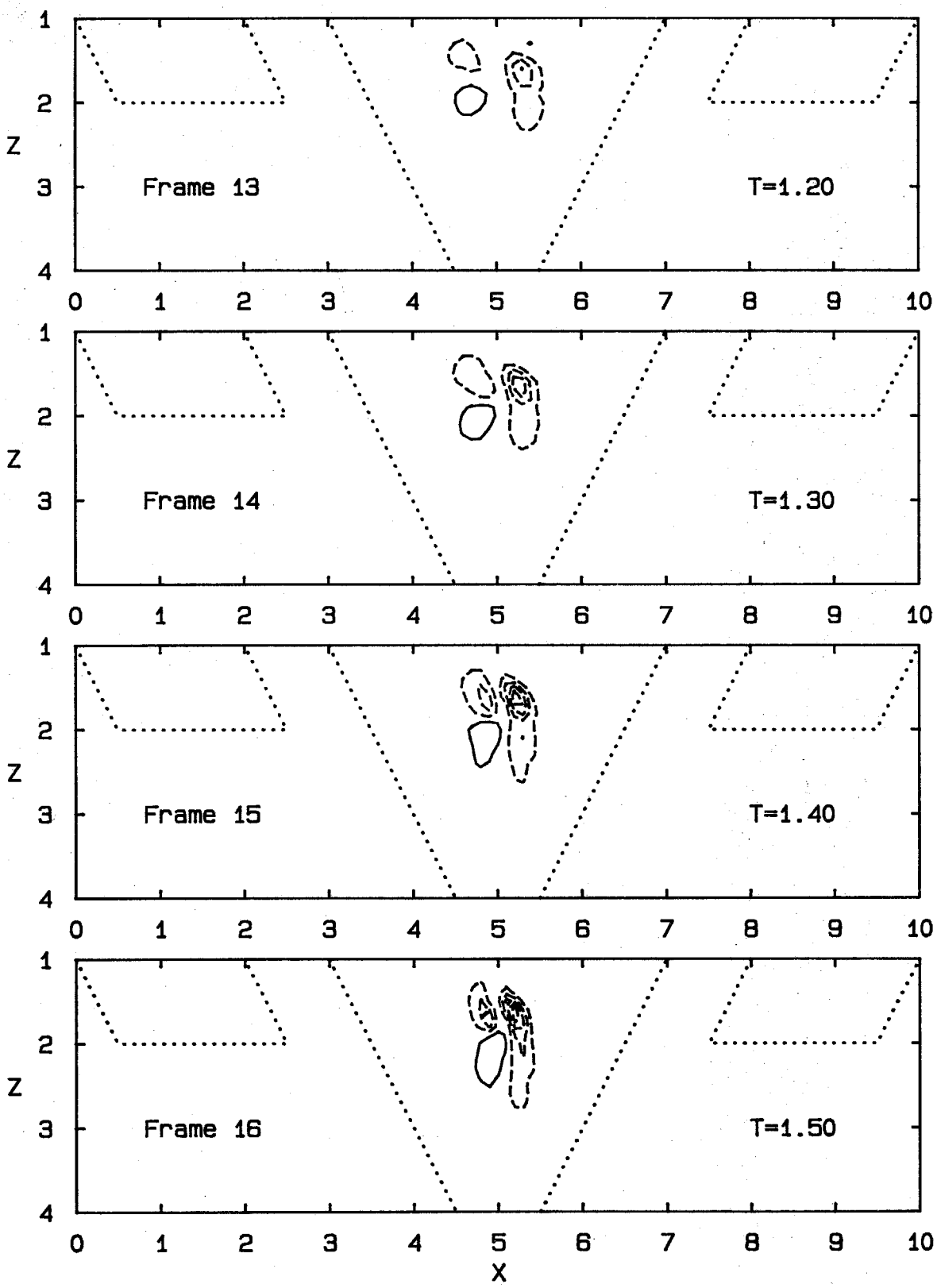

Fig. B.4 Components of Vorticity Equation; ω_y ($\partial v/\partial y$)

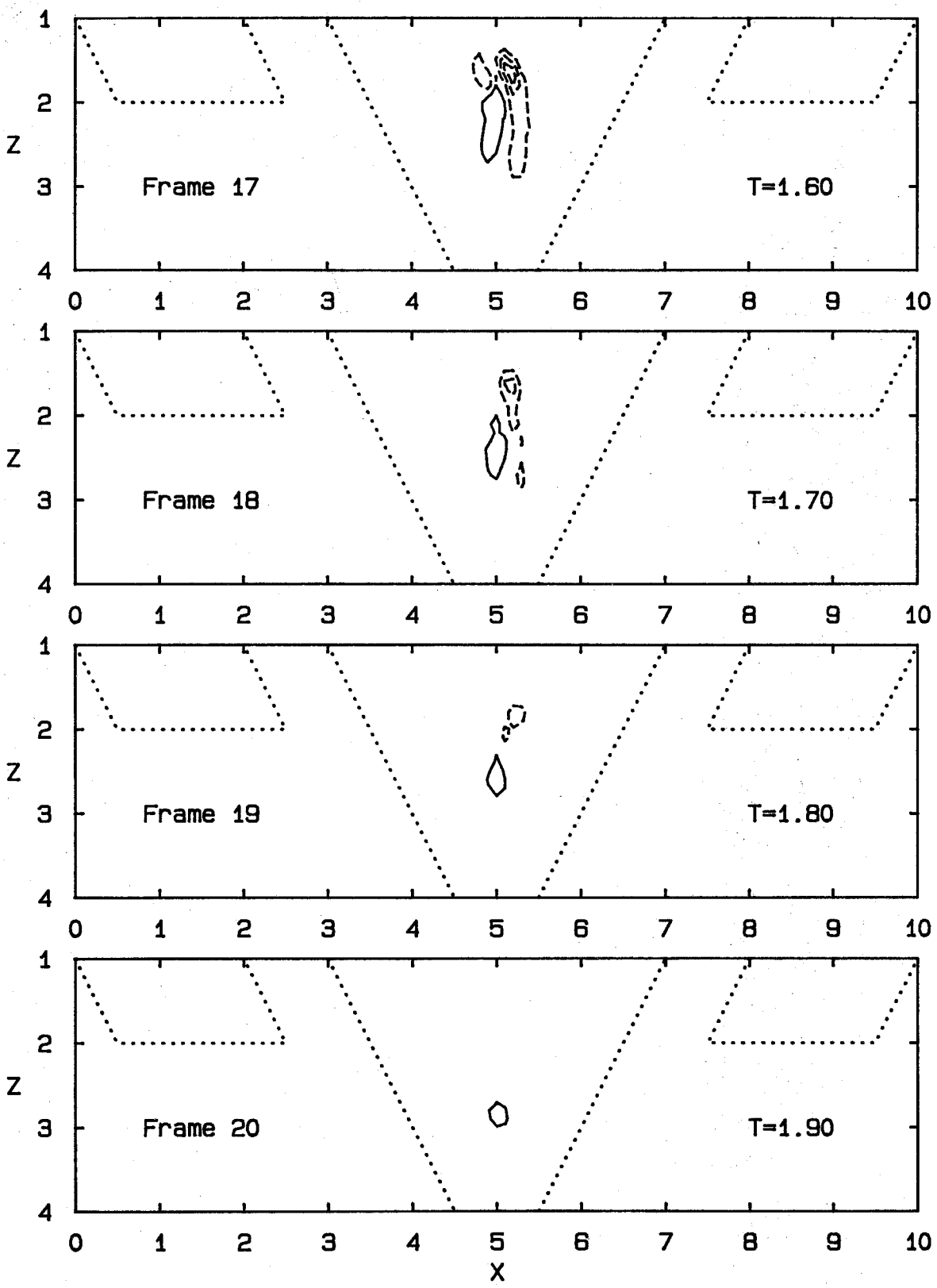

Fig. B.4 Components of Vorticity Equation; $\omega_y (\partial v/\partial y)$

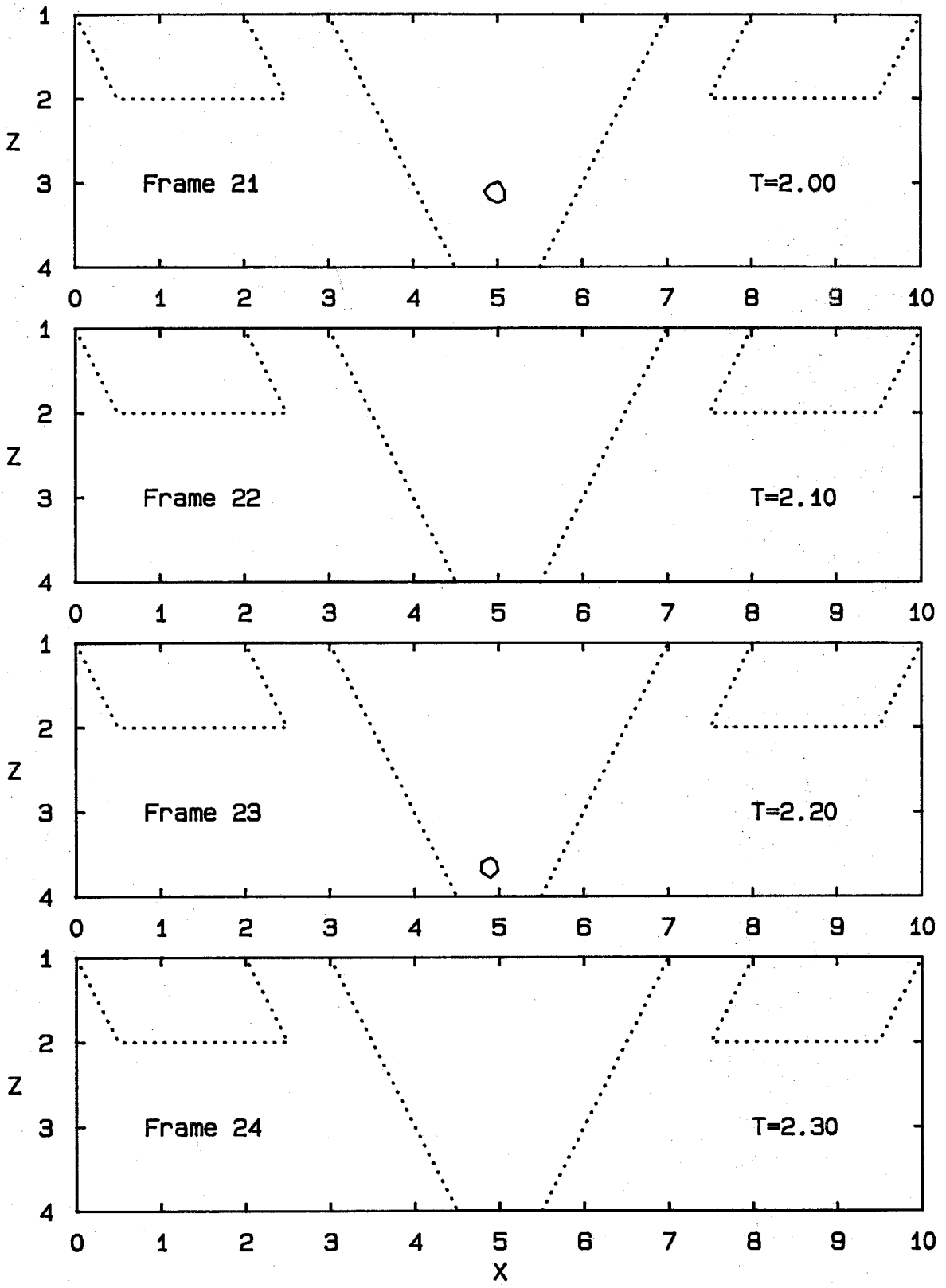

Fig. B.4 Components of Vorticity Equation; $\omega_y (\partial v/\partial y)$

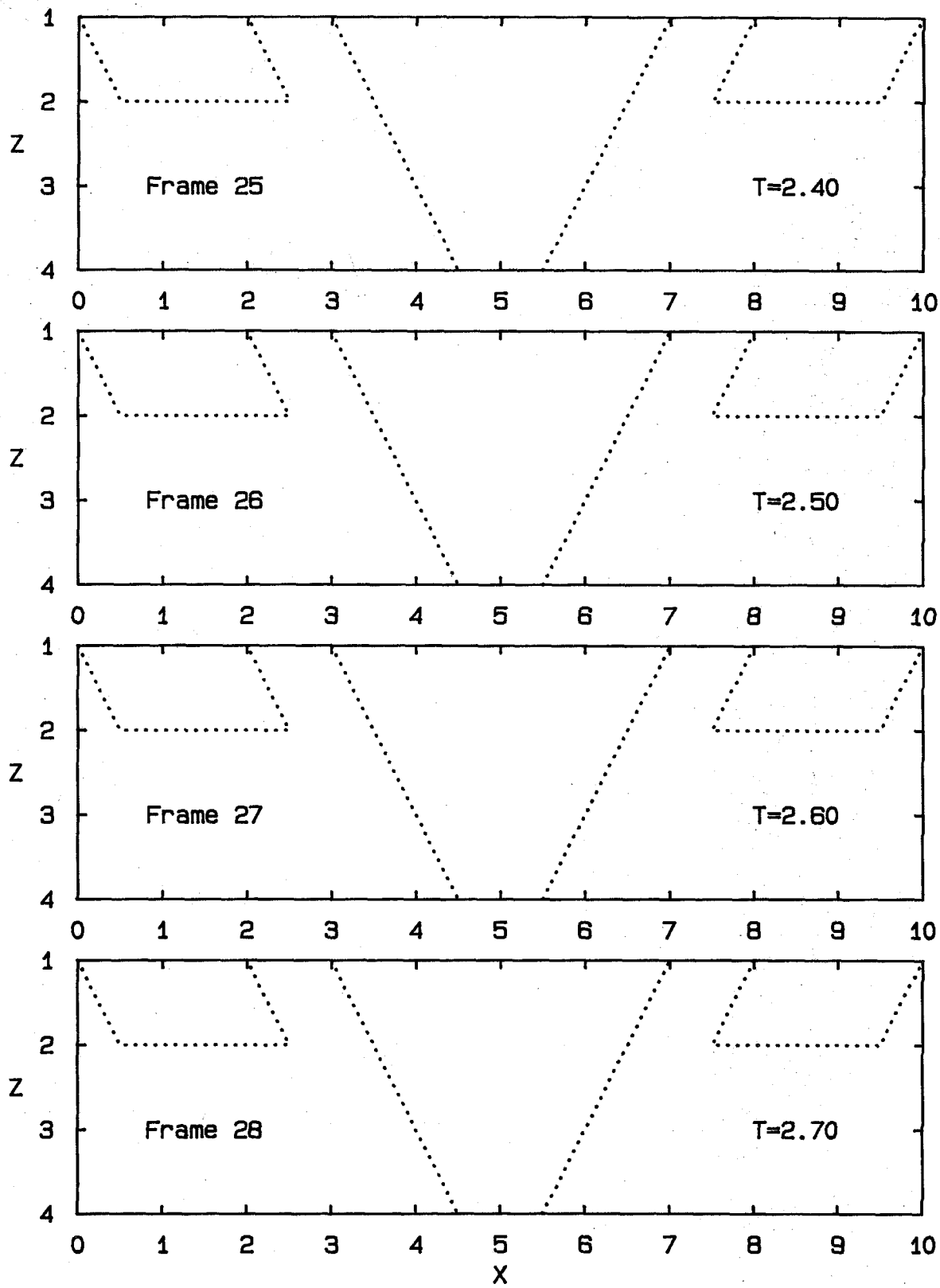

Fig. B.4 Components of Vorticity Equation; ω_y ($\partial v/\partial y$)

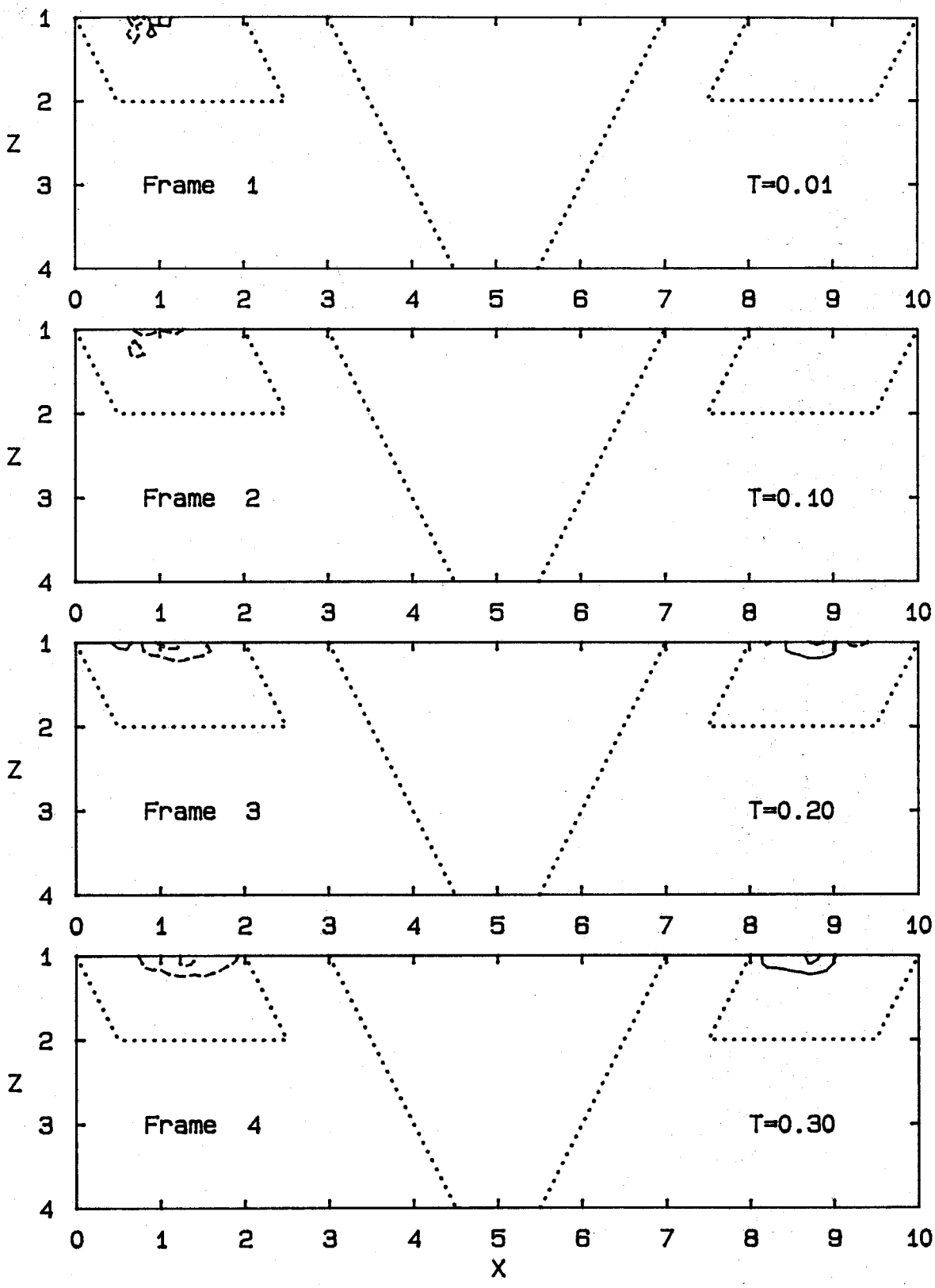

Fig. B.5 Components of Vorticity Equation; $\nu\nabla^2\omega_y$

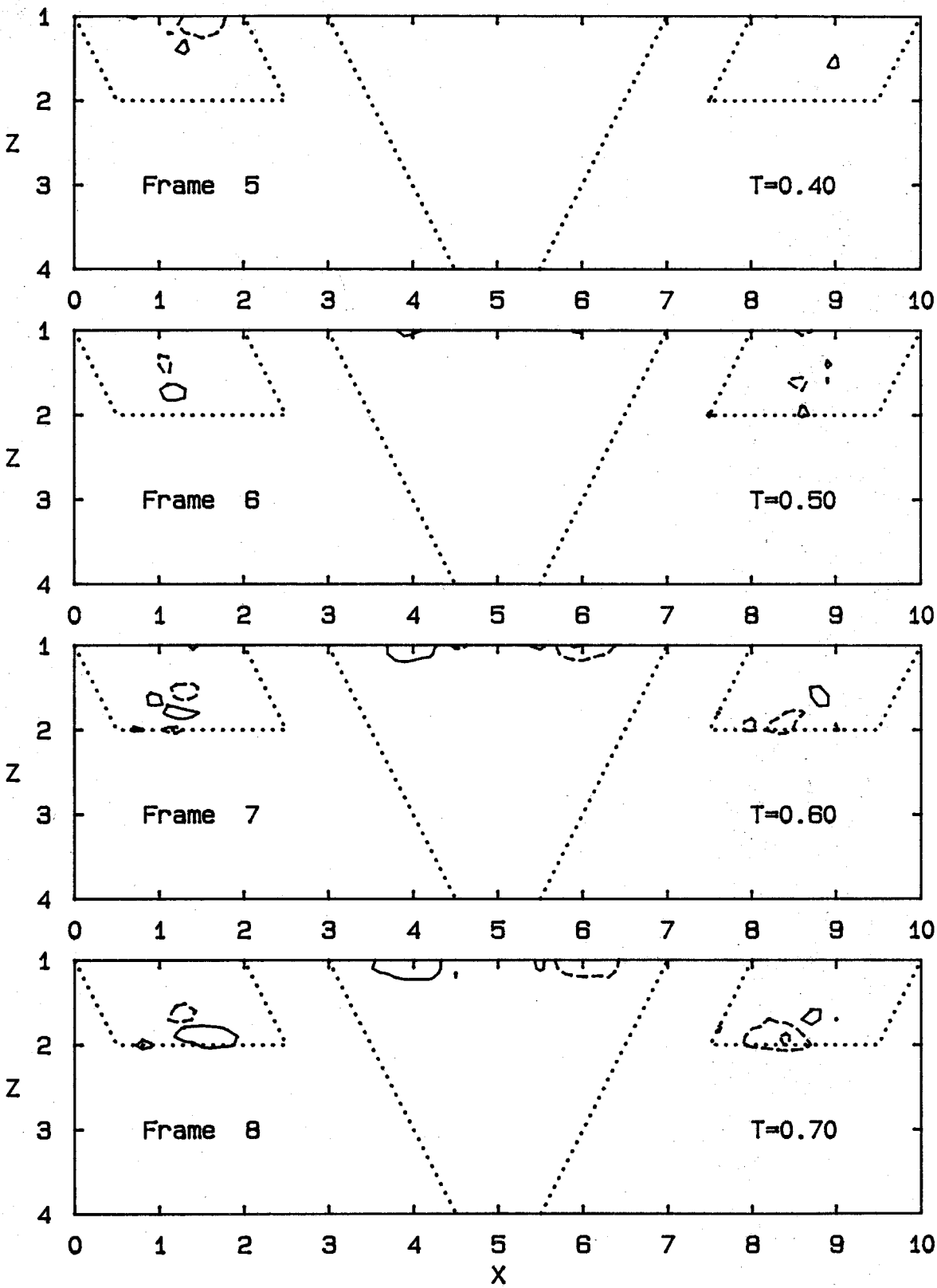

Fig. B.5 Components of Vorticity Equation; $\nu\nabla^2\omega_y$

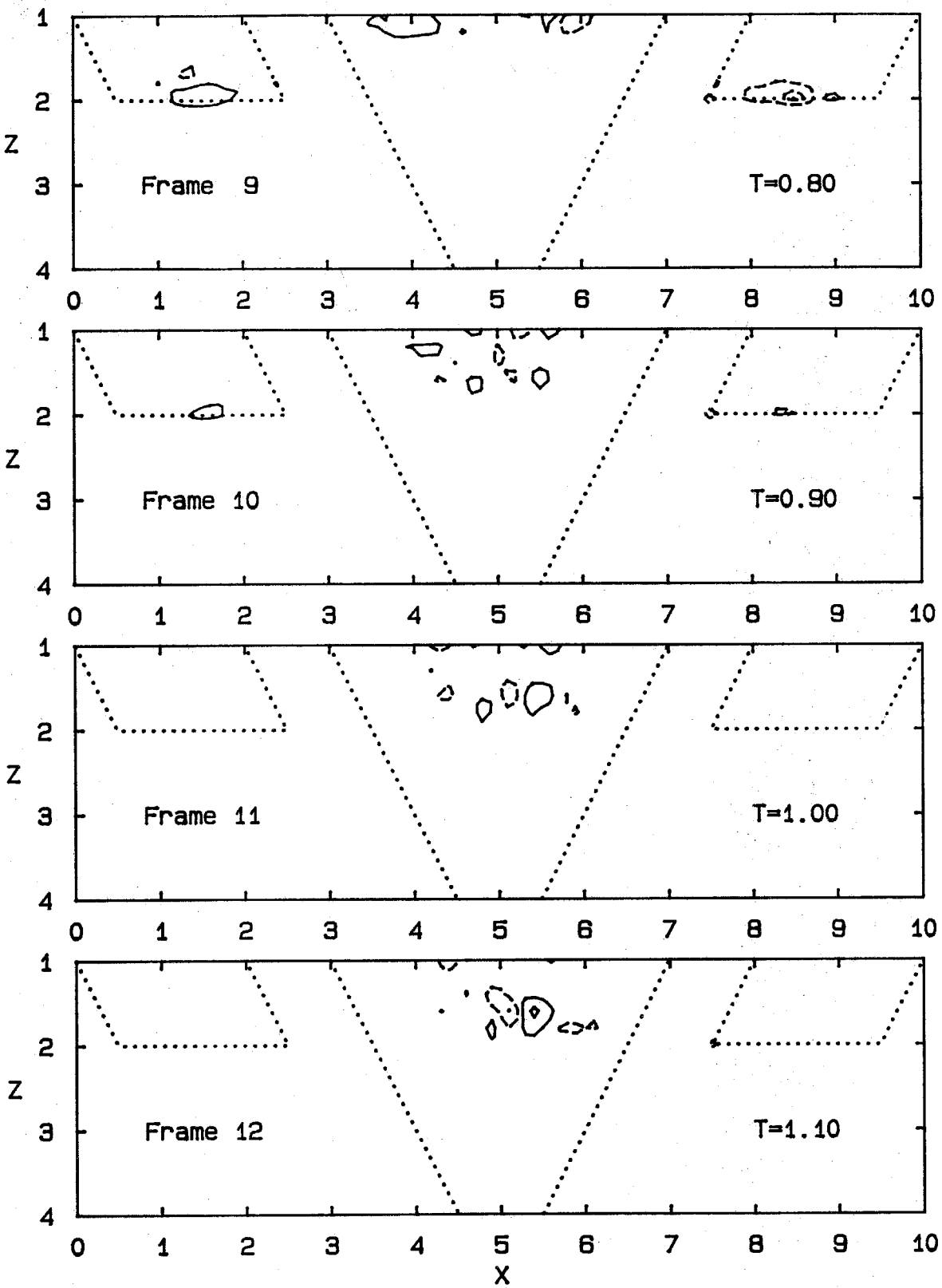

Fig. B.5 Components of Vorticity Equation; $\upsilon\nabla^2\omega_y$

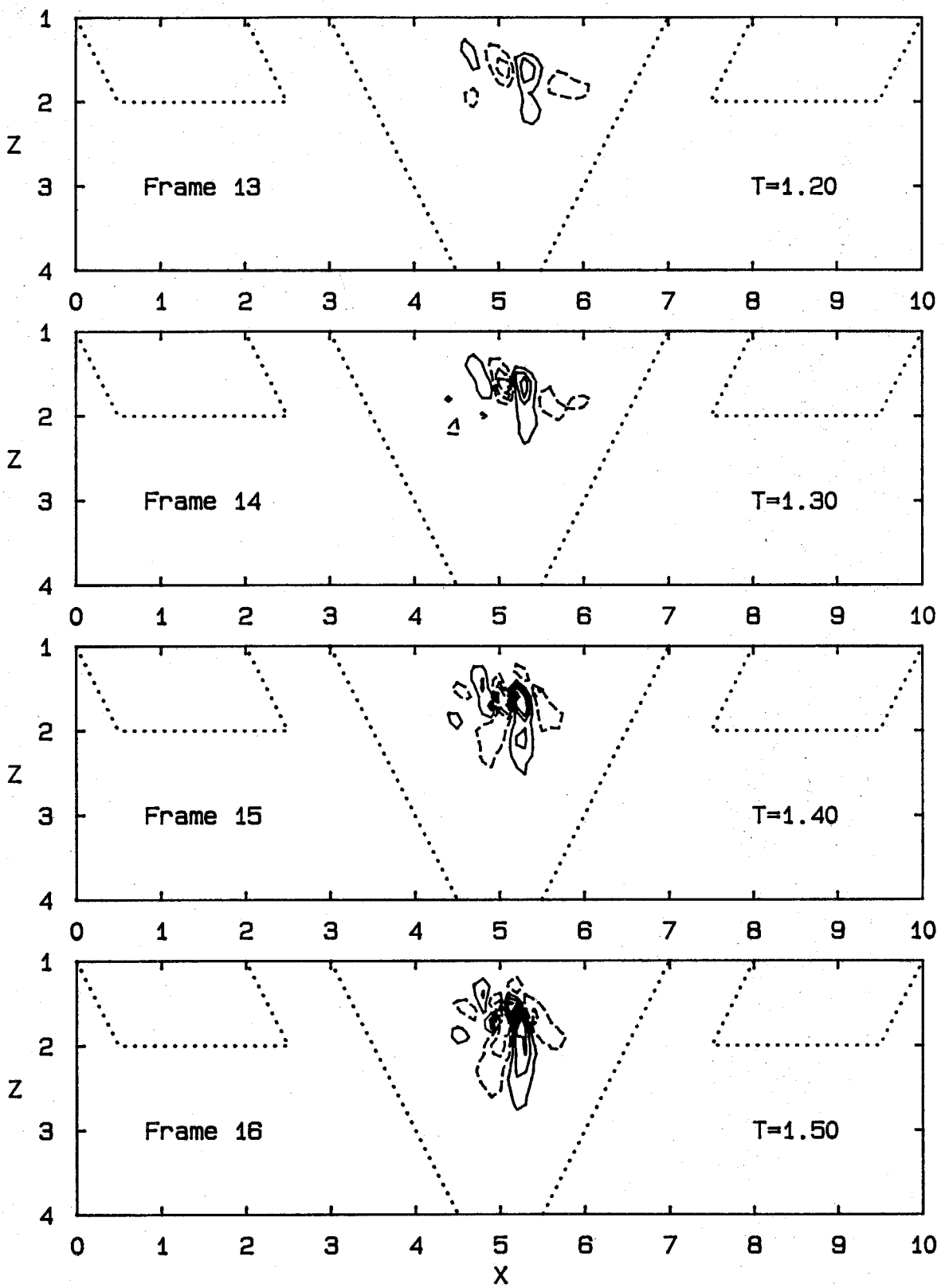

Fig. B.5 Components of Vorticity Equation; $\nu\nabla^2\omega_y$

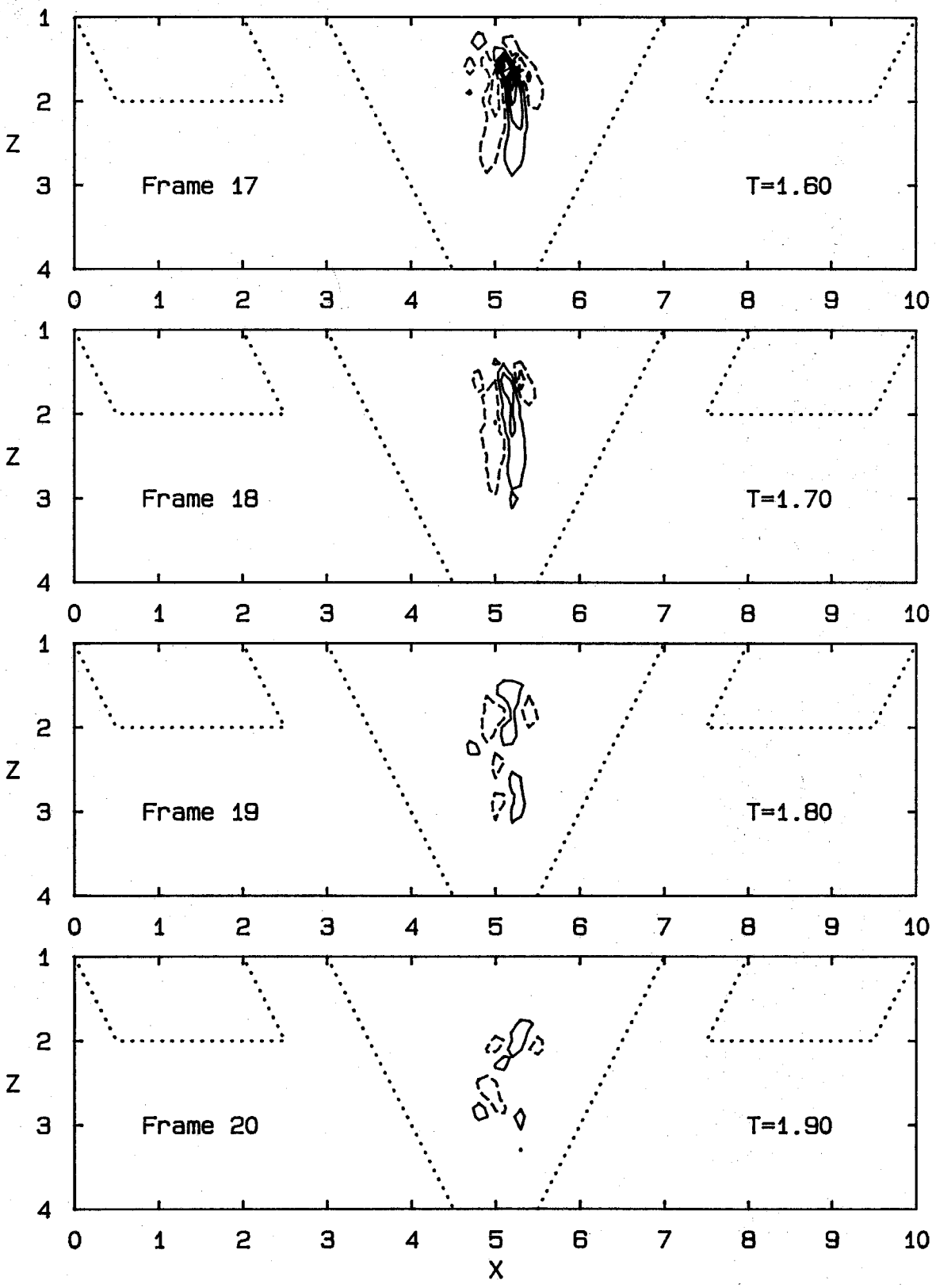

Fig. B.5 Components of Vorticity Equation; $\nu\nabla^2\omega_y$

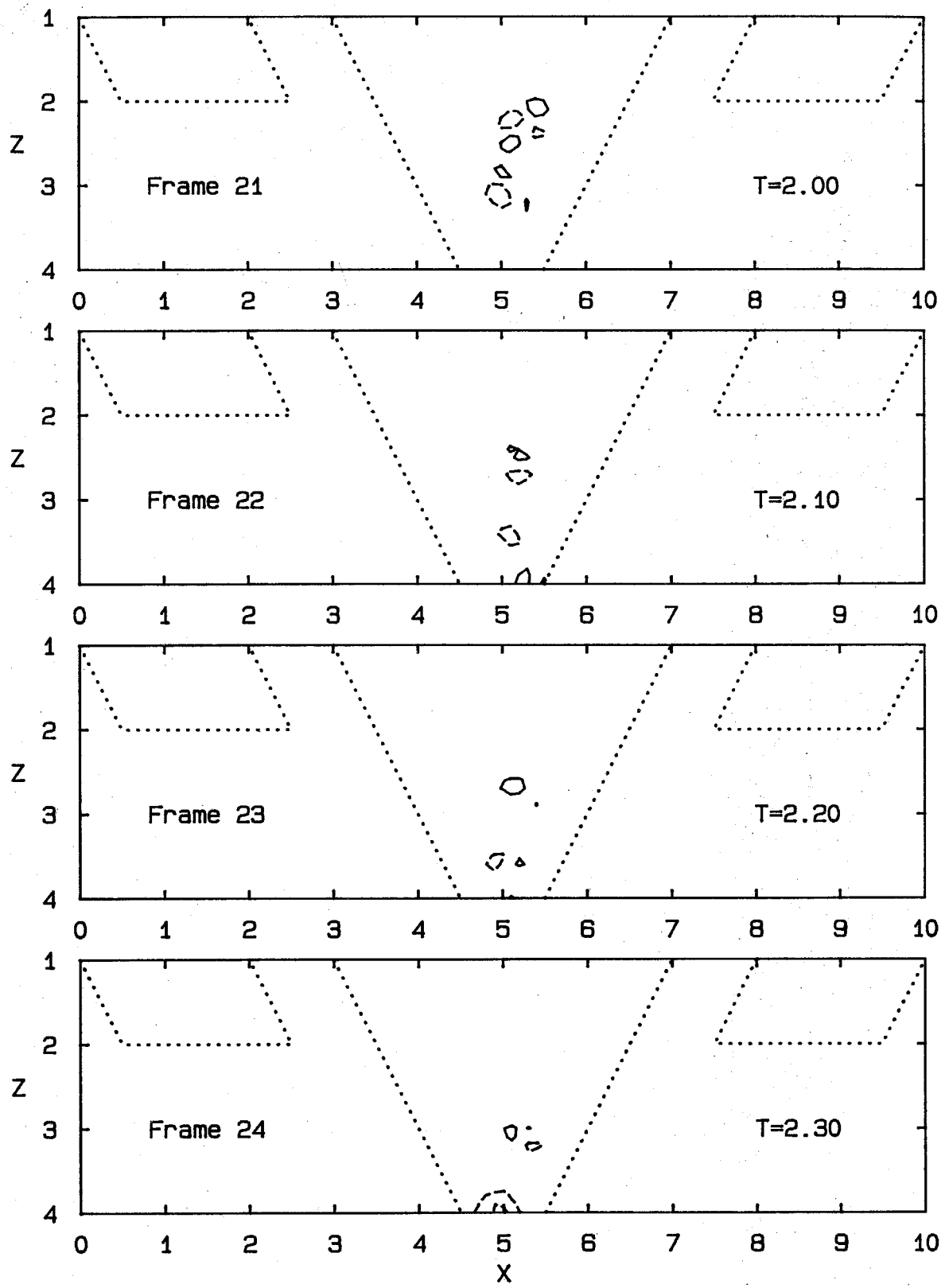

Fig. B.5 Components of Vorticity Equation; $\nu\nabla^2\omega_y$

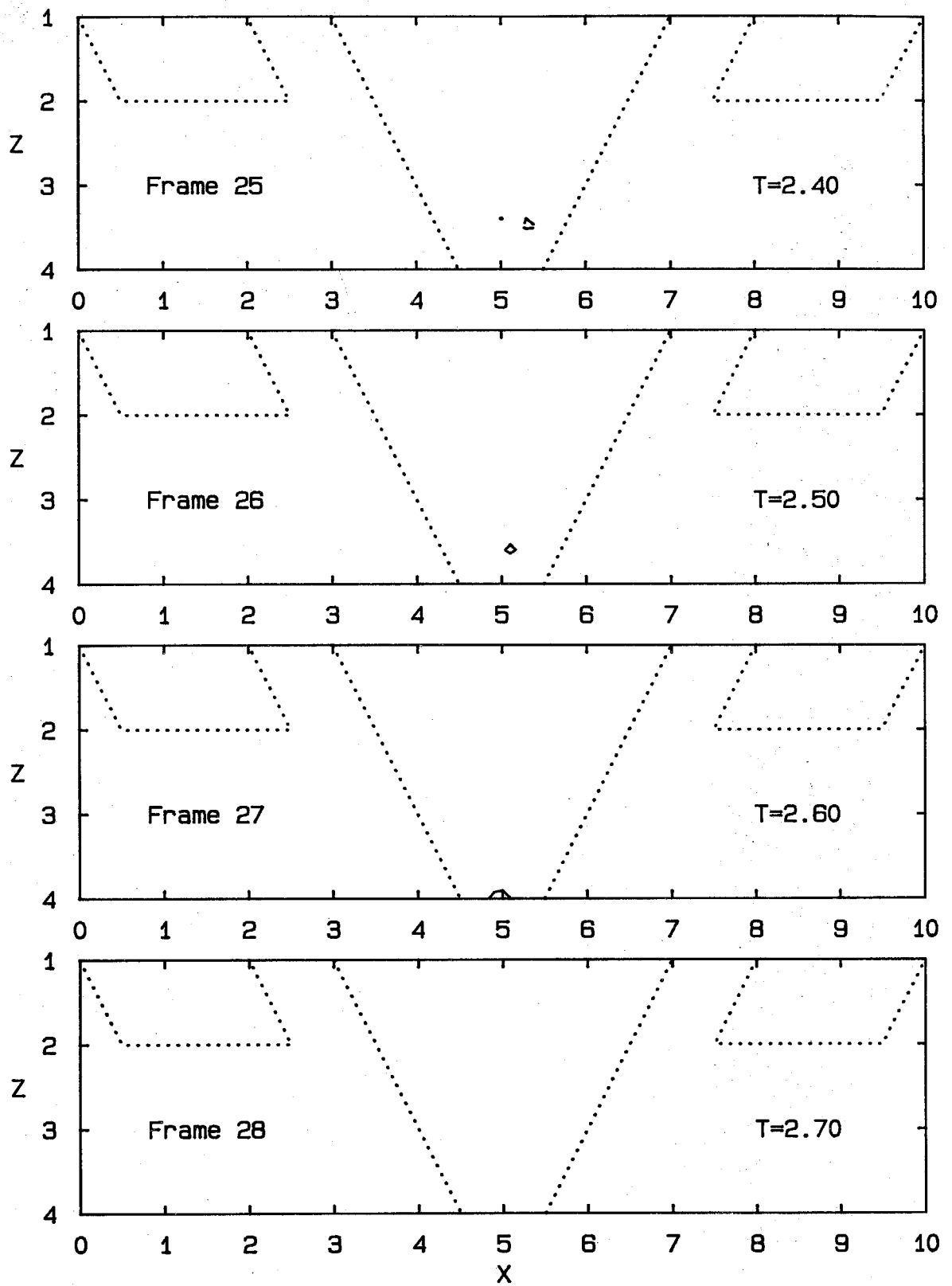

Fig. B.5 Components of Vorticity Equation; $\nu\nabla^2\omega_y$